This is to certify that the
dissertation entitled

DIFFERENTIAL POLARIZATION OF SPIN AND CHARGE DENSITY IN PHENOXY RADICALS, SEMIQUINONE RADICALS, AND NICKEL(II) AND CHROMIUM(III) PHENANTHRENESEMIQUINONE COMPLEXES

presented by

Richard J. Fehir Jr.

has been accepted towards fulfillment
of the requirements for the

Ph.D. degree in Chemistry

Major Professor's Signature

5/8/09

Date

DIFFERENTIAL POLARIZATION OF SPIN AND CHARGE DENSITY IN PHENOXY RADICALS, SEMIQUINONE RADICALS, AND NICKEL(II) AND CHROMIUM(III) PHENANTHRENESEMIQUINONE COMPLEXES

By

Richard J. Fehir Jr.

A DISSERTATION

Submitted to
Michigan State University
in partial fulfillment of the requirements
for the degree of

DOCTOR OF PHILOSOPHY

Chemistry

2009

ABSTRACT

DIFFERENTIAL POLARIZATION OF SPIN AND CHARGE DENSITY IN PHENOXY RADICALS, SEMIQUINONE RADICALS, AND NICKEL(II) AND CHROMIUM(III) PHENANTHRENESEMIQUINONE COMPLEXES

By

Richard J. Fehir Jr.

A density functional theory (DFT) investigation has been conducted on *para*-substituted phenoxy radicals in an effort to understand the factors influencing spin and charge density distribution in open shell systems. The charge density variation correlated well with the Hammett-Brown (σ_p^+) constants for each substituent, indicating that inductive and resonance effects are responsible for charge density variations within the molecule. However, the calculations revealed that the distribution of spin and charge are not correlated: cases were found for which spin and charge move in concert, whereas for other substituents the two quantities exhibit different polarizations. We uncovered an empirical relationship between spin density polarization and the α-HOMO-α-LUMO gap of substituted phenoxy radicals. This led to the development of a model based on a three-electron, two-orbital scheme in which mixing between the HOMO of the substituent and the SOMO of the phenoxy radical largely dictates the nature of the unpaired spin distribution throughout the molecule. DFT calculations were also carried out on 3,6- and 4,5-R-*o*-1,2-semiquinones and 2,7- and 3,6-R-*o*-9,10-phenanthrenesemiquinones and similar trends have been observed.

The effect of coordination upon the spin density distribution in nitro-substituted phenanthrenesemiquinone (PSQ) radicals was examined in gallium(III) 3,6- and 2,7-di-

NO_2-PSQ compounds by electron paramagnetic resonance spectroscopy (EPR) and electron spin echo envelope modulation spectroscopy (ESEEM). The ^{14}N hyperfine coupling constants (HFC) determined from ESEEM spectroscopy indicated a small increase in the spin density polarization in the Ga-3,6-di-NO_2-PSQ complex compared to the free radical ligand, while the Ga-2,7-di-NO_2-PSQ complex exhibited a much larger ^{14}N HFC. The larger ^{14}N for Ga-2,7-di-NO_2-PSQ was determined to be due to direct spin density delocalization onto the nitrogen nucleus, whereas the nitrogens in Ga-3,6-di-NO_2-PSQ attain spin population from only the spin polarization mechanism.

The effect of spin density delocalization on the magnitude of the Heisenberg exchange coupling between a paramagnetic transition metal and the PSQ radical was elucidated from both a DFT and experimental magnetic susceptibility examination of Ni^{II} and Cr^{III}-PSQ complexes. DFT calculations have shown that electron donors increase the exchange coupling constant (J) and decrease the spin density at the oxygen atoms of the PSQ ligand, while electron acceptors exhibit the opposite trend. Analogous to the phenoxy radicals, the HOMO-LUMO gap was observed to be the marker for spin delocalization in both ferromagnetically and antiferromagnetically exchange coupled Ni^{II}-PSQ and Cr^{III}-PSQ complexes, respectively. Experimental magnetic measurements confirmed that an electron donor decreased the J value in the [Ni(tren)(3,6-di-NH_2-PSQ)](BPh_4) (where tren = tris-2-aminoethylamine) complex, since in all other cases J is too strong to be determined experimentally. These results could have implications in the field of molecular magnetism by providing a mechanism for synthetically tuning the magnitude of intramolecular exchange interactions in a rational and predictable fashion.

This thesis is dedicated to Richard Sr., MaryAnn, Sarah, and Margaret Fehir, Mary Knop, the entire Fehir Family, and for Rachel.

ACKNOWLEDGEMENTS

First of all I would like to thank my advisor Jim McCusker for all the help and guidance he has provided me throughout my graduate school career. Jim always had a way to "fire me up" about science and to focus my thoughts on thinking deeply about my project. I thank the entire McCusker group for all their aid during my group meetings, seminar preparations, and for the great moments at the whiteboard. A few members must be singled out, and I thank Joel Schrauben and Dong Guo for their kindness in critically evaluating this thesis. I also thank Dong for bestowing upon me his expert synthetic advice and training in air-sensitive chemistry and for solving all my X-ray structures. I have also enjoyed the times spent with my EPR collaborators Matt Krzyaniak, Joel, and Prof. John McCracken with the "boat anchor" and collecting some great ESEEM data. I also thank Dr. Reza Lolee for his constant assistance with the SQUID magnetometer.

I would also like to thank my family for their unending support during my tenure at Michigan State, and of course Rachel for keeping me sane during the PhD process. I am also grateful to my friends Chris Boy, T-Roy, DB, Joel, Johnny Bravo, the Captain, Mikey, Speedo, Berry, Tana, Kate, Johnny OC, and Blondie for all the great times here at State, and I know we will have many more! I will miss all of our outings to the Dairy Store, Big B, the RIV, and 40's at group meeting. Thanks for making my time here some of the best years of my life.

TABLE OF CONTENTS

LIST OF TABLES

LIST OF FIGURES

Images in this dissertation are presented in color.

Chapter 1. Introduction to Heisenberg Exchange Coupling and the Importance of Spin Density Polarization and Delocalization.

1.1 Introduction to Heisenberg Exchange Coupling

Interest in Heisenberg exchange coupling is expanding from its origins in fundamental electronic structure research to encompass a variety of disciplines from biology to materials science.[1-6] For example, it has been suggested that exchange coupling plays a role in the oxidation of alcohols to aldehydes coupled with the reduction of oxygen to peroxide in the enzyme galactose oxidase.[7,8] The ability to modulate the exchange coupling constant can also have far reaching applicability to aid chemists in designing molecular magnetic materials.[9-14] A number of workers have suggested that increasing the strength of the exchange coupling constant in molecular magnetic materials can increase the critical temperature at which these materials become magnets.[12,15] It is known that the exchange coupling constant can be modulated by molecular confirmation,[6,16] electron delocalization,[17,18] and by substituents[19,20] for organic systems. Shultz et al. have also shown that the exchange coupling constant can be modulated by substituents in Cu^{II}- and Mn^{II}-5-aryl-substituted semiquinones,[21] but the mechanism for the changes was not firmly developed. Several workers have suggested that the magnitude of the Heisenberg exchange coupling interaction is proportional to the spin densities at the interacting atoms.[22-26] Along these lines, spin polarization in radical ligands must be fully understood to aid in the intelligent design of molecular magnetic materials and to properly predict the exchange coupling constants. The overall goal of this thesis is to further our understanding of the relationship between spin density and the

exchange coupling constant. In this regard, the cause and effect relationship of substituent perturbations to the spin density population at a paramagnetic center is critical for the understanding of the mechanism to modulate the exchange coupling interaction.

Exchange coupling is an electrostatic interaction that arises whenever two or more paramagnetic centers are in close proximity.[27] In order for exchange coupling to occur, three general criteria must be met: (1) each constituent undergoing the exchange interaction must have unpaired electrons; (2) there must be an orbital pathway (usually orthogonal or non-orthogonal) for the unpaired spins to interact; and (3) there must be a reasonable energetic match between the orbitals involved in the exchange pathway.[28] These interactions can be present in the excited state as well as the ground state, and spin exchange effects can cause large perturbations to both the ground and excited state electronic structure of molecules. The most common type of exchange coupling is intramolecular exchange, where either direct exchange or superexchange interactions can occur. Direct exchange is the through-bond overlap between two spin centers and has been observed in several transition metal semiquinone,[29] verdazyl,[30] and nitroxide[31] radical complexes. Superexchange coupling occurs through a diamagnetic bridge and has been observed in several transition metal dimers, with those of copper(II) ions being the most thoroughly examined.[1,32-34] Intermolecular or through-space exchange interactions between different molecules can also occur, but are usually found to be very weak in magnitude compared to intramolecular exchange coupling.[35] Additionally, both intra- and intermolecular exchange can be operative in transition metal complexes and each interaction can be important in determining the ground state magnetic properties.[1]

The Heisenberg Hamiltonian (**H**) for the interaction between two spin operators $\mathbf{S}_1$ and $\mathbf{S}_2$ on different centers is depicted in Equation 1, where J_{12} is the exchange integral that measures the magnitude of the electronic coupling between spin centers $\mathbf{S}_1$ and $\mathbf{S}_2$.

$$\mathbf{H} = J_{12}\mathbf{S}_1 \cdot \mathbf{S}_2 \qquad (1)$$

The Hamiltonian in Equation 1 is also represented by using different terms for the exchange coupling constant, i.e. $2J_{12}$, $-J_{12}$, and $-2J_{12}$. The form used in Equation 1 indicates that if $J > 0$ ferromagnetic exchange coupling ensues, and if $J < 0$ there will be antiferromagnetic exchange coupling. The most common types of exchange coupling, ferromagnetic and antiferromagnetic exchange, are described below. For two $S = {}^1/_2$ spin centers undergoing an antiferromagnetic exchange coupling interaction the following energy level diagram for the coupled spin states can be drawn according to Figure 1-1. In the direct exchange regime an antiferromagnetic interaction can occur if there is overlap of the magnetic orbitals between the unpaired spin centers, and following Hund's rules the spins will pair and the singlet state will be lower in energy.

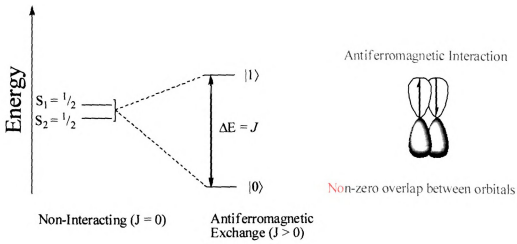

Figure 1-1. Antiferromagnetic exchange coupling interaction between two $S = {}^1/_2$ spin centers leading to a singlet ground state. States are labeled as $|S_T\rangle$, where S_T is the total spin.

The opposite situation occurs for a ferromagnetic interaction between two S = $^1/_2$ spin states and the S = 1 state is lower in energy as seen in Figure 1-2. The magnetic orbitals of the two spin centers must be strictly orthogonal for a ferromagnetic interaction to operate, and following Hund's rule the direction of the spin vectors is the same leading to an S = 1 ground state as depicted in Figure 1-2.

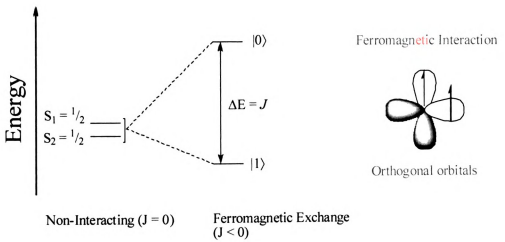

Figure 1-2. Ferromagnetic exchange coupling interaction between two S = $^1/_2$ centers leading to a triplet ground state.

An example in the literature where the above rules can be applied is in the case of [Ni(CTH)(3,5-di-*t*-butylsemiquinone)](PF_6) or Ni^{II}-SQ (CTH = dl-5,7,7,12,14,14-hexamethyl-1,4,8,11-tetraazacyclotetradecane), where strong ferromagnetic coupling between an S = 1 Ni^{II} center and a S = $^1/_2$ semiquinone radical has been experimentally observed.[36] In the case of the Ni^{II}-SQ complex, the $d_{X^2-Y^2}$ and d_{Z^2} magnetic orbitals on the Ni^{II} have σ^*-symmetry and the unpaired electron in the PSQ radical is in a π^*-symmetry orbital. These orbitals are strictly orthogonal and Hund's rules require that the unpaired electrons on the Ni^{II} (S = 1) and the PSQ (S = $^1/_2$) undergo ferromagnetic

exchange coupling, giving rise to a $S = {}^3/_2$ ground state and a $S = {}^1/_2$ excited state, as seen in Figure 1-3.

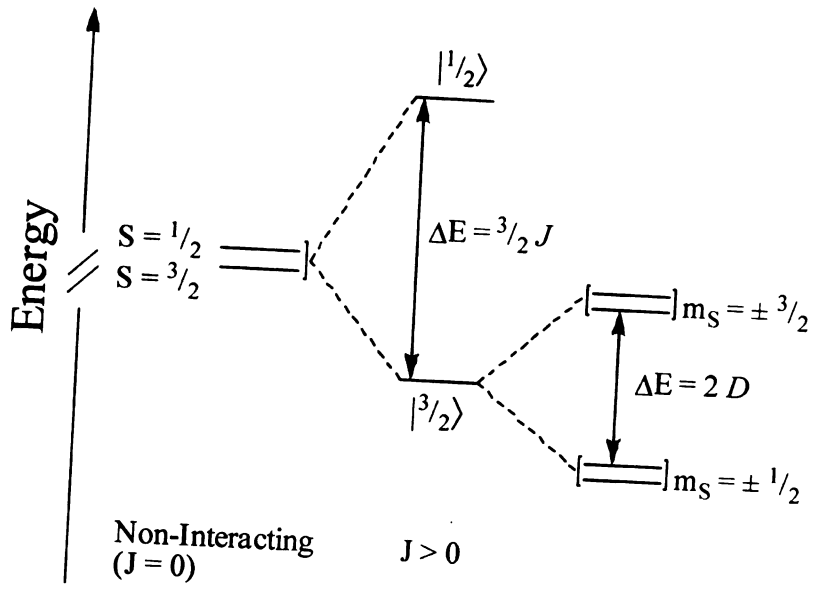

Figure 1-3. Ferromagnetic coupling between the $S = {}^3/_2$ and $S = {}^1/_2$ of [Ni(CTH)(3,5-di-t-butylsemiquinone)](PF_6). The energetic results of zero field splitting of the $S = {}^3/_2$ state is also depicted, where *D* is much smaller in comparison to *J*.

An operator-equalivant form of Eq 1 can be generated by applying the Kambe[37] method of a vector coupling of spin operators, where $\mathbf{S}_T = \mathbf{S}_1 + \mathbf{S}_2$, to yield Equation 2

$$\mathbf{H} = {}^1/_2 \cdot J_{12} \cdot (\mathbf{S}_T{}^2 - \mathbf{S}_1{}^2 - \mathbf{S}_2{}^2) \qquad (2)$$

and recall from quantum mechanics that when a squared operator ($\hat{O}p^2$) operates on the wavefunction the eigenvalue can be determined by Equation 3

$$\hat{O}p^2\Psi = Op(Op + 1)\Psi \qquad (3)$$

and using Equation 3 and the operator-equalivant Hamiltonian the eigenvalues can be determined according to Equation 4

$$E = {}^1/_2 \cdot J_{12} \cdot (S_T(S_T+1) - S_1(S_1+1) - S_2(S_2+1)) \qquad (4)$$

We can utilize Equation 4 to calculate the eigenvalues for the Ni^{II}-SQ spin system as seen below,

$$E_{S=\frac{3}{2}} = -\frac{1}{2}J_{12}\left(\frac{15}{4} - \frac{8}{4} - \frac{3}{4}\right) = -\frac{1}{2}J_{12}$$

$$E_{S=\frac{1}{2}} = -\frac{1}{2}J_{12}\left(\frac{3}{4} - \frac{8}{4} - \frac{3}{4}\right) = J_{12}$$

$$\left|E_{S=\frac{3}{2}} - E_{S=\frac{1}{2}}\right| = \frac{3}{2}J_{12} \qquad (5)$$

where the energy difference between the S = $^3/_2$ and S = $^1/_2$ sates is $^3/_2$ J_{12}. At room temperature, if the magnitude of J >> k_BT then an isolated ground state is observed with no population of the excited state. The lack of thermal population of the S = $^1/_2$ state occurs since the energy gap is much larger than thermal energy available at room temperature (~ 208 cm^{-1}). The magnitude of J in the Ni^{II}-SQ complex has been estimated to be greater than 400 cm^{-1} indicating very strong ferromagnetic coupling and confirming an isolated quartet ground state.

The exchange coupling interaction occurs in zero applied magnetic field, and other interactions may also present that perturb the electronic structure of this Ni^{II}-SQ complex. One possible interaction is called zero field splitting. The magnitude of the splitting is equal to the zero field splitting constant, D. Zero field splitting is one mechanism that lifts the ground state degeneracy and results in the splitting of the S = $^3/_2$ into the m_S = ± $^3/_2$ and ± $^1/_2$ states as depicted in Figure 1-3. The contribution from zero field splitting to lift the degeneracy of the S = $^3/_2$ ground state of the Ni^{II}-SQ cation is a symmetry effect. This state is 4-fold degenerate (2S + 1) and the symmetry of the Ni^{II}-SQ complex can be approximated by the C_{2v} point group which can only support 1-fold

degeneracy, thus the ground state must split according to symmetry rules. The zero field energy gap can be derived in an analogous manner to the exchange coupling constant. The Hamiltonian for zero field splitting is shown in Equation 6, where $\mathbf{S}_Z^2$ is the z-component of the spin angular momentum and $\mathbf{S}_T$ is the total spin.

$$\mathbf{H}_{zfs} = D\cdot\mathbf{S}_Z^2 - {}^1/_3\cdot\mathbf{S}_T^2 \qquad (6)$$

Utilizing Equation 4 and recalling that $\mathbf{S}_Z^2\Psi = m_S^2\Psi$[38] the eigenvalues can be determined by Equation 7,

$$E_{zfs} = D\cdot(m_S^2) - {}^1/_3\cdot S_T\cdot(S_T+1)) \qquad (7)$$

and the energy gap caused by zero field splitting will then be:

$$E_{S_z=\frac{3}{2}} = D\left(\frac{9}{4}-\frac{5}{4}\right) = D$$

$$E_{S_z=\frac{1}{2}} = D\left(\frac{1}{4}-\frac{5}{4}\right) = -D$$

$$\left|E_{S_z=\frac{3}{2}} - E_{S_z=\frac{1}{2}}\right| = 2D \qquad (8)$$

In Figure 1-3, D is assumed to be positive giving the $m_S = \pm {}^1/_2$ states as the lowest in energy, but the sign of the D value must be experimentally determined from EPR spectroscopy. An appreciable zero field splitting can decrease the observed magnitude of the magnetic susceptibility at low temperatures. This is due to non-zero population of the $S = \pm {}^1/_2$ states in Figure 1-3 when compared to only population of the $S = {}^3/_2$ state. When the thermal energy exceeds the zero field splitting then the susceptibility will correspond to the expected $S = {}^3/_2$ state. At low temperatures lower susceptibility values are experimentally observed for the Ni^{II}-SQ complex, which has $D = 2.54\ cm^{-1}$.

For molecular systems the magnitude of J is usually determined from measuring the macroscopic molar magnetization (M) of a sample as a function of temperature. The macroscopic magnetization is a sum of the microscopic magnetizations of all spin states weighted according to the Boltzmann distribution.[1] The magnetization is related to the magnetic susceptibility by the following, where χ is the molar magnetic susceptibility and B is the magnetic field.

$$\chi = \frac{M}{B} \tag{9}$$

The magnetic susceptibility can also be described by the following general expression[1] for the Van Vleck Equation in Eq 10,

$$\chi = \frac{N_A g^2 \mu_B^2}{3kT} \frac{\sum_S S(S+1)(2S+1)e^{-E(S)/kT}}{\sum_S (2S+1)e^{-E(S)/kT}} \tag{10}$$

where N_A is Avogadro's number, k is Boltzmann's constant, g is the gyromagnetic factor of the electron, μ_B is the Bohr Magneton, T is the temperature, S is the total spin quantum number of a given spin state, and E(S) are the eigenvalues from the Heisenberg Hamiltonian (Eq 1) that depend on J. Equation 10 is then compared with the measured values of χ as a function of temperature and the exchange coupling constant(s) can be determined by a least-squares fitting.

1.2 Importance of Spin Polarization and Delocalization

The focus of this dissertation will be on transition metal complexes that are directly coordinated to organic radicals, thus a major factor to control spin density at the paramagnetic centers will be spin delocalization or localization in the organic radicals.

The organic radicals of choice are the *o*-semiquinones (SQ) shown in Scheme 1-1, where the molecule as a whole is non-innocent due to its redox reactivity and can also exist in the quinone and catechol redox states. Transition metal complexes with the semiquinone ligands are well known and have been studied extensively.[39-43] The magnetic properties of transition metal semiquinones has also been reviewed in complexes containing one to three coordinated semiquinone ligands.[29] In order to focus on the effects of spin polarization, this thesis will only focus on transition metals coordinated to one semiquinone radical.

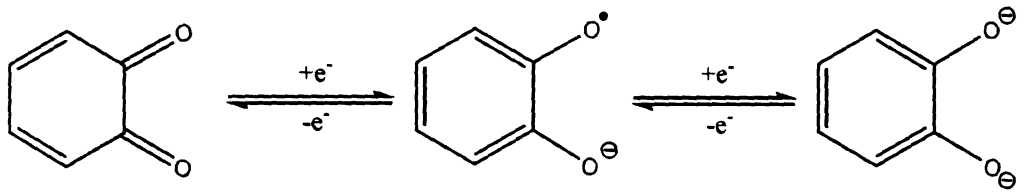

Quinone Semiquinone Catechol

Scheme 1-1. The redox states of the *o*-quinone ligands.

The substituent effects of radical spin delocalization and polarization will be important to develop a prescription to predictably change the spin density population in radicals so that the *J* value can be modulated in transition metal organic radical complexes. If a basic theory that relates the spin density in the radical to *J* can be found, the intelligent design of exchange coupled molecular magnetic materials can be achieved. Efforts to understand and characterize the model that can predictably control the spin density at a magnetic center and the *J* value in an exchange coupled system is the main focus of this work.

1.3 Contents of Dissertation

The heart of this research can be split up into three main fronts; (1) computational studies of spin and charge polarization in phenoxy and semiquinone radicals; (2) electron paramagnetic resonance spectroscopy of semiquinones and gallium complexes; and (3) the synthesis and magnetic characterization of Ni^{II}- and Cr^{III}-semiquinone complexes combined with a DFT study of exchange coupling interactions. The literature is lacking in the deep understanding of the intimate movement of spin and charge density in radicals, and coupled with this is a need to develop a more in-depth knowledge of the substituent effect on the exchange coupling constant. The contributions of this thesis along these lines is highlighted below.

Chapter 2 begins with the DFT examination of a series of *para*-substituted phenoxy radicals in an effort to understand the factors influencing spin and charge density distribution in open-shell systems. The calculations reveal that the distribution of spin and charge are not correlated: cases were found for which spin and charge move together, whereas for other substituents the two quantities exhibit spatially distinct intramolecular polarizations. Charge density variations across the series were found to correlate well with both the Hammett (σ_p) and Hammett-Brown (σ_p^+) constants for each substituent, indicating that inductive and/or resonance effects are primarily responsible for the polarization of charge within the molecule. In contrast, the distribution of unpaired spin density could not be adequately accounted for using any of the typical Hammett-type spin delocalization constants cited in the literature. We uncovered an empirical correlation between the polarization of spin density and the α-HOMO-α-LUMO gap of the substituted phenoxy radicals: this led to the development of a simple

model based on a three-electron, two-orbital bonding scheme in which mixing between the HOMO of the substituent and the SOMO of the phenoxy moiety serves to define the nature and extent of unpaired spin polarization throughout the molecule. This analysis yielded a correlation coefficient of $r > 0.97$ for the 15 substituents examined in the study; spin polarization effects in compounds that exhibited the greatest deviation from this correlation could also be readily explained within the context of the model. The underlying reason for the ability to differentially polarize spin and charge likely stems from the fact that net unpaired spin density is completely carried by the unpaired electron (and thus the spatial characteristics of the SOMO), whereas charge density reflects the behavior of all of the electrons of the system. This research laid down a basic understanding of how to manipulate spin and charge density in a paramagnetic radical ligand. In order to apply this knowledge to transition metal based systems, ligands that can easily bind to a metal center were needed. This led to the examination of substituted *ortho*-semiquinone complexes since transition metal complexes with these ligands are well-known.[29,39-41,44]

Chapter 3 uses DFT to examine the spin and charge polarization in 3,6-*o*-1,2-semiquinones, 4,5-*o*-1,2-semiquinones, and *o*-9,10-phenanthrenesemiquinones. Spin and charge density were found to differentially polarize. In all cases the Hammett substituent constants correlated with the change in charge density at the oxygen atoms. The spin density mechanism was found to be more complicated than in the phenoxy radical case, and unfavorable charge-dipole interactions increased spin density at the oxygen atoms. Substituents that are strong electron donors were found to destabilize the negative charge within the ring, and spin density was localized on the oxygen atoms. Electron acceptors

were found to stabilize the negative charge and decrease the spin density at the oxygen centers. The spin density was again found to correlate with the α-HOMO-α-LUMO gap, but the correlation could not be as easily accounted for using MO theory as the phenoxy radical case. Even though the mechanism of spin delocalization could not be firmly established, it was noted that the trend in the α-HOMO-α-LUMO gap with the spin density is a marker for the spin delocalization. Proper choice of substituents in the semiquinone radicals can lead to increases or decreases in the spin density at the oxygen atoms, and this prescription will be used to see if the same trends are observed in transition metal systems.

In an effort to uncover any changes in spin delocalization/polarization when semiquinone radical ligands are coordinated to a metal center, Ga^{III}-nitro-phenanthrenesemiquinone complexes were examined by DFT and electron paramagnetic resonance (EPR) spectroscopy, which is described in Chapter 4. The nitrated radical ligands 3,6-di-NO_2-phenanthrenesemiquinone (3,6-di-NO_2-PSQ) and 2,7-di-NO_2-phenanthrenesemiquinone (2,7-di-NO_2-PSQ) were perturbed with X-band EPR and electron spin echo envelope modulation spectroscopy (ESEEM) to experimentally determine the spin density population on the nitro-substituents by observing the ^{14}N hyperfine coupling constants (HFC). The 3,6- and 2,7-di-NO_2 radicals were both found to have weak HFC of ^{14}N = 0.35 and 0.15 G, respectively. The ^{14}N HFC is due to spin polarization, which agreed very well with the predicted ^{14}N HFC from DFT calculations. Upon complexation to the Ga^{III} the X-band data are dominated by gallium HFC, and the ^{14}N could not be determined in either complex. ESEEM spectroscopy was successful in determining the ^{14}N for the Ga^{III} complexes, and Ga-3,6-di-NO_2-PSQ ^{14}N = 0.453 G and

Ga-2,7-di-NO_2-PSQ ^{14}N = 2 G. The ESEEM data indicated that there is a large difference in the magnitude of the ^{14}N HFC and the spin density that is delocalized onto the nitrogens. The ESSEM data suggest that direct spin delocalization onto the nitrogen nuclei is operating in the Ga-2,7-di-NO_2-PSQ complex[45] and spin polarization effects are responsible for the smaller HFC in the Ga-3,6-di-NO_2-PSQ system. The DFT results were noted to predict the incorrect spin distribution in the Ga-2,7-di-NO_2-PSQ complex, and the HFC was calculated to be a factor of seven times lower in magnitude. Thus large differences are observed in the spin distribution upon complexation to a metal center, and DFT may not adequately describe the spin density distribution in the Ga-2,7-di-NO_2-PSQ complex.

Chapter 5 pools the collected knowledge of the previous chapters to evaluate the effects of substituents on the spin density distribution and *J* value in Ni^{II} and Cr^{III} phenanthrenesemiquinone systems. A seminal paper by Andrea Dei and coworkers showed that a Ni^{II}-PSQ complex had a decreased *J* value than the comparable 3,6-*t*-butylsemiquinone complex.[46] Consequently substituted PSQ ligands were chosen for our study. The exchange coupling constants were calculated according to the approximate spin projection technique of Yamaguchi et al.[47] by DFT methods. The DFT results for the ferromagnetically coupled Ni^{II}-PSQ complexes indicated that the spin density at the oxygen atoms correlated with the magnitude of the exchange coupling constant, and substituents that increased spin density increased *J* and groups that decreased the spin density decreased *J*. A three-electron, two-orbital MO scheme was used to describe the spin delocalization in these systems. Experimental SQUID data also confirmed that electron donors decrease the *J* value and electron acceptors increase *J*. Analogous results

were also obtained for the antiferromagnetically coupled Cr^{III}-PSQ complexes. These results are significant, since control of the exchange coupling constant with substituents can lead to clever design of molecular magnetic materials. Concluding comments and future directions are included in Chapter 6, where the implications of the previous chapters are reviewed and possible future directions for this research project are outlined.

1.4 References

1 Kahn, O. *Molecular Magnetism*; VCH Publishers: New York, 1993.

2 Kahn, O. *Acc. Chem. Res.* **2000**, *33*, 647.

3 Beltran, L. M. C.; Long, J. R. *Acc. Chem. Res.* **2005**, *38*, 325, and references therein.

4 Holm, R. H.; Kennepohl, P.; Solomon, E. I. *Chem. Rev.* **1996**, *96*, 2239.

5 Yoon, S.; Lippard, S. J. *J. Am. Chem. Soc.* **2005**, *127*, 8386.

6 Shultz, D. A.; Fico, R. M., Jr.; Bodnar, S. H.; Kumar, R. K.; Vostrikova, K. E.; Kampf, J. W.; Boyle, P. D. *J. Am. Chem. Soc.* **2003**, *125*, 11761.

7 Itoh, S.; Taki, M.; Fukuzumi, S. *Coord. Chem. Rev.* **2000**, *198*, 3.

8 Whittaker, M. M.; Ekberg, C. A.; Peterson, J.; Sendova, M. S.; Day, E. P.; Whittaker, J. W. *J. Mol. Catal. B.: Enzym.* **2000**, *8*, 3.

9 Luneau, D. *Curr. Opin. Solid State Mater. Sci.* **2001**, *5*, 123.

10 Öhrstrom, L. *C. R. Chimie* **2005**, *8*, 1374.

11 Shultz, D. A. *Polyhedron* **2001**, *20*, 1627.

12 Caneschi, A.; Gatteschi, D.; Sessoli, R.; Rey, P. *Acc. Chem. Res.* **1989**, *22*, 392.

13 Vostrikova, K. E. *Coord. Chem. Rev.* **2008**, *252*, 1409.

14 Kirk, M. L.; Shultz, D. A.; Depperman, E. C. *Polyhedron* **2005**, *24*, 2880.

15 Kahn, O.; Martinez, C. J. *Science* **1998**, *279*, 44.

16 Shultz, D. A.; Fico, R. M., Jr.; Lee, H.; Kampf, J. W.; Kirschbaum, K.; Pinkerton, A. A.; Boyle, P. D. *J. Am. Chem. Soc.* **2003**, *125*, 15426.

17 Shultz, D. A.; Kumar, R. K. *J. Am. Chem. Soc.* **2001**, *123*, 6431.

18 Franzen, S.; Shultz, D. A. *J. Phys. Chem. A* **2003**, *107*, 4292.

19 Shultz, D. A.; Bodnar, S. H.; Lee, H.; Kampf, J. W.; Incarvito, C. D.; Rheingold, A. L. *J. Am. Chem. Soc.* **2002**, *124*, 10054.

20 West, A. P., Jr.; Silverman, S. K.; Dougherty, D. A. *J. Am. Chem. Soc.* **1996**, *118*, 1452.

21 Shultz, D. A.; Sloop, J. C.; Coote, T.-A.; Beikmohammadi, M.; Kampf, J.; Boyle, P. D. *Inorg. Chem.* **2007**, *46*, 273.

22 Sugiura, K.-I.; Arif, A. M.; Rittenberg, D. K.; Schweizer, J.; Öhrstrom, L.; Epstein, A. J.; Miller, J. S. *Chem. Eur. J.* **1997**, *3*, 138.

23 Osanai, K.; Okazawa, A.; Nogami, T.; Ishida, T. *J. Am. Chem. Soc.* **2006**, *128*, 14008.

24 McConnell, H., M, *J. Chem. Phys.* **1963**, *39*, 1910.

25 Hicks, R. G.; Lemaire, M. T.; Thompson, L. K.; Barclay, T. M. *J. Am. Chem. Soc.* **2000**, *122*, 8077.

26 Shultz, D. A.; Sloop, J. C.; Washington, G. *J. Org. Chem.* **2006**, *71*, 9104.

27 Ginsberg, A. P. *Inorg. Chim. Acta. Rev.* **1971**, *5*, 45.

28 Wheeler, D. E.; McCusker, J. K. *Inorg. Chem.* **1998**, *37*, 2296-2307.

29 Pierpont, C. G.; Attia, A. S. *Collect. Czech. Chem. Commun.* **2001**, *66*, 33.

30 Hicks, R. G. *Aust. J. Chem.* **2001**, *54*, 597.

31 Eaton, S. S.; Eaton, G. R. *Coord. Chem. Rev.* **1988**, *83*, 29.

32 Hay, P. J.; Thibeault, J. C.; Hoffmann, R. *J. Am. Chem. Soc.* **1975**, *97*, 4884.

33 Kahn, O.; Charlot, M. F. *Nouv. J. Chim.* **1980**, *4*, 567.

34 Güdel, H. U.; Stebler, A.; Furrer, A. *Inorg. Chem.* **1979**, *18*, 1021.

35 Schultz, D.; Weyhermüller, T.; Wieghardt, K.; Butzlaff, C.; Trautwein, A. X. *Inorg. Chim. Acta.* **1996**, *246*, 387.

36 Benelli, C.; Dei, A.; Gatteschi, D.; Pardi, L. *Inorg. Chem.* **1988**, *27*, 2831.

37 Kambe, K. *J. Phys. Soc. Japan* **1950**, *5*, 48.

38 Palmer, G. In *Physical Methods in Bioinorganic Chemistry: Spectroscopy and Magnetism*; Que, J., L., Ed.; University Science Books: Sausalito, 2000.

39 Pierpont, C. G.; Buchanan, R. M. *Coord. Chem. Rev.* **1981**, *38*, 45.

40 Pierpont, C. G.; Lange, C. W. *Prog. Inorg. Chem.* **1994**, *41*, 331.

41 Zanello, P.; Corsini, M. *Coord. Chem. Rev.* **2006**, *250*, 2000, and references therein.

42 Pierpont, C. G. *Coord. Chem. Rev.* **2001**, *216-217*, 99.

43 Kaim, W. *Coord. Chem. Rev.* **1987**, *76*, 187.

44 Pierpont, C. G. *Coord. Chem. Rev.* **2001**, *219*, 415.

45 McCracken, J.; Peisach, J.; Cote, C. E.; McGuirl, M. A.; Dooley, D. M. *J. Am. Chem. Soc.* **1992**, *114*, 3715.

46 Bencini, A.; Carbonera, C.; Dei, A.; Vaz, M. G. F. *Dalton Trans.* **2003**, 1701.

47 Yamaguchi, K.; Jensen, F.; Dorigo, A.; Houk, K. *Chem Phys. Lett.* **1988**, *149*, 537.

Chapter 2. Differential Polarization of Spin and Charge Density in Substituted Phenoxy Radicals

2.1 Introduction

Spin and charge represent two of the most fundamental physical properties in nature. Indeed, the role of these quantities in defining the electronic structures of atoms and molecules serves to underscore their importance in virtually all areas of molecular science. From relatively simple ideas such as nucleophilicity to more advanced concepts involving the emerging field of spintronics,[1-3] the interplay between these two related but distinct aspects of electronic structure represents an intriguing aspect of the chemistry of open-shell systems.

Many of our expectations concerning charge distribution in molecular systems are based on the concept of electronegativity. This simple yet fundamental idea provides the foundation for envisioning the polarization of charge in response to compositional changes in a molecule. The correlation of experimental observables with the various Hammett-type relations that have been developed over the years has helped to put these ideas on a more quantitative (though still largely empirical) basis.[4-8] In so doing, the physical-organic community in particular has been able to develop tremendous physical and mechanistic insights into the cause-and-effect relationship between charge polarization and chemical reactivity.[9-13]

A comparable level of understanding of the effect of spin on chemical reactivity suffers in part from the fact that there does not exist a similarly intuitive counterpart to electronegativity for spin polarization. Experimental techniques for measuring the

distribution of unpaired spin density – most notably EPR and ENDOR spectroscopies – have contributed greatly toward describing spin polarization in a wide range of chemical systems. The development of spin-unrestricted formalisms in density functional theory has also emerged as a powerful computational tool, particularly with regard to large molecules.[14-16] Such calculations can provide a description of unpaired spin polarization and provide a theoretical basis for correlating quantum-mechanical descriptions of systems with experimental data that directly[17,18] or indirectly[19-21] probe the spatial distribution of unpaired spin. The question of local spin and spin distribution in molecules, has been considered in detail by Reiher.[22] More recently, Lecomte and co-workers have pioneered the use of high-resolution electron density maps to probe spin-spin interaction mechanisms in a variety of systems based on a detailed analysis of electron density distributions.[23] Both of these efforts represent significant first steps toward making the connection between charge and spin density and assessing its impact on the physical and chemical properties of molecules.

In the field of magnetism, from which our interest in this issue originates, spin and charge play very different roles. For example, in inorganic-organic hybrid systems (e.g., metal-semiquinone complexes),[24-27] large formation constants will generally be favored when the donor atom from the ligand possesses negative charge density sufficient for it to act as a strong Lewis base to the metal ion. In this context, the charge density dictates, to a large extent, the stability of the adduct being formed. The magnitude of the exchange interaction between the paramagnetic constituents will reflect several variables, but significant among these is the spatial distribution of unpaired spin density. All other factors being equal,[28] polarization of unpaired spin density toward (or away) from the

ligating atoms will increase (or decrease) the magnitude of electronic coupling. The notion of altering the magnetic properties of molecules through chemical means has been addressed both computationally[29-32] and experimentally.[33-35] Recent work by Shultz and co-workers, in particular, has clearly demonstrated that spin delocalization contributes to the attenuation of exchange interactions in bridged polynuclear systems.[35-37] In related work, this team has also provided examples of metal-semiquinone complexes in which changes in ring substituents give rise to variations in the magnitude of intramolecular spin exchange.[38] Clearly, the ability to independently manipulate charge and spin density within the molecule has significant potential in terms of tailoring the thermodynamic as well as electronic properties of chemical systems.

At first glance, it would seem that spin and charge density should move in concert: since electrons carry both charge and spin, it seems reasonable that their polarizations should track each other. A case in point is the phenoxy radical, several resonance structures for which are shown in Scheme 1.

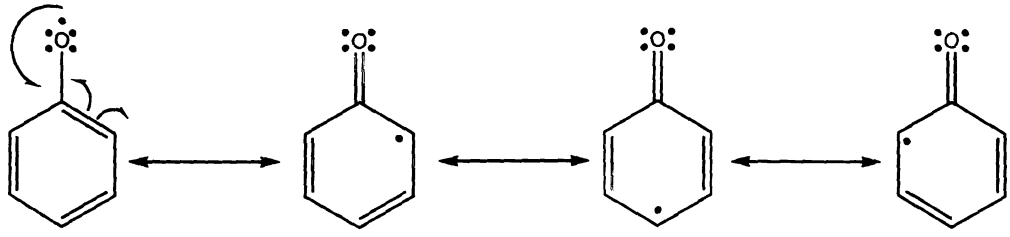

Scheme 1-1. Phenoxy radical resonance structures.

We can see that the unpaired electron can be localized on the oxygen atom as well as the *ortho*- and *para*-positions on the ring. EPR data have confirmed that a significant portion of the spin density is in fact localized at the *ortho*- and *para*-carbon atoms in the ring: ^{17}O hyperfine coupling constants of 2,4,6-tri-*t*-butylphenoxy and 2,4,6-triphenylphenoxy

radicals indicate that the spin density at the oxygen atom is approximately equal to the spin density at the *ortho*-carbons, a result that is wholly consistent with this picture.[39-42] Previous computational studies by various DFT methods support these findings in that a substantial fraction of the spin density was found to be associated with the oxygen atom.[43,44] Not surprisingly, these calculations also revealed that the oxygen carries most of the negative charge density. The combined experimental and theoretical data therefore show that the spin and charge density in the (unsubstituted) phenoxy radical are both polarized in the same direction, i.e. toward the oxygen atom. This case thus conforms to our initial expectations.

Though reasonable and in fact correct for some systems, there are indications that spin and charge polarization may not necessarily track one another. Contrast the above observations with what has been described for the ketyl radical. The resonance structures in Scheme 2 show that the spin or charge density can be accommodated at either the carbonyl carbon or the oxygen atom. DFT calculations have shown that the charge density is largely localized on the oxygen atom,[45] which is again consistent with our expectations based on the electronegativity of oxygen relative to carbon.

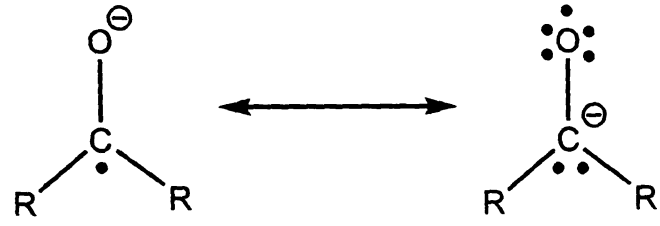

Scheme 1-2. Resonance structures of the ketyl radical.

The EPR spectrum of the benzophenone ketyl radical exhibits ^{17}O and ^{13}C hyperfine coupling constants consistent with the spin density on both atoms of the carbonyl unit,

however, the spin density was shown to be more highly localized at the carbon atom.[46-48] DFT calculations yielded similar results.

These results for two relatively simple chemical systems provide a convenient backdrop for the central question of this investigation: is it possible to design molecules in which spin and charge density can be independently manipulated? To examine this issue, we have carried out a computational study of substituted phenoxy radicals. This system has been examined in some detail by other workers, however, the question of spin versus charge polarization has not been explicitly addressed. In the course of analyzing our results, we have discovered a previously unrecognized correlation between spin polarization and electronic structure which we believe not only supports the notion of differential polarization of spin and charge, but suggests that the potential exists for the independent manipulation of these two variables through chemical means as a mechanism for tailoring the physical properties of molecules.

2.2 Experimental Section

General Methods. All self-consistent field Hartree-Fock and density functional calculations were carried out using Gaussian 98.[49] Both the BLYP and B3LYP functionals were used in the calculations. The BLYP functional contains the gradient corrected Becke (B)[50] exchange functional with the gradient corrected Lee, Yang, and Parr (LYP)[51] correlation functional, whereas the hybrid B3LYP functional contains the three parameter exchange of Becke (B3)[52] with the LYP correlation functional. All calculations were performed using tight convergence criteria.[53] Analysis of the atomic

charges and spin densities were performed using the natural population analysis (NPA) framework developed by Weinhold et al.[54] Calculations were carried out using the Michigan State University Chemistry Supercomputer Facility.

Geometry Optimizations. The initial geometries of the molecules were generated using SPARTAN[55] or GaussView[56] and subsequently optimized in three steps. The first optimization was performed using restricted open-shell Hartree-Fock (ROHF) theory with the STO-3G** basis set. These structures were then subjected to a second optimization using the restricted open-shell density functional ROBLYP with the 3-21G** basis set, followed by a third optimization using the ROB3LYP functional with the 6-31G* basis set. Frequency calculations at the ROB3LYP/6-31G* level of theory were performed on the final optimized structures to ensure that these geometries corresponded to global minima. In several cases (R = NH_2, NMe_2, OMe, and OEt), imaginary frequencies were obtained. For these systems, the molecules were distorted along those coordinates in order to find the lowest energy structure. The structure was then reoptimized at the ROB3LYP/6-31G* level and subjected to a subsequent frequency calculation. This procedure was repeated until no imaginary frequencies were found. In all cases, the final optimized structures were used in the single point calculations described below.

Single Point Calculations. Single point calculations were performed using the unrestricted density functional UB3LYP with the 6-311G** basis set assuming a doublet ground state and a molecular charge of zero. The maximum error for the expectation value of the spin operator $\langle \mathbf{S}^2 \rangle$ differed from the theoretical value for a pure spin state of $S(S + 1)$ (where S is the total spin) by an average error of 4.3%, and in no case exceeded

6%, indicating the degree of spin contamination in the Kohn-Sham Slater determinant is negligible for the molecules investigated.[15,57,58] The UBLYP functional with the 6-311G** basis was also used on a subset of substituents (H, Cl, OMe, NH_2, NO_2, and CF_3) to determine whether any calculated trends in charge and/or spin density distribution were functional dependent. Although specific values for charge and spin density were different, trends in structure, spin and charge density across the series were qualitatively similar. To simplify the discussion, the results reported here derive from calculations at the UB3LYP/6-311G** level.

The substituents examined in these calculations were selected to cover a wide range of possible interactions with the phenoxyl ring and included σ-donors (Me, *t*-butyl, and TMS), a σ-acceptor (CF_3), π-donors (OH, OMe, OEt, NH_2, and NMe_2), π-acceptors (NO_2 and CN), π-donor/σ-acceptors (F, Cl, and Br), and a π-acceptor/σ-donor (vinyl). In all cases the unsubstituted phenoxy radical (i.e., R = H) was used as a reference point for comparisons.

2.3 Results and Discussion

Geometries of *para*-Substituted Phenoxy Radicals. A crystal structure for the phenoxy radical has not been reported, however, it has been studied extensively using a wide range of computational methods.[43] Based on comparisons to the unsubstituted compound, our results indicate that the geometry of the phenoxy radical in terms of both bond distances and bond angles is largely insensitive to changes in the *para*-substituent on the ring. The most significant perturbation arises in the C–O distance for the vinyl

derivative, where a distance of 1.247 Å (versus 1.257 Å for R = H) was noted. A slight increase in double bond character was also observed for the NO_2- and CN-substituted compounds, though to a lesser extent. The resonance structures in Scheme 1 illustrate that the origin of double-bond character in the C–O bond arises from delocalization of lone-pair electrons on the oxygen into the ring. The slight increases in bond order observed for the three π-accepting substituents in this study can therefore be viewed as a reflection of this resonance effect. The influence of electron delocalization will be expanded upon later in the discussion in the context of spin polarization, but in terms of geometry this appears to be the only significant structural perturbation across this series.

Spin and Charge Density Movement in *Para*-substituted Phenoxy Radicals. A. Overview. This work was originally motivated by an interest in magnetic exchange interactions between transition metals and bound organic radicals such as orthosemiquinones.[59-61] For such systems, significant negative charge density at the oxygen atoms coupled with varying degrees of unpaired spin density would provide an entry into a series of compounds having tunable magnetic properties. Our initial computational efforts with this class of compounds were inconclusive due to the presence of competing effects from substituents that simultaneously have different regiospecific interactions with the two ligating oxygen atoms. We therefore sought to simplify the problem sufficiently to extract the basic phenomenological effects of compositional changes on spin and charge polarization that we could then use as a guide for an analysis of more complex systems.

A graphical depiction of our computational results is shown in Figure 2-1. Inspection of this plot provides an immediate answer to one of the central questions of

our study: differential polarization of spin and charge appears to be possible, even facile, given the proper choice of a substituent.

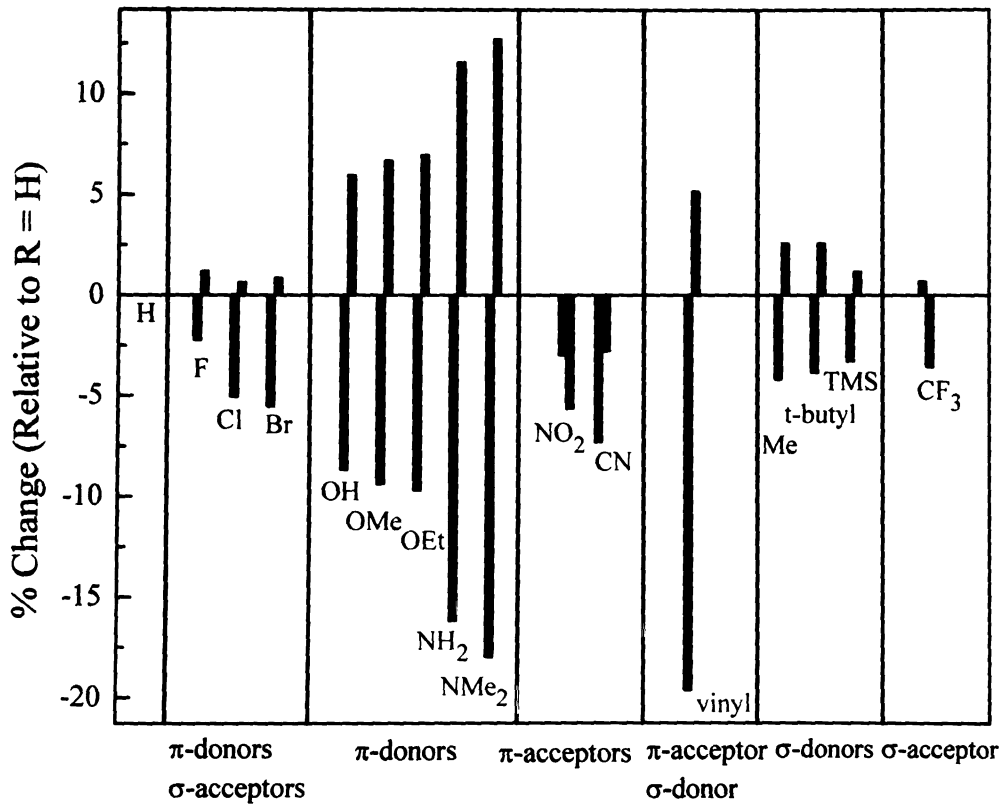

Figure 2-1. Shifts in charge (blue) and unpaired spin (red) density at the oxygen atom for a series of *para*-substituted phenoxy radicals. The % change in both parameters is referenced to values obtained for the unsubstituted compound (i.e. R = H, where spin = 0.43937 α-electrons and charge = -0.48359 electrons). A positive change indicates an increase in the magnitude of negative charge or an increase in spin density.

In fact, there are far more examples evident where shifts in spin and charge density oppose each other rather than track together. In principle, there are four regimes of spin and charge polarization that could be sampled corresponding to an increase and/or decrease of spin and/or charge at the oxygen atom. Figure 2-1 illustrates that three of these four regimes were realized, whereas none of the substituents we chose gave rise to a simultaneous increase in both spin and charge density at the oxygen atom. The degree of

polarization varies considerably depending on the specific identity of the substituent, although the most significant effects appear to be associated with substituents that can couple strongly to the π-system of the molecule. The magnitude of the shifts in spin and charge density in some cases are substantial: dimethylamine, for example, causes a nearly 20% reduction in spin density at the oxygen atom as compared to the unsubstituted phenoxy radical, while at the same time serves to increase the negative charge density at oxygen by over 10%. The vinyl group appears to induce a similar effect on spin, though its influence on charge density is less pronounced. Even seemingly innocuous substituents such as methyl and *t*-butyl are predicted to differentially polarize spin and charge. It is interesting to note that, in general, the substituent effect on spin polarization appears to be larger in a relative sense than the corresponding shift in charge, though exceptions to this trend are apparent (e.g., R = NO_2).

Clearly, spin and charge are responding differently to the perturbations introduced by the various substituents. As mentioned above, this simple observation addresses the question of whether spin and charge can be differentially polarized, however, in order for this to be of use the mechanism(s) of the effect must be understood.

B. Substituent Effects on Charge Density Distribution. Computational methods have been employed by many different groups in an effort to describe charge distributions in molecules.[62-64] Of greatest relevance to our work is a study by Wu and Lai, who employed density functional theory to examine the effect of *para*-substituents on charge density polarization in phenoxy radicals.[65] These authors demonstrated that the change in charge density at the oxygen atom correlates well with the Hammett-Brown[4,66] polar substituent constant (σ_p^+). The σ_p^+ constants derive from data on the solvolysis of *t*-

cumyl chlorides, an S_N1 reaction whose rate depends on the electrophilicity of the tertiary carbocation associated with the transition state. Thus, in the most common interpretation,[67] the σ_p^+ constant reflects the ability of a substituent to donate or remove charge density; based on its original definition,[66] negative values of σ_p^+ correspond to charge-donating substituents whereas positive values are considered electron-withdrawing (all relative to hydrogen). The σ_p^+ constants broadly encompass both inductive (σ-donating or σ-accepting) and resonance (π-accepting or π-donating) effects associated with the substituent.

The results of our calculations fully support the work of Wu and Lai; a plot of the change in charge density at the oxygen atom as a function of the σ_p^+ coefficient for each substituent that we examined is shown in Figure 2-2. The correlation in Figure 2-2 indicates that the individual resonance and inductive effects of the substituents are effective in modulating the charge density at the oxygen atom, with electron-donating and withdrawing substituents increasing and decreasing, respectively, the negative charge density at the oxygen atom. Overall, the results in Figure 2-2 conform to our qualitative expectations given the electronegativity of oxygen and the tendency of π-donors to increase electron density within an aromatic ring system. On a more quantitative level, the linearity of the correlation is consistent with what one expects from a Hammett-type plot, though the underlying reason for the empirical success of such plots is the subject of continued debate.[68] Experimental evidence indicating a correlation between σ_p^+ and the reduction potentials for phenoxy radicals (i.e., $PhO^\bullet + e^- \rightarrow PhO^-$) supports the notion that electron deficient radicals are stabilized by the transfer of negative charge density from the substituent to the oxygen radical.[69] The correlation in Figure 2-2 coupled with

the linear free energy relationship upon which the σ_p^+ constants are defined can therefore be interpreted as reflecting the ability of the substituent to inductively and/or resonantly stabilize the oxygen radical via the modulation of charge density within the molecule.[68]

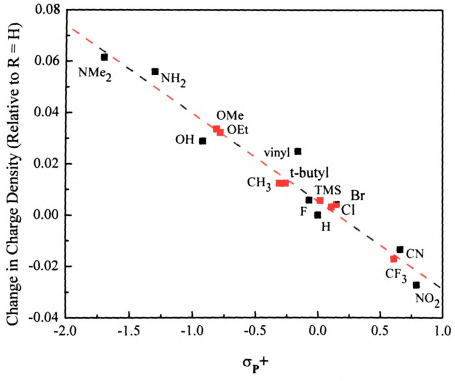

Figure 2-2. Plot of the calculated change in charge density at the oxygen atom as a function of the σ_p^+ coefficient of the R-group in *para*-substituted phenoxy radicals. The value given is relative to that obtained for the unsubstituted radical (i.e. R = H); a positive number indicates an increase in negative charge density at the oxygen atom. The σ_p^+ values were taken from the review by Hansch, Leo, and Taft (cf. 4). See text for further details.

C. Substituent Effects on Spin Polarization. The ability of substituents to influence the distribution of spin density within an aromatic system can be understood qualitatively by extending the resonance picture for the phenoxy radical as shown in Scheme 2-3. In the case of π-donors (A), adherence to the Pauli principle requires that the interaction between the lone-pair of the donor and the aromatic ring involve the effective transfer of an electron whose polarization is opposite to that associated with the carbon at

the *para* position: arbitrarily assigning the spin density within the ring as α, substituents with lone pairs having π-symmetry can therefore be viewed as β-spin donors.

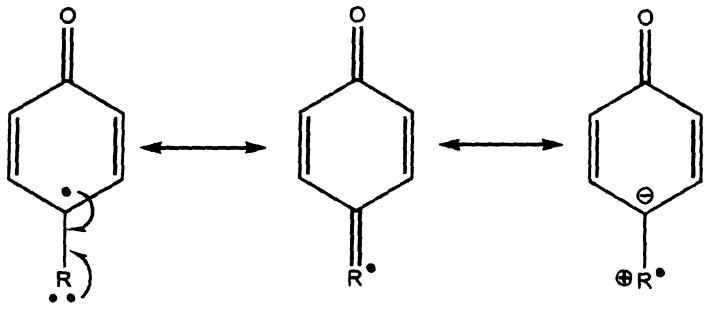

A

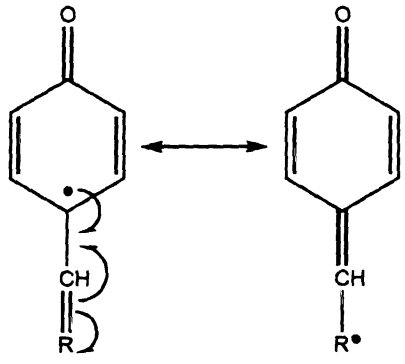

B

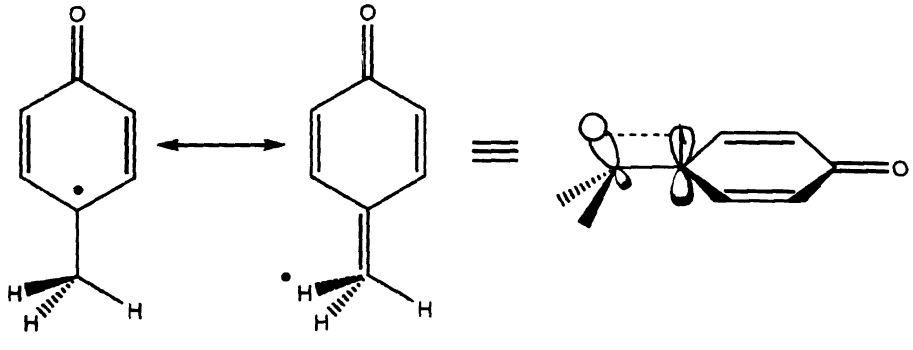

C

Scheme 2-3. Spin delocalization mechanisms in phenoxy radicals: (A) β-spin donor (π-donors); (B) conjugative α-spin acceptor (π-acceptors); (C) hyperconjugative β-spin donors (σ-donors).

The consequence of this interaction is the creation of residual α-spin on the R group and a net redistribution of spin density out of the aromatic ring.[70] Taken to the extreme, complete transfer of the electron from the donor gives rise to the zwitterion depicted on the right side of Scheme 2-3 A, a description reminiscent of the three-electron bonding schemes often invoked to describe such systems.[71] Groups that can act as π-acceptors (e.g., vinyl) can be described in a similar manner (B). Their ability to conjugate to the ring lends to their depiction as α-spin acceptors, however, the net effect in terms of the redistribution of spin polarization to the periphery of the substituent is largely the same as seen for π-donors.

The mechanism by which σ-donors/acceptors influence spin polarization is not as straightforward but can still be viewed in terms of a direct orbital interaction between the substituent and the radical-containing π-system of the ring through hyperconjugation (C). In this context, aliphatic groups such as CH_3 can be considered β-spin donors wherein a σ orbital of the C–H fragment plays a role similar to that depicted for the π-donors. An important difference is that the net transfer of β-spin density from the C–H fragment to the *para*-carbon will serve to destabilize the bonding within the substituent by virtue of delocalization of the bonding pair of electrons to the phenoxy *p*-orbital: this could explain, in part, the generally smaller polarization effect observed for the σ-donor/acceptor-substituents relative to their π-based counterparts.

Common to all three of the spin polarization mechanisms illustrated in Scheme 2-3 is the ability of the substituent to couple into the π system of the phenoxyl ring to redistribute spin density out of the aromatic ring (and, given the resonance structures in Scheme 1, away from the oxygen atom). Although useful from a qualitative perspective,

the scenarios presented above still do not provide sufficient insight as to the relative effectiveness of one substituent versus another at polarizing spin density, nor do they allow us to understand why spin and charge behave independently in terms of the directionality of their polarizations.

Previous Studies. A number of groups have considered substituent effects on spin polarization by correlating spin density distribution with various physical properties (both calculated and experimental). Both Wu and Lai[44] and Brinck et al.[72] have examined the link between spin density polarization and thermodynamics by calculating the O–H bond dissociation energy (BDE) of substituted phenols. A correlation between decreasing BDE and the presence of π-donors was noted suggesting stabilization of the radical is associated with increased spin delocalization of the odd electron.[72] The influence of *para* substituents on the phenoxy radical has also been investigated in an AM1 study by G. P. Bean,[73] who likewise focused on bond dissociation energies of substituted phenols. Bean concluded that the relative stability of the radicals could be understood in the context of the captodative effect,[74-77] a concept first introduced by Dewar[78] in 1952 in which a combination of donors and acceptors within the same compound led to a "push-pull" effect that ultimately stabilized the radical. Viewing the oxygen radical as a strong electron-withdrawing group, this model holds that a strong electron-donating group in the *para*-position of the ring leads to stabilization of the radical (conversely, an electron-withdrawing group would destabilize the radical via an anti-captodative effect). The validity of this idea garners support from the results of Wu and Lai and Brinck et al.[44,72] – and to some extent our own – insofar as strong donors are observed to promote redistribution of spin polarization away from the oxygen atom and toward the substituent.

Correlations with bond dissociation energies represent one of many ways in which workers have sought to systematize the effects of substituents on spin polarization. These efforts have resulted in numerous Hammett-type radical scales: among the more commonly employed are (1) the $\sigma_{JJ}^{\bullet}$ scale of Jiang and Ji,[79,80] which is based on cycloaddition reactions of α,β,β-trifluorstyrenes, (2) the $\sigma_{\alpha}^{\bullet}$ scale of Arnold,[70,81] which relates spin density to hyperfine interactions in substituted benzyl radicals, (3) $\sigma_C^{\bullet}$, which Creary used to describe the rearrangement of 2-aryl-3,3-dimethylmethylenecyclopropanes,[82,83] (4) Jackson's $\sigma_J^{\bullet}$ parameter, which was derived from the thermal decomposition of dibenzyl mercurials,[84,85] (5) Fisher's $\sigma_F^{\bullet}$ parameter based on the bromination of 4-substituted 3-cyanotoluenes by NBS,[86,87] and (6) the ΔD scale of Adam,[66] which correlates spin density with zero-field splitting in substituted 1,3-diarylcyclopentane triplet diradicals. The success of these various parameters at describing substituent effects on spin polarization in a broader context has been mixed. For example, Wu and Lai modeled the change in spin density (ΔS) at the oxygen atom in their study using $\sigma_{JJ}^{\bullet}$; the authors acknowledged that the correlation they reported was not as compelling as what they observed between σ_p^+ and charge density, although it was clear that spin delocalization was maximized with π-donor ligands. It should be noted that these authors made a point of noting that spin delocalization effects in the phenoxy system could be quite different than in the benzyl radicals upon which the $\sigma_{JJ}^{\bullet}$ constants are based, implying that a correlation between spin density and $\sigma_{JJ}^{\bullet}$ perhaps should not be expected in the case of substituted phenoxy radicals. In Figure 2-3 are shown our calculated results for the 15 substituents examined in this study plotted against two of the

Hammett parameters most commonly invoked to describe substituent effects on spin distribution.

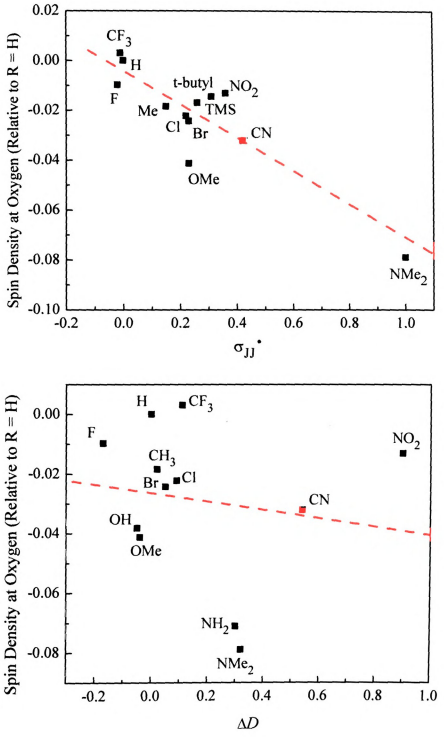

Figure 2-3. Plots of the change in spin density at the oxygen atom of *para*-substituted phenoxy radicals as a function of the $\sigma_{JJ}^{\bullet}$ (top) and ΔD (bottom) Hammett-type spin delocalization parameters.

It can be seen upon inspection that neither of these parameters (as well as $\sigma_C^{\bullet}$ and $\sigma_\alpha^{\bullet}$, not shown) yields a particularly good correlation. Indeed, the ΔD parameter, which we initially believed held the greatest promise due to the fact that zero-field splitting in diradicals should correlate quite well with unpaired spin density, actually does the worst in terms of describing the polarization of spin away from the oxygen atom in the phenoxy radical. The correlation appears to be strongest with the $\sigma_{JJ}^{\bullet}$ parameter – similar to what was reported by Wu and Lai – though in our case this observation is clearly dependent upon inclusion of the data on the dimethylamino derivative. Figure 2-3 reinforces the suggestion by Wu and Lai that while these various spin delocalization scales may work quite well for their parent systems, they do not appear to be transferable between different systems to any significant degree.[72] We therefore looked to our calculations to see if there was another, more robust marker for spin polarization that could provide us with greater insight into the origin of these substituent effects.

HOMO-LUMO Gap Correlation. After an extensive analysis of our data, we uncovered an empirical relationship between the polarization of spin density within the compounds being examined and the energy gap between their highest-occupied and lowest-unoccupied molecular orbitals. Before we describe these results, we must first define what we mean by the LUMO of a molecule within the context of this study.

As mentioned in the Experimental section, we carried out our calculations using a spin-unrestricted formalism. This approach is necessary in order to allow the spatial characteristics of each spin polarization to behave independently, but a drawback of this method is that the orbitals produced within this formalism are one-electron constructs. As a result, each one-electron orbital of the molecule is a distinct eigenvector with its own

eigenvalue. The challenge is therefore to correlate these one-electron orbitals with a two-electron orbital picture of the kind that chemists typically invoke to describe bonding interactions in molecules. Amos and Hall have argued that this can be done in a straightforward manner provided that the spatial overlap of a given pair of α- and β-spin orbitals approaches unity.[88-90] In this circumstance, the α- and β-spin one-electron orbitals calculated within the spin-unrestricted formalism can be thought of as describing essentially the same molecular orbital (i.e., the corresponding two-electron orbital), differing only in the polarization of the electron.

This idea can be understood by examining the relevant wavefunctions of one of the compounds from our study. Energetically, the true HOMO-LUMO gap in an $S = {}^1/_2$ system within a spin-unrestricted formalism is typically the α-HOMO-β-LUMO gap: this was found to be the case in all of the molecules whose properties are summarized in Figure 2-4. In Figure 2-4 are shown the α-HOMO, β-LUMO, and α-LUMO of the *p*-NH_2-phenoxyl radical.

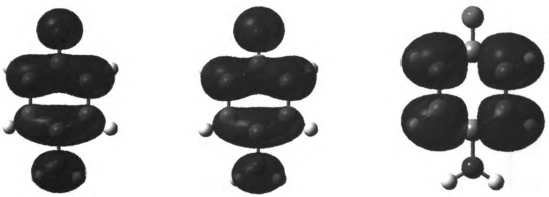

α-HOMO **β-LUMO** **α-LUMO**

Figure 2-4. Comparison of the α-HOMO, β-LUMO, and α-LUMO Kohn-Sham molecular orbitals of the *p*-NH_2-phenoxy radical. The orbitals were generated at the UB3LYP/6-311G** level of theory and visualized using GaussView with an isosurface value of 0.020.

It can be seen that the α-HOMO and β-LUMO of *p*-NH_2-phenoxyl radical are essentially identical in terms of their spatial properties,[91] whereas the α-LUMO reflects completely distinct bonding characteristics. Within the context of Amos and Hall's corresponding orbital transformation,[88-90] the α-HOMO and β-LUMO, despite having different eigenvalues in the spin-unrestricted calculation, can be viewed as representing the same molecular orbital when projected onto a two-electron picture. An analogous result was found for all 15 compounds examined in this study. We therefore believe that the α-LUMO represents the physically significant orbital for defining the HOMO-LUMO gaps of these open-shell systems.[92-96]

A plot of the change in spin density at the oxygen atom versus the HOMO-LUMO gap of all 15 of the *p*-substituted phenoxy radicals we examined is shown in Figure 2-5.

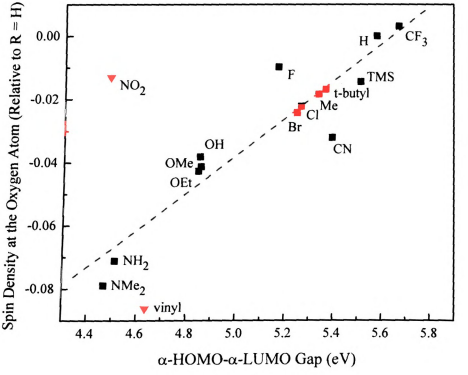

Figure 2-5. A plot of the calculated changes in spin density at the oxygen atom versus the α-HOMO-α-LUMO gaps for a series of *para*-substituted phenoxy radicals calculated at the UB3LYP/6-311G** level of theory.

Our results clearly show a strong correlation between these two variables.[97] While this correlation is not as strong as was observed between charge density and σ_{p+} (Figure 2-2), a comparison of these results with Figure 2-3 illustrates that the HOMO-LUMO gap is a significantly better marker for changes in spin density across this series than any of the commonly invoked Hammett-type radical constants that have been described in the literature.[98] Molecules with smaller HOMO-LUMO gaps are seen to exhibit a greater degree of spin polarization away from the oxygen atom: closer inspection reveals that this region is dominated by π-donating substituents, whereas larger HOMO-LUMO gaps are associated with substituents whose primary influence is σ-based. It is interesting to note that, although the general grouping of substituents (e.g., π-donors, σ-acceptors, etc.) is similar to what was observed for charge polarization effects, the specific ordering within these subgroups is different, a point that underscores the general result from Figure 2-1 concerning the distinct nature of charge and spin polarization in this system. The correlation is clearly not perfect: NO_2 and vinyl derivatives all fall significantly off the line, the former having a smaller gap than expected given the spin density at oxygen calculated for *p*-NO_2-phenoxyl, while the vinyl-containing compound exhibits an anomalously large splitting. Nevertheless, the overall trend evident in Figure 2-5 suggests that the factors influencing spin polarization and the HOMO-LUMO gap in this series of compounds are related.

D. Mechanism of Spin Polarization. The overall correlation illustrated in Figure 2-5 can be explained in the context of a simple molecular orbital scheme (Figure 2-6). In accord with the resonance picture illustrated in Scheme 2-3, the dominant interaction is

proposed to occur between the lone pair associated with the π-donor and the π-orbital(s) containing the unpaired electron of the phenoxy radical.[71,99]

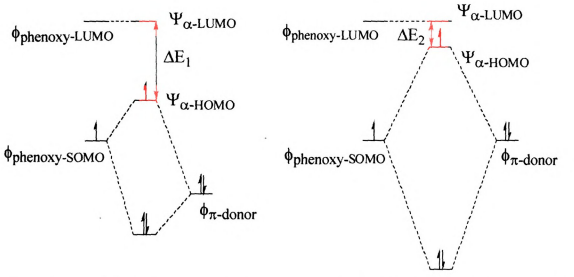

Figure 2-6. Molecular orbital-based description of the spin delocalization mechanism proposed for π-donor-containing phenoxy radicals. The interaction of the $\phi_{\pi\text{-donor}}$ orbital of the substituent with the phenoxy $\phi_{\text{phenoxy-SOMO}}$ results in a net one-electron stabilization. The degree of interaction between these two orbitals dictates the α-HOMO-α-LUMO energy gap, which in turn alters the composition of the α-HOMO and thus the spatial distribution of unpaired spin density.

Assuming that the degree of spatial overlap between the donor and the π-system of the ring is roughly invariant, the extent of destabilization of the HOMO will be dictated primarily by the relative energies of the $\phi_{\pi\text{-donor}}$ and $\phi_{\text{phenoxy-SOMO}}$ orbitals: as these two orbitals become more energetically equivalent the degree of this destabilization will increase. This will have two immediate consequences: (1) The wavefunction corresponding to the SOMO of the adduct will exhibit an enhanced contribution from the substituent, the net effect of which will be to redistribute the electron density associated with the unpaired electron onto the substituent and away from the oxygen atom; and (2)

The HOMO-LUMO gap will decrease provided the α-LUMO of the phenoxy radical is essentially non-bonding with respect to the substituent.

The results from the calculations we have carried out provide considerable support for this picture. For example, it can be seen in Figure 2-5 that decreasing the electronegativity of the donor atom from oxygen in R = OMe to nitrogen in R = NMe_2 leads to a smaller HOMO-LUMO gap, consistent with the notion that the lone pair of nitrogen in dimethylamine should present a better energetic match with the aromatic ring than does the methoxy group. More compelling is the fact that the redistribution of electron density due to mixing between the $\phi_{\text{phenoxy-SOMO}}$ and $\phi_{\pi\text{-donor}}$ orbitals suggested in Figure 2-6 is reflected in the spatial characteristics of the wavefunctions. In Figure 2-7, the $\Psi_{\alpha\text{-HOMO}}$ Kohn-Sham molecular orbitals of both *p*-NH_2- and *p*-CF_3-phenoxyl are shown as an example underscoring the significant contribution of the NH_2 group to the overall composition of the SOMO orbital as compared to the (relatively) small perturbation induced by the CF_3 substituent.

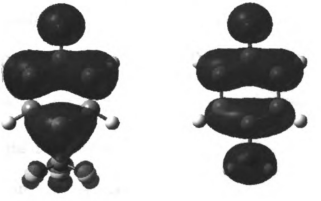

p-CF_3-phenoxyl *p*-NH_2-phenoxyl

Figure 2-7. Comparison between the Kohn-Sham α-HOMO molecular orbitals of *p*-CF_3- and *p*-NH_2-substituted phenoxy radicals.

Quantitative support for this model is afforded by examining the composition of the $\Psi_{\alpha\text{-HOMO}}$ orbitals explicitly. According to our model, this wavefunction is

$$\Psi_{\alpha\text{-HOMO}} = c_1 \cdot \phi_{\text{phenoxy-SOMO}} + c_2 \cdot \phi_{\pi\text{-donor}} \qquad (1)$$

where $c_1^2 + c_2^2 = 1$. As the $\phi_{\pi\text{-donor}}$ orbital increases in energy (i.e. shifting from left to right in Figure 2-6), more extensive orbital mixing should result in an increase in c_2 at the expense of c_1. The data in Table 2-1 confirms these expectations: as the HOMO-LUMO gap decreases, the wavefunction corresponding to the HOMO exhibits a systematic increase in the percent contribution from the substituent (%R) and a corresponding decrease in oxygen character (%O). Since the unpaired electron carries all of the excess spin density of the molecule, the delocalization of the SOMO onto the substituent implied by its increased contribution to the wavefunction has the net effect of shifting polarization of spin away from the oxygen atom. This simple MO explanation, which essentially expands upon the concept of the captodative effect[75,77] and three-electron bonding,[71,100] thus accounts in a general way for the correlation evident in Figure 2-5.

Deviations from the HOMO-LUMO Gap Correlation. Implicit in the model just described – and in particular the use of the HOMO-LUMO gap as a marker for spin polarization – is the notion that the $\Psi_{\alpha\text{-LUMO}}$ is not perturbed upon incorporation of the substituent. Defining the α-LUMO as,

$$\Psi_{\alpha\text{-LUMO}} = c_3 \cdot \phi_{\text{phenoxy-LUMO}} + c_4 \cdot \phi_{\pi^*\text{-substituent}} \qquad (2)$$

we can see from Table 2-1 that c_4 is, in fact, either zero or relatively small (i.e., < 10%) for most of the substituents included in our study. Two glaring exceptions to this are NO_2

and vinyl: these groups contribute 69% and 48% to their respective LUMOs. We now consider each of these cases to determine whether their properties can be understood within the context of the model we have developed.

Table 2-1. Percent atomic contributions for oxygen (%O) and the substituent (%R) group in the α-HOMO and α-LUMO Kohn-Sham MO's for a series of *para*-Phenoxy radicals.

R	% O α-HOMO	% R α-HOMO	% O α-LUMO	% R α-LUMO	ΔS
Reference					
H	27.28	0.03	0	0	0
π-donor					
OH	22.23	15.48	0	0	-0.0382
OMe	21.31	19.05	0	2.99	-0.0413
OEt	21.1	19.86	0	3.41	-0.0427
NH_2	19.95	22.61	0	0	-0.0711
NMe_2	18.01	31.9	0	7.91	-0.0789
π-donor, σ-acceptor					
F	24.51	9.24	0	0	-0.0098
Cl	21.06	18.01	0	0	-0.0222
Br	20.07	21.78	0	0	-0.0243
π-acceptor					
NO_2	24.98	8.37	4.58	69.04	-0.0131
CN	23.42	11.97	10.58	15.95	-0.0321
π-acceptor, σ-donor					
vinyl	20.17	21.31	7.25	47.9	-0.0863
σ-donor					
Me	24.72	5.84	0	6.24	-0.0184
t-butyl	24.07	9.33	0	14.94	-0.0169
TMS	24.52	9.27	0	10.7	-0.0145
σ-acceptor					
CF_3	26.22	4.97	0	0.45	0.0031

[a] $[\Sigma n^2_{\text{a.o.}} / \Sigma n^2_{\text{m.o.}}] * 100$ = % contribution. $\Sigma n^2_{\text{a.o.}}$ is the sum of the squares of the atomic orbital coefficients of the atom or group of interest and $\Sigma n^2_{\text{m.o.}}$ is the sum of the squares of all atomic orbital coefficients in a specific molecular orbital.

The results we obtained for *p*-NO_2-phenoxyl constitute the most significant deviation from the HOMO-LUMO gap correlation illustrated in Figure 2-5. Specifically, our calculations indicate that the HOMO-LUMO gap for this compound is substantially smaller than expected based on the calculated redistribution of spin density away from the oxygen atom. The origin of this result can be understood quite easily by examining the frontier orbitals of this compound. Figure 2-8 presents a comparison of the LUMOs for phenoxyl and *p*-NH_2-phenoxyl with the LUMO and LUMO+1 of *p*-NO_2-phenoxyl.

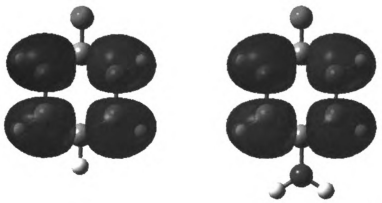

phenoxyl *para*-NH_2-phenoxyl

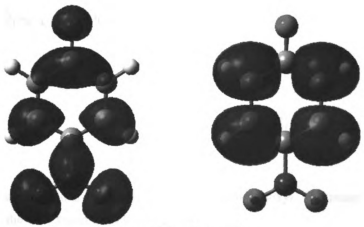

para-NO_2-phenoxyl:

α-LUMO α-LUMO + 1

Figure 2-8. Comparison of the α-LUMO orbitals for phenoxyl and *p*-NH_2-phenoxyl radicals with the LUMO and LUMO+1 orbitals of *p*-NO_2-phenoxyl.

These plots clearly show that the character of the LUMO changes upon incorporation of the NO_2 group, wherein the orbital corresponding to the LUMO in most of the other compounds in our study is now the next-highest energy orbital (LUMO+1) in this system. This situation arises due to the presence of a low-lying π^* acceptor orbital associated with the NO_2 group, allowing for a new interaction between the substituent and the LUMO+1 of the free phenoxyl moiety and the stabilization of that orbital in *p*-NO_2-phenoxyl; a qualitative molecular orbital diagram depicting this situation is shown in Figure 2-9.

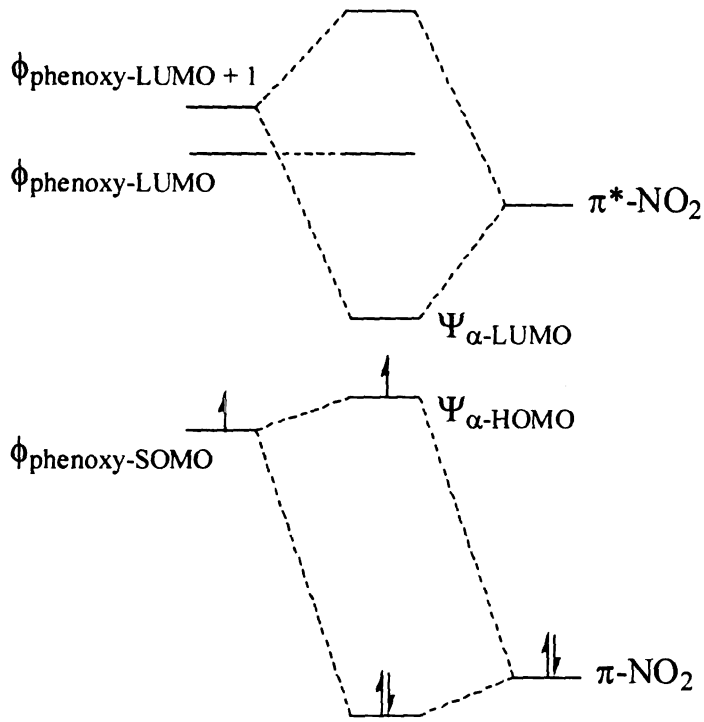

Figure 2-9. Proposed molecular orbital diagram for *p*-NO_2-phenoxyl. The presence of a low-energy empty π^* orbital on the NO_2 group leads to a change in the nature of the LUMO and is responsible for the deviation exhibited by *p*-NO_2-phenoxyl from the correlation illustrated in Figure 5.

It should be noted that the polarization of spin density is still driven by the character of the HOMO as described above: Table 1 shows that the contribution of NO_2 to the HOMO

is comparable to other substituents exhibiting similar degrees of spin polarization. In this regard, we believe that the model we have developed remains conceptually robust, but the HOMO-LUMO gap correlation breaks down in the case of NO_2 due to the presence of a new interaction not present in the other compounds and thus not accounted for in the simple two-orbital, three-electron scheme depicted in Figure 6.

The vinyl group also shows significant contributions to the LUMO as well, as exhibiting the same LUMO/LUMO+1 inversion as seen for *p*-NO_2-phenoxyl. However, the situation for *p*-vinyl-phenoxyl is fundamentally different: whereas the NO_2 adduct displays less spin polarization than the HOMO-LUMO gap would suggest, the vinyl group appears to be just the opposite. In fact, the results from Figure 1 show that the vinyl group is the most effective at polarizing unpaired spin away from the oxygen atom of any substituent we examined. This enhanced delocalizing ability of the vinyl group has also been noted by Radom et al. in a study of substituted methyl radicals.[101] The contrast between NO_2 and vinyl implies that α-spin resonance delocalization coupled with β-spin donation is the best mechanism to delocalize spin, but the ability of NO_2 to delocalize spin is attenuated compared to the vinyl group. This attenuation is most likely due to the inductive electron withdrawing ability of these substituents: it is known in the literature[102-107] that an electron-withdrawing group usually plays a duel role in radical stability. A withdrawing group can stabilize a radical by resonance delocalization (π-withdrawing) and at the same time destabilize the radical by electron induction (σ-withdrawing). Destabilization by electron induction is not surprising due to the electron deficient nature of the oxygen radical center, and can be thought of as an unfavorable "pull-pull" dipole-dipole interaction.[108] Therefore, we believe that the enhanced spin

delocalization in the vinyl group can be linked to two contributing factors: (1) σ donation by the vinyl group in the absence of inductive destabilization, the combination of which increases β-spin density at the oxygen center, and (2) stabilization of the radical by resonance delocalization of α spin density. The latter appears to be a particularly effective mechanism for delocalizing the spin in these systems.

Using the vinyl substituent as a starting point, we sought even stronger spin delocalizing substituents. To this end, there are substituents known as "super radical stabilizers", such as *p*-N=N(O)-^{t}Bu, *p*-N=N-Ph, and *p*-CH=N(O)-^{t}Bu.[109,110] Incorporation of the CH=N(O)-^{t}Bu group at the *para* position phenoxy radical decreased unpaired spin density at the oxygen atom by 60% in part due to an increase in β-spin density at the oxygen atom, in line with our expectations based on the model just described.

σ-donors and σ-acceptors. The σ-donor substituents CH_3, *t*-butyl, and TMS decrease the spin density at the oxygen atom, but to a lesser extent than that of the π-donors. This trend in spin delocalization is also mirrored in the larger HOMO-LUMO gaps for these substituents as compared to the π-donors. The delocalization of spin in these substituents can be accounted for by the hyperconjugation β-spin donation mechanism already discussed above and depicted in Scheme 3. A three-electron, two-orbital interaction can again be invoked to describe the spin delocalization in these substituents, where the interaction between a filled σ-orbital with the partially filled π-orbital of the phenoxy radical leads to a stabilizing interaction.[99] The degree of stabilization between the substituents is small, and literature reports suggest that branching of the alkyl chain will lead to less effective hyperconjugation.[70] This is exactly what is observed in the phenoxy radical complexes: the composition of the relevant

molecular orbitals indicates delocalization of the wavefunction onto the substituent via mixing between the $\phi_{phenoxy\text{-}SOMO}$ and a filled σ-orbital of the σ-donor substituents.

With regard to σ-acceptor groups, studies by Brinck et al.[72] as well as Bean[73] indicate that CF_3 is a radical destabilizing substituent which in the present context corresponds to increasing the spin density at the oxygen atom. Bean suggests this can be attributed to an anti-captodative effect arising from a "pull-pull" effect in the system due to decreased conjugation. Brinck et al. points out that this substituent has been shown to be destabilizing in other radical delocalization scales such as $\sigma_\alpha^\bullet$ and $\sigma_{JJ}^\bullet$. A similar mechanism is likely operative in *p*-F-phenoxyl, since $\sigma_{JJ}^\bullet$, $\sigma_\alpha^\bullet$, and $\sigma_C^\bullet$ have shown *p*-F to be destabilizing. It should be noted that, in the case of CF_3, we observed a functional dependence as to whether CF_3 increased or decreased spin density at the oxygen: calculations at the UBLYP/6-311G** level gave $\Delta S = -0.002$, whereas a value of $\Delta S = 0.003$ was obtained with the hybrid UB3LYP functional. Given these differences, we are reluctant to draw any distinctive conclusions concerning the role of σ-acceptors in this system.

2.4 Concluding Comments

The goal of this study was to examine whether spin and charge density could be independently manipulated in a simple molecular system, and to understand the underlying mechanism for such a process. Using *para*-substituted phenoxy radicals as a test case, we carried out calculations using a wide range of substituents. A strong

correlation between the Hammett σ_p^+ polar substituent constants and changes in charge density at the oxygen atom support previous work suggesting that resonance and inductive effects are largely responsible for charge polarization. Simple electronegativity arguments can be applied, wherein electron acceptors withdraw charge density and electron donors increase the charge density at the oxygen atom in the substituted phenoxy radicals. In contrast, the spin density at the oxygen atom behaved in a manner quite distinct from the charge; none of the commonly invoked spin polarization parameters were adequate for understanding our results. A correlation was established between the α-HOMO-α-LUMO gap and the spin density at the oxygen centers whereby increasing/decreasing spin delocalization coincided with a decrease/increase in the α-HOMO-α-LUMO gap. A simple three-electron, two-orbital model was used to explain the correlation between the changes in spin density at the oxygen atom with the α-HOMO-α-LUMO gap for the π-donor *para*-substituted phenoxy radicals. The amount of mixing between the $\phi_{\text{phenoxy-SOMO}}$ and the $\phi_{\pi\text{-donor}}$ was identified as the dominating mechanism that controls both the HOMO-LUMO gap and the spin delocalization in these systems. π-acceptor substituents were found to deviate from the correlation due to additional interactions from unoccupied π* orbitals of the substituent with the $\phi_{\text{phenoxy-LUMO+1}}$, giving rise to a change in the character of the LUMO relative to other members of the series. Substituents that can serve as both a π-acceptor and a σ-donor (e.g. vinyl) were found to have the greatest propensity for redistributing spin density within the molecule.

Our results suggest that it should be possible to differentially polarize spin and charge through synthetic means by judicious choice of substituents. This could be of considerable use in the field of molecular magnetism, for example, whereby control of spin density at the radical centers could be used to manipulate intramolecular exchange interactions. One could also envision use of this approach in the design of catalysts for radical-radical coupling reactions, in which spatially distinct polarization of α and β spin density could facilitate the formation of σ bonds. Efforts to implement some of the ideas generated from the results described in this report are on going.

2.5 References and Notes

1 Wolf, S. A.; Awschalom, D. D.; Buhrman, R. A.; Daughton, J. M.; von Molnár, S.; Roukes, M. L.; Chtchelkanova, A. Y.; Treger, D. M. *Science* **2001**, *294*, 1488.

2 Fert, A. *Rev. Mod. Phys.* **2008**, *80*, 1517.

3 Bogani, L.; Wernsdorfer, W. *Nature Mater.* **2008**, *7*, 179.

4 Hansch, C.; Leo, A.; Taft, R. W. *Chem. Rev.* **1991**, *91*, 165.

5 Ewing, D. F. In *Correlation Analysis in Chemistry: Recent Advances*; Chapman, N. B., Shorter, J., Eds.; Plenum Press: New York, 1978.

6 Yang, J. S.; Liu, K. T.; Su, Y. *J. Phys. Org. Chem.* **1990**, *3*, 723.

7 Pratt, D. A.; Dilabio, G. A.; Mulder, P.; Ingold, K. U. *Acc. Chem. Res.* **2004**, *37*, 334.

8 Sekigawa, K. *Tetrahedron* **1972**, *28*, 505.

9 Fernández, I.; Frenking, G. *J. Org. Chem.* **2006**, *71*, 2251.

10 Wiberg, K. B. *J. Org. Chem.* **2002**, *67*, 4787.

11 Liu, L.; Fu, Y.; Liu, R.; Li, R. Q.; Guo, Q. X. *J. Chem. Inf. Comput. Sci.* **2004**, *44*, 652.

12 Krygowski, T. G.; Stępień, B. T. **2005**, *105*, 3482.

13 Genix, P.; Jullien, H.; Le Goas, R. *J. Chemometrics* **1996**, *10*, 631.

14 Head-Gordon, M. *J. Phys. Chem. A* **1996**, *100*, 13213.

15 Koch, W.; Holthausen, M. C. *A Chemist's Guide to Density Functional Theory*; Weinheim; Chichester: Wiley-VCH, 2000.

16 Parr, R. G.; Yang, W. *Density-Functional Theory of Atoms and Molecules*; Clarendon: Oxford, 1989.

17 Claiser, N.; Souhassou, M.; Lecomte, C.; Gillon, B.; Carbonera, C.; Caneschi, A.; Dei, A.; Gatteschi, D.; Bencini, A.; Pontillon, Y.; Lelièvre-Berna *J. Phys. Chem. B* **2005**, *109*, 2723.

18 Zheludev, A.; Barone, V.; Bonnet, M.; Delley, B.; Grand, A.; Ressouche, E.; Rey, P.; Subra, R.; Schweizer, J. *J. Am. Chem. Soc.* **1994**, *116*, 2019.

19 McConnell, H., M, *J. Chem. Phys.* **1956**, *24*, 764.

20 Remenyi, C.; Reviakine, R.; Kaupp, M. *J. Phys. Chem. B* **2007**, *111*, 8290.

21 Nguyen, M. T.; Creve, S.; Vanquickenborne, L. G. *J. Phys. Chem. A* **1997**, *101*, 3174.

22 Reiher, M. *Faraday Discuss.* **2007**, *135*, 97.

23 Pillet, S.; Legrand, V.; Weber, H. P.; Souhassou, M.; Letard, J. F.; Guionneau, P.; Lecomte, C. *Zeitschrift Fur Kristallographie* **2008**, *223*, 235.

24 Pierpont, C. G. *Coord. Chem. Rev.* **2001**, *216-217*, 99.

25 Pierpont, C. G.; Buchanan, R. M. *Coord. Chem. Rev.* **1981**, *38*, 45.

26 Pierpont, C. G.; Lange, C. W. *Prog. Inorg. Chem.* **1994**, *41*, 331.

27 Kaim, W. *Coord. Chem. Rev.* **1987**, *76*, 187.

28 Shultz, D. A.; Sloop, J. C.; Washington, G. *J. Org. Chem.* **2006**, *71*, 9104.

29 Adam, W.; Borden, W. T.; Burda, C.; Foster, H.; Heidenfelder, T.; Heubes, M.; Hrovat, D.; Kita, F.; Lewis, S.; Scheutzow, D.; Wirz, J. *J. Am. Chem. Soc.* **1998**, *120*, 593.

30 West, A. P., Jr.; Silverman, S. K.; Dougherty, D. A. *J. Am. Chem. Soc.* **1996**, *118*, 1452.

31 Geise, C. M.; Hadad, C. M. *J. Org. Chem.* **2000**, *65*, 8348.

32 Mitani, M.; Yamaki, D.; Takano, Y.; Kitagawa, Y.; Yoshioka, Y.; Yamaguchi, K. *J. Chem. Phys.* **2000**, *113*, 10486.

33 Eaton, G. R.; Eaton, S. S. *Acc. Chem. Res.* **1988**, *21*, 107.

34 Eaton, S. S.; Eaton, G. R. *Coord. Chem. Rev.* **1988**, *83*, 29.

35 Shultz, D. A.; Bodnar, S. H.; Lee, H.; Kampf, J. W.; Incarvito, C. D.; Rheingold, A. L. *J. Am. Chem. Soc.* **2002**, *124*, 10054.

36 Shultz, D. A.; Fico, R. M., Jr.; Bodnar, S. H.; Kumar, R. K.; Vostrikova, K. E.; Kampf, J. W.; Boyle, P. D. *J. Am. Chem. Soc.* **2003**, *125*, 11761.

37 Shultz, D. A.; Fico, R. M., Jr.; Lee, H.; Kampf, J. W.; Kirschbaum, K.; Pinkerton, A. A.; Boyle, P. D. *J. Am. Chem. Soc.* **2003**, *125*, 15426.

38 Shultz, D. A.; Sloop, J. C.; Coote, T.-A.; Beikmohammadi, M.; Kampf, J.; Boyle, P. D. *Inorg. Chem.* **2007**, *46*, 273.

39 Stone, T. J.; Waters, W. A. *J. Chem. Soc.* **1964**, 213.

40 Waters, W. A.; Stone, T. J. *Proc. Chem. Soc. London* **1962**, 253.

41 Dixon, W. T.; Norman, R. O. C. *J. Chem. Soc.* **1964**, 4587.

42 Scheffler, K.; Stegmann, H. B. *Elektronenspinresonanz*; Springer: Berlin, 1970.

43 Qin, Y.; Wheeler, R. A. *J. Chem. Phys.* **1995**, *22*, 1689.

44 Lai, D. K. W.; Wu, Y. *J. Org. Chem.* **1996**, *61*, 7904.

45 Kawai, A.; Hirakawa, M.; Abe, T.; Obi, K.; Shibuya, K. *J. Phys. Chem. A* **2001**, *105*, 9628.

46 Broze, M.; Luz, Z. *J. Chem. Phys.* **1969**, *51*, 738.

47 Broze, M.; Luz, Z. *J. Chem. Phys.* **1969**, *51*, 749.

48 Hirota, N. *J. Chem. Phys.* **1962**, *37*, 1884.

49 Frisch, M. J.; Trucks, G. W.; Schlegel, H. B.; Scuseria, G. E.; Robb, M. A.; Cheeseman, J. R.; Zakrzewski, V. G.; Montgomery, J. A., Jr.; Stratmann, R. E.; Burant, J. C.; Dapprich, S.; Millam, J. M.; Daniels, A. D.; Kudin, K. N.; Strain, M. C.; Farkas, O.; Tomasi, J.; Barone, V.; Cossi, M.; Cammi, R.; Mennucci, B.; Pomelli, C.; Adamo, C.; Clifford, S.; Ochterski, J.; Petersson, G. A.; Ayala, P. Y.; Cui, Q.; Morokuma, K.; Malick, D. K.; Rabuck, A. D.; Raghavachari, K.; Foresman, J. B.; Cioslowski, J.; Ortiz, J. V.; Stefanov, B. B.; Liu, G.; Liashenko, A.; Piskorz, P.; Komaromi, I.; Gomperts, R.; Martin, R. L.; Fox, D. J.; Keith, T.; Al-Laham, M. A.; Peng, C. Y.; Nanayakkara, A.; Gonzalez, C.; Challacombe, M.; Gill, P. M. W.; Johnson, B.; Chen, W.; Wong, M. W.; Andres, J. L.; Gonzalez, C.; Head-Gordon, M.; Replogle, E. S.; Pople, J. A. *Gaussian 98, revision A.4*, Gaussian, Inc.: Pittsburgh, PA, 1998.

50 Becke, A. D. *Phys. Rev. A* **1988**, *38*, 3098.

51 Lee, C.; Yang, W.; Parr, R. G. *Phys. Rev. B* **1988**, *37*, 785.

52 Becke, A. D. *J. Chem. Phys.* **1993**, *98*, 5648.

53 Frisch, M. J.; Frisch, A. *Gaussian 98 User's Reference*; Gaussian, Inc.: Pittsburgh, 1998.

54 Glendening, E. D.; Reed, A. E.; Carpenter, J. E.; Weinhold, F. *NBO 3.1*, Theoretical Chemistry Institute, University of Wisconsin: Madison, WI, 1996.

55 *SPARTAN*, 5.0 ed.; Wavefunction Inc.: Irvine, CA, 1997.

56 *GaussView*, 2.1 ed.; Gaussian, Inc.: Pittsburgh, PA, 2001.

57 Baker, J.; Scheiner, A.; Andzelm, J. *Chem. Phys. Lett.* **1993**, *216*, 380.

58 Laming, G. J.; Handy, N. C.; Amos, R. D. *Mol. Phys.* **1993**, *80*, 1121.

59 Pierpont, C. G.; Attia, A. S. *Collect. Czech. Chem. Commun.* **2001**, *66*, 33.

60 Pierpont, C. G. *Coord. Chem. Rev.* **2001**, *219*, 415.

61 Poddel'ski, A.; Cherkasov, V. K.; Abakumov, G. A. *Coord. Chem. Rev.* **2009**, *253*, 291.

62 Merino, G.; Vela, A.; Heine, T. *Chem. Rev.* **2005**, *105*, 3812.

63 Baerends, E. J.; Ellis, D. E.; Ros, P. *Chem. Phys.* **1973**, *2*, 41.

64 Wiberg, K. B.; Rablen, P. R. *J. Comp. Chem.* **1993**, *14*, 1504.

65 Wu, Y.; Lai, D. K. W. *J. Org. Chem.* **1996**, *61*, 7904.

66 Brown, H. C.; Okamoto, Y. *J. Am. Chem. Soc.* **1958**, *80*, 4979.

67 *Correlation Analysis in Chemistry: Recent Advances*; Plenum Press: New York and London, 1978.

68 Shorter, J. *Correlation analysis in oganic chemistry: an introduction to linear free-energy relationships*; Oxford University Press: Oxford, 1973.

69 Lind, J.; Shen, X.; Eriksen, T. E.; Merényi, G. *J. Am. Chem. Soc.* **1990**, *112*, 479.

70 Wayner, D. D. M.; Arnold, D. R. *Can. J. Chem.* **1985**, *63*, 2378.

71 Bauld, N. L. *Radicals, Ion Radicals, and Triplets: The Spin-Bearing Intermediates of Organic Chemistry*; Wiley-VHC, Inc., 1997.

72 Brinck, T.; Haeberlein, M.; Jonsson, M. *J. Am. Chem. Soc.* **1997**, *119*, 4239.

73 Bean, G. P. *Tertahedron* **2002**, *58*, 9941.

74 Viehe, H. G.; Janousek, Z.; Merényi, R.; Stella, L. *Acc. Chem. Res.* **1985**, *18*, 148.

75 Viehe, H. G.; Merényi, R.; Stella, L.; Janousek, Z. *Agnew. Chem. Int. Ed. Engl.* **1979**, *18*, 917.

76 Klessinger, M. *Agnew. Chem. Int. Ed. Engl.* **1980**, *19*, 908.

77 Sustmann, R.; Korth, H.-G. *Adv. Phy. Org. Chem.* **1990**, *26*, 131.

78 Dewar, M. J. S. *J. Am. Chem. Soc.* **1952**, *74*, 3353.

79 Jiang, X.-K. *Acc. Chem. Res.* **1997**, *30*, 283.

80 Jiang, X.; Ji, G. *J. Org. Chem.* **1992**, *57*, 6051.

81 Dust, J. M.; Arnold, D. R. *J. Am. Chem. Soc.* **1983**, *105*, 1221.

82 Creary, X. *J. Org. Chem.* **1980**, *45*, 280.

83 Creary, X.; Mehrsheikh-Mohammadi, M. E.; McDonald, S. *J. Org. Chem.* **1987**, *52*, 3254.

84 Dincturk, S.; Jackson, R. A.; Townson, H.; Agribas, H.; Bellingham, N. C.; March, G. J. *J. Chem. Soc. Perkin Trans. 2* **1981**, 1121.

85 Jackson, R. A.; Dincturk, S. *J. Chem. Soc. Perkin Trans. 2* **1981**, 1127.

86 Fisher, T. H.; Meierhoefer, A. W. *J. Org. Chem.* **1978**, *43*, 221.

87 Fisher, T. H.; Meierhoefer, A. W. *J. Org. Chem.* **1978**, *43*, 224.

88 Amos, A. T.; Hall, G. G. *Proc. R. Soc. Ser. A.* **1961**, *263*, 483.

89 King, H. F.; Stanton, R. E.; Kim, H.; Wyatt, R. E.; Parr, R. G. *J. Chem. Phys.* **1967**, *47*, 1936.

90 Neese, F. *J. Phy. Chem. Solids* **2004**, *65*, 781.

91 Ohta, K. *J. Mol. Struct. Theochem* **2002**, *587*, 33.

92 There has been some discussion about the possibility and usefulness of the Kohn-Sham orbitals,[95-97] but good approximations to experimental excitation energies can be made from them.[98]

93 Stowasser, R.; Hoffmann, R. *J. Am. Chem. Soc.* **1999**, *121*, 3414.

94 Bickelhaupt, F. M.; Baerends, E. J. In *Rev. Comput. Chem.*; Lipkowitz, K. B., Boyd, D. B., Eds.; Wiley-VCH: New York, 2000; Vol. 15, p 1-86.

95 Chong, D. P.; Gritsenko, O. V.; Baerends, E. J. *J. Chem. Phys.* **2002**, *116*, 1760.

96 Savin, A.; Umrigar, C. J.; Gonze, X. *Chem. Phys. Lett.* **1998**, *288*, 391.

97 Hartee Fock calculations at the UHF/6-311g** level have also been done, and the same correlation is observed between the α-HOMO-α-LUMO gap and the spin density at the oxygen atom. The overall shapes of the α-HOMO and α-LUMO wavefunctions are also qualitatively similar.

98 We stress that the form of Figure 5 is not meant to imply that spin density is a linear *function* of the HOMO-LUMO gap, merely that there appears to be a correlation between the two variables.

99 Bernardi, F.; Epiotis, N. D.; Cherry, W.; Schlegel, H. B.; Whangbo, M.; Wolfe, S. *J. Am. Chem. Soc.* **1976**, *98*, 469.

100 Clark, T. In *Substituent Effects in Radical Chemistry*; Reidel: Dordrecht, 1986, p 49.

101 Henry, D. J.; Parkinson, C. J.; Mayer, P. M.; Radom, L. *J. Phys. Chem. A* **2001**, *105*, 6750.

102 Cheng, J.; Liu, B.; Zhao, Y.; Wen, Z.; Sun, Y. *J. Am. Chem. Soc.* **2000**, *122*, 9987.

103 Cheng, J.; Zhao, Y. *Tertahedron* **1993**, *49*, 5267.

104 Pasto, D. J.; Krasnansky, R.; Zercher, C. *J. Org. Chem.* **1987**, *52*, 3062.

105 Fu, Y.; Liu, R.; Guo, Q.-X. *J. Phys. Org. Chem.* **2005**, *18*, 529.

106 Bordwell, F. G.; Harrelson, J. A., Jr.; Zhang, X. *J. Org. Chem.* **1991**, *56*, 4448.

107 Zipse, H. *Top. Curr. Chem.* **2006**, *263*, 163.

108 Bordwell, F. G.; Zhang, X.-M.; Satish, A. V.; Chen, J.-P. *J. Am. Chem. Soc.* **1994**, *116*, 6605.

109 Creary, X. *Acc. Chem. Res.* **2006**, *39*, 761.

110 Creary, X.; Engel, P. S.; Kavaluskas, N.; Pan, L.; Wolf, A. *J. Org. Chem.* **1999**, *64*, 5634.

Chapter 3. Differential Polarization of Spin and Charge Density in ortho-semiquinone Radicals

3.1 Introduction

The results of our previous density functional theory (DFT) examination of phenoxy radicals indicated that spin and charge density can be differentially polarized.[1] The proper choice of substituent can lead to an increase or decrease in the spin population at a paramagnetic center, and workers in the field of magnetism have suggested that the spin density at two paramagnetic centers will be proportional to the magnitude of the exchange coupling between those centers.[2-6] Extending the knowledge learned in the phenoxy radical systems to design transition metal radical systems that exhibit tunable electron exchange coupling is the overall goal of this project. Transition metal complexes with phenoxy radicals are known, but they usually incorporate a macrocyclic phenoxy moiety due to the inherent weaker donating ability of the neutral radical ligand.[7-9] Incorporation of substituents in these phenoxy ligand systems may be difficult, and other bidentate radical ligands were sought out. One requirement for synthesizing transition metal radical complexes is that the radical ligands act as strong Lewis bases. Increasing the Lewis basicity will allow for a stronger tendency for complexation of the radicals to the metal by increasing the formation constant.[10] A type of ligand that suits this requirement quite nicely is the *o*-catechol, which is the fully reduced member of the redox series shown in Scheme 3-1. The *o*-quinone ligands can exist as *o*-benzoquinones (Q), *o*-semiquinones (SQ) and *o*-catecholates (CAT), which are all related by the addition or removal of an electron as seen in Scheme 3-1.

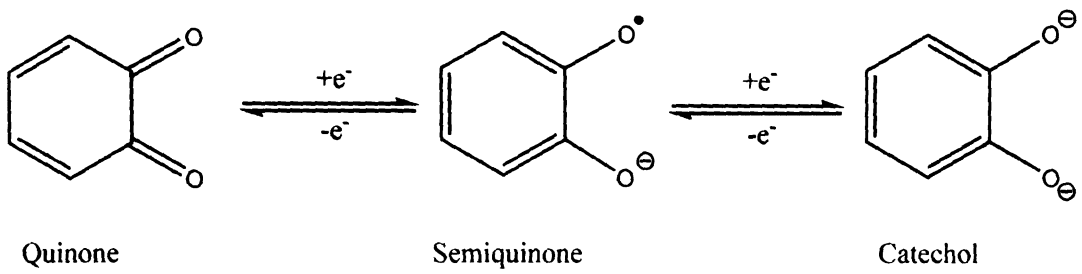

Scheme 3-1. Redox chemistry of the quinone ligands.

The *o*-catechol type ligands are dianions, and a significant amount of negative charge density is localized on the oxygen atoms.[11] The large excess negative charge density at the oxygen centers of these ligands makes them strong Lewis bases. Once a metal-catechol complex is synthesized it can be easily oxidized to the semiquinone form, which can effectively turn on the Heisenberg exchange coupling interaction when the radical is bound to a paramagnetic metal. Transition metal catechol, semiquinone, and quinone complexes are well known, and have been studied extensively in the literature for the past 40 years.[12-17] It has been discussed in this dissertation that spin and charge density can be controlled by substituents in the phenoxy radical. The next logical step is to examine the effects of spin polarization in substituted *o*-semiquinone ligands and look for similar trends as those found in the substituted phenoxy radicals.

The first part of this investigation will focus on substituted *o*-1,2-semiquinones (SQ), and the second part will focus on substituted *o*-9,10-phenanthrenesemiquinones (PSQ). These semiquinone ligands are synthetically available in the literature, and transition metal complexes with these ligands can be made.[18] Therefore, they will be an excellent starting point to examine which substituents increase or decrease the spin density at the oxygen centers of the semiquinone ligand. If a prescription for the

modulation of the spin density in semiquinone ligands can be found with our theoretical examination, then it might be possible to implement these ideas in terms of ligand design. The effects of substituents could then be experimentally determined by measuring spin exchange constants or spin densities in transition metal systems.

3.2 Theoretical Calculations

All DFT and Hartree-Fock geometry optimizations, frequency, and single point calculations were carried out with the same procedures as was described for the phenoxy radicals in Chapter 2 of this thesis. Substituents were placed at the positions *ortho and meta* (3,6) as well as *para* and *meta* (4,5) to the oxygens of the *o*-1,2-semiquinone radicals (Scheme 3-2) and at the 2,7- and 3,6-positions for the *o*-9,10-phenanthrenesemiquinones.

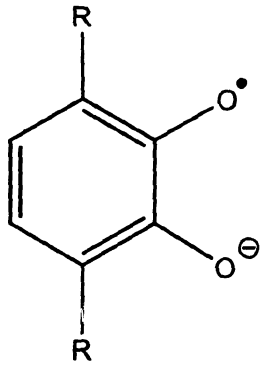

3,6-R-*o*-1,2-semiquinone

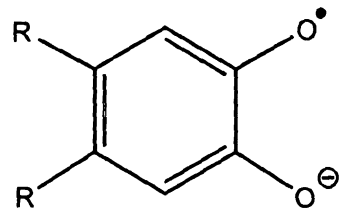

4,5-R-*o*-1,2-semiquinone

Scheme 3-2. Substituted *o*-1,2-semiquinones.

In all cases spin and charge density populations were calculated at the oxygen atoms and reported as the average value. The calculations were carried out assuming a molecular charge of –1 and a doublet spin state for all substituted semiquinones. Spin

contamination of the doublet state was found to be negligible in all cases, and the largest deviation from the theoretical value of $\langle S^2 \rangle$ was found to be 3 %.

The substituents examined in these calculations were selected to cover a wide range of possible interactions with the semiquinone ring and included σ-donors (Me), a σ-acceptor (CF_3), π-donors (OH, OMe, and NH_2), π-acceptors (NO_2 and CN), π-donor/σ-acceptors (F, Cl, and Br), and a π-acceptor/σ-donor (vinyl). In all cases the unsubstituted semiquinone radicals (i.e., R = H) were used as a reference point for comparisons.

3.3 Results and Discussion

3.3.1 Substituted *o*-1,2-semiquinones

Geometry. The crystal structure for the *o*-1,2-quinone[19] ligand has been reported, and Wheeler et al.[11] have shown that the UB3LYP/6-31g* level yielded structures that were nearly identical to the experimental X-ray data. This gives confidence that the *o*-semiquinone structures calculated at the same level of theory will be accurate representations of their true geometries. Based on comparisons to the unsubstituted compound, our results indicate that the geometry of the *o*-semiquinone radicals in terms of both bond distances and bond angles is largely insensitive to changes in the substituents on the ring. The most significant perturbation arises in the C–O distance for the 3,6-R-*o*-1,2-semiquinones and the geometries had variations in the range of ± 0.03 Å, while smaller changes of ± 0.01 Å were observed for the 4,5-R-*o*-1,2-semiquinones. Additionally, the calculated structures with the 3,6-OMe, -NO_2, and -NH_2 substituents were found to deviate from the semiquinone plane, and the 4,5-NO_2, OMe, vinyl, and

NH_2 *o*-1,2-semiquinones substituents were also canted from the plane of the semiquinone ring.

Spin and Charge Density Movement of Substituted 3,6-R-*o*-1,2-semiquinones. A graphical depiction of our computational results concerning the change in charge and spin density at the oxygen atom for all 3,6-R-*o*-1,2-semiquinones (3,6-SQ) is shown in Figure 3-1. A positive inflection in Figure 3-1 indicates an increase in spin/charge density at the oxygen center relative to R = H (spin = 0.26345 α-electrons and charge = -0.6345 electrons), and a negative inflection indicates the opposite trend.

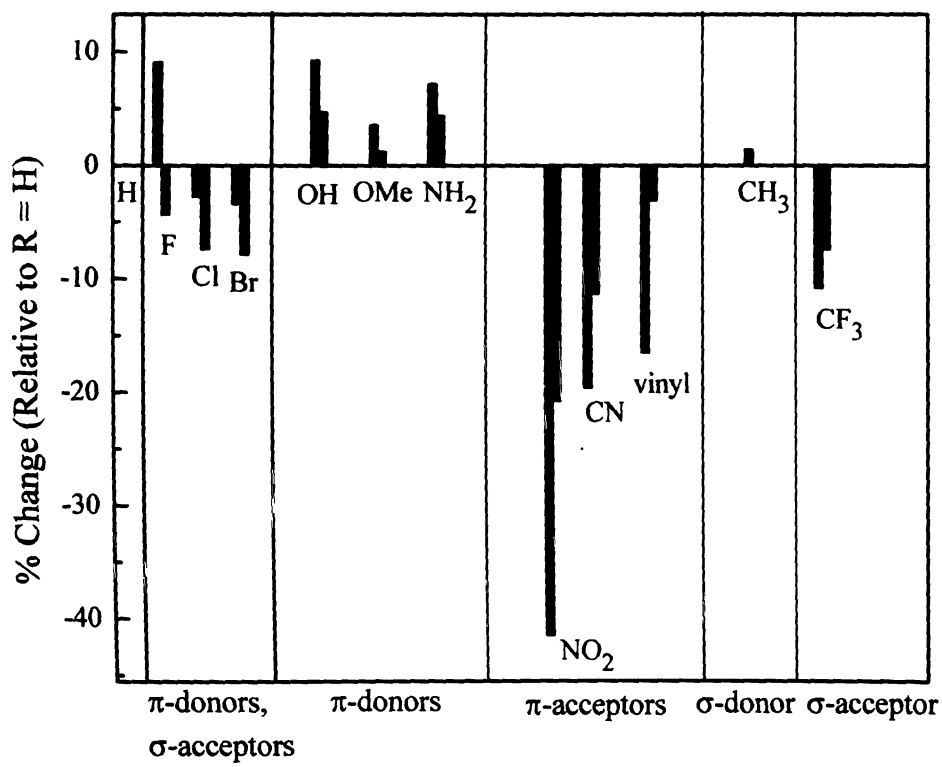

Figure 3-1. Spin density (red) and charge density (blue) polarization in 3,6-R-*o*-1,2-semiquinones.

In principle, there are four regimes of spin and charge polarization that could be sampled corresponding to an increase and/or decrease of spin and/or charge at the oxygen atom.

Figure 3-1 illustrates that three of these four regimes were realized, whereas none of the substituents we chose gave rise to an increase in charge density and decrease in spin density at the oxygen atoms. The degree of polarization varies considerably depending on the specific identity of the substituent, although the more significant effects appear to be with the π-acceptor substituents. The most important qualitative conclusion we can immediately draw from the results shown in Figure 3-1 is that differential polarization of spin and charge is not as pronounced as was seen in the phenoxy case. Except for the fluoro substituent, spin and charge density actually track together. This indicates that the mechanism for the modulation of spin and charge density could be different in these radicals. In comparison to the phenoxy radical, the overall charge polarizations are the same, except for vinyl substituent which withdraws charge density from the oxygens. Additionally, we observe the regime where spin and charge density are both increased, but in the substituted phenoxy radicals this regime was not seen. Most interesting of all is the observed shift from spin delocalization in the phenoxy radicals to spin localization at the oxygens in the 3,6-R-o-1,2-semiquinones by the π-donor substituents, F, and Me (to a smaller degree). Possible mechanisms for these deviations from the phenoxy systems will be elaborated upon in the following sections.

Charge Density Polarization in 3,6-R-*o*-1,2-semiquinones. In general, the 3,6-SQ results were similar to what was seen in the substituted phenoxy radicals, in that the electron withdrawing substituents decreased the negative charge density at the oxygen atom and electron donating substituents increased the charge density at the oxygens. The mechanism of charge density polarization is slightly more complicated in the case of the substituted 3,6-R-*o*-1,2-semiquinones, since the substituents are both *ortho* and *meta* to

the oxygen atoms. Hammett constants, σ_p^-, have been defined for electron rich systems from the dissociation of phenols in water.[20] These are the most logical choice to correlate charge in an electron rich system, but these constants have not been experimentally determined for *meta* substituents. In order to account for both the *ortho* and *meta* effects an additive Hammett parameter that encompasses both the *ortho* and *meta* substituent constants, i.e. $\sigma = \sigma_m + \sigma_o$ will be used.[21] This additive effect explains why the vinyl substituent is electron withdrawing in the *o*-semiquinone case and not for the vinyl substituted phenoxy radical. In the 3,6-SQ case, the vinyl σ_m Hammett parameter is dominating, where σ_m (vinyl) = 0.06 and σ_o (vinyl) = -0.0264, leading to an overall positive (σ_{vinyl} = 0.034, electron withdrawing) Hammett parameter.[22] The charge density polarization correlates (r = 0.95) rather well with the sum of the *ortho* and *meta* Hammett substituent constants as shown in Figure 3-2. The same correlations with σ_o and σ_m gave r = 0.94 and 0.92, respectively, and are depicted in Figure 3-3 and Figure 3-4.

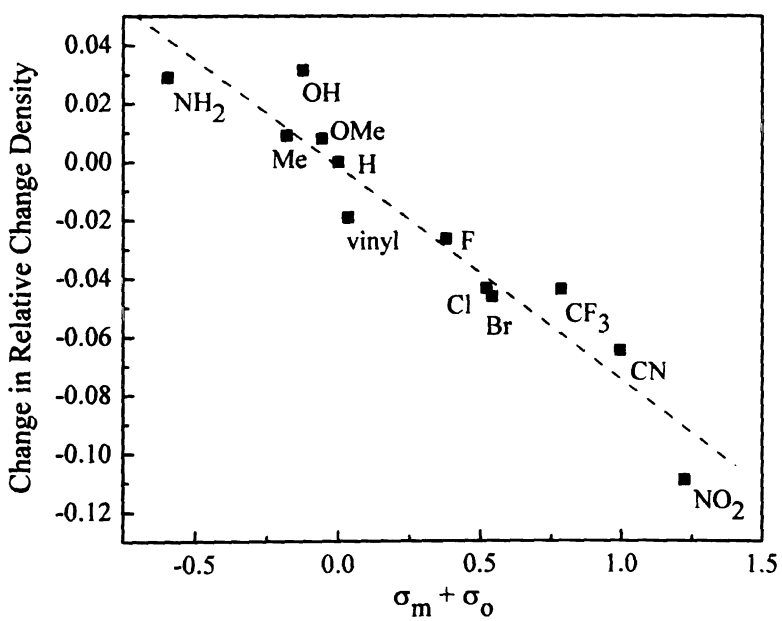

Figure 3-2. Charge density vs. additive Hammett parameter for 3,6-R-*o*-1,2-semiquinones.

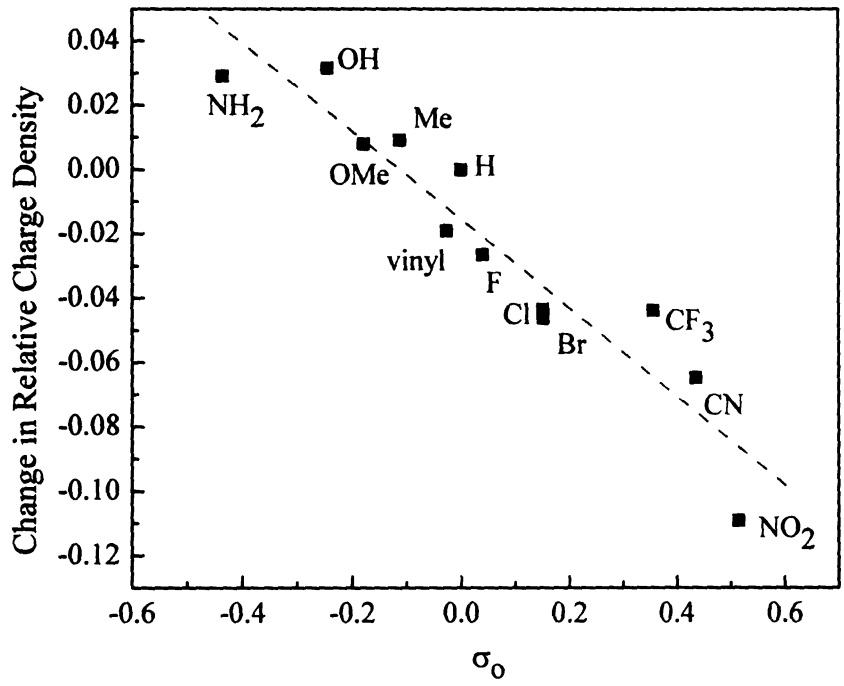

Figure 3-3. Charge density vs. σ_o Hammett parameter for 3,6-R-*o*-1,2-semiquinones.

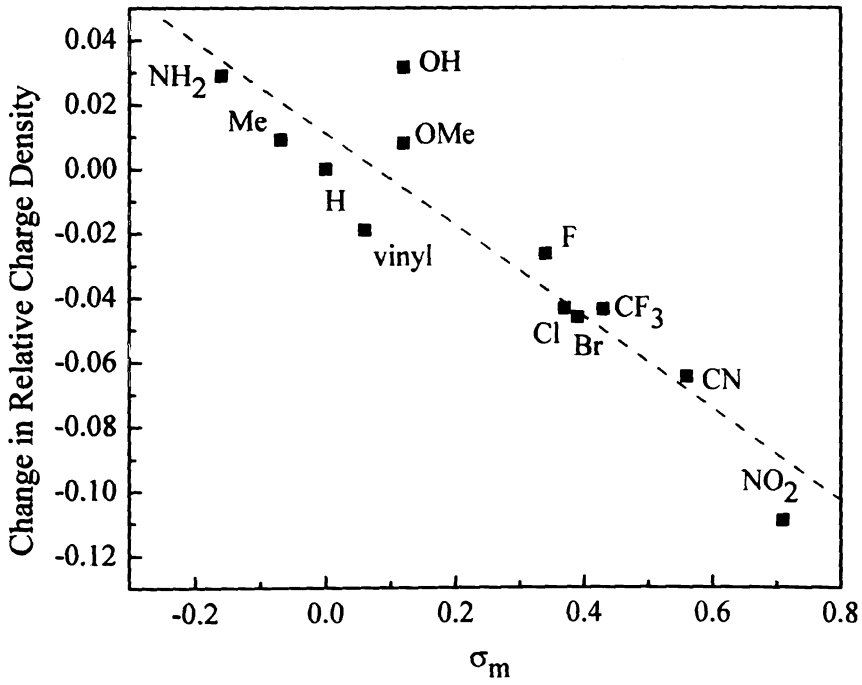

Figure 3-4. Charge density vs. σ_m Hammett parameter for 3,6-R-*o*-1,2-semiquinones.

The increased correlation with σ_o indicates that π-effects are likely more dominant than the inductive effects of the substituents, since the σ_m constants reflect stronger inductive effects (σ_I) than resonance/π-effects (σ_R), i.e. $\sigma_m = \sigma_I + 0.33\ \sigma_R$ compared to $\sigma_o = \sigma_I + \sigma_R$.[23] Overall the combined substituent constant gives the best correlation, and the Hammett constants reflect the charge distribution in the 3,6-R-*o*-1,2-semiquinones.

Spin Density Polarization in 3,6-R-*o*-1,2-semiquinones. Examination of Figure 3-1 reveals that the π-donors (NH_2, OH, and OMe) and F increase spin density at the oxygen atom. The Me group also increases the spin at the oxygen center, but to a much lesser extent. These results are in contrast with the data from the phenoxy radical study, and indicates that the mechanism for the spin delocalization is inherently different in these anion radicals. The π-donors are again β-spin donors,[24] and will produce a charge separated resonance structure as shown in Figure 3-5 (left) with α-spin delocalized onto the substituent.

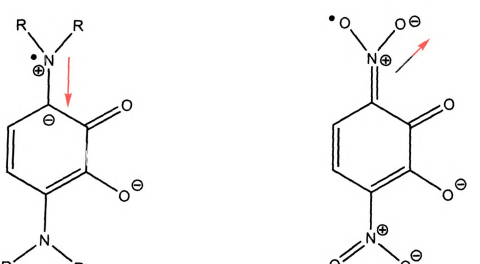

Figure 3-5. Spin resonance interactions of a β-spin donor with the semiquinone radical (left) and α-spin acceptor (right). The red arrows represent the donation or withdrawal of charge density from the negatively charged semiquinone.

A possible explanation for these substituents increasing spin density at oxygen is that the charge separated resonance structure is destabilizing to the radical system. Unfavorable electrostatic repulsion will occur between the negative charge density delocalized onto the semiquinone ring (the SQ ligand is negatively charged) and the negative charge created resulting from the β-spin donation of the π-donor ligand (Figure 3-5 left). This effect can be visualized as occurring through a charge-dipole repulsion type interaction[25] represented by the red arrow in Figure 3-5, where the negative charge density in the ring system is destabilized by the donation of electron density from the π-donor ligands and ultimately leads to spin localization at the oxygen centers. The magnitude of the destabilization is related to the DFT calculated strength of the electron donation, and the strongest donor of charge density (OH in Figure 3-1) exhibits the largest spin localization at the oxygens. Similar dipole-dipole interactions have also been argued by Bordwell et. al[26] and Clark and Arnold[25] to be responsible for the increase in bond dissociation energy of phenols substituted with electron acceptors, since the ground state energy can be destabilized due to the substituent. This argument can be equated to the inductive electron withdrawing destabilizing effects observed for other systems in the literature. As discussed in Chapter 1, increases in the bond dissociation energy are usually correlated with spin localization. This electrostatic repulsion is likely to be responsible for the increase in spin density at the oxygen atom for these ligands, since a trend is observed between the calculated donor strength and spin localization at oxygen.

There is a lack of an opposing charge-dipole interaction in the π-acceptors (Figure 3-5 right), since these ligands are α-spin acceptors[24] and the negative charge density at the semiquinone oxygens will be stabilized by electron withdrawal. These substituents

were all observed to decrease the spin density at the oxygen atoms, analogous to the phenoxy radicals. In fact, the stabilization of the charge density in the 3,6-SQ by the nitro group is one factor that leads to the larger spin delocalizing ability of the π-acceptors. The spin delocalization in the 3,6-R-*o*-1,2-semiquinones is depicted in Figure 3-6 and for both the α-spin acceptor and β-spin donor spin density is delocalized onto the substituents.

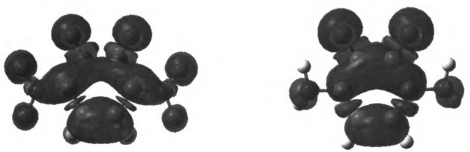

Figure 3-6. Spin density distribution in 3,6-NO_2- and 3,6-NH_2-*o*-1,2-semiquinones.

Although both α-spin acceptor and β-spin donor substituents delocalize spin density onto the substituent, the unfavorable charge-dipole interaction of the π-donors causes increased spin localization at the oxygens to avoid participation of this resonance interaction. The DFT results for the movement of spin and charge density support these arguments, and substituents that participate in charge separated resonance structures (π-donors) localize spin, and groups where this is less likely (π-acceptors) will delocalize spin density from oxygen. Thus, the spin density is modulated to a large extent by charge-dipole interactions in these systems.

Fluorine is also in the group of substituents that increase the spin density at the oxygen atom. The F-substituent has been shown to be destabilizing in the $\sigma_{JJ}^{\bullet}$, $\sigma_{\alpha}^{\bullet}$, and

$\sigma_C^{\bullet}$ Hammett spin delocalization scales. The expected strong inductive stabilization from the fluorine substituent should aid in the spin delocalization, but this is not observed and another mechanism must be responsible. The Hammett polar substituent constants for an electron rich system, σ_p-,[20, 22] indicate that F is slightly electron donating and this could be a possible cause for the observed deviation since the calculations indicate that donors increase the spin density at the oxygen atoms.

The change in spin density was also correlated with the Hammett $\sigma_C^{\bullet}$, $\sigma_{JJ}^{\bullet}$, and the ΔD_p spin delocalization constants,[27-29] and the results were generally inconsistent (Figures 3-7 to 3-9) with r = -0.87, r = -0.63, and r = -0.88, respectively. The best correlation (r = -0.94) was observed for an additive type ΔD parameter[29] ($\Delta D = \Delta D_m + \Delta D_o$), where the ΔD_o value was approximated by $0.66 \cdot \Delta D_p$, shown in Figure 3-10.[30]

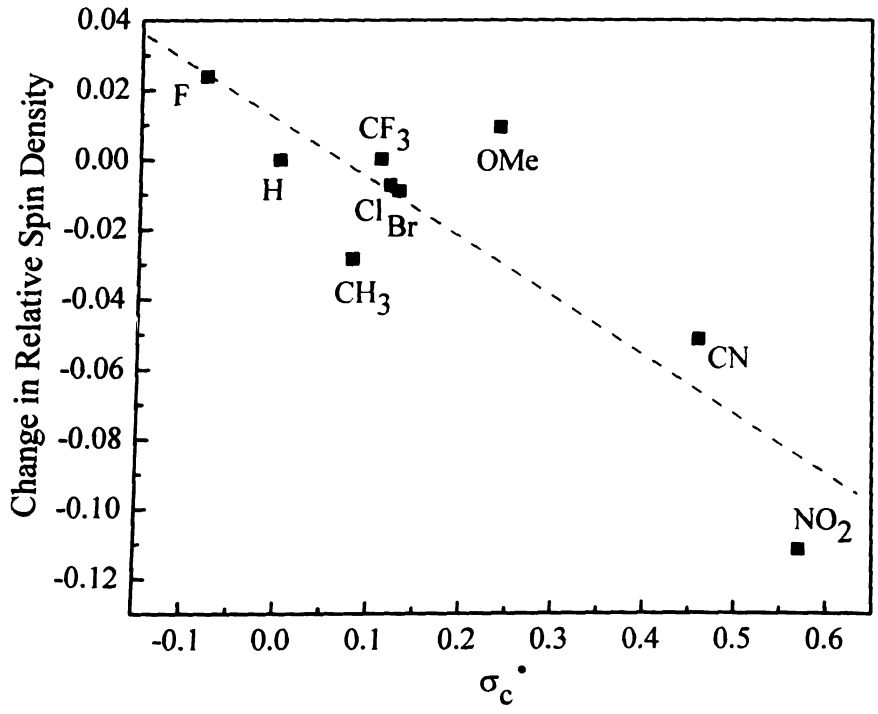

Figure 3-7. Spin density correlation with the $\sigma_C^{\bullet}$ constant in 3,6-R-*o*-1,2-semiquinones.

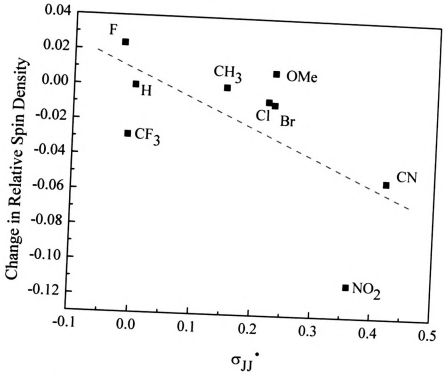

Figure 3-8. Spin density correlation with the $\sigma_{JJ}^{\bullet}$ substituent constant in 3,6-R-*o*-1,2-semiquinones.

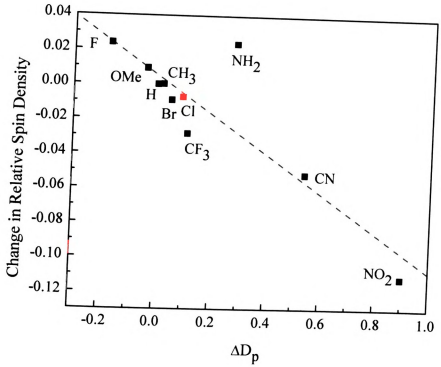

Figure 3-9. Spin density correlation with the ΔD_p substituent constant in 3,6-R-*o*-1,2-semiquinones.

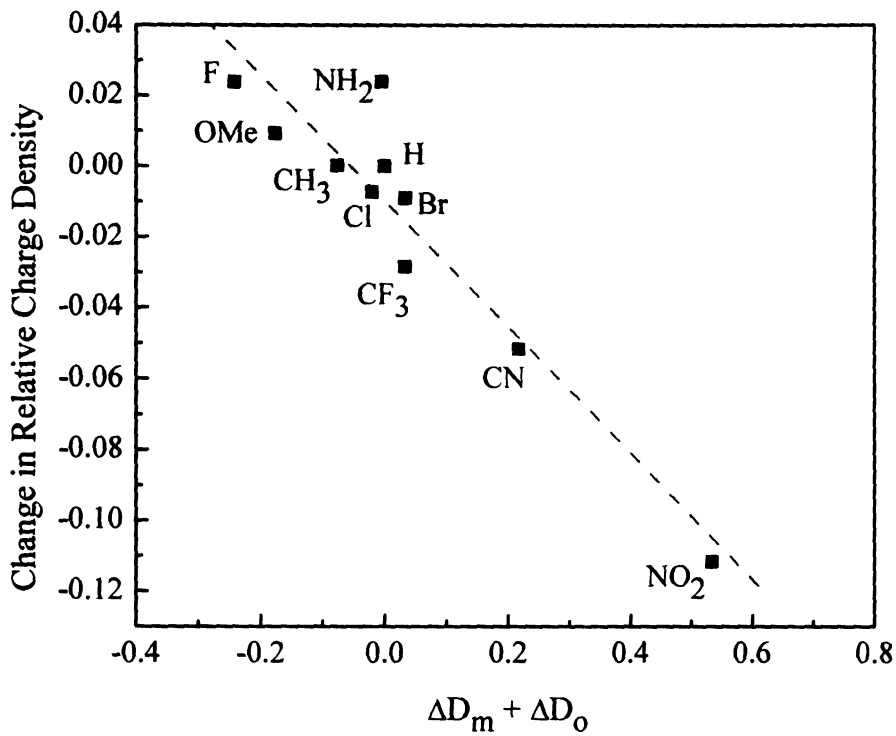

Figure 3-10. Spin density correlation with the additive ($\Delta D_m + \Delta D_o$) substituent constant in 3,6-R-*o*-1,2-semiquinones.

Given the known non-transferability[31] of the Hammett type spin delocalization constants for different systems and the observed inconsistency other correlations were sought. As was done for the phenoxy radicals, the change in spin density was correlated with the α-HOMO-α-LUMO gap. Figure 3-11 indicates that as the α-HOMO-α-LUMO gap is decreased the spin density at the oxygen atom decreases. This appears to be a marker for identifying the magnitude of spin delocalization in the neutral and anion radicals studied thus far. The correlation is strong (r = 0.96) with the vinyl substituent is the only outlier (the correlation coefficient including the vinyl group is r = 0.92). We checked the compositions of the α-HOMO and α-LUMO wavefunctions to uncover any orbital interactions that would give evidence to support the removal of the vinyl substituent as was done for the phenoxy systems. The results of this analysis are shown in Table 3-1.

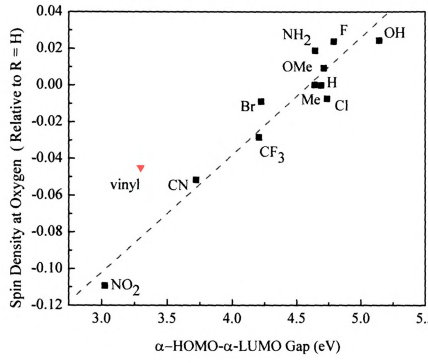

Figure 3-11. Spin density correlation with α-HOMO-α-LUMO gap in 3,6-R-*o*-1,2-semiquinones.

Table 3-1. Percent composition of 3,6-R-*o*-1,2-semiquinone frontier orbitals.

Substituent	% O α-HOMO	%R α-HOMO	%O α-LUMO	%R α-LUMO	Spin[a]	Gap (eV)
H	19.85	0.007	5.28	0.03	0.26345	4.69128
F	21.45	1.68	5.77	0.29	0.28741	4.79033
Cl	17.64	2.82	0.35	12.04	0.25621	4.73727
Br	17.72	2.78	0.42	18.25	0.25448	4.22297
NH_2	21.63	3.19	1.22	27.60	0.28231	4.64420
OH	23.77	1.804	5.24	0.50	0.28786	5.14381
OMe	18.99	2.929	0.64	37.66	0.27281	4.71251
CH_3	19.01	1.91	4.09	14.38	0.26368	4.64067
CF_3	16.19	1.46	7.37	10.38	0.23504	4.20501
CN	14.75	3.34	9.46	14.52	0.21184	3.72173
NO_2	10.51	8.30	9.34	29.32	0.15423	3.02375
Vinyl	16.51	4.66	6.62	28.96	0.21843	3.29750

[a] Average spin at oxygen.

Recall that a large % R contribution to the α-LUMO molecular orbital was evidence for the deviation of the outlying substituents in the mechanism put forth for the phenoxy radical correlation of spin density and α-HOMO-α-LUMO gap. Upon examination of Table 3-1, we can see that the Cl, Br, NH_2, OMe, CF_3, CH_3, NO_2, and vinyl substituents have a moderate to significant contribution to the α-LUMO. Multiple substituents having a contribution to the α-LUMO in the 3,6-R-*o*-1,2-semiquinones indicates that the mechanism controlling the spin polarization is more complicated for these systems when compared to the phenoxy radicals. Thus, we can not use the orbital composition data for support of the removal of the vinyl substituent from the α-HOMO-α-LUMO gap correlation. Another possible explanation for the vinyl group straying from the correlation is the competing *ortho* and *meta* electronic effects in the 3,6-R-*o*-1,2-semiquinones. Literature reports have shown that *meta*-electron withdrawing substituents in general are radical destabilizing.[32] In the case of the 3,6-vinyl-*o*-1,2-semiquinone, the spin localizing σ-effects can outweigh the *ortho* (π-effect), and this could be responsible for the observed deviation.

Due to the large % R in the α-LUMO orbital in several of the substituents it is hypothesized that a four-orbital (or possibly more) interaction is the likely mechanism modulating the HOMO-LUMO gap. Interactions with higher lying orbitals were also suggested in the phenoxy radical case to explain larger % R values in the α-LUMO orbital. We were unable to firmly establish this hypothesis using the data in Table 3-1 due to the higher complexity of the multiple orbital interactions, but it is evident that the correlation between the α-HOMO-α-LUMO gap and the spin density at oxygen is a marker to quantify the spin delocalization in these anion radicals.

Spin and Charge Density Movement of Substituted 4,5-R-*o*-1,2-semiquinones. A graphical depiction of our computational results concerning the change in charge and spin density at the oxygen atom for all 4,5-R-*o*-1,2-semiquinones is shown in Figure 3-12. As with Figure 3-1, a positive inflection in Figure 3-5 indicates an increase in spin/charge density at the oxygen center, and a negative inflection indicates the opposite trend. Only three of the 4 possible regimes for spin and charge density variation were observed, including: (1) decrease spin density and increase negative charge density at the oxygen atom (OH, NH_2, and Me); (2) decrease spin density and decrease negative charge density at oxygen (halogens, π-acceptors, and OMe); and (3) increase spin density and decrease negative charge density at the oxygen center (CF_3).

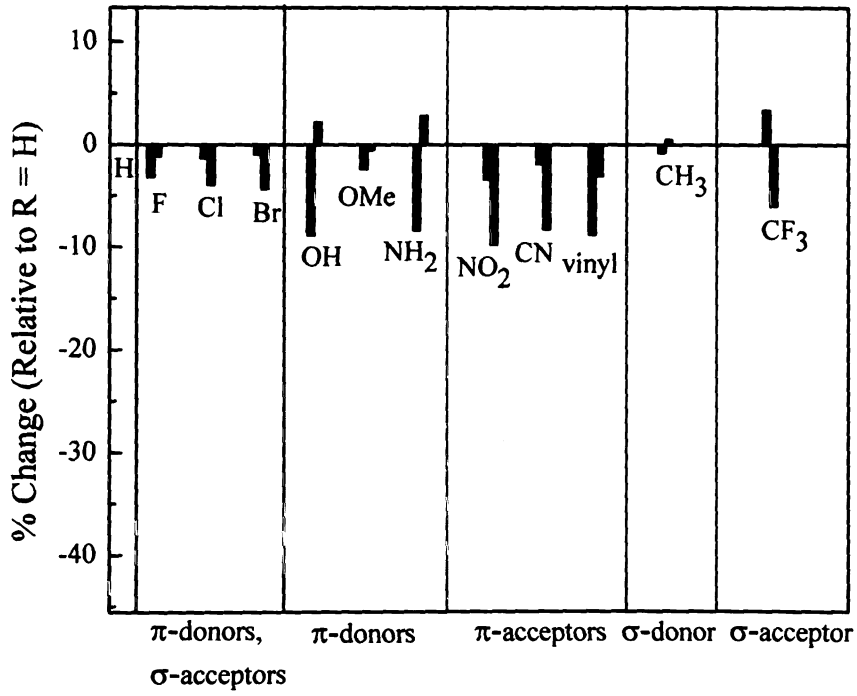

Figure 3-12. Spin density (red) and charge density (blue) polarization in 4,5-R-*o*-1,2-semiquinones.

In general, all spin and charge density changes are smaller when compared to the 3,6-isomers. Two notable differences in spin and charge polarization between the isomers

were observed. First, the CF_3 group is the only substituent that increases the spin density in the 4,5-R-*o*-1,2-semiquinones, and the increase spin, increase charge regime is not observed with these isomers. Second, the OMe substituent decreases charge density, which is the opposite trend for the other π-donors in this system and from the 3,6-isomers. Possible mechanisms for the deviations between the 4,5- and 3,6-isomers will be elaborated upon in the following sections.

Charge Density Polarization in 4,5-R-*o*-1,2-semiquinones. The changes in charge density are similar to the 3,6-R-*o*-1,2-semiquinone isomers except for the methoxy substituent which decreases charge density at the oxygen atoms. The optimized structure of the 4,5-OMe-*o*-1,2-semiquinone reveals that the OMe group is not planar with the semiquinone ring, and this is a possible cause for the deviation in charge density. The Hammett parameters were again added together to take into consideration both the *para* and *meta* polar effects of the substituents, as shown in Figure 3-13.

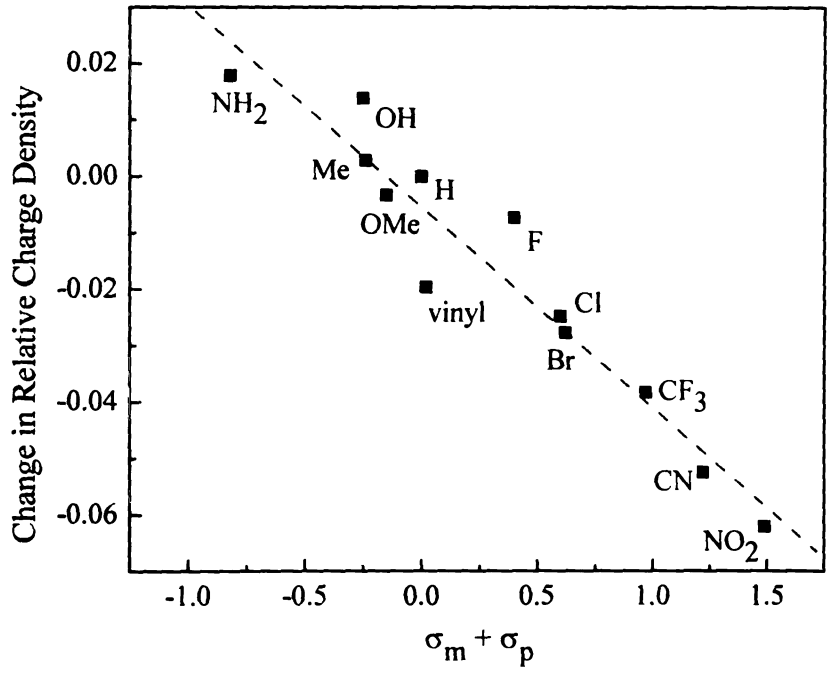

Figure 3-13. Charge density vs. additive Hammett parameter for 4,5-R-*o*-1,2-semiquinones.

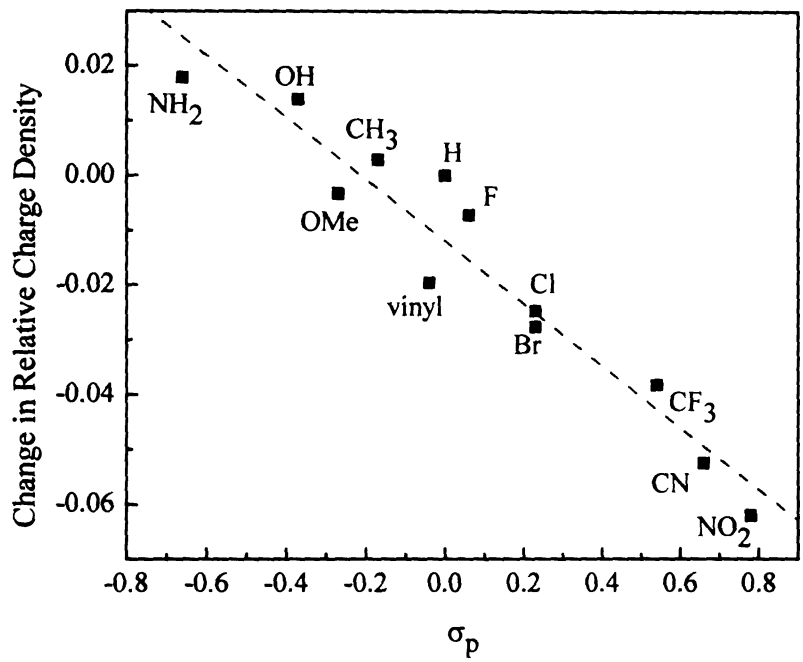

Figure 3-14. Charge density vs. σ_p Hammett parameter for 4,5-R-*o*-1,2-semiquinones.

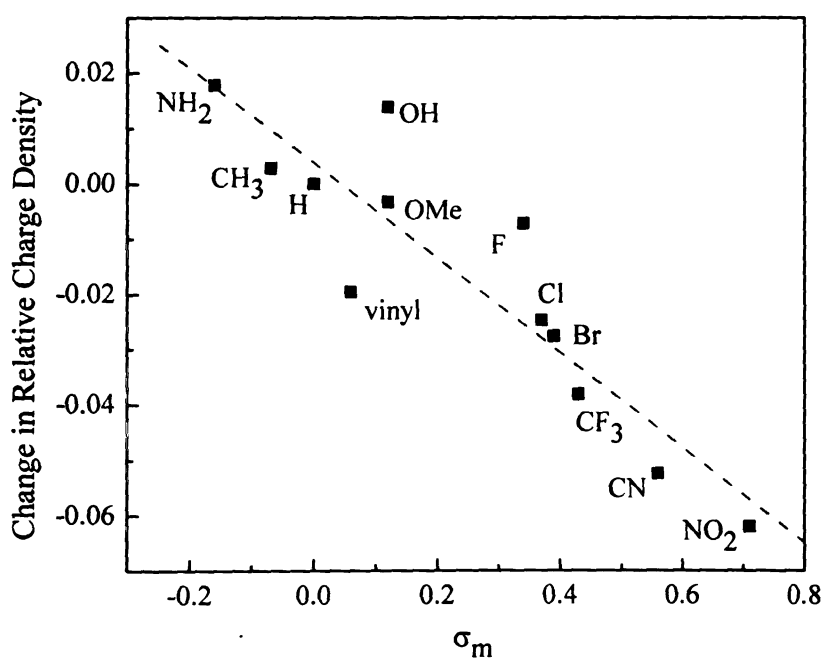

Figure 3-15. Charge density vs. σ_m Hammett parameter for 4,5-R-*o*-1,2-semiquinones.

The change in charge density correlates rather nicely with the additive Hammett parameter with r = 0.96. We also attempted the same correlation with only the σ_p and σ_m

substituent constants, and the correlation resulted in r = 0.96 (Figure 3-14) and r = 0.90 (Figure 3-15), respectively. As before in the 3,6-SQ isomers the better match with the σ_p constants indicates that π-effects are more dominate than the σ-polar effects of the 4,5-isomers.

Spin Density Polarization in 4,5-R-*o*-1,2-semiquinones. Major differences are noted in the spin density distribution in the 4,5-R-*o*-1,2-semiquinones when compared to the 3,6-isomers. First, the π-donors, fluorine, and methyl (weakly) decreased the spin density in the 4,5-isomers, and in the 3,6-isomers the opposite trend was seen. Secondly, in the 4,5-SQ series the CF_3 substituent is the only substituent to increase the spin density at the oxygen atom. Third, the magnitude of the changes in spin density are attenuated in the 4,5-R-*o*-1,2-semiquinones. To explain these differences and find the mechanism for the spin delocalization we searched for correlations between the changes in spin density with the Hammett spin delocalization constants, the C–O bond distance, and the α-HOMO-α-LUMO gap. All the correlations with the Hammett parameters, C–O bond distance, and even the α-HOMO-α-LUMO gap gave poor correlation constants, and the points were highly scattered. As an example, the poor correlation with the α-HOMO-α-LUMO gap can be seen in Figure 3-16. The differences in the spin density distribution and the lack of any correlation with the α-HOMO-α-LUMO gap are most likely due to steric factors between the substituents. The competing *meta* and *para* electronic factors could also be a cause of the deviations, but the correlation of the 3,6-isomers with the α-HOMO-α-LUMO gap was decent even when all substituents were used. There are less steric repulsive interactions in the 3,6-SQ isomers since the substituents are not *ortho* to one another as seen in the comparative NO_2 example in Figure 3-17. Even though both

isomers deviate from planarity with the SQ ring, the 4,5-isomer canting is much more pronounced due to the proximity of both nitro groups.

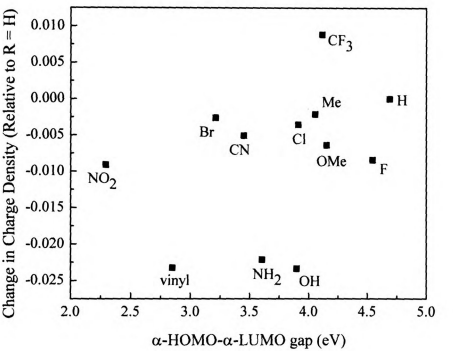

Figure 3-16. Correlation of spin density with the α-HOMO-α-LUMO gap in 4,5-R-*o*-1,2-semiquinones.

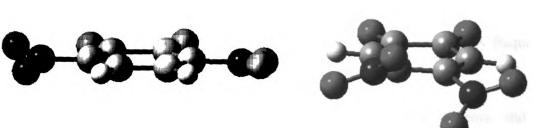

Figure 3-17. DFT optimized structures depicting the steric interactions in 3,6-NO_2-*o*-1,2-semiquinone (left) and 4,5-NO_2-*o*-1,2-semiquinone (right).

The results of the 3,6-R-*o*-1,2-semiquinones then suggest that geometric fluctuations in the 4,5-R-*o*-1,2-semiquinones are likely the major factor causing the deviations in the spin and charge distribution. Recall that the geometry optimizations indicated that the

NO_2, vinyl, OMe, and NH_2 substituents are not planar with the semiquinone ring. Due to the non-planarity and steric crowding between the substituents the spin distribution mechanism will be difficult to interpret, and therefore the spin delocalization mechanism can not be determined in this case.

3.3.2 Substituted 9,10-Phenanthrenesemiquinone Anion Radicals

Geometry Optimizations of Substituted 9,10-Phenanthrenesemiquinones. The crystal structure for the 9,10-phenanthrenequinone ligand has been reported,[33] and Praseuth[34] has shown that calculations at the UB3LYP/6-31g* level yielded structures that were nearly identical to the experimental X-ray data. Analogous to the case of the *o*-1,2-semiquinones, the DFT optimized structures are then good estimates of the true geometries. The optimized geometries of the 2,7-Phenanthrenesemiquinones (2,7-PSQ) and 3,6-phenanthrenesemiquinones (3,6-PSQ) had no large structural variations, and the largest C–O bond distance variations were found to be ± 0.019 Å. The only substituents that were found to deviate from planarity were the 2,7-NMe_2 and 3,6-NMe_2 substituted radicals. All optimized structures corresponded to global minima verified by frequency calculations.

The phenanthrenesemiquinone ligands are polycyclic ring systems, and the numbering scheme of the carbon atoms is indicated in Scheme 3-3. Virtually all positions of the phenanthrenesemiquinones can be substituted, but for our purposes we wanted to have symmetric substitution within the ring system to facilitate a more straightforward analysis of the charge and spin distributions. To this end the 2,7-(*meta*) and 3,6-(*para*) substituted radicals were studied. Substitution at these positions will not

be susceptible to steric crowding as was the case for the substituted *o*-1,2-semiquinones. We shall look at each set of phenanthrenesemiquinone isomers individually, and look for similar trends in spin and charge density polarization as we observed for the *o*-1,2-semiquinone and phenoxy radical systems.

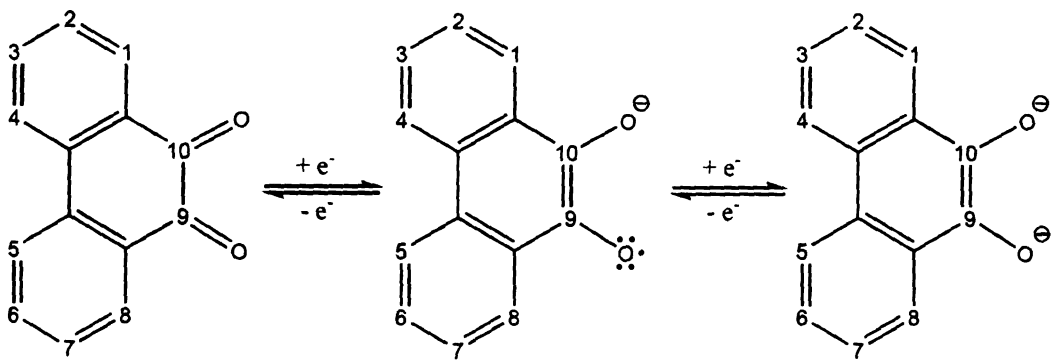

Scheme 3-3. Redox properties of the phenanthrenesemiquinones.

Spin and charge density polarization in 2,7-phenanthrenesemiquinones. At the oxygens, the unsubstituted PSQ has spin = 0.25703 α-electrons and charge = -0.6329 electrons. Of the four possible regimes for the increase/decrease of spin and charge density only the increase charge, decrease spin was not observed (Figure 3-18). The spin and charge polarization in the 2,7-phenanthrenesemiquinones is nearly identical to the 3,6-R-*o*-1,2-semiquinones, except for the OH and CH_3 substituents. In these radicals the OH substituent actually decreases the charge at the oxygen atom, which contrasts with the results from the 3,6-R-*o*-1,2-semiquinones. Additionally, the methyl group decreases spin density with essentially no change in charge density, while the opposite trend was observed for the 3,6-R-*o*-1,2-semiquinones. The underlying trends and possible mechanisms for spin and charge delocalization will be discussed below.

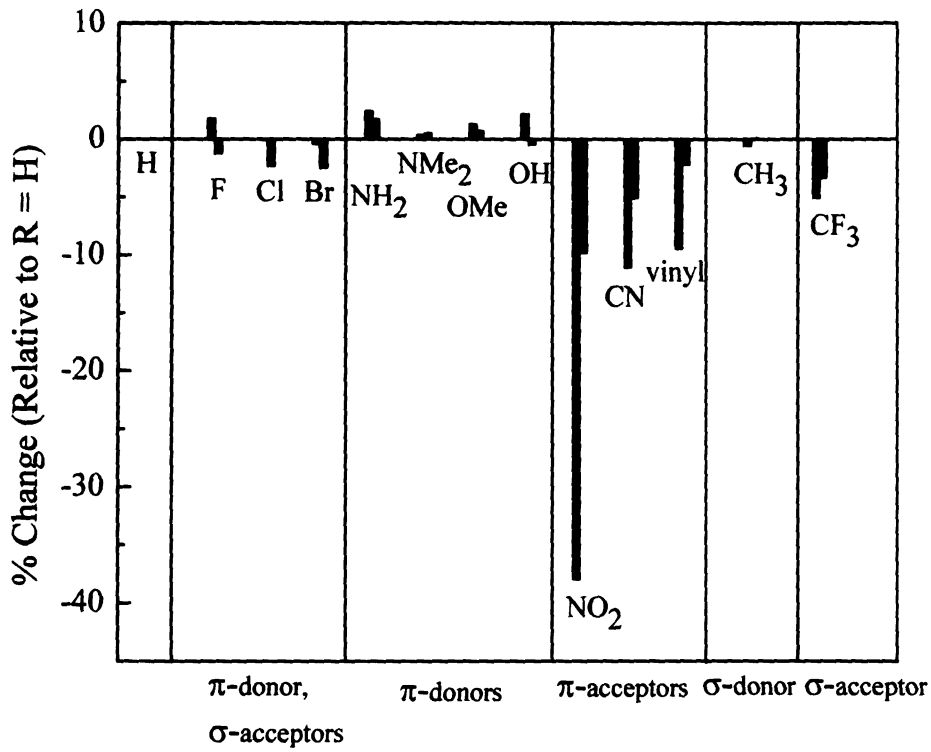

Figure 3-18. Spin (red) and charge (blue) polarization for 2,7-R-phenanthrenesemiquinones.

Charge Density Polarization in 2,7-phenanthrenesemiquinones. The charge density was correlated with the Hammett parameters (σ_m, σ_p, and σ_p^-) and the best resulting correlation was with the σ_p^-. The correlation constants for the varying Hammett parameters are $r(\sigma_m) = 0.88$ (Figure 3-19), $r(\sigma_p) = 0.86$ (Figure 3-20), and $r(\sigma_p^-) = 0.94$ (Figure 3-21). The σ_p^- Hammett constant is usually invoked in an electron rich system, and it is not surprising then that the σ_p^- parameter has the best correlation with the change in charge density, since the semiquinone ring is an anion.[21] The correlation constant should increase if σ_m^- type-constants were available (2,7 is formally a *meta* isomer), but no comprehensive list of these constants is reported in the literature. The overall trend in

this system is comparable to what we have observed in the other semiquinone anion radicals.

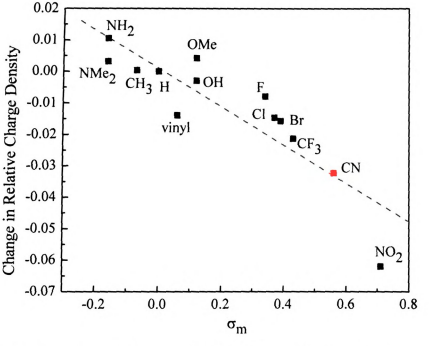

Figure 3-19. Charge density vs. Hammett σ_m correlation for 2,7-R-phenanthrenesemiquinones.

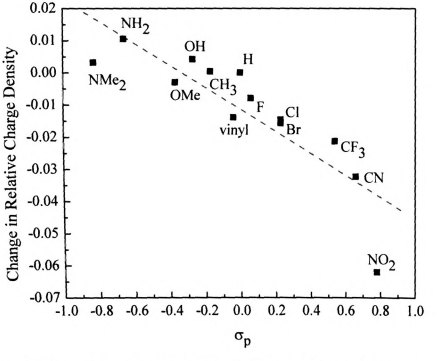

Figure 3-20. Charge density vs. Hammett σ_p correlation for 2,7-R-phenanthrenesemiquinones.

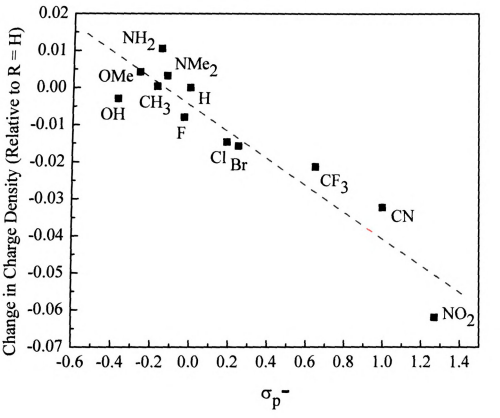

Figure 3-21. Charge density vs. Hammett σ_p^- correlation for 2,7-R-phenanthrenesemiquinones.

Spin Density Distribution in 2,7-phenanthrenesemiquinones. The calculations have shown that the strong π-donors and fluorine increase the spin density at the oxygen atoms, while all other substituents decrease the spin at the oxygen centers. It should be noted that the increase in spin at the oxygens is much weaker in comparison to the 3,6-SQ radicals. The substituents in the 2,7-phenanthrenesemiquinones and the 3,6-R-*o*-1,2-semiquinones have similar spin polarization regimes, and it is likely then that the 2,7-phenanthrenesemiquinones will have comparable polarization mechanisms. Analogous resonance interactions can occur, and the π-donors will participate in charge separated resonance structures (Figure 3-22 left). A much weaker charge-dipole type-repulsion is exhibited in the calculations of the 2,7-phenanthrnesemiquinone systems, where the

negative charge density in the ring system is destabilized by the donation of electron density from the π-donor ligands.

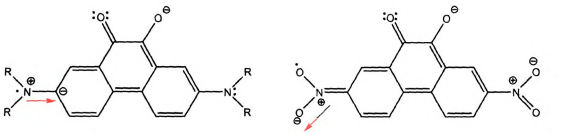

Figure 3-22. Spin resonance structures of 2,7-R-phenanthrenesemiquinone substituted with a π-donor (left) and π-acceptor (right). The red arrows represent charge donation or withdrawal from the PSQ anion.

The magnitude of the spin localization was found to be related to the calculated donating strength of the substituents, and in the 2,7-PSQ radicals the calculated π-donation is weaker and the corresponding spin localization is decreased.

Again analogous to the 3,6-R-*o*-1,2-semiquinones, there are no charge destabilizing interactions in the α-spin acceptors (Figure 3-22 right) and these substituents were found to increase spin delocalization in the radicals. The spin polarization mechanism can also be qualitatively verified by examining the spin density distributions in 2,7-NH_2- and 2,7-NO_2-phenanthrenesemiquinones. Figure 3-23 indicates that the spin density is easily delocalized onto the NO_2 substituent, and there is a lack of spin population on the NH_2 substituents. The spin delocalization onto the nitro substituents is consistent with no destabilizing charge-dipole type interactions being present. Very little spin density is delocalized onto the NH_2 substituent, since formation of the charge separated resonance structure is minimized by weak β-spin donation. The weaker β-spin donation accounts for the attenuated spin localization in the 2,7-PSQ

compared to the 3,6-SQ radicals. Therefore, the spin distribution in the 2,7-phenanthrenesemiquinones supports a weaker charge repulsion mechanism.

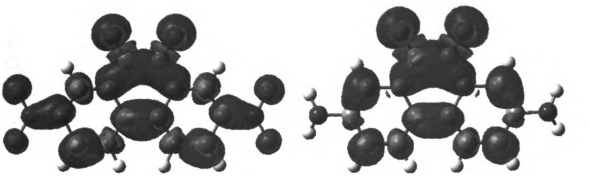

Figure 3-23. Spin density delocalization in 2,7-NH_2- and 2,7-NO_2-phenanthrenesemiquinone.

The spin density was again correlated with the α-HOMO-α-LUMO gap shown in Figure 3-24. The NO_2 substituent is an obvious outlier in the correlation with r = 0.957. Just as in the case of the 3,6-R-*o*-1,2-semiquinones, the percent contribution of the substituents to the frontier orbitals was examined, and is tabulated in Table 3-2.

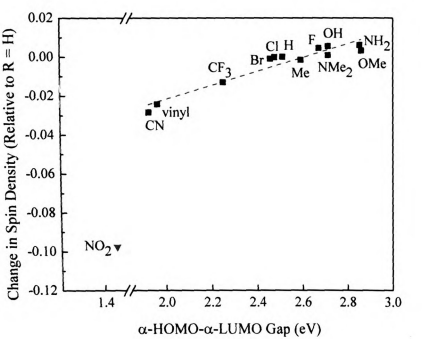

Figure 3-24. Change in spin density vs. α-HOMO-α-LUMO gap for 2,7-phenanthrenesemiquinones.

Table 3-2. Percent contribution to the frontier orbitals of 2,7-phenanthrenesemiquinones.

Substituent	% R α-HOMO	% O α-HOMO	% R α-LUMO	% O α-LUMO	Spin Density[a]	Gap[b]
H	0.00	18.23	0.00	0.40	0.2570	2.515
F	0.20	18.40	1.34	0.06	0.2616	2.675
Cl	0.36	17.82	1.82	0.32	0.2569	2.480
Br	0.35	17.77	1.65	0.36	0.2560	2.462
OH	0.34	18.58	1.89	0.00	0.2626	2.715
OMe	0.68	18.43	2.83	0.05	0.2603	2.861
NH_2	0.70	18.29	4.65	0.00	0.2632	2.854
NMe_2	1.27	17.04	13.51	0.16	0.2579	2.715
CH_3	0.94	17.87	3.24	0.39	0.2555	2.595
CF_3	0.57	16.70	3.70	1.31	0.2440	2.254
CN	1.25	15.60	6.88	2.54	0.2286	1.930
NO_2	8.49	10.52	20.60	6.81	0.1595	1.430
vinyl	2.46	16.13	17.91	2.54	0.2328	1.968

[a] The average spin density at oxygen. [b] The α-HOMO-α-LUMO gap is measured in electron volts.

The NO_2 substituent does have a 20.6 % contribution to the α-LUMO, but the vinyl and NMe_2 substituents both also have a large contribution to the α-LUMO orbital. The nitro substituent can't be excluded based on the %R data in the α-LUMO, since other substituents fall nicely on the line with elevated %R contributions. A dominating electron withdrawing σ-effect argument similar to the exclusion of the vinyl substituent in the 3,6-R-*o*-1,2-semiquinones can be suggested for the NO_2 substituent here. Literature reports have indicated that the electron withdrawing σ-effects of NO_2 at the *meta*-position is destabilizing in nature.[24,32,35] Further evidence for the dominating electron withdrawing σ-effects causing the NO_2 deviation will be revealed in the examination of the 3,6-isomers (vide infra). The correlation of the spin density with the

α-HOMO-α-LUMO gap and the %R data in Table 3-2 supports invoking a similar four-orbital mechanism that was used for the 3,6-R-*o*-1,2-semiquinones.

Spin and Charge Density Polarization in 3,6-phenanthrenesemiquinones. Only two regimes for spin and charge density variation are observed for the 3,6-phenanthrenesemiquinones compared to the 2,7-isomers, and these changes are shown in Figure 3-25. All substituents decrease spin density at the oxygen atoms. The substituents that decrease spin density and decrease negative charge density at oxygen are NO_2, CN, vinyl, CF_3, F, Cl, and Br, and the substituents that decrease spin density and increase negative charge density at the oxygen center are NH_2, NMe_2, OMe, OH, and CH_3.

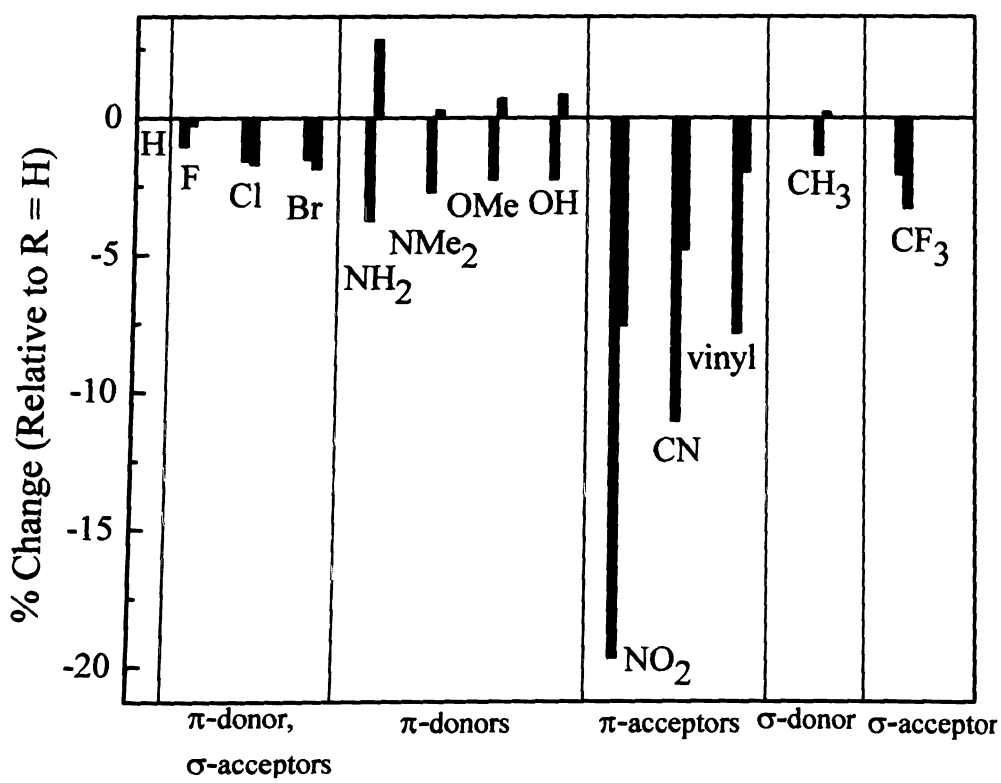

Figure 3-25. Spin density (red) and charge density (blue) polarization in 3,6-R-phenanthrenesemiquinones.

The changes in charge density are similar in the two sets of phenanthrenesemiquinone isomers, but there is a difference in the spin polarization of the π-donors. The changes in spin density for the π-donors are small, and difficult to quantify. A reasonable assumption for the shift in spin delocalizing ability of the π-donors is that the charge-dipole repulsion interaction is decreased or inoperable compared to the 2,7-PSQ. In other words, there is a larger donor destabilizing effect in the 2,7-PSQ ligands. The π-donors decrease spin density at the oxygen atoms and α-spin density is delocalized onto the substituent, thus the theoretical spin density data for the 3,6-PSQ complexes supports the lack of charge-dipole destabilizations. The opposite was true for the 2,7-PSQ isomers, and spin density was increased at the oxygen centers. The spin density distribution for the 3,6-NO_2 and 3,6-NH_2-PSQ's can be seen in Figure 3-26, and the spin distribution supports the proposed mechanism for decreased charge dipole repulsion.

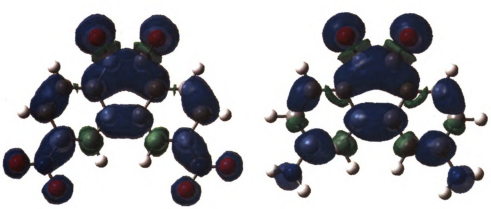

Figure 3-26. Spin density delocalization in 3,6-NH_2-PSQ and 3,6-NO_2-PSQ.

Charge Density Polarization in 3,6-phenanthrenesemiquinones. The charge density distribution for the 3,6-phenanthrenesemiquinones was correlated with the Hammett σ_p^- substituent constants, and the correlation is shown in Figure 3-27. The

correlation coefficient, r = 0.955, is strong and the substituents follow typical electronegativity arguments as was seen in the other semiquinones studied above. Therefore, in all anion radicals examined here the Hammett correlations hold.

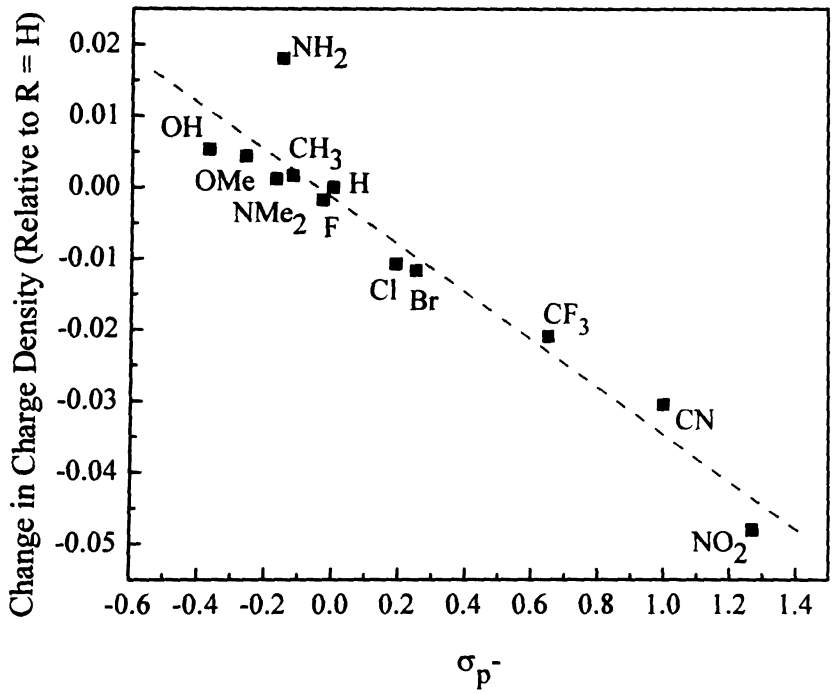

Figure 3-27. Charge density polarization in 3,6-phenanthanrenesemiquinones.

Spin Density Polarization in 3,6-R-phenanthrenesemiquinones. The spin density was again found to correlate with the α-HOMO-α-LUMO gap, as shown in Figure 3-28. No substituents were removed from the regression line to achieve a correlation constant of r = 0.948, but the correlation does rely heavily on the nitro-substituent to achieve a correlation coefficient close to one. Interestingly, upon examination of the percent atomic contributions to the α-LUMO orbitals of the NO_2, CN, and vinyl substituents, they were found to have large % R character. This data supports our hypothesis that a complicated four-orbital (or higher) interaction is the mechanism that could modulate the spin density in the semiquinone radicals. The lack of any firm

correlations in the orbital data preclude us from quantifying this interaction. Although the α-HOMO-α-LUMO gap correlation with spin density is present, due to the heavy dependence on NO_2 the reliability of the correlation remains unclear. It is noteworthy that all radicals examined did exhibit the correlation with the α-HOMO-α-LUMO gap, and the HOMO-LUMO gap suggests the degree of spin delocalizing ability of the substituents.

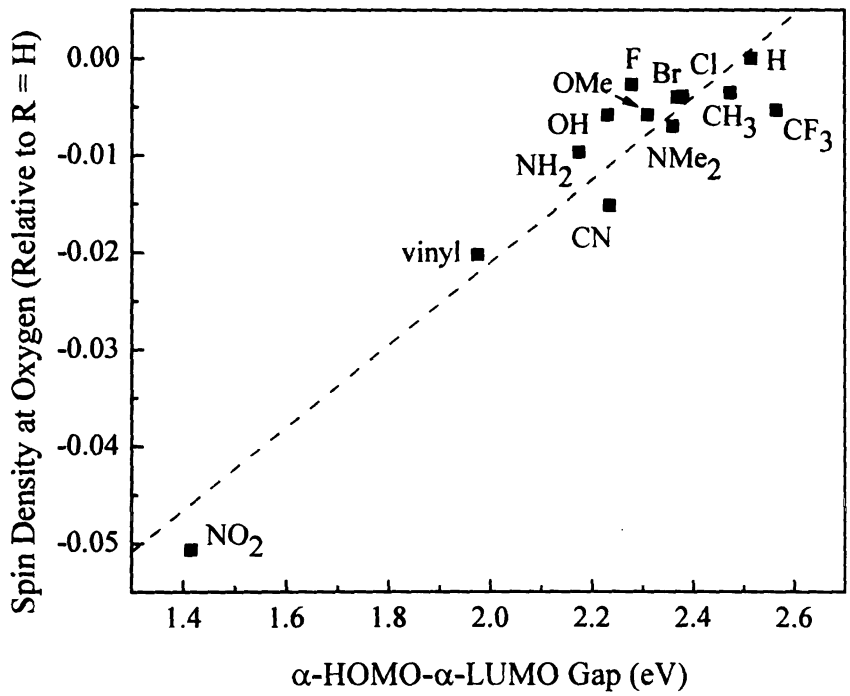

Figure 3-28. Change in spin density vs. α-HOMO-α-LUMO gap for 3,6-phenanthrenesemiquinones.

3.4 Concluding Comments.

The investigations of the spin and charge density polarization for *o*-1,2-semiquinones and *o*-9,10-phenanthrenesemiquinones have revealed that the negative

charge density is well represented by the Hammett substituent constants, resulting in strong correlations with the different substituent constants (σ_p, σ_m, σ_p^-, etc.). In the 3,6-SQ and 2,7-PSQ radicals the interaction between the electron donor and acceptor substituents with the delocalized negative charge density in the SQ ring impacted the spin delocalizing ability of the substituents. The dipole resulting from the charge separated resonance structure of a π-donor interacts unfavorably with the negative charge in the ring resulting in spin density localization at the oxygen centers. This localization is a direct result of the energetically unfavorable charge-dipole repulsion interaction in the semiquinone ring. This accounts for the change is spin delocalizing ability observed between the π-donors in the phenoxy radical and 3,6-R-SQ and 2,7-PSQ radicals, since the phenoxy radical is a neutral radical the destabilizing charge repulsion interaction is not likely. The electron acceptors stabilize the negative charge and were all found to increase spin delocalization in the *o*-semiquinones.

The spin density at the oxygen atoms in the *o*-semiquinones can be correlated with the α-HOMO-α-LUMO gap (except for the 4,5-o-1,2-semiquinones), and this correlation seems to be a general result for both neutral and anion radicals. In contrast to the phenoxy radicals, a firm mechanism to describe the spin delocalization using molecular orbital theory was not determined. It is hypothesized that a complicated four-orbital (or higher) interaction could be modulating the spin density in these systems, but this could not be confirmed based on the DFT data. Choices of the proper substituent for the synthesis of transition metal semiquinone complexes to modulate exchange interactions based on these DFT results will then be of a more empirical basis. More work is needed to quantify the spin polarization mechanisms in order to intelligently

design exchange coupled complexes. Experimental work along these lines using electron paramagnetic resonance spectroscopy to determine the substituents effect on the spin delocalization/polarization mechanisms of substituted PSQ radicals and gallium(III)-PSQ radical complexes will be examined, and is the topic of Chapter 4.

3.5 References

1. Fehir Jr., R. J.; McCusker, J. K. *J. Am. Chem. Soc.* **2009,** submitted.

2. Sugiura, K.-I.; Arif, A. M.; Rittenberg, D. K.; Schweizer, J.; Öhrstrom, L.; Epstein, A. J.; Miller, J. S. *Chem. Eur. J.* **1997,** 3, 138.

3. Osanai, K.; Okazawa, A.; Nogami, T.; Ishida, T. *J. Am. Chem. Soc.* **2006,** 128, 14008.

4. McConnell, H., M, *J. Chem. Phys.* **1963,** 39, 1910.

5. Hicks, R. G.; Lemaire, M. T.; Thompson, L. K.; Barclay, T. M. *J. Am. Chem. Soc.* **2000,** 122, 8077.

6. Shultz, D. A.; Sloop, J. C.; Washington, G. *J. Org. Chem.* **2006,** 71, 9104.

7. Chaudhuri, P.; Wieghardt, K. *Prog. Inorg. Chem.* **2001,** 50, 151.

8. Müller, J.; Kikuchi, A.; Bill, E.; Weyhermüller, T.; Hildebrandt, P.; Ould-Moussa, L.; Wieghardt, K. *Inorg. Chim. Acta.* **2000,** 297, 265.

9. Rotthaus, O.; Thomas, F.; Jarjayes, O.; Philouze, C.; Saint-Adam, E.; Pierre, J.-L. *Chem. Eur. J.* **2006,** 12, 6953.

10. Mishustin, A. I. *Russ. J. Inorg. Chem.* **2008,** 53, 1376.

11. Wheeler, D. E.; Rodriguez, J. H.; McCusker, J. K. *J. Phys. Chem. A* **1999,** 103, 4101.

12. Pierpont, C. G.; Buchanan, R. M. *Coord. Chem. Rev.* **1981,** 38, 45.

13. Pierpont, C. G.; Lange, C. W. *Prog. Inorg. Chem.* **1994,** 41, 331.

14. Pierpont, C. G. *Coord. Chem. Rev.* **2001,** 216-217, 99.

15. Kaim, W. *Coord. Chem. Rev.* **1987,** 76, 187.

16. Zanello, P.; Corsini, M. *Coord. Chem. Rev.* **2006,** 250, 2000, and references therein.

17. Poddel'ski, A.; Cherkasov, V. K.; Abakumov, G. A. *Coord. Chem. Rev.* **2009,** 253, 291.

18. Pierpont, C. G.; Attia, A. S. *Collect. Czech. Chem. Commun.* **2001,** 66, 33.

19. Macdonald, A. L.; Trotter, J. *J. Chem. Soc. Perkin Trans. 2* **1973**, 473.

20. *Correlation Analysis in Chemistry: Recent Advances*. Plenum Press: New York and London, 1978.

21. Exner, O. *Correlation Analysis of Chemical Data*. Plenum Publishing Corporation: New York, NY, 1988.

22. Hansch, C.; Leo, A.; Taft, R. W. *Chem. Rev.* **1991,** 91, 165.

23. Shorter, J. *Correlation analysis in organic chemistry: an introduction to linear free-energy relationships*. Oxford University Press: Oxford, 1973.

24. Wayner, D. D. M.; Arnold, D. R. *Can. J. Chem.* **1985,** 63, 2378.

25. Clark, K. B.; Wayner, D. D. M. *J. Am. Chem. Soc.* **1991,** 113, 9363.

26. Bordwell, F. G.; Zhang, X.-M.; Satish, A. V.; Chen, J.-P. *J. Am. Chem. Soc.* **1994,** 116, 6605.

27. Creary, X. *J. Org. Chem.* **1980,** 45, 280.

28. Jiang, X.-K. *Acc. Chem. Res.* **1997,** 30, 283.

29. Adam, W.; Harrer, H. M.; Kita, F.; Korth, H.; Nau, W. M. *J. Org. Chem.* **1997,** 62, 1419.

30. Korth, H.-G.; de Heer, M. I.; Mulder, P. *J. Phys. Chem. A* **2002,** 106, 8779.

31. Brinck, T.; Haeberlein, M.; Jonsson, M. *J. Am. Chem. Soc.* **1997,** 119, 4239.

32. Fisher, T. H.; Dershem, S. M.; Prewitt, M. L. *J. Org. Chem.* **1990,** 55, 1040.

33. Matsuzaki, S. Y.; Gotoh, M.; Kuboyama, A. *Mol. Cryst. Liq. Cryst.* **1987,** 142, 127.

34. Praseuth, R. T. Michigan State University, 2002.

35. Creary, X.; Mehrsheikh-Mohammadi, M. E.; McDonald, S. *J. Org. Chem.* **1987,** 52, 3254.

Chapter 4. Density Functional Theory and Electron Paramagnetic Resonance Spectroscopy of Dinitophenanthrenesemiquinone Radicals and Their Gallium(III) Complexes

4.1 Introduction

After the prescription for the movement of spin and charge density was realized for the phenoxy radicals and substituted semiquinone complexes, a natural extension of that work is to see if the same rules that govern spin density distribution can also apply in transition metal radical complexes. It is well known in the literature that transition metal complexes have a combination of spin polarization and spin delocalization mechanisms that describe the total spin density distribution within a molecule.[1,2] The examples cited by Alvarez and coworkers[1,2] mostly consist of paramagnetic transition metals ligated with diamagnetic donor ligands. The general picture of spin density distribution in such a system can be seen in Figure 4-1 below.

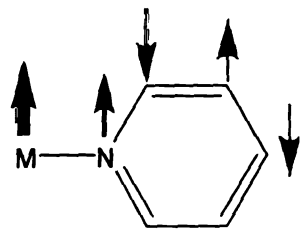

Figure 4-1. General spin density distribution in a metal-ligand complex.

In Figure 4-1, the nitrogen donor atom carries positive spin density (upward arrow), because spin delocalization is the dominant mechanism since it is directly bonded to the paramagnetic metal, and the rest of the atomic π-orbitals alternate spin density due to spin polarization being the dominant mechanism. Remenyi and Kaupp[3] have shown that spin polarization is important in the unrestricted Kohn-Sham description of the electronic

structure of open-shell systems. There are also several examples in the literature of paramagnetic transition metals with organic radicals such as semiquinones,[4,5] nitroxides,[6,7] and verdazyls[8] where spin density delocalization and polarization can play an important role in creating new molecular magnetic materials. The impact that bonding of the semiquinone radicals with different diamagnetic metals has on the spin density distribution has also been examined by Cherkasov and coworkers.[9] They determined that the magnitudes of the hyperfine coupling constants vary when semiquinones are bound to a metal, but there is still a significant amount of spin density that is delocalized in the semiquinone ring and usually < 1 % of the spin is delocalized onto the metal.

We will examine the changes in spin density distribution in the semiquinone radical upon complexation to a gallium diamagnetic metal center. A report from Oshio et al.[10] compares the spin density distribution of a nitroxide radical to transition metal complexes of the same radical, with the authors noting that upon coordination the spin density within the radical moiety changes only slightly. It should be noted that the metal complexes in Oshio's work were not directly coordinated to the atoms with the highest spin density, whereas semiquinones are experimentally[11,12] and theoretically[13] known to have the highest α-spin population at the oxygen atoms which coordinate directly to the metal center. Rockenbauer et al.[14] have examined tetrahedral copper(I) phenanthrenesemiquinone complexes, and have shown that spin density is transferred to carbons closer to the semiquinone oxygens upon coordination based on changes in the ^{1}H hyperfine coupling constants in the semiquinone ring. Mixing between the radical SOMO and a filled 3d-orbital on the copper(I) center was put forth to account for the spin transfer.[14] The Rockenbauer et al. report also gives experimental evidence to support that

changes in spin distribution occur when a semiquinone radical is coordinated to a metal center. To further examine the coordination effects of diamagnetic metals on the spin density distribution, gallium(III)-phenanthrenesemiquinone complexes will be examined. Both EPR experiments and DFT methods were employed to probe any changes in spin density distribution. Thus, a theoretical and experimental picture of the coordination effects will help uncover any mechanisms that describe the effects of complexation on the spin density population.

DFT calculations on the 2,7-dinitrophenanthrenesemiquinone (2,7-di-NO_2-PSQ) (**1**) and 3,6-dinitrophenanthrenesemiquinone (3,6-di-NO_2-PSQ) (**2**) radicals and their corresponding gallium(III) complexes, [Ga(tren)(2,7-dinitrophenanthrenesemiquinone)]$^{2+}$ (Ga-2,7-di-NO_2-PSQ) (**3**) and [Ga(tren)(3,6-dinitrophenanthrenesemiquinone)]$^{2+}$ (Ga-3,6-di-NO_2-PSQ) (**4**), where tren = tris-2-aminoethylamine, were undertaken to see if the spin density distribution in the radicals changed upon coordination to a metal center (Chart 1). Specifically, we wish to uncover any changes coordination has on the α-spin density delocalization onto the nitrogen and hydrogen atoms. This will manifest itself by the magnitudes of the ^{1}H and ^{14}N hyperfine coupling constants (HFC). In order to prove experimentally what the DFT calculations predict, EPR was also carried out on the free ligands and gallium complexes. Gallium(III) is ideal for this EPR experiment, since it is a d^{10} metal with no Heisenberg magnetic exchange interactions to complicate the EPR spectrum. The EPR experiments will determine the experimental ^{1}H and ^{14}N hyperfine coupling constants in each radical and gallium complex. The importance of the accurate determination of the ^{14}N HFC's stems from our goal to properly examine the effects of spin delocalization and polarization on the nitro-substituent itself, and compare the results

when these same radical ligands are bound to gallium. These values can then be compared with those calculated by density functional theory methods to interpret the overall mechanism of spin delocalization/polarization. If this mechanism can be found, then the rational design of transition metal organic-radical molecular magnetic materials can be accomplished.

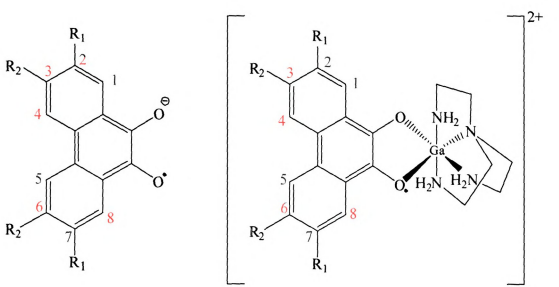

2,7-di-NO_2-PSQ (1): $R_1 = NO_2$ and $R_2 = H$

3,6-di-NO_2-PSQ (2): $R_1 = H$ and $R_2 = NO_2$

Ga-2,7-di-NO_2-PSQ (3): $R_1 = NO_2$ and $R_2 = H$

Ga-3,6-di-NO_2-PSQ (4): $R_1 = H$ and $R_2 = NO_2$

Chart 4-1. Free di-NO_2-PSQ radicals (left) and gallium(III)-di-NO_2-PSQ complexes.

The spin density at the carbon atoms around the semiquinone ring can be approximated experimentally from the ^1H hyperfine coupling constants by using the well known McConnell relationship,[15] seen here in Equation 1.

$$A(^1H) = Q_{CH}{}^{H}\rho_C \qquad (1)$$

In Eq 1, $A(^1H)$ is the experimentally determined proton hyperfine coupling constant (in Gauss), $Q_{CH}{}^{H}$ is a constant which describes the σ-π interaction between carbon and

hydrogen (for the hydrogen nucleus), and ρ_C is the π-spin density at the carbon atom that the hydrogen is directly bonded to.[15] The experimentally determined spin density can then be compared to what has been calculated by DFT. The isotropic HFC associated with a given nucleus N can be calculated using Equation 2.

$$A_{iso}(N) = \frac{4}{3}\pi g_e g_n \beta_e \beta_n \langle S_Z \rangle^{-1} \rho(N) \qquad (2)$$

where g_e and g_n are the electronic and nuclear g-factors, β_e and β_n are the electronic and nuclear Bohr magneton constants, and $\rho(N)$ is the Fermi contact integral which corresponds to the spin density at N. By substituting the appropriate constants into Equation 2, Nguyen et al.[16] derived the following conversion factors:

$$A_{iso}(^1H) = 1594.9\rho(^1H) \qquad (3a)$$

$$A_{iso}(^{14}N) = 57.6\rho(^{14}N) \qquad (3b)$$

and from which one can extract the total s-orbital spin densities for ^1H and ^{14}N given the experimental number for $A_{iso}(N)$ (in Gauss).

4.1.1 Electron Paramagnetic Resonance Spectroscopy

Electron paramagnetic resonance spectroscopy (EPR), also referred in the literature as electron spin resonance spectroscopy (ESR), is a technique that probes the environment of a paramagnetic species by characterizing the interaction of that species with an applied magnetic field. This method can provide detailed information about the spin density distribution within a paramagnetic species if there is spin density at a nucleus with $I \neq 0$, where I is the nuclear spin. The basis for EPR is the existence of the two different spin states of the electron, which become distinguishable in an applied magnetic

field. The interaction of the α and β spin states of the electron with an applied magnetic field is depicted in Figure 4-2, and this is called the electronic Zeeman interaction.

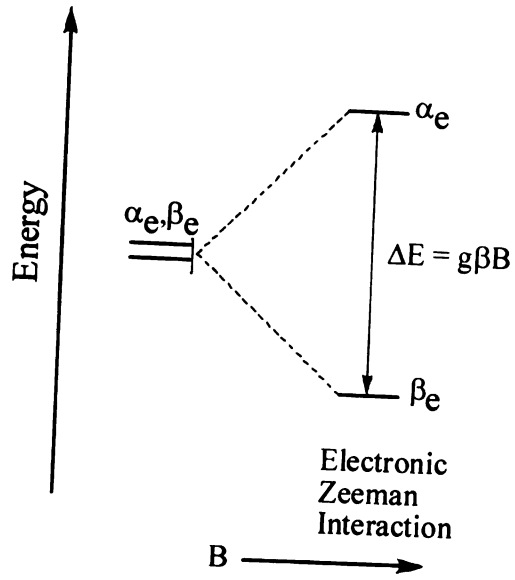

Figure 4-2. Interaction of the α and β spin states of the electron with an applied magnetic field.

The Zeeman Hamiltonian (**H**) for the interaction of the spin of the electron and the magnetic field is shown in Equation 4, where $\mathbf{S_Z}$ is the spin operator, B is the external magnetic field applied along the z-axis, g is the g-factor, and β is the electronic Bohr magneton.

$$\mathbf{H} = g\beta B\mathbf{S_Z} \tag{4}$$

When this Hamiltonian operates on the electron spin functions, α and β, the eigenvalues produced are m_s.[17] The energy of the electron spin states then become

$$E = m_S g\beta B \tag{5}$$

The electron has $m_S = {}^1/_2$ (the α_e spin state) and $m_S = -{}^1/_2$ (the β_e spin state), and when we solve Equation 5 for the energy the $m_S = -{}^1/_2$ state is lower in energy (due to the magnetic moment of the electron). An EPR transition occurs when microwave radiation that

equals the separation between the two spin states is absorbed, i.e. when the microwave radiation is at resonance with $\Delta E = g\beta B$.

The fine structure usually seen in EPR experiments arises from electron-nuclear hyperfine coupling, which is the interaction between the magnetic moment of the electron with that of magnetic nuclei in the molecule. The magnitude of this interaction is represented by the hyperfine coupling constant (HFC), A, and can easily be visualized by examining the hydrogen atom. Both g and A are usually represented as 3 x 3 tensors; but in the hydrogen atom the spherical symmetry eliminates all anisotropic interactions and we can assume colinearity of these tensors with projections along *x*, *y*, and *z*. B is again applied along the z-axis. The corresponding effective spin Hamiltonian for hydrogen must now take into consideration the interaction of the nuclear spin magnetic moment with the magnetic field and the hyperfine interaction, and this is shown in Equation 6.

$$\mathbf{H} = g\beta B\mathbf{S_Z} - g_n\beta_n B\mathbf{I_Z} + A\mathbf{S}\cdot\mathbf{I} \qquad (6)$$

The eigenvalues resulting from solving the Schrödinger equation with this Hamiltonian are given by Equation 7.[17]

$$E(m_S m_I) = m_S g\beta B - m_I g_n\beta_n B + A m_S m_I \qquad (7)$$

The first term in Equation 6 is the electronic Zeeman interaction as already discussed above. The second term is the interaction between the nuclear spin magnetic moment (**I**) and the applied field, and it is called the nuclear Zeeman interaction. The last term is the electron-nuclear hyperfine interaction, representing the coupling of the nuclear and electron magnetic moments. The sum of these interactions can be visualized in the EPR energy level diagram of the hydrogen atom. The electron-nuclear spin states of the hydrogen atom are depicted in Figure 4-3. The electronic Zeeman interaction gives rise

to the splitting of the β and α spin states of the electron. Hydrogen has a nuclear spin of I = $^1/_2$, and the nuclear Zeeman interaction splits the $m_I = {}^1/_2$ (α_p) and $m_I = -{}^1/_2$ (β_p) proton spin states. Due to the charge of the proton the magnetic moment vector is directed opposite to that of the electron, resulting in the $m_I = {}^1/_2$ (α_p) state being lower in energy.

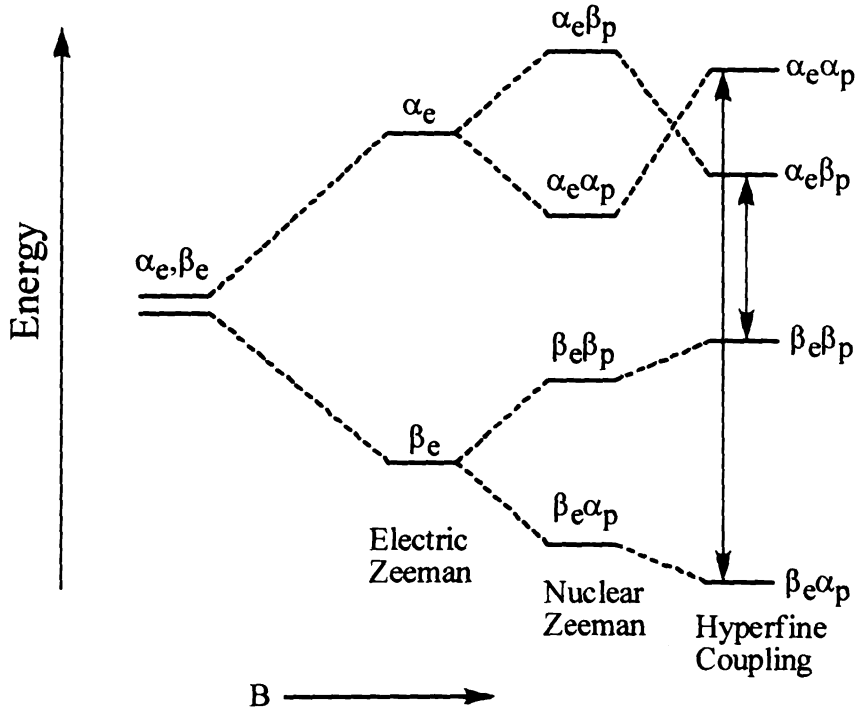

Figure 4-3. Electron-nuclear spin states of the hydrogen atom.

According to Equation 4, the energetic consequence of proton-electron hyperfine coupling is Am_Sm_I. In the lower spin manifold the $\beta_e\alpha_p$ ($m_S = -{}^1/_2$ and $m_I = {}^1/_2$) state will be lower in energy, and in the upper spin manifold, the $\alpha_e\beta_p$ ($m_S = {}^1/_2$ and $m_I = -{}^1/_2$) state will be stabilized. If we assume a large A then the states in the upper spin manifold can cross due to the increased stabilization as depicted in Figure 4-3. There are two EPR transitions observed for the hydrogen atom, shown with arrows in Figure 4-3. These

transitions are "spin flips", and the absorptions occur when the microwave radiation equals the energy difference between the $\Delta m_S = \pm {}^1/_2$ states. The selection rules for EPR transitions are $\Delta m_S = \pm 1$ and $\Delta m_I = 0$ for a typical microwave experiment.

4.1.2 Electron Spin Echo Envelope Modulation Spectroscopy (ESEEM)

The ESEEM experiment monitors NMR transitions indirectly, via mixing of the frequencies of the semi-forbidden and allowed EPR transitions which have been coherently excited using short, intense microwave pulses.[18] The resonant microwave pulses create electron spin echoes, and the spin echo decay envelop is then measured by plotting the integrated intensity of these echoes as a function of the times between pulses.[19] The result shows an overall decay of the electron spin magnetization that is modulated by electron-nuclear hyperfine couplings.[19] The common three-pulse ESEEM experimental spectral lines correspond to nuclear frequencies, which simplifies the identification of nuclei in the data. The ^{14}N nitrogen nucleus we wish to examine is a quadrupole with a nuclear spin of $I = 1$, therefore the nuclear-quadrupole interaction must be taken into consideration. The spin Hamiltonian for an $S = {}^1/_2$ and $I = 1$ system is shown in Equation 8.

$$\mathbf{H} = g\beta\mathbf{S}\cdot\mathbf{B} - g_n\beta_n\mathbf{I}\cdot\mathbf{B} + A\mathbf{S}\cdot\mathbf{I} + \mathbf{I}\cdot\mathbf{Q}\cdot\mathbf{I} \qquad (8)$$

The first three terms were already discussed above, and the fourth term is the interaction of the nuclear spin with the quadrupole of the nuclei. **Q** is the nuclear quadrupole tensor which is traceless and is only non-zero for $I > {}^1/_2$. Five parameters effectively describe the nuclear quadrupole interaction (NQI): e^2qQ, the quadrupole coupling constant; η, the asymmetry parameter, and α, β, and γ, the Euler angles that describe the orientation of the

e^2qQ principal axis system with respect to the principal axis system of the hyperfine tensor.[20] The energy level diagram for a rhombic quadrupole interaction ($\eta \neq 0$) with both A and g assumed to be isotropic is shown in Figure 4-4.

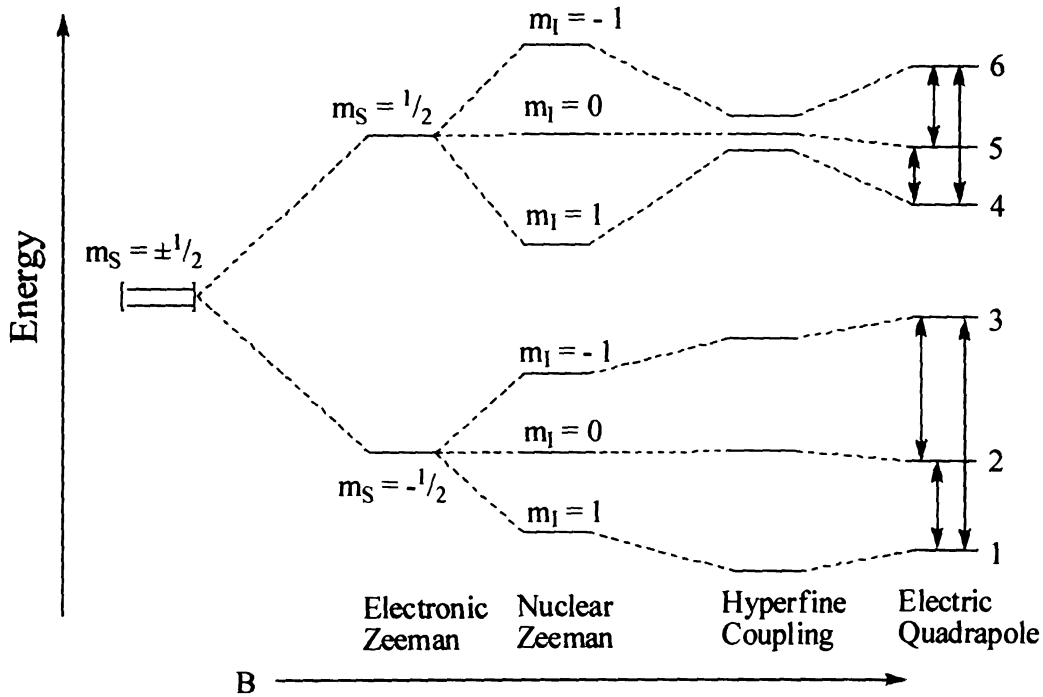

Figure 4-4. Energy level diagram for an $S = 1/2$, $I = 1$ system near exact cancellation[21] conditions.

The energies of the states are obtained by solving the 3 x 3 secular determinant in the nuclear basis functions $|m_I\rangle$ ($m_I = 0, \pm 1$) for each $m_S = \pm 1/2$ state, where the parameter K $= e^2qQ/4h$ and the nuclear Zeeman, $\upsilon_n = g_n\beta_n B/h$. Six transitions are allowed[2]

$$\nu_{56} = 3K + \sqrt{\left(\frac{A}{2} - \nu_n\right)^2 + \eta^2 K^2} \qquad (9a)$$

$$\nu_{45} = -3K + \sqrt{\left(\frac{A}{2} - \nu_n\right)^2 + \eta^2 K^2} \qquad (9b)$$

$$\nu_{46} = 2\sqrt{\left(\frac{A}{2} - \nu_n\right)^2 + \eta^2 K^2} \qquad (9c)$$

$$\nu_{23} = 3K + \sqrt{\left(\frac{A}{2} + \nu_n\right)^2 + \eta^2 K^2} \qquad (10a)$$

$$\nu_{12} = -3K + \sqrt{\left(\frac{A}{2} + \nu_n\right)^2 + \eta^2 K^2} \qquad (10b)$$

$$\nu_{13} = 2\sqrt{\left(\frac{A}{2} + \nu_n\right)^2 + \eta^2 K^2} \qquad (10c)$$

where, Equations 9 a-c correspond to the upper $m_S = {}^1/_2$ state, and 10 a-c give the energies of the $m_S = -{}^1/_2$ spin manifold. A total of six allowed transitions are possible in the experiment, but the number observed depends on the mixing between the various states. The extent of mixing will depend upon the magnitudes of the quadrupole and hyperfine terms in the Hamiltonian.

4.2 Experimental

General. All reagents were obtained from commercial sources and used without further purification. HPLC grade methanol was distilled from Mg and I_2, and degassed 15 times by gas exchange with N_2. Elemental analyses, mass spectra, and ESI-MS were obtained through the analytical facilities at Michigan State University. ^{1}H NMR spectra were recorded either on a Varian INOVA 300 MHz or a Varian Utility-Plus 500 MHz spectrometer.

2,7-dinitrophenanthrenequinone. The synthesis of this ligand has been modified from literature procedures.[23,24] A flask was charged with 3.00 g (14.4 mmol) of

phenanthrenequinone and then 40 ml of fuming nitric acid (D = 1.5) and 5 ml of sulfuric acid was added. The reaction mixture was refluxed for 30 minutes, and then allowed to cool to room temperature. The mother liquor was then added to 300 ml of distilled water and a yellow voluminous precipitate was immediately formed. The precipitate was collected on a glass frit and washed with distilled water until the washings were neutral. Once neutral, the precipitate was further washed with ethanol (20 ml x 3) and ether (20 ml x 3) and dried in vacuo. Recrystallization from 300 ml of hot glacial acetic acid yielded 1.92 g (45 %) of yellow needles. Anal. Calcd for $C_{14}H_6N_2O_6$: C, 56.38; H, 2.03; N, 9.39; Found: C, 55.83; H, 1.91; N, 9.14. mp = 299-300 °C. ^{1}H NMR (tfashake-DMSO-d_6)[25] δ 8.71 (d, J_{Hz} = 4.15), 8.69 (d, J_{Hz} = 1.95), 8.56 (dd, J_{Hz} = 2.20, 6.59).

2,7-dinitrophenanthrenesemiquinone (1). The generation of this radical was modified from published procedures.[26] In an oxygen free drybox, an excess of K metal was added to a 1 mmol/L solution of 2,7-di-NO_2-phenanthrenequinone in THF. The solution was then stirred for 3-5 minutes, and during this time the color of the solution turns pink in color. The solution was filtered, and then used immediately for EPR experiments. Upon freezing the solution in liquid nitrogen the color changes to green, which has been attributed to diamagnetic dimer formation.[27]

If the solution is stirred for an additional 30-40 minutes in the presence of excess K metal a precipitate falls out of solution. Based on the EPR spectrum (vide infra), this precipitate is paramagnetic and can be attributed to formation of a contact radical ion pair where potassium is coordinated to the 2,7-dinitrophenanthrnesemiquinone radical.

2,7-dinitrophenanthrenecatechol. The synthesis of this ligand has been slightly modified from literature procedures.[23] A suspension of 1.00 g (3.35 mmol) of 2,7-di-

NO_2-phenanthrenequinone in 35 ml ethanol was heated to 55-60 °C, then a mixture of 2.5 ml 80 % glacial acetic acid and 0.355 g (3.28 mmol) of phenylhydrazine was added drop wise while stirring. The solution slowly becomes clear and red in color upon addition of the phenylhydrazine/acetic acid mixture. The solution was stirred for 5 minutes and filtered with a glass frit, and upon addition of 150 ml of distilled water a brick red precipitate was immediately formed. The brick red precipitate was collected on a glass frit and dried in vacuo. Yield 0.958 g (96 %). The complex should be stored under nitrogen to prevent oxidation and solutions of the compound are very air sensitive. Anal. Calcd for $C_{14}H_8N_2O_6 \cdot 0.5H_2O$: C, 54.38; H, 2.93; N, 9.06; Found: C, 54.36; H, 2.71; N, 8.76.

Phenanthrenecatechol-SO_2. The synthesis of this complex has been modified from literature procedures.[28] *Caution: when using any UV-light source, proper safety glasses and protective clothing must be used to protect the eyes and skin. Additionally, due to the production of ozone by the lamp the reaction must be carried out in a fume hood.* The experimental setup is depicted in Figure 4-5, and during the reaction the glass plates of the fume hood are covered to avoid accidental UV-light exposure. A quartz schlenk flask was charged with 1.15 g (5.52 mmol) of phenanthrenequinone and 40 ml of benzene. SO_2 (g) was bubbled through the stirring suspension for 20-25 minutes, and the schlenk flask was capped and placed under positive pressure of SO_2. The quartz schlenk flask was then placed into a quartz water bath directly in the path of a 450 W HgH lamp as depicted in Figure 4-5. The suspension was irradiated with the HgH lamp for 36 hours, and the schlenk flask was rotated by 120° every 12 hours to ensure maximum penetration of light (some blackening occurs on the flask in the light path).

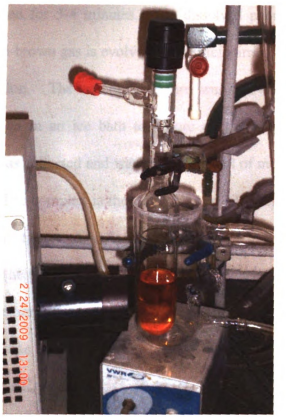

Figure 4-5. The experimental setup for the 36 hour photolysis reaction. The equipment pictured is a quartz Schlenk flask, quartz water bath, and 450W HgH lamp.

A white precipitate forms after approximately 12 hours of irradiation, but the reaction is not yet complete. After 36 hours the fine gray-white precipitate was collected on a glass frit and washed with ether (10 ml x 3) and dried in vacuo to give 1.10 g of product (77 % yield). The complex can be recrystallized from hot chloroform to give white needles. Anal. Calcd for $C_{14}H_8O_4S$: C, 61.76; H, 2.96; Found: C, 61.62; H, 2.65. mp = 200-202 °C. ^{1}H NMR ($CDCl_3$) δ 8.692 (m), 7.956 (m), 7.73 (m). IR (KBr, cm^{-1}) 1669 s, 1603 s, 1452 s, 1412 s, 1348 s, 1214 s, 858 s, 808 s, 750 s, 718 s, 699 s.

3,6-dinitrophenanthrenecathchol-SO_2. The synthesis of this complex has been modified from literature procedures.[28] 3.0 g (11 mmol) of phenanthrenecatechol-SO_2 was added to 100 ml of ACS grade nitric acid (D = 1.4) at 110 °C, the solution is then quickly

heated to boiling and stirred for 3-4 minutes. The dissolved phenthrenecatechol-SO_2 gives a red solution and red-brown gas is evolved, after brief stirring a yellow precipitate falls out of the hot solution. The reaction mixture was allowed to cool to room temperature and then cooled in an ice bath to ensure all the precipitate falls out of solution. The precipitate was collected and washed with 30 ml of methanol and 30 ml of ether and dried in vacuo. The complex is then dissolved in 170 ml of simmering acetic anhydride, and left out to crystallize. The flask was then placed in a freezer overnight to complete precipitatation. The precipitate was collected on a glass frit and washed with methanol (30 ml x 4) and ether (30 ml x 4) and dried in vacuo to give 1.3 g (33 %) of yellow needles. The precipitate was reported to be light sensitive and should be protected from light.[28] Anal. Calcd for $C_{14}H_6N_2O_8S$: C, 46.42; H, 1.67; N, 7.73; Found: C, 46.60; H, 1.27; N, 8.07. mp = 240-241 °C.

3,6-dinitrophenanthrenequinone. The synthesis of this compound was based on methods already developed in the literature.[28] 1.3 g of 3,6-di-NO_2-phenanthrenecatechol-SO_2 was heated in a sand bath at 250 °C until the evolution of SO_2 (g) ceases (typically 30-45 minutes). The complex is then recrystallized from a minimum amount of hot acetic anhydride to give orange-yellow plates. Yield 0.78 g (73 %). Anal. Calcd for $C_{14}H_6N_2O_6$: C, 56.39; H, 2.03; N, 9.39; Found: C, 56.80; H, 1.61; N, 9.39. mp = 292-295 °C. ^{1}H NMR (CD_3CN) δ 9.32 (m, 2H), 8.35 (d, 4H).

3,6-dinitrophenanthrenesemiquinone (2). The generation of this radical was done using the same procedure for the 2,7-isomer. The color of the radical solution in THF is violet/purple, and upon freezing the color of the solution turns green again most

likely due to diamagnetic dimer formation.[27] The solution was immediately used for EPR experiments.

3,6-dinitrophenanthrenecatechol. The synthesis of this ligand has been slightly modified from literature procedures for the 2,7-di-NO_2 isomer.[23] A suspension of 0.415 g (1.39 mmol) of 3,6-NO_2-phenanthrenequinone in 20 ml ethanol was heated to 55-60 °C, then a mixture of 1.00 ml 80% glacial acetic acid and 0.137 ml (1.36 mmol) of phenylhydrazine was added drop wise while stirring. The solution slowly becomes clear and red in color upon addition of the phenylhydrazine/acetic acid mixture. The solution was stirred for 15 minutes and filtered with a glass frit, and upon addition of 150 ml of distilled water a red-orange precipitate was immediately formed. The red-orange precipitate was collected on a glass frit and dried in vacuo. The complex should be stored under nitrogen to prevent oxidation, and solutions of the compound are very air sensitive. Yield 0.384 g (92 %). Anal. Calcd for $C_{14}H_8N_2O_6$: C, 56.01; H, 2.69; N, 9.33; Found: C, 56.62; H, 2.67; N, 9.10.

Acetyl-ferrocenium Tetrafluoroborate. A literature procedure for this complex has been published,[29] but another synthetic preparation was adapted that yielded better results.[30] In a schlenk flask, a filtered solution of 60 ml ether and 0.21 g (1.9 mmol) of *p*-quinone was degassed for 5 minutes by bubbling N_2 through the solution, then the flask is placed under positive pressure of N_2. 0.63 ml of $HBF_4 \cdot OEt_2$ was then added to the ethereal solution of *p*-quinone. Immediately after the $HBF_4 \cdot OEt_2$ addition, a filtered solution of 0.22 g (0.96 mmol) acetyl-ferrocene in $CHCl_3$ was then added dropwise to the stirring solution under N_2. The solution immediately turns deep blue in color, and after stirring for 10 minutes the solution is filtered and the blue precipitate is washed with

ether (30 ml x 4) and dried in vacuo. The complex is stored under nitrogen to prevent oxidation, and solutions of the compound are very air sensitive. Yield: 0.24 g (81 %). Anal. Calcd for $C_{12}H_{12}FeOBF_4$: C, 45.77; H, 3.84; Found: C, 45.09; H, 3.95.

[Ga(tren)Cl_2]Cl. In the dry box, 0.858 g (4.87 mmol) of anhydrous $GaCl_3$ was dissolved in EtOH and added slowly in a drop wise fashion to a stirring solution of 0.784 g (5.36 mmol) of tris-2-aminoethylamine in EtOH, and during the addition a white precipitate begins to form. The mixture was stirred for an additional 15 minutes, and then the precipitate was filtered off and washed with EtOH (20 ml x 3) and ether (30 ml x 4) and dried in vacuo. The complex should be stored and used in the drybox, because it is very hygroscopic. Yield: 1.30 g (83 %). Anal. Calcd for $C_6H_{18}N_4GaCl_3$: C, 22.36; H, 5.63; N, 17.38; Found: C, 22.43; H, 6.16; N, 17.11.

[Ga(tren)(2,7-di-NO_2-PCAT)]Cl. In the dry box, a flask was charged with 0.068 g of 2,7-NO_2-phenanthrenecatechol (0.23 mmol) and was partially dissolved with 10 ml of degassed MeOH, and then 0.019 g NaOH (0.48 mmol) in 10 ml of methanol was added to this solution. The solution changes in color from red to blue-purple. The solution was then stirred for 5 minutes to ensure that all solids were dissolved. In a separate flask, 0.068 g [Ga(tren)Cl_2]Cl (0.21 mmol) was dissolved in 20-30 ml of MeOH, and then filtered. The [Ga(tren)Cl_2]Cl MeOH solution was then added drop wise to a stirring solution of the deprotonated 2,7-di-NO_2-phenanthrenecatechol, and during the addition a dark blue-purple precipitate forms. The solution was then stirred for 45 minutes in the dry box. The dark blue-purple precipitate was filtered off and washed with MeOH (5 ml x 3) and ether (5 ml x 3). The complex was used without further

purification. Yield: 0.052 g (45 %). MS [ESI, *m/z* (rel. int.)]: [Ga(tren)(2,7-di-NO_2-PCAT)·2NaOH]$^+$ 593.2 (100) [Ga(tren)(2,7-di-NO_2-PCAT)]$^+$ 513.2 (10).

[Ga(tren)(2,7-di-NO_2-PSQ)](Cl)(BF_4) (3). In the dry box, a vial was charged with 0.024 g of [Ga(tren)(2,7-di-NO_2-PCAT)]Cl (0.044 mmol) and 10 ml acetonitrile. The stirring suspension was oxidized with 0.014 g acetyl-ferrocenium tetrafluoroborate (0.044 mmol) in 2 ml of acetonitrile, and the color immediately changed from blue-purple to dark green. Also, upon the addition of the oxidant the suspension goes into solution. The solution was stirred for 5 minutes and filtered. Ether was added until the solution turned cloudy, and brown microcrystals formed upon standing. The complex was washed with CH_2Cl_2 (5 ml x 3) to remove any unreacted oxidant. The complex can be recrystallized from acetonitrile/ether mixtures. Yield: 0.010 g (37 %) Anal. Calcd for $C_{20}H_{24}N_6O_6GaClBF_4 \cdot 0.5CH_2Cl_2$: C, 36.83; H, 3.68; N, 12.27; Found: C, 37.39; H, 3.36; N, 12.59.

[Ga(tren)(3,6-di-NO_2-PCAT)]Cl. In the dry box, a flask was charged with 0.060 g of 3,6-dinitrophenanthrenecatechol (0.20 mmol) and was partially dissolved with 10 ml of degassed MeOH, and then 0.016 g NaOH (0.40 mmol) in 10 ml of methanol was added to this solution. The solution changes in color from red to red-purple. The solution was then stirred for 5 minutes to ensure that all solids were dissolved. In a separate flask, 0.058 g [Ga(tren)Cl_2]Cl (0.18 mmol) was dissolved in 20-30 ml of MeOH, and then filtered. The [Ga(tren)Cl_2]Cl MeOH solution was then added drop wise to a stirring solution of the deprotonated 3,6-di-NO_2-phenanthrenecatechol, and during the addition a dark-purple precipitate forms. The solution was then stirred overnight in the dry box. The dark-purple precipitate was filtered off and washed with MeOH (5 ml x 3),

EtOH (5 ml x 3), and ether (5 ml x 3). The complex was used without further purification. Yield: 0.080 g (82 %). MS [ESI, *m/z* (rel. int.)]: [Ga(tren)(3,6-di-NO_2-PCAT)]$^+$ 513.2 (20).

[Ga(tren)(3,6-di-NO_2-PSQ)]$(BF_4)_2$ (4). This gallium semiquinone radical was generated by first adding 0.024 g of [Ga(tren)(3,6-di-NO_2-PCAT)]Cl (0.044 mmol) and 10 ml of acetonitrile to a flask. This suspension was stirred and 0.0090 g of $AgBF_4$ (0.046 mmol) was added in 1 ml of acetonitrile to exchange the Cl^- for BF_4^-. The solution was stirred for an additional 15 minutes and then filtered through celite. The purple solution was then oxidized by adding 0.014 g of acetyl-ferrocenium tetrafluoroborate (0.044 mmol) in 2-3 ml of acetonitrile, and the color immediately changed to red-brown. Only freshly prepared solutions were used for EPR experiments, and the solution is very air sensitive.

EPR Spectroscopy. In general, X-band EPR spectra were acquired on samples (~ 10 mmol/L) and prepared in a dry, inert atmosphere (N_2). The details of each sample preparation are described below. Room temperature continuous-wave (cw) X-band EPR spectra for all samples were obtained with a Bruker ESP300E spectrometer. Spectra of radicals **1** and **2** were acquired with a perpendicular-mode cavity (Bruker ST4102/8943) with resonances around 9.46 GHz, while complexes **3** and **4** required an EPR flat cell for acquisition at room temperature with a room temperature cavity (Bruker 4103TM) that has resonances around 9.67 GHz. The power dependence of all signals was checked to ensure that data acquisition was carried out below saturation. All simulations of X-band EPR spectra were carried out using the Bruker XSOPHE program.[31-33]

Electron Spin Echo Envelop Modulation (ESEEM) spectra for **1**, **2**, **3**, and **4** were acquired using a Bruker E-680X pulsed X-band spectrometer with a model ER4118-MD-X-5W1 probe that employs a 5 mm dielectric resonator. The sample temperature was maintained at 50 K using an Oxford Instruments liquid helium flow system equipped with a CF-935 cryostat and a ITC-503 temperature controller. ESEEM data were collected using a three-pulse, stimulated echo sequence (90°–τ–90°–T–90°) with 90° microwave pulse widths of 16 ns (full width at half maximum) and peak powers of 250 W. A four-step phase cycling sequence, (+x, +x, +x), (–x, +x, +x), (+x, –x, +x), (–x, –x, +x), together with the appropriate addition and subtraction of the integrated spin echo intensities served to actively remove the contributions of two-pulse echoes and baseline offsets from the data.[34] An integration window of 24 ns was used to acquire spin echo amplitudes, and data set lengths were 512 points. ESEEM spectra were tapered with a Hamming window and Fourier transformed.[35] ESEEM spectra were obtained by taking the absolute value of the Fourier transformations.

ESEEM simulations of the I = 1 ^{14}N hyperfine coupling constants were accomplished by using software written in MATLAB. Calculations used the density matrix formalism of Mims to simulate the time domain ESEEM data.[36,37] MATLAB scripts were then used to assemble the simulations according to the product rule and to complete the Fourier analysis to obtain simulated ESEEM spectra. The processing and Fourier transformation procedure was identical to that outlined above for the Bruker software. The spherical model approximation to the product rule was used for simulations of ESEEM patterns of multiple nuclei.[38]

Calculations. Previous DFT calculations on semiquinone radicals have shown that hybrid functionals such as B3LYP are suitable for calculating hyperfine coupling constants and spin densities.[39] The DFT calculation of ^{14}N hyperfine coupling constants was shown to be basis set dependent with the 6-31g* basis set and the B3LYP functional yielding the best results with experimental data.[40] It has also been shown that solvent has a strong influence on the hyperfine coupling constants of semiquinone radicals.[41] Taking previous work into consideration, the starting structures for the radical ligands were generated using GaussView,[42] and then optimized using Gaussian 03[43] with the UB3LYP functional and the 6-31g* basis set. Further single point gas phase calculations were then done using the UB3LYP, UB3PW91, and UPBE1PBE functionals with the 6-31g* basis set, and the hyperfine coupling constants were calculated by the Fermi analysis method in the Gaussian 03 program. The spin density was examined by the natural population analysis (NPA)[44] method and by the Mulliken population analysis scheme incorporated in Gaussian 03. The influence of solvent on the hyperfine coupling constants was represented by the static isodensity surface polarized continuum model (IPCM).[45] The hyperfine coupling constants were also calculated in tetrahydrofuran using the UB3LYP, UB3PW91, and UPBE1PBE functionals with the 6-31g* basis set including the scrf = IPCM keyword with the isodensity value of 0.0004 (default) and a dielectric constant of 7.58. All single point calculations were done using tight convergence criteria,[46] and the calculations assumed a charge of –1 and a doublet spin state.

The starting structures for the gallium complexes (**3** and **4**) were adapted from the crystal structure of an analogous $[Ni(tren)(PSQ)]^+$ complex (replacing Ni^{II} with Ga^{III}) using GaussView, then optimized with Gaussian 03 using the UB3LYP functional with

the LanL2DZ basis set. Previous calculations of gallium(III) semiquinone dimer systems have shown that hybrid functionals give good estimates of the corresponding experimental hyperfine coupling constants and spin densities.[47] Subsequent single point calculations were then carried out using the UB3LYP, UB3PW91, and UPBE1PBE functionals with the 6-31g* basis set, and the isotropic hyperfine coupling constants were calculated by means of the Fermi analysis method in the Gaussian 03 program. The spin density was examined by the natural population analysis (NPA)[44] method and by the Mulliken population analysis scheme incorporated in Gaussian 03. The effect of solvent on the hyperfine coupling constants was also explored by means of the polarizable continuum model (PCM)[48-51] and IPCM models. All single point calculations were done using tight convergence criteria, and the calculations assumed a charge of +2 and a doublet spin state.

4.3 Results and Discussion

4.3.1 Hyperfine Coupling in 2,7- and 3,6-dinitrophenanthrenesemiquinone Radicals

There are 3 sets and 1 set of equalivant protons and nitrogens, respectively, in complexes **1** and **2** (Figure 4-6). In Figure 4-6, the protons are labeled by the carbon atom that they are bonded to, for example the equivalent protons bonded at positions 1 and 8 are labeled as $^{1}H_{1,8}$. The room temperature EPR spectrum of **1** was recorded previously by Maruyama in 1964,[26,27] and the hyperfine coupling constants were determined to be $A(^{14}N_{2,7}) = 0.0$ G, $A(^{1}H_{3,6}) = 1.94$ G, $A(^{1}H_{1,8}) = 0.97$ G, and $A(^{1}H_{4,5}) = 0.44$ G.

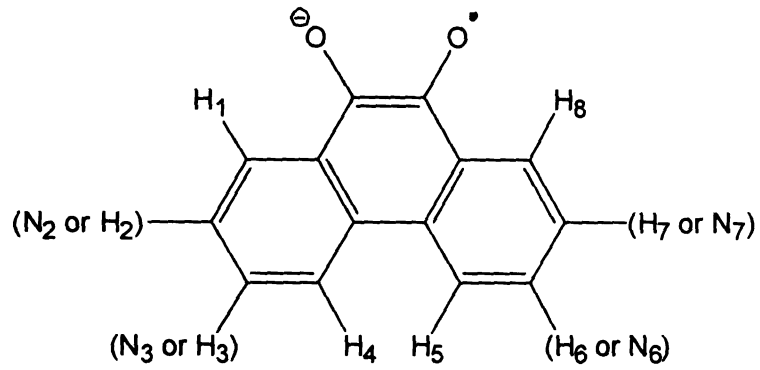

Figure 4-6. Generic proton labeling in the 2,7-di-NO_2-PSQ (**1**) and 3,6-di-NO_2-PSQ (**2**) radicals.

To our knowledge there is no previous EPR spectrum of the corresponding 3,6-di-NO_2-phenanthrenesemiquinone (complex 2). In our efforts to determine the spin distribution in these complexes, an analysis of the room temperature X-band EPR spectra of both of the radicals was carried out. Specifically, the ^{14}N HFC's are important in this examination, since the HFC constant suggests how much spin is delocalized onto the nitrogen nucleus of the NO_2 substituent. In essence, we can experimentally approximate the spin delocalizing effect of the nitro-substituent in the PSQ ring. EPR spectra of **1** and **2** generated by reduction of the quinones with excess K metal in THF solution under a nitrogen atmosphere are depicted in Figures 4-7 and 4-8, respectively. The simulation of **1** does not include a contribution from the two equalivant $^{14}N_{2,7}$ nuclei of the nitro groups consistent with what was observed by Maruyama. The simulation of the data is good and all lines are accounted for except for the peaks on the ends of the spectrum. Although, if the simulation of the spectrum included two ^{14}N nuclei the two side peaks could be simulated, but the overall results were not as good as depicted in Figure 4-7. Thus, it appears necessary that ^{14}N HFC is needed to accurately simulate the side peaks in the spectrum, but the coupling is probably very weak. The proton hyperfine coupling constants agree quite nicely with the reported data as seen in Table 4-1. DFT calculations

at the UB3LYP/6-31g* level were used to aid in the assignment of the proton HFC's, and the agreement between experiment and theory is good with the deviations being less than 0.35 Gauss. These deviations are within the range of errors of 0.10-0.90 G observed by O'Malley in the DFT calculated ^{1}H HFC of semquinones.[39,52]

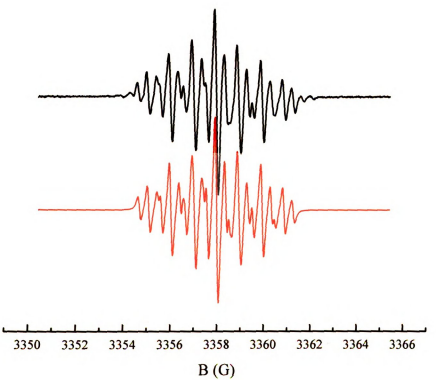

Figure 4-7. Experimental X-Band EPR spectra of 2,7-di-NO_2-PSQ (**1**) in black (top) acquired in THF at room temperature, and simulation in red (bottom). The simulation parameters are: g = 2.01023, $A(H_{1,8})$ = 0.936 G, $A(H_{3,6})$ = 1.952 G, $A(H_{4,5})$ = 0.393 G, and linewidth = 0.15 G. Experimental Conditions: frequency = 9.4479, modulation amplitude = 0.1 G, and power = 1.25 mW.

The EPR spectrum and simulation of complex **2** are shown in Figure 4-8. The simulation in this case did include a contribution from the ^{14}N nuclei in the radical, and the hyperfine coupling constants are compared with results from DFT calculations shown in Table 4-1. The assignments of the ^{1}H isotropic HFC's for **2** was again aided by DFT calculations at the UB3LYP/6-31g* level and by comparison with complex **1**.

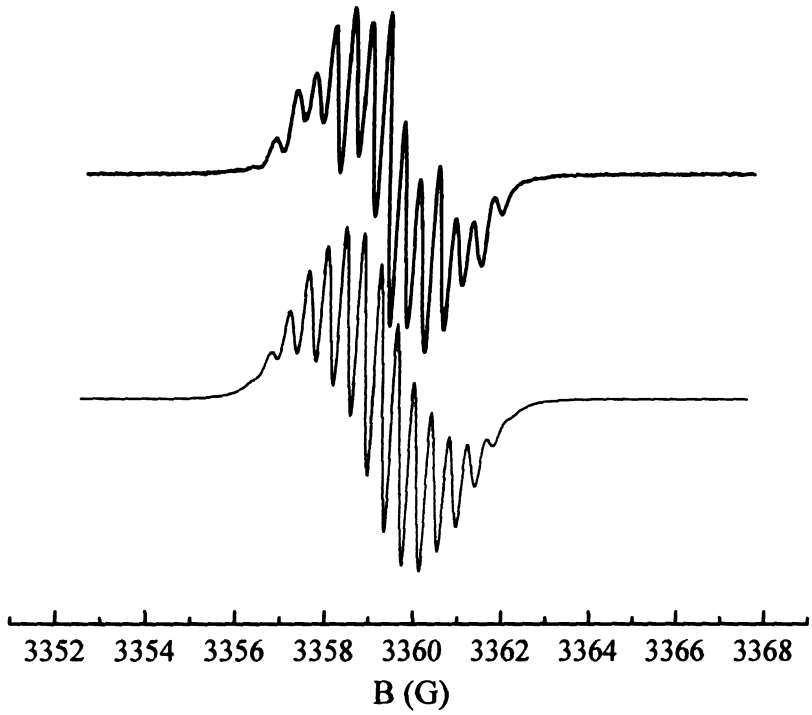

Figure 4-8. Experimental X-Band EPR spectra of 3,6-di-NO_2-PSQ (**2**) in black (top) acquired in THF, and simulation in red (bottom). The simulation parameters are: g = 2.0106., $A(N_{3,6})$ = 0.406 G, $A(H_{1,8})$ = 0.413 G, $A(H_{2,7})$ = 1.197, $A(H_{4,5})$ = 0.407, and linewidth = 0.262 G.

The overall agreement between the UB3LYP/6-31g* calculated and experimental ^{1}H HFC's is good with a maximum deviation of approximately 0.20 Gauss. The calculation of the ^{14}N HFC's at the UB3LYP level gave a reasonable comparison with what was experimentally determined with a difference of 0.28 G. This is in excellent agreement with literature calculations, since typical deviations between calculated and experimental ^{14}N HFC's in the literature were on the order of 1.67 G for a large series of nitrogen centered radicals.[40] The ^{14}N of 1 can be estimated to be smaller than 0.413 G based on the DFT and the data for 2. These small HFC constants imply that spin polarization is largely responsible for the spin density on the nitrogen nucleus, since nitroaromatic radicals in the literature exhibit much larger ^{14}N HFC when spin is directly delocalized onto the nitrogen atom.[53-56]

Table 4-1. Experimental and DFT isotropic HFC's for 2,7-di-NO_2-PSQ (**1**) and 3,6-di-NO_2-PSQ (**2**).

Radical	Exp. HFC (G):	DFT-gas[b] HFC (G):			DFT-IPCM[b,c] HFC (G):		
		B3LYP	B3PW91	PBE1PBE	B3LYP	B3PW91	PBE1PBE
1							
$^1H_{1,8}$	0.94 (0.97)[a]	0.788	0.87701	1.03855	0.64384	0.69379	0.79198
$^{14}N_{2,7}$	0.0 (0.0)[a]	0.151	0.10046	0.04056	0.28668	0.22278	0.15991
$^1H_{3,6}$	1.95 (1.94)[a]	-2.31	-2.49943	-2.5529	-2.57818	-2.79495	-2.87572
$^1H_{4,5}$	0.39 (0.44)[a]	0.117	0.15014	0.20617	0.20052	0.24994	0.33512
2							
$^1H_{1,8}$	0.413	-0.498	-0.53699	-0.5224	-0.5416	-0.63843	-0.70544
$^1H_{2,7}$	1.197	-1.018	-1.0966	-1.12191	-0.90553	-0.928	-0.88268
$^{14}N_{3,6}$	0.406	0.171	0.11801	0.05853	0.55098	0.41096	0.2925
$^1H_{4,5}$	0.407	0.477	0.53473	0.67852	0.42527	0.51362	0.69666

[a] Ref. [29]. [b] Using the 6-31g* basis set. [c] Dielectric constant = 7.58, and isodensity = 0.0004 for 2,7-di-NO_2-PSQ and isodensity = 0.003 for 3,6-di-NO_2-PSQ.

We also used the B3PW91 and PBE1PBE functionals with the 6-31g* basis set to see if we could get better agreement/estimates of the ^{14}N and ^1H HFC for both **1** and **2**. In some cases the HFC's improved, but in others there were larger deviations observed in the HFC's, as seen by examining Table 4-1. The effect of solvent on the ^{14}N HFC's was also examined with the IPCM solvent model as suggested by Langgård and Spanget-Larsen[41], and we did exploratory calculations using isodensity values of 0.0004, 0.001, and 0.003 for both radicals, with the results generally having greater agreement with the experimental values. The isodensity value is an empirical parameter that is usually adjusted for differences in protic and aprotic solvents, and increasing this parameter effectively increases the strength of the solvent reaction field.[41] Using the IPCM model with THF as the solvent, an isovalue of 0.0004 was empirically found to give reasonable HFC's for **1**. In the case of **2** also in THF, an isodensity parameter of 0.003 improved the

magnitude of the ^{14}N HFC. It is interesting that the isomers needed different isodensity values to better compare with experiments, and it is not clear why this is the case. We also did the calculations using an isodensity value of 0.0004 for **2** which resulted in increased errors compared to the gas phase calculations. Thus the improvements were not consistent. Although there were improvements seen in the ^{14}N HFC's by including solvent for both radicals, there are greater errors in some of the ^{1}H HFC's, most notably the $^{1}H_{3,6}$ HFC. The larger errors in ^{1}H HFC's with the solvent models and the fact that the isodensity values were different for the two isomers prompted us to use the gas phase calculations for our comparisons with experimental values. The UB3LYP results gave us the best overall comparisons with experiments, therefore these results will be used throughout the rest of this work.

The DFT calculated ^{1}H HFC's for **1** and **2** revealed both shifts in magnitude and sign of the HFC between the two complexes. In order to better visualize and interpret the results, the total spin density surfaces for both radicals are shown in Figure 4-9.

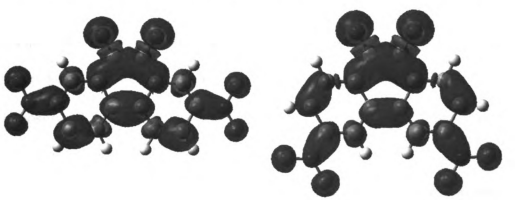

Figure 4-9. Spin density distribution in **1** (left) and **2** (right), where the blue color represents excess α-spin density and the green represents excess β-spin density.

The spin density distribution calculated by the NPA analysis and Mulliken are qualitatively similar, and we shall focus on the Mulliken population analysis for the

discussion of the results. The α-spin densities for the carbon, hydrogen, and nitrogen atoms have been tabulated in Table 4-2.

Table 4-2. Experimental and calculated spin densities in 2,7-di-NO_2-PSQ (**1**) and 3,6-di-NO_2-PSQ (**2**).

Radical	Experimental HFC (G)	s-orbital ρ (H or N)[a]	p-orbital ρ (C)[b]	Calculated HFC (G)	s-orbital ρ (H or N)	p-orbital ρ (C)[c]
1						
$^1H_{1,8}$	0.936	0.000584	0.03928	0.788	0.001066	-0.04003
$^{14}N_{2,7}$	0.0	0.0		0.151	0.00033	0.04056
$^1H_{3,6}$	1.952	0.001236	0.083206	-2.31	-0.004435	0.07921
$^1H_{4,5}$	0.393	0.000263	0.017679	0.117	0.000351	-0.01903
2						
$^1H_{1,8}$	0.413	0.000259	0.017426	-0.498	-0.001385	0.01075
$^1H_{2,7}$	1.197	0.000751	0.050506	-1.02	-0.001933	0.03245
$^{14}N_{3,6}$	0.406	0.007049		0.171	0.00037	0.04427
$^1H_{4,5}$	0.407	0.000255	0.017172	0.477	0.000871	-0.02546

[a] Calculated using Equation 3a or 3b. [b] The carbon p-π-spin density calculated using Equation 1 and using the experimental $^1H_{x,y}$ HFC and $Q_{CH}^H = 23.7$.[57] [c] Average total p-orbital spin density on the carbon atoms bonded to the proton or nitrogen nucleus.

According to the DFT calculated HFC's and from visualizing the spin density plots for **2**, the $^1H_{1,8}$ and $^1H_{2,7}$ HFC's are negative in sign due to β-spin polarization of the s-orbital spin density by the excess α-π-spin density at the 1, 8, 2, and 7-carbon atoms.[58] The $^1H_{4,5}$ HFC is positive due to s-orbital α-spin polarization from the β-spin density at the 4,5-carbons. Similar arguments can also be made for the signs of the 2,7-di-NO_2-PSQ HFC's. The agreement between DFT and the experimentally determined s-orbital spin densities for the protons and the π-spin densities at the carbons is good using Equation 3a and 3b. For isotropic hyperfine coupling (Fermi contact) to occur there must be excess spin population at the nucleus, therefore the important variable is the s-orbital spin density at the nucleus. The s-orbital spin density at a nucleus is directly proportional to

the magnitude of the isotropic HFC. For example, in **2** there is more calculated Mulliken s-orbital spin density at the 2,7-hydrogens (0.000751) then at the 1,8-protons (0.000259), and the corresponding HFC's at the 2,7-protons are larger. The magnitudes of all the experimental HFC's agree within the range of calculated HFC's. The largest shifts between the two radicals occurs at the $^{1}H_{1,8}$ HFC. Figure 4-8 (and Table 4-2) shows that the spin density in **1** is more centralized on the 2,7-carbons, whereas increased α-spin population is present on the 2,7- and 1,8-carbons of **2**, which is likely a result of increased spin delocalization effects. Additionally, the s-orbital spin density polarization onto the nitrogen atom is the same for both radicals as predicted by DFT: we can say to a first approximation that the spin delocalizing ability onto the nitro group at the 2,7- and 3,6-positions is equivalent, but further experiments will be required to quantify experimental ^{14}N values for the radicals.

Now that **1** and **2** have been examined by X-band EPR spectroscopy, we will further quantify the experimental ^{14}N HFC's by using the Electron Spin Echo Envelope Modulation (ESEEM) technique. ESEEM is a pulsed EPR experiment that is often used to elucidate weak hyperfine couplings that are sometimes masked by inhomogeneous broadening of the EPR lineshape.[19] In our case, we wish to complement the experimental determination of the ^{14}N HFC's that was suggested in the room temperature X-Band EPR experiments of the radical PSQ ligands with ESEEM data. Additionally, gallium(III) may broaden the EPR lineshape as already seen in the literature,[47] requiring us to use ESEEM spectroscopy for comparisons of ^{14}N between the radicals and the gallium complexes (vide infra). This broadening is usually due to the larger contribution of gallium HFC compared to hydrogen or nitrogen HFC.

4.3.2 ESEEM Spectroscopy of 2,7- and 3,6-di-NO_2-phenanthrenesemiquinones

The experimental conditions were identical for generating **2** in the X-band EPR experiments, and the ESEEM data were collected in frozen THF solution at 50 K. The resulting data and simulation are shown in Figure 4-10.

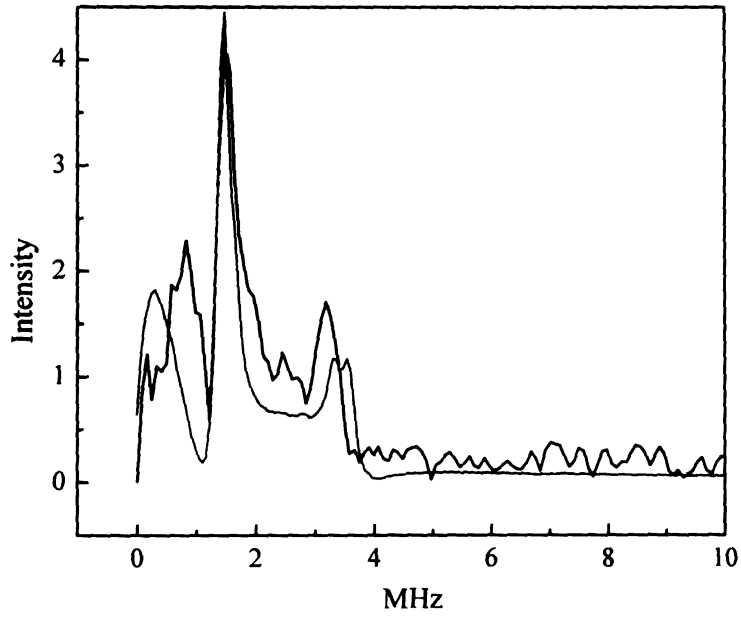

Figure 4-10. Stimulated echo detected ESEEM spectra of 3,6-di-NO_2-PSQ (**2**) (black) at 50 K with frequency = 9.682 GHz; center field = 3445 G; τ = 136 ns; starting T = 40 ns; time increment = 16 ns. Simulation (red) parameters: g = isotropic, A = (1.3, 1.1, 0.9) MHz, e^2qQ = 1.2 MHz, Euler = (0.0, 0.4, 0.0), and η = 0.8. Spectra were obtained by normalizing the raw data and subtracting the bi-exponential decay followed by application of a Hamming window and Fourier transformation. Absolute value spectra are shown. Recall, 1.0 G = 0.1 mT = 2.8025 MHz.

It should be noted that simulation of ESEEM spectra is much more complicated than X-band EPR spectra, and all ESEEM simulations presented in this chapter are within 10-20 % of the experimental data. Work is currently ongoing to improve all simulations, and the best results are reported henceforth. The critical step in all ESEEM data simulation is the accurate simulation of the experimental time domain data as well as the frequency domain spectra. For **2** the experimental ^{14}N ESEEM modulations are observed at 0.82,

1.47, and 3.18 MHz. The simulation of the ^{14}N ESEEM spectra in Figure 4-10 were done numerically and employed a spin Hamiltonian that included the nuclear Zeeman, electron-nuclear hyperfine, and nuclear quadrupole interactions. The simulation parameters were identical for three τ values used to acquire the experimental spectra: g = isotropic, A = (1.3, 1.1, 0.9) MHz for (A_{XX}, A_{YY}, A_{ZZ}), η = 0.80, and e^2qQ = 1.2 MHz. The isotropic ^{14}N HFC is equal to $^1/_3$ the trace of the anisotropic HFC tensor, or 0.39 G (1.0 G = 2.8025 MHz), and this is in reasonable agreement with ^{14}N = 0.43 G estimated from simulating the room temperature X-band spectra.

One regime for observing ^{14}N ESEEM frequencies is a circumstance near exact cancellation conditions,[21,59,60] where the nuclear Zeeman frequency, υ_n, is equal to one-half the hyperfine coupling constant A (i.e. $\upsilon_n = {}^A/_2$). These terms cancel making the quadrupole interaction the dominant factor in the upper spin manifold transitions (Figure 4-10). Three nuclear quadrupole transitions υ_{56}, υ_{45}, and υ_{46} in the upper $m_S = {}^1/_2$ spin manifold and a higher frequency double quantum transition υ_{dq} ($\Delta m_I = 2$) in the lower manifold (Figure 4-9) are observed and given below.

$$\begin{aligned} \nu_{56} &= \nu_0 = 2K\eta \\ \nu_{45} &= \nu_- = K(3-\eta) \\ \nu_{46} &= \nu_+ = K(3+\eta) \end{aligned} \tag{11}$$

$$\nu_{13} = \nu_{dq} = 2\left[\left(\nu_n + \frac{A}{2}\right)^2 + K^2(3+\eta^2)\right]^{1/2} \tag{12}$$

The first two transitions υ_{56} and υ_{45} essentially add up to υ_{46}, and the υ_{dq} transition is usually observed at 4-6 MHz for exact cancellation conditions. In this case the data

indicate conditions near cancellation, where four frequency components are also usually resolved.[61] The first peak in Figure 4-10 at 0.82 MHz is most likely the combination of two frequencies which add to the peak observed at 1.47 MHz. Additionally, the peak observed at 3.18 MHz can be assigned to the υ_{dq} transition.

ESEEM was also attempted using the same experimental conditions as above for **1**. Deep modulations were not observed in the THF data, but the characteristic nitrogen lines near exact cancellation were observed. The signal to noise was quite high and a quantitative ^{14}N could not be determined, but it can be approximated that the ^{14}N HFC is quite small and less than 0.39 G observed for the 3,6-di-NO_2-PSQ radical.

4.3.3 EPR and ESEEM Spectroscopy of Gallium 3,6- and 2,7-di-NO_2-PSQ

The room temperature X-band EPR data for **3** and **4** are shown in Figure 4-11 and 4-12 below, respectively.

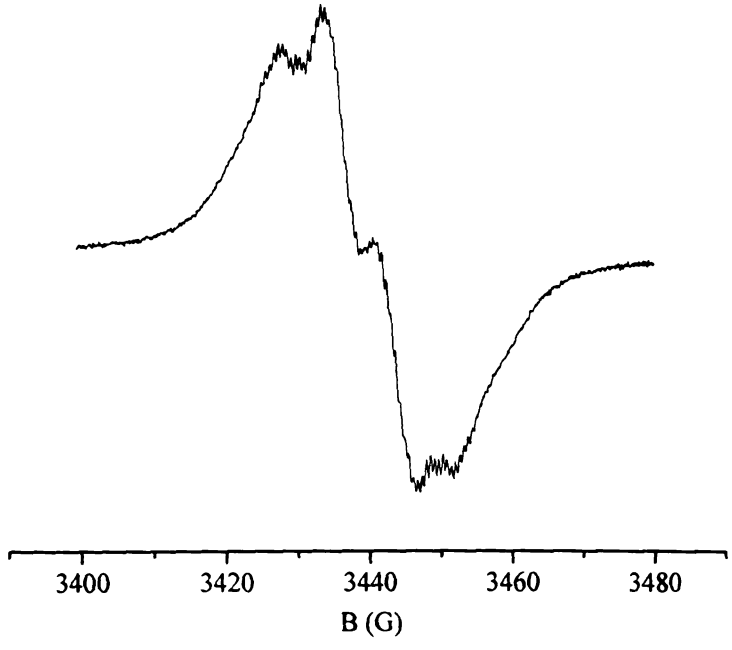

Figure 4-11. The room temperature X-band EPR spectrum of [Ga(tren)(2,7-di-NO_2-PSQ)](Cl)(BF_4) (**3**) in acetonitrile. Experimental conditions: frequency = 9.772 GHz, power = 5 mW, modulation frequency = 100 G, modulation amplitude = 0.2 G. See text for further details.

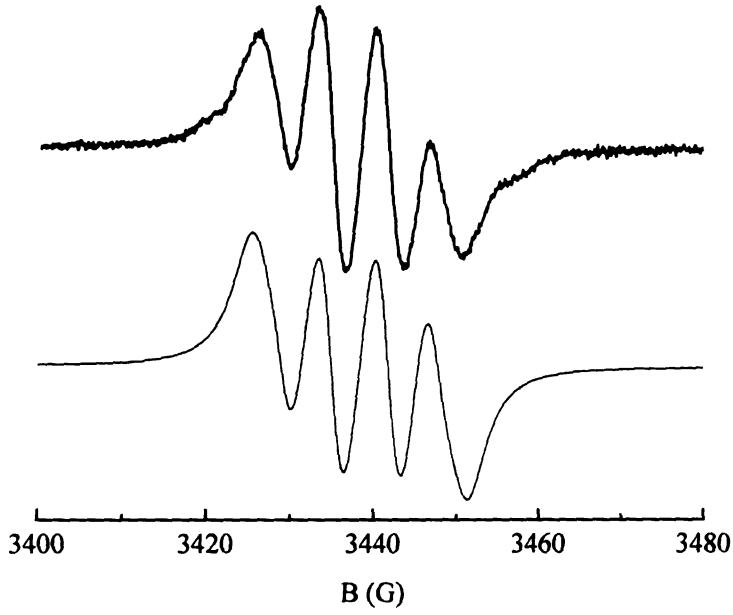

Figure 4-12. The room temperature X-band EPR spectrum (top) and simulation (bottom) of [Ga(tren)(3,6-di-NO_2-PSQ)]$(BF_4)_2$ (**4**) in acetonitrile. Simulation parameters: g = 2.00979, A(Ga) = 6.20 G, A(H) = 0.90 G, line width = 2.90 G. Experimental conditions: frequency = 9.672 GHz, power = 5 mW, modulation frequency = 100 G, modulation amplitude = 0.2 G. See text for further details.

Figure 4-12 depicts the expected 4 line pattern (2I +1) from a single Ga (I = $^3/_2$) nucleus, and the signal is relatively broad and featureless analogous to other Ga-SQ complexes reported in the literature.[47] The experimental spectrum for **4** could be fit reasonably well using only Ga HFC, yielding g = 2.00987, A(Ga) = 6.74 G, and a line width = 3.4 G (not shown), but Figure 4-11 shows an improved simulation by including pair of equivalent protons.

The room temperature spectrum of **3** is different from **4** but does resembles a similar gallium(III) *o*-iminobenzosemiquinonate radical dimer from the work of Wieghardt and coworkers,[62] where an identical line shape and pattern due to Ga^{III} hyperfine coupling (I = $^3/_2$) is observed. From the isotropic A(Ga) = 4.6 G in the Wieghardt and coworkers complex, and from the peak positions of the Ga-2,7-di-NO_2-PSQ spectrum we estimate a gallium HFC of about 6.2 G. We were unable to simulate

the spectrum by using Ga^{III} alone, and several features point to the fact that other hyperfine interactions are contributing significantly to this spectrum. The broad, unresolved Ga^{III} HFC and considerable fine structure on top of the peaks (the second derivative spectrum reveals much of this structure, but we have been unable to simulate it at this point) points to contributions from other nuclei (^{14}N and/or ^{1}H). This fine structure was not observed in complex **4**, and suggests that the ^{14}N and/or ^{1}H HFC's are larger in magnitude in **3** due to the additional fine structure that is observed. The magnitude changes in the ^{14}N HFC will also be examined by ESEEM spectroscopy below, which may confirm our suspicions for a larger magnitude ^{14}N coupling constant in **3**.

The ESEEM spectrum and simulation of **4** are shown in Figure 4-13 below. The data reveal ^{14}N modulations at 0.73, 1.52, and 2.30 MHz which are typical of transitions near exact cancellation conditions for the upper spin manifold, and the double quantum transition of the lower spin manifold at 3.39 MHz is also observed. The transition at 4.62 MHz is due to a combination of the 0.73, 1.52, and 2.30 MHz frequency components, and this peak usually arises when more than one nucleus with the same magnetic coupling gives rise to the ESEEM.[63] The experimentally determined A = (2.0, 1.3, 0.8) MHz gives an isotropic ^{14}N of 0.487 G, which is increased in comparison with the free ligand experimental data. We note that the simulation is not as good as in complex **2**, and within the 10-20 % conservative error bars, the ^{14}N for the free ligand and gallium complex are qualitatively the same. The absence of any large anisotropy in the ^{14}N HFC tensor indicates that the spin density at the nitrogen nucleus is mainly due to spin polarization. Thus, only a small change if any is observed in the ^{14}N HFC upon the

binding of the 3,6-di-NO_2-PSQ ligand to gallium(III). More accurate simulations are required to quantitatively compare these complexes.

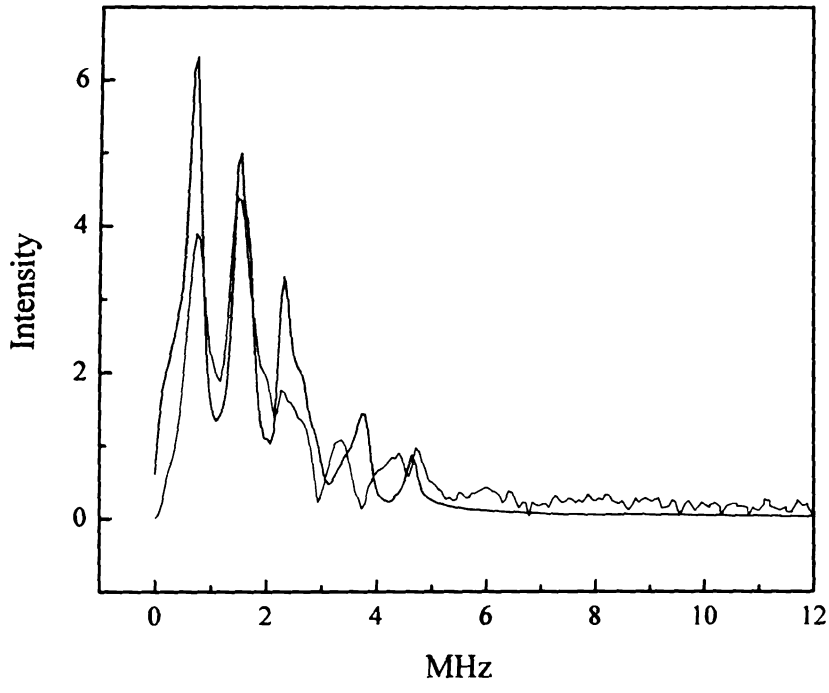

Figure 4-13. Stimulated echo detected ESEEM spectra of [Ga(tren)(3,6-di-NO_2-PSQ)]$(BF_4)_2$ (**4**) (black) at 50 K in acetonitrile with frequency = 9.694 GHz (black); center field = 3450 G; starting T = 40 ns; τ = 136 ns; time increment = 16 ns. Simulation (red) parameters: g = isotropic, A = (2.0, 1.3, 0.8) MHz, e^2qQ = 2.5 MHz, η = 0.60, and Euler angles = (0.0,0.9,0.0). Spectra were obtained by normalizing the raw data and subtracting the bi-exponential decay followed by application of a Hamming window and Fourier transformation. Absolute value spectra are shown.

The ^{14}N ESSEEM spectra for **3** (Figure 4-14) depicts a broad feature centered at 2.9 MHz, which differs from exact or near exact cancellation conditions. This feature results from hyperfine splittings that are dominated by electron-nuclear hyperfine coupling where both the isotropic and anisotropic contributions are large.[61] This broad peak has been assigned to a "$\Delta M_I = 1$" transition, and its assignment is discussed in detail by McCracken et al.[61] and will not be further elaborated upon here. The large anisotropic HFC of the ^{14}N in this complex is evident in the spectral simulation, where

^{14}N = (-2.1, -2.1, 21) MHz for (A_{XX}, A_{YY}, A_{ZZ}) and the isotropic HFC is also quite large with ^{14}N = 2.0 G.

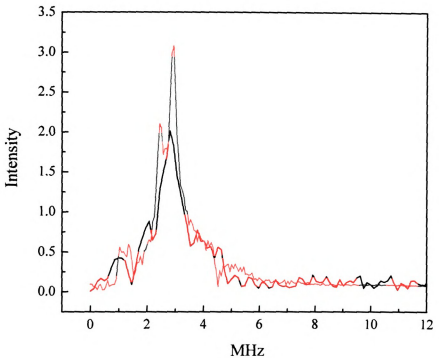

Figure 4-14. Stimulated echo detected ESEEM of [Ga(tren)(2,7-di-NO_2-PSQ)](Cl)(BF_4) (**3**) (black) at 50 K in acetonitrile with frequency = 9.676 GHz; center field = 3450 G; τ = 136 ns; starting T = 40 ns; time increment = 16 ns. Simulation (red) parameters: g = isotropic, A = (-2.1, -2.1, 21) MHz, e^2qQ = 1.6 MHz, η = 0.60, and Euler angles = (0.0, 0.9, 0.0). Spectra were obtained by normalizing the raw data and subtracting the bi-exponential decay followed by application of a Hamming window and Fourier transformation. Absolute value spectra are shown.

If the unpaired spin density is largely localized in the p_z-π-orbital of the radical, then the hyperfine coupling would be expected to have a large anisotropic contribution.[61] In the present case, this implies that spin density is most likely directly delocalized into the nitrogen atom's p_z orbital by the spin delocalization mechanism. The resonance structure on the right shown in Figure 4-15 is then deemed to be highly important for this complex. The large increase in ^{14}N from **1** to **3** is most likely real, since even with a possible error of 20 % there is still a large increase in the magnitude of the hyperfine coupling constant.

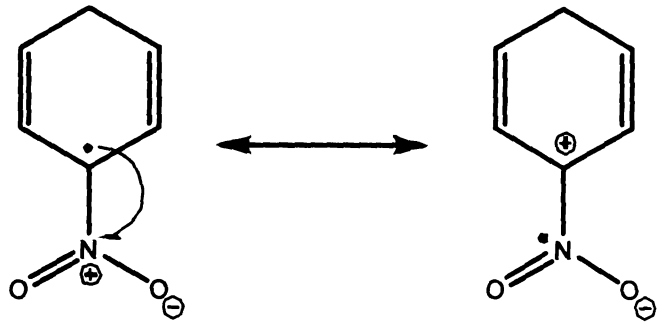

Figure 4-15. A representation of the spin delocalization mechanism onto the nitrogen of the NO_2 group in the [Ga(tren)(2,7-di-NO_2-PSQ)](Cl)(BF_4) (**3**) complex.

The room temperature X-band data also support a larger contribution from the ^{14}N HFC due to the observed fine structure on top of the Ga^{III} HFC. Thus, the X-band EPR data and more conclusively the ESEEM of complex **3** indicate that the spin density is more highly localized at the nitrogen than for the corresponding Ga-3,6-di-NO_2-PSQ isomer. The direct spin delocalization onto the nitrogen atom is most likely responsible for the large experimental ^{14}N HFC, and the smaller HFC for **4** is more in line with a mechanism like spin polarization dominating in the population of unpaired spin density on the nitrogen atoms. This experimental examination then indicates that there is a greater population of spin density at the 2,7-positions than the 3,6-positions in the PSQ ring, and substituents in the 2,7-positons will most likely delocalize spin density to a greater extent than at the 3,6-positions.

4.3.4 Potassium 2,7-di-NO_2-PSQ Contact Radical Ion Pair

In an effort to obtain better ESEEM data for the 2,7-di-NO_2-PSQ radical, a fortuitous observation was noted. During the reaction to generate the anion radical it was observed that a dark precipitate fell out of the THF solution. The precipitate was dissolved in ethanol and the EPR spectrum was collected using a flat cell (Figure 4-16).

It should be noted that only very pure 2,7-di-NO_2-PQ ligand, potassium metal, and THF were used during the reaction where this precipitate was formed. Interestingly, the observed spectrum is quite different from the radical species (complex 1) that is soluble in THF (Figure 4-6). The likely species in solution during the reduction reaction are 2,7-di-NO_2-PQ, 2,7-di-NO_2-PCAT, 2,7-di-NO_2-PSQ, K^+, K^0, and THF. It is highly unlikely then that the spectrum in Figure 4-16 is due to any other species except the 2,7-di-NO_2-PSQ radical, since this is the only paramagnetic species generated.

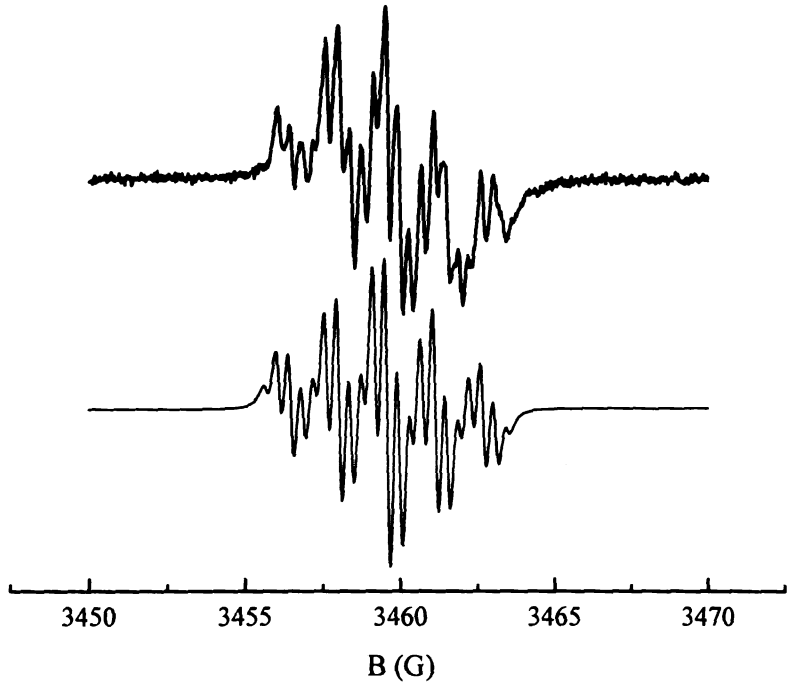

Figure 4-16. X-Band CW spectrum in ethanol at room temperature of potassium 2,7-di-NO_2-PSQ contact radical ion pair (top) and simulation (bottom). Simulation parameters: g = 2.01030, A(N) = 1.5545 G, A(H) = 0.398 G, A(H) = 0.383 G, and linewidth = 0.215 G. Experimental conditions: frequency = 9.734 GHz, modulation amplitude = 0.1 G, and power = 1mW. See text for further details.

It is hypothesized then that the precipitate is a potassium radical anion salt, where potassium is directly coordinated to the semiquinone oxygens. This would explain the greater solubility of the precipitate in more polar solvents. These species are known in the literature as contact radical ion pairs, and their X-ray and EPR spectra have been

reported.[64] The species reduced in THF (Figure 4-6) can then be described as a solvent separated radical ion pair, where the potassium is not directly coordinated to the radical. Additionally, the lineshape of the K-2,7-di-NO_2-PSQ radical is analogous to the 3-bis(2-pyridyl)quinoxaline potassium contact radical ion pair,[65] which suggests that the 2,7-di-NO_2-PSQ may be coordinated to potassium in this case. The spectrum of both contact radical ion pairs is dominated by the interaction of the unpaired electron with the nitrogen nucleus producing five hyperfine splitting lines (2nI + 1). Contributions from the remaining nuclei are also superimposed on the nitrogen lines in both cases. The observed fine structure corroborates with the structure observed in the X-band CW spectrum of **3**. The simulation of the K-2,7-di-NO_2-PSQ data yields a ^{14}N = 1.55 G, in qualitative agreement with the ^{14}N = 1.23 G of a dinitrobenzene contact radical ion pair[65] and with the A(^{14}N) determined from ESEEM for **3**. Therefore, this data support both the ESEEM and X-band EPR data for **3**, where the ^{14}N was found to be larger when compared to complex **4**.

ESEEM was also collected on the K-2,7-di-NO_2-PSQ complex, and upon freezing the solution in ethanol a color change from brown to violet-red was observed. Recall that the solvent separated potassium radical is pink in solution. The color change upon freezing then suggests that the K-2,7-di-NO_2-PSQ is dissociating upon cooling to give a more concentrated solution of solvent separated anion radicals. This hypothesis is supported by literature precedence, since the dissociation of contact radical ion pairs can result from favorable counterion solvation at low temperature.[65,66] The resulting ESEEM spectrum is shown in Figure 4-17. The spectrum resembles conditions away from exact cancellation, and the signal is very weak with the isotropic ^{14}N = 0.15 G.

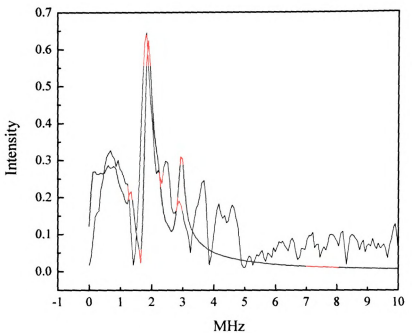

Figure 4-17. Stimulated echo detected ESEEM spectra of 2,7-di-NO_2-PSQ (**1**) (black) at 50 K in ethanol with frequency = 9.685 GHz; center field = 3450 G; τ = 136 ns; starting T = 40 ns; time increment = 16 ns. Simulation (red) parameters: g = isotropic, A = (0.65, 0.35, 0.05) MHz, e^2qQ = 1.1 MHz, η = 0.80, and Euler angles = (0.0, 0.2, 0.0). Spectra were obtained by normalizing the raw data and subtracting the bi-exponential decay followed by application of a Hamming window and Fourier transformation. Absolute value spectra are shown. See text for further details.

The additional two experimental peaks that were not simulated could be do to another species that is present in the system due to non-isotropic conditions. Although, the ^{14}N value is identical to the DFT calculated ^{14}N at the UB3LYP/6-31g* level for **1**, and lends additional support for the simulated ESEEM data. This ESEEM data corresponds to a spin polarization mechanism for populating spin density at the nitrogen nuclei and the HFC is in the range of what has been observed for **2**. Thus, the ESEEM data indicate that the species in frozen solution is most likely the solvent separated 2,7-di-NO_2-PSQ radical, and the spin density at the nitrogen nucleus is very small and agrees with the prediction from the THF experimental ESEEM data. Therefore, the combined data for the contact radical ion pair and the dissociated ligand contribute additional strong

experimental support for the spin density being directly delocalized onto the nitrogen atom in **3**, and for spin polarization being the dominate factor for **4**.

A possible mechanism for the different spin delocalization/polarization in the gallium complexes is based upon experimental data in the literature from the work of Rockenbauer et al.[14] where the EPR data of a tetrahedral Cu^{I}-2,7-di-NO_2-PSQ analogue determined that the $^{1}H_{1,8} > {}^{1}H_{3,6}$ in contrast with what has been observed in the 2,7-di-NO_2-PSQ free ligand examination, where $^{1}H_{3,6} > {}^{1}H_{1,8}$. Additionally, they observed that 2,7-di-*t*-butyl-PSQ had a more evenly distributed spin delocalization, with the $^{1}H_{1,8}$ and $^{1}H_{3,6}$ HFC being close in magnitude. The mechanism used to explain the spin transfer was an interaction between a filled orbital on the copper(I) metal center with the SOMO of the radical. They also proposed that the charge density changes in a direction opposite to the spin density. An identical situation is possible with the Ga-2,7-di-NO_2-PSQ complex (and 3,6-isomer). Since the molecule has C_{2v} symmetry the Ga^{III}-$3d_{xz}$ orbital has the correct symmetry to interact with the 2,7-di-NO_2-PSQ SOMO orbital of b_1 symmetry[67] (Figure 4-18). The spin delocalization in the SOMO molecular orbital of the metal complex is dependent upon the degree of orbital mixing between the Ga^{III}-$3d_{xz}$ and 2,7-di-NO_2-PSQ SOMO. Recall from MO theory, that when two orbitals are more energetically matched a stronger interaction occurs between the orbitals. Based on Rockenbauer's EPR data, the larger $^{1}H_{1,8}$ HFC for the 2,7-di-NO_2-PSQ radical could be due to the fact that the NO_2 group is more electron withdrawing than *t*-butyl, so that and the NO_2-SOMO will be lower in energy than the 2,7-di-*t*-butyl-PSQ SOMO. The spin will then localize more at the oxygen atoms due to the decreased mixing between the $3d_{xz}$ and 2,7-di-NO_2-PSQ SOMO compared to the higher energy 2,7-di-*t*-butyl-PSQ SOMO,

which will display increased mixing between the orbitals. The increased spin or decreased spin delocalization from the oxygen toward the PSQ ring will then account for the observed spin density changes in the carbon atoms.

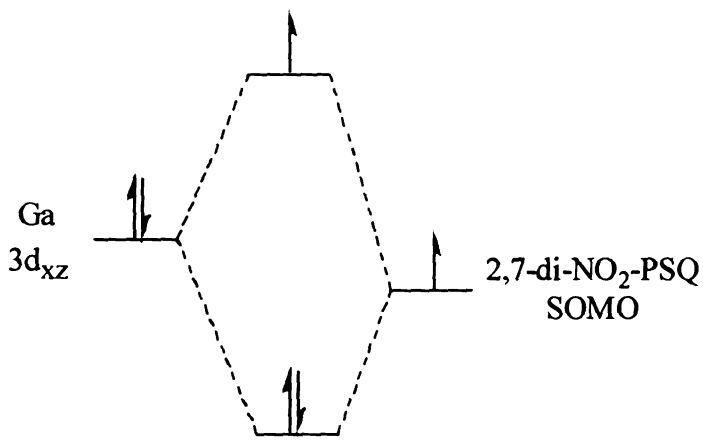

Figure 4-18. Interaction between the filled Ga(III) $3d_{XZ}$ and the 2,7-di-NO_2-PSQ SOMO.

It is known that **2** is more electron withdrawing than **1**, based on their corresponding half-wave reduction potentials.[68] The above mechanism then implies the spin density should be more localized at the oxygen atoms in **2** resulting in less overall spin density delocalization in the PSQ ring. This would predict larger ^{14}N HFC in **4** if spin delocalization is the dominating mechanism, but this is not observed experimentally. It has been hypothesized that the main mechanism for spin population at the nitrogen is spin polarization in complex **4** and this is known to have a decreased effect at transferring spin density compared to spin delocalization.[58] It is unclear then if this mechanism can be used to account for the different spin delocalization/polarization in the gallium complexes compared to the free ligands. To determine why such a dramatic change in spin population occurs for one isomer and not the other, a full DFT examination will be

undertaken to see if a model can be elucidated to explain the experimental observations in better detail. Additionally, Chapter 5 of this thesis will examine the mechanisms of spin delocalization more intensively with a variety of substituted Ni-PSQ complexes.

4.3.4 Density Functional Theory of Gallium Phenanthrenesemiquinones

The gas phase DFT calculations were done using the UB3LYP, UB3PW91, and the UPBE1PBE functionals using the 6-31g* basis set. Two key points regarding the DFT calculations can be made by examining the results in Table 4-3.

Table 4-3. DFT calculated HFC's and spin densities for $[Ga(tren)(2,7\text{-di-}NO_2\text{-PSQ})]^+$ (**3**) and $[Ga(tren)(3,6\text{-di-}NO_2\text{-PSQ})]^+$ (**4**).

Compound	Experimental HFC (G):	Calculated HFC (G): B3LYP	B3PW91	PBE1PBE	s-orbital ρ (H or N)[a]	p-π ρ (C)[b]
3						
$^1H_{1,8}$		-2.9723	-3.2629	-3.4804	-0.00499	0.10837
$^{14}N_{2,7}$	2.0	0.1944	0.2211	0.2791	0.00085	-0.05038
$^1H_{3,6}$		-3.0670	-3.3630	-3.5590	-0.00516	0.11193
$^1H_{4,5}$		0.4392	0.5736	0.7721	0.000850	-0.02545
4						
$^1H_{1,8}$		-3.0741	-3.3703	-3.5994	-0.00564	0.11538
$^1H_{2,7}$		1.0199	1.1820	1.3893	0.00176	-0.0477
$^{14}N_{3,6}$	0.487	-0.5681	-0.5958	-0.6610	-0.00233	0.10276
$^1H_{4,5}$		0.6691	0.8087	1.0244	0.00121	-0.03399

[a] Mulliken spin densities form the UB3LYP/6-31g* level of theory. [b] Average total p-orbital spin density on the carbon atoms bonded to the proton or nitrogen nucleus as indicated in the left column.

First, the DFT calculated ^{14}N hyperfine coupling constant for **3** is 1 order of magnitude too small, while **4** has an ^{14}N HFC that is in excellent agreement with experiment. The DFT calculated trend in the ^{14}N HFC is not consistent with the experimental data with **4** exhibiting the largest ^{14}N HFC. Secondly, the sign of the ^{14}N HFC's for the complexes

changes upon coordination (not determined in the EPR and ESEEM experiments) and contrasts the free radical DFT data. Interestingly, the spin density at the 2,7- and 3,6-carbon atoms in the gallium complexes exhibits opposite polarization, which also contrasts the free ligand calculations. After the above discrepancies were discovered, calculations were also done using the PCM and IPCM solvent continuum models in an attempt to calculate ^{14}N values closer to the experimental numbers. Unfortunately, the results of the solvent calculations predicted ^{14}N HFC's that were smaller in magnitude than the gas phase calculations.

A complete examination of the spin density distribution may possibly elaborate upon the disagreement between the experimental and calculated ^{14}N for **3**, and this is depicted in the total spin density plots for both complexes in Figure 4-19.

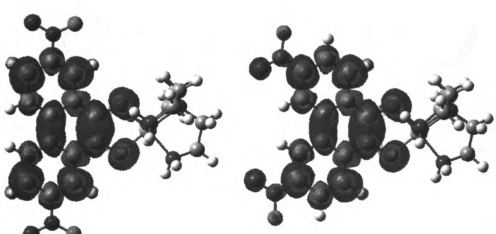

Figure 4-19. Total spin density distribution in **3** (left) and **4** (right).

In both gallium radical complexes, the polarization of spin density is identical, and the large α-spin density on the C–O group of the PSQ radicals causes the alternating β-spin and α-spin density polarization within the π-structure in the ring. The DFT spin density

data can be interpreted to predict that strong spin delocalization is operative at the 3,6-carbon atoms (large α-spin density), while spin polarization at the 2,7-carbons is the dominant mechanism (smaller β-spin density). This is not surprising since spin polarization is known to cause negative spin densities in similar ruthenium *o*-semiquinone type complexes.[3] The difference in sign for the ^{14}N in **3** and **4** is reflected in the opposing spin polarization mechanisms due to the different carbon atom spin populations. The Mulliken total p_z-π-spin density populations for each fragment is depicted in Figure 4-20.

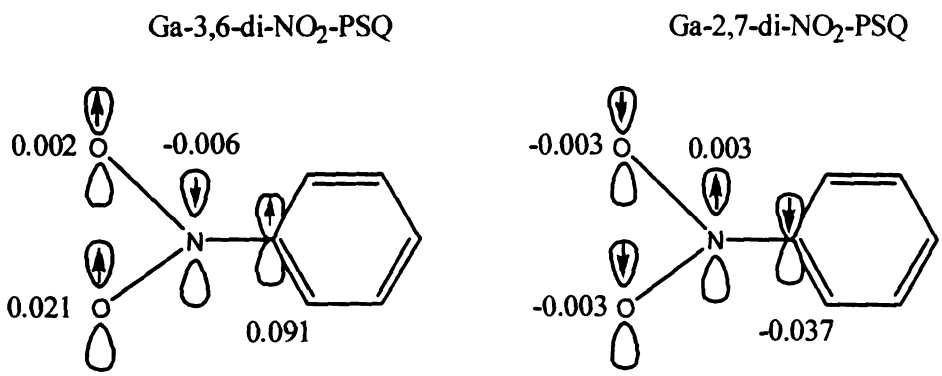

Figure 4-20. The polarization of π-spin density is depicted as it is predicted by DFT calculations for the Ga-2,7- and Ga-3,6-carbon atoms and NO_2 groups. In order for a simple comparison, the PSQ ligands are represented by a benzene ring.

The polarization of p_z-π-spin density is represented by an upward arrow for α-spin or a downward arrow for excess β-spin. It is evident in Figure 4-20 that the magnitude of spin density at the 3,6-carbons is a factor of 2.5 times greater than in the 2,7-isomer, and the N spin density is also 2 times greater (but negative). In all cases spin polarization is predicted to place spin density on the nitrogen atoms according to the DFT calculations. If spin delocalization were operative, the sign of the spin density on the carbon and nitrogen atoms would be the same to indicate the delocalization.

Based on the experimental results an incorrect physical picture is then predicted by the DFT calculations for complex **3** and no large excess α-spin or β-spin density is delocalized onto the 2,7-carbon atoms. *Caution* must be used since the ESEEM experiments have not determined the sign of the ^{14}N HFC only the magnitude. Overall, the DFT calculated spin density distribution supports the *DFT calculated* HFC's and spin densities, but the opposite trend is observed in the experimental ESEEM data. Interestingly, the free ligand calculations of the spin density distribution in the two radicals is consistent with the spin density being delocalized onto the nitrogen center of the NO_2 group in both complexes. A comparison between the α-HOMO's of **2** and **4** are depicted in Figure 4-21 to further investigate the Ga-DFT data.

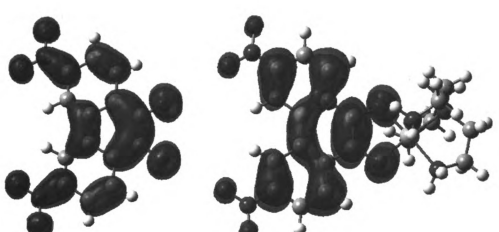

Figure 4-21. α-HOMO of **2** (left) and **4** (right).

The results shown in Figure 4-21 are for the 3,6-isomer, but identical conclusions can also be drawn for the 2,7-analogue since the coordination effects yield the same general results. There is a noticeable shift in the radical wavefunction upon coordination to gallium, with the wavefunction delocalizing away from the 2,7-positions in the gallium

complex. The depletion of the SOMO wavefunction away from the 2,7-carbons is one cause for the lack of spin density at these centers. It is also recognized that there is no large amplitude of the wavefunction on the nitrogen atoms in either Ga-complex. A simple explanation for the change in the α-HOMO upon complexation for the DFT data is that gallium(III) is a strong Lewis acid and it draws electron density away from the PSQ ring toward the carbonyl groups. This general idea supports the experimental data from Rockenbauer and the ^{14}N ESEEM data in the gallium complexes, since a shift in spin density toward the metal centers is observed. DFT also supports the role of Lewis acidity in increasing wavefunction localization at the carbonyl carbon atoms. The calculated carbon coefficient in the α-HOMO wavefunction more than doubles from 7 % for **2** to 15.5 % carbon for **4**, and there is a factor of 7 increase in the α-spin density at the carbonyl carbon atoms. Similar increases are also observed from **1** to **3**. The large localization of spin at the carbonyl carbons, causes the unpaired spin to be polarized in the alternating β-spin, α-spin, pattern (Figure 4-19). Therefore, the Lewis acid effect could be responsible for the DFT pattern of spin polarization in the gallium complexes, and may be the reason why we do not see it in the free ligands. The disagreement between the experimental and theoretical data likely stems from the DFT overestimation of the spin polarizing effect of the Ga^{III} Lewis acid.

The above arguments explain the trend in the DFT results, but do not explain why there is an observed deviation from the experimental values. In the literature it is known that spin polarization effects are difficult to model accurately;[69,70] and errors in A(Ga) as much as 22 G have been reported for the neutral gallium boraamidinate radicals.[71] Spin contamination of the ground state wavefunction was also noted to overestimate spin

polarization due to large UHF contributions in hybrid functionals,[3] but the $\langle S^2 \rangle_2$ values for the gallium radicals indicated negligible contamination ($\langle S^2 \rangle_2 = 0.75$ for a pure spin state), and the maximum value found with all hybrid functionals was $\langle S^2 \rangle_2 = 0.77$. Functionals such as BLYP and SVWN, which have no Hartree-Fock exchange included in their description, actually had larger deviations in magnitude from the experimental ^{14}N HFC and predicted the same spin density distribution. Increasing the size of the basis set from 6-31g* to 6-311g** for all atoms or using the cc-pVQZ basis set for N atoms also did not show any improvement in the calculation of the ^{14}N HFC. A survey of the literature did find another possible explanation of the incorrect spin distribution, due to large self interaction errors in DFT.[72] Piquemal et al. have shown that self interaction error is largely responsible for incorrect spin delocalization in tyrosinase models such as $[Cu_2O_2]^{2+}$ and Zn^{II}-imidazole complexes.[73,74] The overpolarization of spin density in the complexes is explained by the presence of a strong electric field generated by the transition metals.[73,74] The gallium electric field could then possibly "overpolarize" the spin density distribution in **3** and **4**. To test this hypothesis a DFT calculation in the presence of an electric dipole field applied along the y-axis (the y-axis goes through the oxygen atoms in the PSQ plane) using the Gaussian 03 keyword field = y+200 was done, and the results are depicted in Figure 4-22. The field value of y+200 indicates that a field of 0.02 au is applied in the y-direction based upon the standard orientation of the molecule. The use of the electric dipole field applied along the y-axis polarized the spin density, and negative spin density is observed on the 2,7-carbon atoms identical to that observed in complexes **3** and **4** (and K-coordinated complex, not shown). In fact, the entire spin density distribution seen in **3** and **4** is modeled by using an electric dipole field

applied along the y-axis for the 2,7-di-NO_2-PSQ ligand. This attests to the fact that the calculated spin density in the Ga^{III} complexes might be overpolarized by the gallium electric field, resulting in the absence of spin delocalization to the nitro group in complex **3**. Higher level calculations are likely required to get an accurate description of the spin density distribution in these systems, and will be pursed in the future.

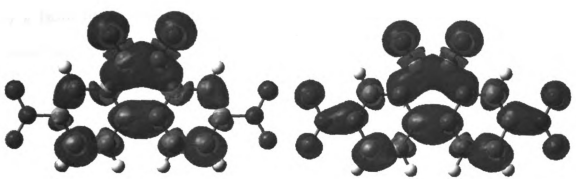

Figure 4-22. The results of a UB3LYP/6-31g* total spin density field calculation for 2,7-di-NO_2-PSQ (left) along with the result from the same calculation without the field keyword (right). The Gaussian 03 field = y+200 keyword was used in the field calculation. Identical spin polarization results were also obtained for the 3,6-di-NO_2-PSQ complex with the same electric field (not shown).

4.4 Concluding Comments

Several salient results concerning the experimental and DFT spin density distribution and hyperfine coupling constants in the 2,7-di-NO_2-PSQ (**1**) and 3,6-di-NO_2-PSQ (**2**) radical ligands and the corresponding Ga-2,7-di-NO_2-PSQ (**3**) and Ga-3,6-di-NO_2-PSQ (**4**) complexes have been realized. The experimental X-band EPR and DFT calculated HFC and spin densities for the radical ligands are in excellent agreement. The magnitudes of the ^{14}N HFC for the radical ligands are in the same range, and indicate the spin density on each nitrogen atoms results from spin polarization. Upon coordination to gallium, the ^{14}N HFC was found to be a factor of 4 times greater in **3** then in **4**.

Although, the ESEEM simulations may have errors as great as 20 % for the ^{14}N HFC, the trend in the data is real. The increased HFC in **3** is due to direct spin delocalization onto the nitrogen atom, and the smaller HFC for **4** is likely the result of spin polarization. The experiments then indicate that substituents at the 2,7-positions will delocalize more spin density away from the oxygen atoms. DFT calculated ^{14}N HFC for **4** was consistent with the value determined from ESEEM spectroscopy, but the ^{14}N for **3** was found to deviate by a factor of 7. The DFT deviations could be the result of self-interaction errors overpolarizing the spin density distribution in the gallium complexes, whereby spin delocalization is masked. More work is needed to verify a model to describe the spin delocalization/polarization mechanism both experimentally and theoretically. It must be stressed that only the relative magnitudes of the ^{14}N HFC have been determined, and the signs of the HFC are needed to unambiguously experimentally determine the spin delocalization model in these systems.

The above model for the shifting of spin density towards the gallium center is still possibly valid, but DFT calculations overestimated the polarization of the spin density of the π-system in complex **3**. In order to determine a bulletproof experimental mechanism, the determination of all the signs of the HFC is needed. This can be accomplished by using a combination of EPR, ENDOR, and TRIPLE spectroscopies.[75,76] The sign determination is of course predicated upon observing the ENDOR and TRIPLE EPR signals, but if they can be determined then it can be deduced where α- and β-spin density resides in the complexes, enabling determination of a correct spin delocalization mechanism. Another experimental option to model this effect is ^{17}O. This would be useful to determine the shifts in magnitude of the spin density nearest to the gallium. ^{15}N

labeling of the tren capping ligand would also be highly desired to inconclusively prove the ^{14}N HFC is from the dinitro radical ligands. Additionally, the effect of π-donor ligands such as di-NH_2-PSQ along with the π-acceptor di-NO_2-PSQ radicals on the magnitude of ^{14}N and ^{17}O HFC would give strong evidence for the support or failure of the spin density shifting model. Future work along these lines will be undertaken.

4.5 References

1 Ruiz, E.; Cirera, J.; Alvarez, S. *Coord. Chem. Rev.* **2005**, *249*, 2649.

2 Cano, J.; Ruiz, E.; Alvarez, S.; Verdaguer, M. *Comments. Inorg. Chem.* **1998**, *20*, 27.

3 Reymenyi, C.; Kaupp, M. *J. Am. Chem. Soc.* **2005**, *127*, 11399.

4 Dei, A.; Gatteschi, D.; Sangregorio, C.; Sorace, L. *Acc. Chem. Res.* **2004**, *37*, 827.

5 Vostrikova, K. E. *Coord. Chem. Rev.* **2008**, *252*, 1409.

6 Lin, H.-H.; Wei, H.-H.; Lee, G.-H.; Wang, Y. *Polyhedron* **2001**, *20*, 3057.

7 Caneschi, A.; Gatteschi, D.; Sessoli, R.; Rey, P. *Acc. Chem. Res.* **1989**, *22*, 392.

8 Hicks, R. G. *Aust. J. Chem.* **2001**, *54*, 597.

9 Abakumov, G. A.; Cherkasov, V. K.; Nevodchikov, V. I.; Druzhkov, N. O.; Kuropatov, V. A. *Russ. Chem. Bull.* **1998**, *47*, 875.

10 Oshio, H.; Yamamoto, M.; Ito, T.; Kawauchi, H.; Koga, N.; Ikoma, T.; Tero-Kubota, S. *Inorg. Chem.* **2001**, *40*, 5518.

11 Broze, M.; Luz, Z.; Silver, B. L. *J. Chem. Phys.* **1967**, *46*, 4891.

12 Broze, M.; Luz, Z. *J. Chem. Phys.* **1969**, *51*, 738.

13 Wheeler, D. E.; Rodriguez, J. H.; McCusker, J. K. *J. Phys. Chem. A* **1999**, *103*, 4101.

14 Rockenbauer, A.; Györ, M.; Speier, G.; Tyeklár, Z. *Inorg. Chem.* **1987**, *26*, 3293.

15 McConnell, H., M, *J. Chem. Phys.* **1956**, *24*, 764.

16 Nguyen, M. T.; Creve, S.; Vanquickenborne, L. G. *J. Phys. Chem. A* **1997**, *101*, 3174.

17 Palmer, G. In *Physical Methods in Bioinorganic Chemistry: Spectroscopy and Magnetism*; Que, J., L., Ed.; University Science Books: Sausalito, 2000.

18 Deligiannakis, Y.; Louloudi, M.; Hadjiliadis, N. *Coord. Chem. Rev.* **2000**, *204*, 1.

19 McCracken, J. L. In *Handbook of Electron Spin Resonance*; Poole, J., C. P., Farach, H. A., Eds.; Springer-Verlag: New York, 1999; Vol. 2, p 69.

20 McCracken, J.; Vassiliev, I. R.; Yang, E.-C.; Range, K.; Barry, B. A. *J. Phys. Chem. B* **2007**, *111*, 6586.

21 Jiang, F.; McCracken, J.; Peisach, J. *J. Am. Chem. Soc.* **1990**, *112*, 9035.

22 Chasteen, N. D.; Snetsinger, P. A. In *Physical Methods in Bioinorganic Chemistry: Spectroscopy and Magnetism*; University Science Books: Sausalito, CA, 2000, p 187.

23 Schmidt, J.; Kämpf, A. *Chem. Ber.* **1902**, *35*, 3117.

24 Schmidt, J.; Kämpf, A. *Chem. Ber.* **1903**, *36*, 3738.

25 Urbanek, R. A.; Suchard, S. J.; Steelman, G. B.; Knappenberger, K. S.; Sygowski, L. A.; Veale, C. A.; Chapdelaine, M. J. *J. Med. Chem.* **2001**, *44*, 1777.

26 Maruyama, K.; Otsuki, T. *Bull. Chem. Soc. Japan* **1968**, *41*, 444.

27 Maruyama, K. *Bull. Chem. Soc. Japan* **1964**, *37*, 553.

28 Schenck, G. O.; Schmidt-Thombée, G. A. *Ann. Chem.* **1953**, *584*, 199.

29 Connelly, N. G.; Geiger, W. E. *Chem. Rev.* **1996**, *96*, 877.

30 Vierling, P.; Guillon, C. *J. Organomet. Chem.* **1994**, *464*, C42.

31 *XSOPHE*, Computer Simulation Software Suite 1.1.4; Center for Magnetic Resonance and Department of Mathmatics, The University of Queensland (Brisbane, Queensland, Australia 4072) and Bruker Biospin GMBH (formerly Buruker Analytik; Rheinstetten, Germany): 1993-2004.

32 Wang, D.; Hanson, G. *J. Mag. Reson. Ser. A* **1995**, *117*, 1.

33 Hanson, G.; Gates, K. E.; Noble, C. J.; Griffen, M.; Mitchell, A.; Benson, S. *J. Inorg. Biochem.* **2004**, *98*, 903.

34 Gemperle, C.; Aebli, G.; Schweiger, A.; Ernst, R. R. *J. Magn. Reson.* **1990**, *88*, 241.

35 Schweiger, A.; Jeschke, G. *Principals of Pulsed Electron Paramagnetic Resonance*; Oxford University Press: New York, 2001.

36 Mims, W. B. *Phys. Rev. B: Condens Matter* **1972**, *5*, 2409.

37 Mims, W. B. *Phys. Rev. B: Condens Matter* **1972**, *6*, 3543.

38 Dikanov, S. A.; Tsvetkov, Y. D. In *Electron Spin Echo Envelope Modulation Spectroscopy*; CRC Press: Boca Raton, Fl, 1992, p 17.

39 O'Malley, P. J. *Antiox. Redox. Sig.* **2001**, *3*, 825.

40 Hermosilla, L.; Calle, P.; García de la Vega, J. M.; Sieiro, C. *J. Phys. Chem. A* **2006**, *110*, 13600.

41 Langgård, M.; Spanget-Larsen, J. *J. Mol. Struct. THEOCHEM* **1998**, *431*, 173.

42 *GaussView*, 2.1 ed.; Gaussian, Inc.: Pittsburgh, PA, 2001.

43 M. J. Frisch, G. W. T., H. B. Schlegel, G. E. Scuseria; M. A. Robb, J. R. C., J. A. Montgomery, Jr., T. Vreven; K. N. Kudin, J. C. B., J. M. Millam, S. S. Iyengar, J. Tomasi; V. Barone, B. M., M. Cossi, G. Scalmani, N. Rega; G. A. Petersson, H. N., M. Hada, M. Ehara, K. Toyota; R. Fukuda, J. H., M. Ishida, T. Nakajima, Y. Honda, O. Kitao; H. Nakai, M. K., X. Li, J. E. Knox, H. P. Hratchian, J. B. Cross; V. Bakken, C. A., J. Jaramillo, R. Gomperts, R. E. Stratmann; O. Yazyev, A. J. A., R. Cammi, C. Pomelli, J. W. Ochterski; P. Y. Ayala, K. M., G. A. Voth, P. Salvador, J. J. Dannenberg; V. G. Zakrzewski, S. D., A. D. Daniels, M. C. Strain; O. Farkas, D. K. M., A. D. Rabuck, K. Raghavachari; J. B. Foresman, J. V. O., Q. Cui, A. G. Baboul, S. Clifford; J. Cioslowski, B. B. S., G. Liu, A. Liashenko, P. Piskorz; I. Komaromi, R. L. M., D. J. Fox, T. Keith, M. A. Al-Laham; C. Y. Peng, A. N., M. Challacombe, P. M. W. Gill; B. Johnson, W. C., M. W. Wong, C. Gonzalez, and J. A. Pople, *Gaussian 03*, Revision D.01; Gaussian, Inc.: Wallingford CT, 2004.

44 Glendening, E. D.; Reed, A. E.; Carpenter, J. E.; Weinhold, F. *NBO 3.1*, Theoretical Chemistry Institute, University of Wisconsin: Madison, WI, 1996.

45 Foresman, J. B.; Keith, T. A.; Wiberg, K. B.; Snoonian, J.; Frisch, M. J. *J. Phys. Chem.* **1996**, *100*, 16098.

46 Frisch, M. J.; Frisch, A. *Gaussian 98 User's Reference*; Gaussian, Inc.: Pittsburgh, 1998.

47 Schrauben, J. N.; Guo, D.; McCracken, J. L.; McCusker, J. K. *Inorg. Chim. Acta.* **2008**, *361*, 3539.

48 Cancès, M. T.; Mennucci, B.; Tomasi, J. *J. Chem. Phys.* **1997**, *107*, 3032.

49 Cossi, M.; Barone, V.; Mennucci, B.; Tomasi, J. *Chem. Phys. Lett.* **1998**, *286*, 253.

50 Mennucci, B.; Tomasi, J. *J. Chem. Phys.* **1997**, *106*, 5151.

51 Cossi, M.; Scalmani, G.; Rega, N.; Barone, V. *J. Chem. Phys.* **2002**, *117*, 43.

52 O'Malley, P. J.; Collins, S. J. *Chem. Phys. Lett.* **1996**, *259*, 296.

53 Rieger, P. H.; Fraenkel, G. K. *J. Chem. Phys.* **1963**, *39*, 609.

54 Corrie, J. E. T.; Gilbert, B. C.; Munasinghe, V. R. N.; Whitwood, A. C. *J. Chem. Soc. Perkin Trans. 2* **2000**, 2483.

55 Morales-Morales, J. A.; Frontana, C.; Aguilar-Martínez, M.; Bautista-Martínez, A.; González, F. J.; González, I. *J. Phys. Chem. A* **2007**, *111*, 8993.

56 Kazakova, V. M.; Pesterev, P. A.; Minina, N. E. *Rus. J. Gen. Chem.* **2003**, *73*, 1114.

57 Dehl, R.; Fraenkel, G. K. *J. Chem. Phys.* **1963**, *39*, 1793.

58 Adamo, C.; Barone, V.; Subra, R. *Theor. Chem. Acc.* **2000**, *104*, 207.

59 Flanagan, H. L.; Singel, D. J. *J. Chem. Phys.* **1987**, *87*, 5606.

60 Mims, W. B.; Peisach, J. *J. Chem. Phys.* **1978**, *69*, 4921.

61 McCracken, J.; Peisach, J.; Cote, C. E.; McGuirl, M. A.; Dooley, D. M. *J. Am. Chem. Soc.* **1992**, *114*, 3715.

62 Beckmann, U.; Bill, E.; Weyhermüller, T.; Wieghardt, K. *Eur. J. Inorg. Chem.* **2003**, 1768.

63 McCracken, J.; Pember, S.; Benkovic, S. J.; Villafranca, J. J.; Miller, R. J.; Peisach, J. *J. Am. Chem. Soc.* **1988**, *110*, 1069.

64 Lü, J. M.; Rosokha, S. V.; Neretin, I. S.; Kochi, J. K. *J. Am. Chem. Soc.* **2006**, *128*, 16708.

65 Lü, J. M.; Rosokha, S. V.; Lindeman, S. V.; Neretin, I. S.; Kochi, J. K. *J. Am. Chem. Soc.* **2005**, *127*, 1797.

66 Hirota, N. *J. Phys. Chem.* **1967**, *71*, 127.

67 Gordon, D. J.; Fenske, R. F. *Inorg. Chem.* **1982**, *21*, 2907.

68 Mukherjee, T. K. *J. Phys. Chem.* **1967**, *71*, 2277.

69 Munzarová, M. L. In *Calculation of NMR and EPR parameters: Theory and Applications*; Kaupp, M., Bühl, M., Malkin, V. G., Eds.; VCH, Weinheim: 2004, p 463-482.

70 Kaupp, M.; Munzarová, M. L. *J. Phys. Chem. A* **1999**, *103*, 9966.

71 Chivers, T.; Eisler, D. J.; Fedorchuk, C.; Schatte, G.; Tuononen, H. M.; Boeré, R. T. *Chem. Commun.* **2005**, 3930.

72 Zhang, Y.; Yang, W. *J. Chem. Phys.* **1998**, *109*, 2604.

73 Piquemal, J. P.; Pilmé, J. *J. Mol. Struct.* **2006**, *764*, 77.

74 Piquemal, J. P.; Marquez, A.; Parisel, O.; Giessner-Prettre, C. *J. Comp. Chem.* **2005**, *26*, 1052.

75 Stegmann, H. B.; Dao-Ba, H.; Mäurer, M.; Scheffler, K.; Buchner, H.; Hartmann, E.; Mannschreck, A. *Mag. Res. Chem.* **1988**, *26*, 547.

76 Kay, C. W. M.; Feicht, R.; Schulz, K.; Sadewater, P.; Sancar, A.; Bacher, A.; Möbius, K.; Richter, G.; Weber, S. *Biochemistry* **1999**, *38*, 16740.

Chapter 5. The Substituent Effect in the Modulation of the Heisenberg Exchange Coupling Interaction in Ni(II) and Cr(III) Phenanthrenesemiquinones: A Combined Experimental and Theoretical Examination.

5.1 Introduction.

The applications for manipulating exchange coupling in transition metals could be applied to many disciplines from magnetism to biology. For example, if the mechanism for spin density delocalization/polarization can be determined using both experimental and theoretical tools, then advances in the design of transition metal-radical molecular magnetic materials could be accomplished.[1-6] Additionally, the control of spin density at a radical center could be utilized in the design of catalysts that participate in σ-bond forming reactions. Thus it is a great importance to many scientists to elucidate the mechanism of spin delocalization/polarization in transition metal radical complexes.

The previous results from the examination of the polarization of spin and charge density in neutral and anion radicals have revealed that both spin and charge density can be differentially polarized. This work will be extended to utilize the knowledge of spin and charge polarization to design paramagnetic transition metal radical complexes that could exhibit tunable ferromagnetic and antiferromagnetic Heisenberg exchange coupling interactions. The charge density polarization information will aid in the synthesis of the semiquinone complexes, since increasing the negative charge density at the oxygen centers in the semiquinone (SQ) radicals will increase the Lewis basicity of these ligands and the formation constant.[7] The strength of the Heisenberg exchange coupling interaction has been shown to be proportional to the spin densities at the interacting

atoms,[8-12] and control of the spin density polarization with substituents can then be used to increase or decrease the strength of the metal-radical exchange coupling interaction. Previous work from Shultz et al.[13] has shown that substituents can modulate the exchange coupling interactions in Mn(II) and Cu(II) 5-aryl-substituted semiquinones, but no mechanisms concerning spin density distribution have been put forth. It is the goal of this work to examine the effects of substituents on the spin density distribution, and determine any mechanisms that account for the modulations in the magnitude of ferromagnetic and antiferromagnetic Heisenberg exchange coupling constants.

It is well known that the unpaired electron in the SQ radical is housed in an orbital of π-symmetry.[14] In order to examine the effects of substituents on ferromagnetic exchange coupling nickel(II) will be used, and in order to simplify the exchange coupling interaction we will focus on six coordinate complexes that contain only one semiquinone radical. Six coordinate nickel(II) is a d^8 transition metal and its unpaired electrons are in the $d_{X^2-Y^2}$ and d_{Z^2} orbitals which have σ-symmetry. The σ-orbitals of Ni^{II} and the π* SQ orbital are strictly orthogonal, and Hund's rule will apply and the electrons will experience a ferromagnetic interaction.[15,16] Conversely, chromium(III) is a d^3 transition metal having unpaired electrons in the d_{XZ}, d_{YZ}, and d_{XY} orbitals of π-symmetry. Due to the π-orbital overlap, Cr(III) will undergo an antiferromagnetic interaction with the SQ radical.[15,16] Nickel(II)[17,18] and Chromium(III)[19] semiquinone compounds with the tetradentate CTH counterligand (CTH = *dl*-5,7,7,12,14,14-hexamethyl-1,4,8,11-tetrazacyclotetradecane) are experimental examples of the ferromagnetic and antiferromagnetic exchange coupling interaction found in these types of transition metal radical complexes. It must be noted that no temperature dependence was seen in the

experimental magnetic susceptibility data for either the Cr(III) and Ni(II) complexes, barring any firm determination of J and only allowing a lower limit for J to be established. For experimental J values to be determined, thermal population of the doublet state is required to determine the energy gap and a lack of a temperature dependence in the Ni(II) complex indicates an isolated quartet ground state with no thermal population of the antiferromagnetic doublet state. Based on the magnetic data, experimental estimates for the exchange coupling constants in these systems have been in excess of 400 cm^{-1} in both cases.

The broken symmetry formalism[20-23] has been applied to calculate J in several transition metal organic radical complexes[24-28] including semiquinone compounds.[29-33] A recent report from Bencini et al.[31] for the $[Ni(CTH)(PSQ)]^{2+}$ and $[Ni(CTH)(3,5\text{-}DTBSQ)]^{2+}$ (PSQ = 9,10-phenanthrenesemiquinone and 3,5-DTBSQ = 3,5-di-*tert*-butylsemiquinone) complexes has calculated J = 285 and 356 cm^{-1}, respectively, from broken symmetry density functional theory (DFT). For our purposes we wish to be able to experimentally determine J, and in order to do so we need J values that will be small enough to allow for temperature dependence in the magnetic susceptibility measurements. Therefore, for these reasons we will prepare Nickel(II) and Chromium(III) complexes of substituted PSQ's, since the Bencini DFT calculations predicted that the PSQ ligand should lead to decreased exchange coupling.

For the transition metal complexes studied here, the tetradentate tren (tren = tris-2-aminoethylamine) ligand will be used as the counter ligand, since only one isomer can be formed when bound to a metal (the CTH ligand can exist in both meso and racemic forms). The $[M(tren)(2,7\text{-}R\text{-}PSQ)]^{n+}$ and $[M(tren)(3,6\text{-}R\text{-}PSQ)]^{n+}$ (where M = Cr(III)

and Ni(II), 2,7-R_1 = NO_2, H, and NH_2 and 3,6-R_2 = NO_2, H, and NH_2 , and for Cr(III) n = 2 and for Ni(II) n = 1) depicted in Chart 5-1 will be examined using a combination of DFT and magnetic susceptibility measurements in an effort to determine the effects of substituents on the spin density distribution and on the corresponding *J* values. The 2,7-R-PSQ ligands are easiest to prepare synthetically and the free ligands showed variable spin polarization at the oxygen atoms, thus this will be the starting point of this work.

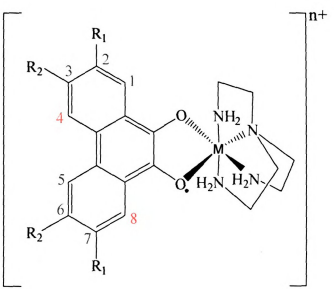

Chart 5-1. General formula for the metal-radical complexes examined.

5.2 Experimental.

General Methods. All reagents were obtained from commercial sources and used without further purification. HPLC grade methanol was distilled from Mg and I_2, and degassed 15 times by gas exchange with N_2. Elemental analyses and mass spectra were obtained through the analytical facilities at Michigan State University, ESI-MS experiments used standard conditions and all spectra agreed with appropriate simulations.

The 3,6-dinitrophenanthrenequinone,[34] 3,6-dinitrophenanthrenecatechol,[34] 2,7-dinitrophenanthrenesemiquinone,[34] 2,7-dinitrophenanthrenecatechol,[34] acetyl-ferrocenium tetraphenylborate,[34] and $[Cr(tren)Cl_2]Cl$[35] compounds have been prepared as previously described.

Phenanthrenecatechol. The procedure for the preparation of this ligand has been modified from a published procedure.[36] To a schlenk flask containing 2.5 g (12 mmol) of phenanthrenequinone in 125 ml of degassed ethanol, 2.6 g (48 mmol) of solid KBH_4 was added over a period of three hours. The addition of KBH_4 to the reaction mixture under N_2 was done every 20 minutes, and upon the addition of KBH_4 the orange suspension gradually goes into solution and the color changes to yellow. The solution was stirred under nitrogen for 48 hours, then cooled in an ice bath. Dilute aqueous HCl was then added to deactivate the excess potassium borohydride. When the deactivation with HCl was complete (no H_2 (g) evolution), the ethanol solution was poured over 500 ml of an ice-water mixture and a white precipitate was immediately formed. The product was collected on a glass frit washed with water and dried in vacuo. The ligand is stored under nitrogen to prevent oxidation, and solutions of the compound are very air sensitive. Yield: 2.0 g (80 %) Anal. Calcd for $C_{14}H_{10}O_2 \cdot 0.5H_2O$: C, 76.70; H, 5.06; Found: C, 77.05; H, 4.57.

2,7-diaminophenanthrenecatechol. The synthesis of this compound was based on methods already developed in the literature.[37] A flask was charged with 0.36 g (1.2 mmol) of 2,7-dinitrophenanthrenequinone and 0.85 g (7.1 mmol) Sn^0 and then 100 ml of 12 M HCl was added to the flask, and the solution was refluxed until it turns clear and becomes yellow in color. Not all the solids dissolved, so approximately 20 ml of distilled

water was added to the reaction flask to help dissolve all remaining solids. The reaction mixture is then filtered hot and upon slow cooling white crystals precipitate out of solution. The complex was recrystallized by boiling in a 12 M HCl solution and allowing the flask to slowly cool to room temperature. The white crystals were collected on a glass frit and dried in vacuo. Yield: 0.27 g (92 %). The complex is stored under nitrogen to prevent oxidation and solutions of the compound are very air sensitive. Anal. Calcd for $C_{14}H_8N_2O_6 \cdot 0.5H_2O \cdot 2HCl$: C, 52.19; H, 4.69; N, 8.69; Found: C, 52.09; H, 5.09; N, 8.67.

3,6-diaminophenanthrenecatechol. The synthesis of this compound was based on methods already developed in the literature and is similar to the 2,7-di-NH_2-isomer above.[37] In a roundbottom flask 0.25 g (0.82 mmol) 3,6-dinitrophenanthrenequinone and 0.59 g Sn^0 (5.0 mmol) and 150 ml of 12 M HCl was refluxed for 45 minutes or until the solution turns yellow and slightly cloudy. 20 ml of water was then added to the hot solution to aid in the solubility of the product. The reaction mixture is then filtered hot and left out to crystallize. The flask was then placed in the fridge overnight to ensure all the precipitate fell out of solution. The precipitate was washed with cold ACN and ether and dried in vacuo. Yield: yellow-white crystalline solid 0.17 g (84 %). The complex is stored under nitrogen to prevent oxidation, and solutions of the compound are very air sensitive. Anal. Calcd for $C_{14}H_{12}N_2O_2 \cdot 0.5H_2O \cdot 2HCl$: C, 52.19; H, 4.69; N, 8.69; Found: C, 52.48; H, 4.27; N, 8.71.

Ferrocenium Tetraphenylborate. The synthesis of this compound was based on methods already developed in the literature.[38] To a stirring solution of ferrocene 0.50 g (2.7 mmol) in a solution of 20 ml of water and 20 ml of acetone was added 0.61 g

anhydrous $FeCl_3$ (3.8 mmol) under N_2. After stirring for 15 minutes the deep blue solution was filtered and 1.3 g (3.8 mmol) of $NaBPh_4$ was added, resulting in the formation of a fine dark blue precipitate. Tetrahydrofuran (ca. 100 ml) was then added to the reaction flask until all solids dissolved. The solution was filtered and concentrated under a stream of nitrogen and deep blue crystals fell out of solution. The crystals were washed with acetone and ether, and the complex is immediately stored in a dry box. The sample should be used the same day it is synthesized, since it is unstable even under an atmosphere of dry nitrogen. Anal. Calcd for $C_{34}H_{30}BFe{\cdot}2OC(CH_3)_2$: C, 77.31; H, 6.81; Found: C, 77.38; H, 6.53.

Ferrocenium Chloride. Although a literature procedure using Cl_2 (g) as a reagent for this complex has been reported,[39] a new synthetic procedure based upon the synthesis of a similar ferrocenium salt was adapted in order to exclude the use of the hazardous Cl_2 (g).[40] 4 ml of 2.0 M hydrogen chloride in ether was added to a to a degassed filtered solution of 0.33 g (3.0 mmol) 1,4-quinone under nitrogen. Then 0.37 g ferrocene (2.0 mmol) was dissolved in ether and filtered, and added to the stirring solution under N_2. The solution darkens in color and was stirred for 15 minutes under N_2, during which time a blue-green precipitate falls out of solution. The precipitate was filtered off and washed with ether (30 ml x 3) and dried in vacuo. Yield: 0.20 g (44 %). Anal. Calcd for $C_{10}H_{10}FeCl{\cdot}0.3HCl$: C, 51.68; H, 4.47; Found: C, 51.49; H, 4.19.

$TlBAr^f$. *Caution: thallium salts are known to be highly toxic and care should be taken during all manipulations using any thallium reagent.* The synthesis of this complex has been published,[41] but a much less synthetically intensive procedure based on the silver analogue[42] was found to give similar results. 0.40 g of $NaBAr^f$ (0.45 mmol)

was dissolved in 15 ml of ether then filtered into a separatory funnel. 0.24 g (0.90 mmol) of $TlNO_3$ was dissolved in 10 ml of water and added to the funnel. The funnel was then shaken for 5 minutes (periodically releasing the pressure), and then the layers were allowed to separate. The ether layer was evaporated to dryness with a nitrogen stream, and then the complex was dried in vacuo. The complex was then washed with water (3 x 30 ml) and hexanes (3 x 30 ml), and further dried in vacuo. Yield: 0.37 g (77 %). Anal. Calcd for $C_{32}H_{12}TlBF_{24}\cdot 0.5CH_3CH_2OCH_3CH_2$: C, 36.97; H, 1.55; Found: C, 36.75; H, 1.37.

Ni(tren)Cl_2. The synthesis of this compound was based on methods already developed in the literature.[43] 1.46 g (10.0 mmol) of tren (tris-2-aminoethylamine) was dissolved in ethanol and 2.38 g (10.0 mmol) of $NiCl_2\cdot 6H_2O$ was added to the stirring solution. The solution was stirred for one hour during which time a blue precipitate forms. The precipitate is filtered off and washed with ethanol, and then the product was recrystallized from hot ethanol to give dark blue crystals. The complex is stored in a desiccator since its highly hydroscopic. Recrystallized yield: 0.963 g (35 %) Anal. Calcd for $C_6H_{18}Cl_2N_4Ni\cdot H_2O$: C, 24.53; H, 6.86; N, 19.07; Found: C, 25.37; H, 6.79; N, 18.71.

[Ni(tren)(PSQ)](BPh$_4$) (1). The synthesis of this compound was based on methods already developed in the literature.[31] Under N_2, 0.24 g (0.86 mmol) of Ni(tren)Cl_2 was dissolved in 20 ml methanol, and to this solution was added a 20 ml methanol solution of 0.20 g (0.96 mmol) phenanthrenecatechol and 0.076 g (1.9 mmol) NaOH. The gold colored reaction mixture was stirred for 30 minutes and then oxidized with 0.32 g (0.96 mmol) of $[FeCp_2](PF_6)$ under N_2, and the color changed to brown-black. The solution was stirred for an additional 15 minutes after adding the oxidant, and

was then filtered under nitrogen. A concentrated methanol solution of 3.3 g (9.6 mmol) $NaBPh_4$ was slowly added to the filtered reaction mixture and it was left out to crystallize in the dry box. A gold-brown microcrystalline product was recovered and washed with methanol (10 ml x 3) and ether (10 ml x 3) and dried in vacuo. The product can be recrystallized by adding 200 ml of ether to a concentrated acetonitrile solution of the complex under N_2. Crystals suitable for X-ray diffraction were obtained by carefully layering a $NaBPh_4$/methanol solution under the filtered reaction mixture in the dry box. Yield: 0.42 g (67 %). Anal. Calcd for $C_{44}H_{47}BN_4NiO_2$: C, 72.16; H, 6.33; N, 7.65; Found: C, 71.96; H, 6.72; N, 7.72. MS [ESI, *m/z* (rel. int.)]: $[Ni(tren)(PSQ)]^+$ 412.1 (80).

[Ni(tren)(2,7-di-NO_2-PSQ)](BPh_4) (2). Under a N_2 atmosphere, 0.083 g (0.30 mmol) $Ni(tren)Cl_2$ was dissolved in 30 ml of methanol, and to this solution was added a 30 ml methanol solution of 0.10 g (0.33 mmol) 2,7-dinitrophenanthrenecatechol and 0.027 g (0.68 mmol) NaOH. The solution was stirred for 1 hour and then oxidized with 0.099 g (0.30 mmol) $[FeCp_2](PF_6)$ and the solution turns red-black in color and was stirred for an additional 15 minutes. The reaction mixture is then filtered under nitrogen and a concentrated methanol solution of 1.0 g (3.0 mmol) $NaBPh_4$ was slowly added. A red-brown precipitate was recovered and washed with methanol (10 ml x 3). Yield: 0.16 g (64 %). The product is recrystallized from hot acetonitrile with a 41 % yield. X-ray quality crystals were grown by slow evaporation of concentrated ACN solutions. Anal. Calcd for $C_{44}H_{44}BN_6NiO_6$: C, 64.26; H, 5.39; N, 10.22; Found: C, 64.15; H, 5.74; N, 10.46. MS [ESI, *m/z* (rel. int.)]: $[Ni(tren)(2,7\text{-di-}NO_2\text{-PSQ})]^+$ 502 (100).

[Ni(tren)(2,7-di-NO_2-PSQ)](BAr^f) (3). This salt was prepared by first making the [Ni(tren)(2,7-di-NO_2-PSQ)]Cl intermediate. The nickel chloride salt was synthesized

under N_2 by dissolving 0.058 g (0.21 mmol) Ni(tren)Cl_2 in 30 ml of methanol, and to this solution was added a 20 ml methanol solution of 0.070 g (0.23 mmol) 2,7-dinitrophenanthrenecatechol and 0.027 g (0.47 mmol) NaOH. The dark-blue solution was stirred for 1 hour and then oxidized with 0.052 g (0.24 mmol) of [$FeCp_2$]Cl, and the solution turns black in color and was stirred for an additional 15 minutes. The reaction mixture was then filtered, and the filtrate was evaporated to dryness in the dry box. The recovered dark-brown/black precipitate was washed with water (30 ml x 3), isopropanol (30 ml x 3), and ether (30 ml x 3) and dried in vacuo. Additional washing with CH_2Cl_2 (5 ml x 3) was done under N_2 in the drybox. Yield: 0.096 g (84 %). This complex was then used without further purification.

Under N_2, 0.0670 g (0.124 mmol) of [Ni(tren)(2,7-di-NO_2-PSQ)]Cl was suspended in 20 ml CH_2Cl_2, and 0.133 g (0.124 mmol) of $TlBAr^f$ in 10 ml of CH_2Cl_2 was added with stirring. Care was taken to ensure that equal molar amounts of each reactant are used. Upon the addition of the $TlBAr^f$ the suspension goes into solution with the formation of a white precipitate (TlCl). The solution was stirred for 1 day under nitrogen, and then filtered through celite under N_2. The filtrate was evaporated to dryness in the drybox yielding a brown precipitate, and dried in vacuo. Yield: 0.142 g (83 %). Anal. Calcd for $C_{52}H_{36}BF_{24}N_6NiO_6$: C, 45.71; H, 2.66; N, 6.15; Found: C, 45.61; H, 2.87; N, 5.40.

[Ni(tren)(2,7-di-NH_2-PSQ)](BPh$_4$) (4). Under a N_2 atmosphere, 0.103 g (0.375 mmol) of Ni(tren)Cl_2 was dissolved in 20 ml of methanol, and to this solution was added a 10 ml methanol solution of 0.100 g (0.416 mmol) of 2,7-diaminophenanthrenecathechol and 0.0600 g (1.50 mmol) NaOH. Excess base is required due to the presence of 2

equivalents of HCl in the elemental analysis of the ligand. The golden-yellow solution was stirred for 30 minutes, then the solution was oxidized with 0.124 g (0.375 mmol) of $[FeCp_2](PF_6)$, which caused the color to change to dark-brown. The solution was stirred for an additional 15 minutes and was filtered in the dry box. A saturated methanol solution of 1.28 g (3.75 mmol) of $NaBPh_4$ was layered under the reaction mixture to give a brown crystalline solid. The product was washed with methanol (5 ml x 3) and ether (10 ml x 3) and dried in vacuo. Yield: 0.154 g (54 %). X-ray quality crystals were grown by layering a $NaBPh_4$/methanol solution under the reaction mixture in the dry box. Anal. Calcd for $C_{44}H_{48}BN_6NiO_2 \cdot MeOH$: C, 68.03; H, 6.60; N, 10.58; Found: C, 68.18; H, 6.65; N, 10.84. MS [ESI, *m/z* (rel. int.)]: $[Ni(tren)(2,7\text{-di-}NH_2\text{-PSQ})]^+$ 442.1 (100).

[Ni(tren)(3,6-di-NO_2-PSQ)](BPh$_4$) (5). Under a N_2 atmosphere, 0.054 g (0.19 mmol) $Ni(tren)Cl_2$ was dissolved in 30 ml of methanol, and to this solution was added a 30 ml methanol solution of 0.070 g (0.23 mmol) 3,6-dinitrophenanthrenecatechol and 0.027 g (0.47 mmol) NaOH. The dark purple-red solution was stirred for 1 hour and then oxidized with 0.064 g (0.23 mmol) $[FeCp_2](BF_4)$ and the solution turns blue-black in color and was stirred for an additional 15 minutes. The mixture is then filtered and a concentrated methanol solution of 1.2 g (3.5 mmol) $NaBPh_4$ was slowly added. Upon sitting under nitrogen, deep-blue needles precipitate out of solution. The product was then collected on a glass frit and washed with methanol (10 ml x 3) and ether (10 ml x 3) and dried in vacuo. The product can be recrystallized by adding ether to a concentrated acetonitrile solution of the complex. X-ray quality crystals were obtained by slow ether diffusion into a ACN solution of the complex. Yield: 0.069 g (43 %). Anal. Calcd for

$C_{44}H_{44}BN_6NiO_6 \cdot 0.5MeOH$: C, 63.75; H, 5.53; N, 10.02; Found: C, 63.59; H, 5.49; N, 10.18. MS [ESI, *m/z* (rel. int.)]: $[Ni(tren)(3,6\text{-di-}NO_2\text{-PSQ})]^+$ 502.1 (100).

[Ni(tren)(3,6-di-NH_2-PSQ)](BPh$_4$) (6). Under a N_2 atmosphere, 0.066 g (0.24 mmol) of $Ni(tren)Cl_2$ was dissolved in 10 ml of methanol, and to this solution was added a 10 ml methanol solution of 0.063 g (0.26 mmol) of 3,6-diaminophenanthrenecathechol and 0.042 g (1.1 mmol) NaOH. Excess base is required due to the presence of 2 equivalents of HCl in the elemental analysis of the ligand. The golden-yellow solution was stirred for 30 min, then the solution was oxidized with 0.079 g (0.24 mmol) of $[FeCp_2](PF_6)$, which caused the color to change to deep red-black. The solution was stirred for an additional 15 minutes and was filtered in the dry box. A saturated methanol solution of 1.35 g (3.9 mmol) of $NaBPh_4$ was slowly added to the reaction mixture and upon standing overnight red-black crystals were formed. The product was washed with methanol (10 ml x 3) and ether (10 ml x 3) and dried in vacuo. Yield: 0.055 g (32 %). X-ray quality crystals were grown by layering a $NaBPh_4$/methanol solution under a concentrated solution of the reaction mixture in the dry box. Anal. Calcd for $C_{44}H_{48}BN_6NiO_2 \cdot H_2O$: C, 67.72; H, 6.46; N, 10.77; Found: C, 67.54; H, 6.51; N, 10.78. MS [ESI, *m/z* (rel. int.)]: $[Ni(tren)(3,6\text{-di-}NH_2\text{-PSQ}) \cdot H]^+$ 443.2 (100).

[Cr(tren)(PCAT)](BPh$_4$) (7). A schlenk flask was charged with 0.13 g (0.43 mmol) of $[Cr(tren)Cl_2]Cl$ that was dissolved in 10 ml of water and 50 ml of methanol, then this solution was degassed for 30 minutes by bubbling N_2 through the stirring solution. The flask was connected to a reflux condenser and placed under N_2, then a oxygen free solution of 0.10 g (0.48 mmol) of phenanthrenecatechol and 0.038 g (0.95 mmol) NaOH in 20 ml methanol was added to the $[Cr(tren)Cl_2]Cl$ solution using a

cannula. The solution was then refluxed for 24 hours, and filtered under N_2 into a flask containing 1.6 g (4.7 mmol) of $NaBPh_4$. As the solution cools, a brown microcrystalline product forms and was collected on a glass frit and washed with water (20 ml x 3) and dried in vacuo.

A second method of preparation involves adding the deprotonated ligand to a stirring suspension of $[Cr(tren)Cl_2]Cl$ in methanol. This suspension is then stirred for 24 hours in the dry box, and 1.2 equivalents of $[FeCp_2](BPh_4)$ was added. After stirring for 2 hours the solution is filtered and a 10 fold excess of $NaBPh_4$ is added to precipitate out brown crystals. X-ray quality crystals were obtained by slow evaporation of the reaction mixture in the dry box. Yield: 0.16 g (51 %). Anal. Calcd for $C_{44}H_{46}BN_4CrO_2$: C, 72.82; H, 6.39; N, 7.72; Found: C, 72.27; H, 6.53; N, 7.76. MS [ESI, *m/z* (rel. int.)]: $[Cr(tren)(PCAT)]^+$ 406.1 (100).

$[Cr(tren)(PSQ)](BPh_4)_2$ (8). Utilizing the same reaction conditions for the second method of preparation of the $[Cr(tren)(PCAT)]^+$ complex, except for stirring for 48 hours, the reaction mixture was oxidized with 0.22 g (0.43 mmol) of freshly prepared $[FeCp_2](BPh_4)$. The reaction was stirred for 2 hours with the oxidant and then filtered, and a concentrated methanol solution of 0.92 g (2.7 mmol) of $NaBPh_4$ was added and black crystals fell out of solution. X-ray quality crystals were obtained by slow evaporation of the reaction mixture in the dry box. Yield 0.13 g (43 %) Anal. Calcd for $C_{44}H_{46}BN_4CrO_2 \cdot MeOH$: C, 76.95; H, 6.55; N, 5.20; Found: C, 76.57; H, 6.85; N, 5.48. MS [ESI, *m/z* (rel. int.)]: $\{[Cr(tren)(PSQ)]^{2+} \cdot CH_3CN\}$ 244.1 (100).

$[Cr(tren)(3,6\text{-di-}NO_2\text{-PCAT})](BF_4)$ (9). In a schlenk flask fitted with a reflux condenser, 0.059 g (0.19 mmol) of $[Cr(tren)Cl_2]Cl$ was dissolved in a mixture of 30 ml

H_2O and 45 ml of methanol, and this solution was degassed by bubbling N_2 through the stirring solution for 30 minutes. Under N_2, 0.070 g (0.23 mmol) of 3,6-di-NO_2-PCATH_2 was dissolved in 10 ml of methanol and deprotonated with 0.019 g of NaOH (0.47 mmol) in 10 ml of methanol. The deprotonated catechol ligand was then added via cannula to the stirring [Cr(tren)Cl_2]Cl solution under N_2. The mixture is then refluxed for 16 hours, and filtered hot under N_2 into a Schlenk flask containing 0.38 g (15 fold molar excess) of $NaBF_4$ in a minimum amount of water. The solution was then allowed to cool to room temperature and concentrated until a purple-brown precipitate forms. The precipitate is then filtered off and washed with H_2O (20 ml x 3) and ether (20 ml x 3). The complex can be recrystallized from ACN/ether mixtures. Yield: 0.055 g (48 %). An analogous procedure can also be used for the BPh_4 salt (56 % Yield). Anal. Calcd for $C_{44}H_{44}BN_6CrO_6 \cdot 2H_2O$: C, 62.05; H, 5.68; N, 9.87; Found: C, 61.8; H, 5.51; N, 9.99. MS [ESI, *m/z* (rel. int.)]: [Cr(tren)(3,6-di-NO_2-PCAT)]$^+$ 496.2 (20).

[Cr(tren)(3,6-di-NO_2-PSQ)]$(BF_4)_2$ (10). 0.031 g (0.047 mmol) of [Cr(tren)(3,6-di-NO_2-PCAT)](BF_4) was dissolved in 5 ml of acetonitrile and 0.015 g (0.047 mmol) of acetylferrocenium tetrafluoroborate in 2 ml of acetonitrile was added to a stirring solution of the catechol, and the color immediately changes from purple to dark brown. The solution was stirred for 5 minutes then filtered, and ether was added until the solution turned cloudy. A brown precipitate was recovered and washed with dichloromethane (5 ml x 3) and ether (5 ml x 3). Yield: 0.028 g (78 %). Anal. Calcd for $C_{20}H_{24}B_2F_8N_6CrO_6 \cdot H_2O$: C, 34.91; H, 3.81; N, 12.21; Found: C, 34.84; H, 3.84; N, 12.39. MS [ESI, *m/z* (rel. int.)]: [Cr(tren)(3,6-di-NO_2-PSQ)]$^+$ 496 (100).

[Ga(tren)(PCAT)](BPh$_4$) (11). Under a dry atmosphere of N_2, a methanol solution of 0.10 g (0.48 mmol) phenanthrenecatechol and 0.04 g (0.95 mmol) of NaOH was added to a stirring methanol solution of 0.19 g (0.43 mmol) of GaI_3, and the cloudy yellow solution was stirred for 1 hour. A solution of 0.060 g (0.43 mmol) of tren in 5 ml of methanol was then added resulting in a clear yellow solution, and the reaction was stirred under N_2 overnight. The solution was filtered and a concentrated methanol solution of 1.6 g (4.7 mmol) $NaBPh_4$ was added, and upon standing a yellow microcrystalline precipitate was recovered. X-ray quality crystals were grown from slow evaporation of methanol solutions of the complex. Yield: 0.19 g (59 %). Anal. Calcd for $C_{44}H_{46}BGaN_4O_2$: C, 71.09; H, 6.24; N, 7.54; Found: C, 70.61; H, 6.38; N, 7.48.

[Ga(tren)(PSQ)](BPh$_4$)$_2$ (12). To a concentrated stirring solution of [Ga(tren)(PCAT)](BPh$_4$) in acetonitrile, 1.1 equivalents of [FeCp$_2$](BF$_4$) in 2 ml of acetonitrile was added changing the yellow color to brown. The solution was filtered and added to 15 equivalents of $NaBPh_4$ (no solvent) and then 300 ml of ether was added to precipitate out brown microcrystals. Anal. Calcd for $C_{68}H_{66}B_2GaN_4O_2 \cdot MeOH$: C, 75.71; H, 6.45; N, 5.12; Found: C, 75.60; H, 6.29; N, 5.45.

Physical Measurements: X-ray Crystallography. Single-crystal X-ray diffraction for **1, 2, 4, 5, 6, 7, 8,** and **11** were acquired at the X-ray facility at Michigan State University. A total of four single crystals of **4** were used to collect the X-ray data, and only one data set could be solved to yield a reasonable R1 value. Diffraction data were collected on a Siemens SMART diffractometer with graphite-monochromatic Mo Kα radiation (λ = 0.71073 Å). Data were collected at –100 °C by using an Oxford Cryosystems low temperature device. Lattice parameters were obtained from least-

squares analyses and data were integrated with the program SAINT.[44] The integration method employed a three-dimensional profiling algorithm and all data were corrected for Lorentz and polarization factors, as well as for crystal decay effects. The absorption correction program SADABS was employed to correct the data for absorption effects.[45] The structures were solved by direct methods and expanded Fourier techniques. All structure calculations were performed with the SHELXTL 6.12 software package.[46] Anisotropic thermal parameters were refined for all non-hydrogen atoms. Hydrogen atoms were localized in their calculation positions and refined by using the riding model. Further details concerning the structure determinations may be found in the text.

Cyclic Voltammetry. Electrochemical measurements were carried out in a Ar filled dry box using a BAS CV-50W electrochemical analyzer. A standard three-electrode configuration was employed consisting of a Pt working electrode, a graphite counter electrode, and $Ag/AgNO_3$ reference electrode. Compounds were dissolved in CH_3CN that was 0.10 M in NBu_4PF_6; the CH_3CN has been run through a dry still and degassed by the freeze-pump-thaw method. Data were corrected for ferrocene as an internal standard, and run at a scan rate of 100 $mV \cdot s^{-1}$.

Electronic Absorption Spectroscopy. Extinction coefficients were determined using a Hewlett-Packard 8452A diode-array spectrometer in CH_3CN. Data were obtained on samples dissolved in CH_3CN that had been run through a dry still and oxygen gas was removed by gas exchange with nitrogen (15 cycles), and stored under an inert atmosphere. All solutions were prepared under an inert atmosphere in 1 cm pathlength sealed optical cells.

Magnetic Susceptibility. Solution susceptibility was estimated based on the chemical shifts of *t*-butanol using variable temperature Evans NMR.[47] In the N_2 atmosphere dry box, the paramagnetic sample was dissolved in d_7-DMF containing 2-3 % *t*-butanol and placed into a melting point tube. The open end of the tube was sealed with epoxy, and then placed into a standard NMR tube containing d_7-DMF and 2-3 % *t*-butanol. Typical paramagnetic solution concentration's were 3.0×10^{-2} M and the temperature of the 500 MHz NMR spectrometer was calibrated with standard techniques using CH_3OH. The solution susceptibility of a known compound with an $S = {}^3/_2$ ground state, $Cr(acac)_3$ (acac = acetylacetonate), was run prior to the Evans to ensure the accuracy of the experiments.

Magnetic susceptibility data were also collected using a Quantum Design MPMS SQUID magnetometer interfaced with a IBM PC. The solid samples were ground with a mortar and pestle and placed in a plastic freezer bag and rolled into a drinking straw. The bag was placed 50 mm from the bottom of the straw, and the size of the sample in the straw was less than 10 mm in height to ensure the samples proper placement in the SQUID coils. **NOTE:** if the height of the sample in the straw was greater than 10 mm, we experienced reduced magnetization due to the sample's position outside the SQUID measurement range. Data were typically collected in an applied field of 1 T in a temperature range of 5-350 K. Following each temperature change, the system was kept at the new temperature for an additional 5 minutes before data collection to ensure thermal equilibrium of the sample. Data were corrected for diamagnetism of the sample using Pascal's constants and for the measured susceptibility of the sample holder and bag and are reported herein as effective magnetic moments. Solution SQUID susceptibility

measurements[48,49] were collected in a laboratory fabricated quartz sample tube (Chart 5-2) with a 5 mm ID and 7 mm OD that was equipped with a Pyrex vacuum adapter. The sample holder had a quartz plug 50 mm from the bottom of the tube, so that sample could be placed into the tube. An additional 70 mm (or more) of quartz tube was above the plug to ensure that the environment above and below the sample was identical. To collect good liquid phase data the sample needed to be as concentrated as possible without powdering out of solution when frozen. Again, the height of the frozen solution was kept below 10 mm to ensure the correct SQUID signal measurement. Typically 0.075 ml of an approximately 1.0 M solution (for S = $^3/_2$ systems) was used in the experiment, and the diamagnetism of the solvent and sample holder were corrected for by subtracting their magnetic susceptibility determined in a separate experiment. The liquid sample was then degassed by the freeze-pump-thaw technique at least 5 times and flame sealed under vacuum.

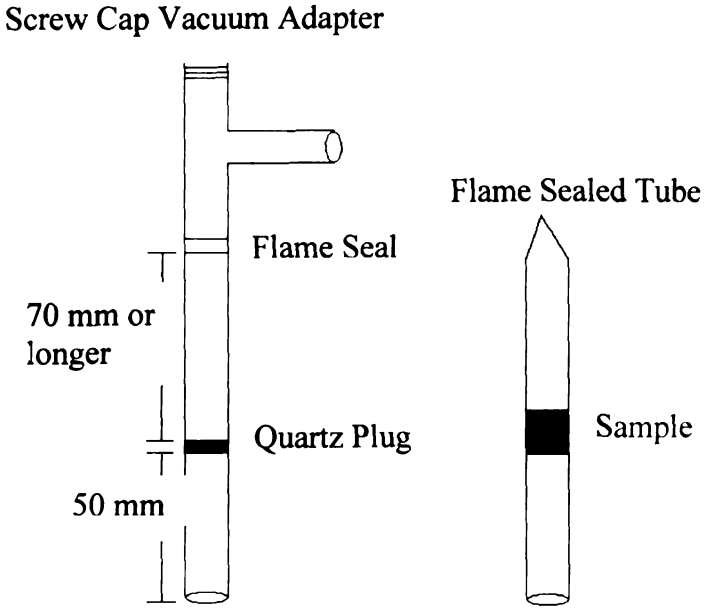

Chart 5-2. Liquid phase SQUID sample holder.

Calculations. Previous calculations have shown that the B3LYP functional gives reasonable results in the calculation of J values.[31] The starting geometries for all complexes were adapted from the crystal structures of either the $[Ni(tren)(PSQ)]^+$ or $[Cr(tren)(PSQ)]^{2+}$ complexes using GaussView,[50] and the quartet spin state of the Ni-PSQ complexes and the triplet spin state of Cr-PSQ analogues were then optimized using either Gaussian 98[51] or 03[52] with the UB3LYP functional with the LANL2DZ basis set. The calculated energy differences between the Gaussian 98 and 03 results were indistinguishable (identical J values resulted), as tested for the $[Ni(tren)(PSQ)]^+$ and $[Cr(tren)(PSQ)]^{2+}$ complexes. For both the nickel and chromium compounds further single point calculations for the doublet and quartet, and triplet and quintet spin states, respectively, were done using the optimized geometries with the UB3LYP functional with the 6-311g** basis set. In some cases an energetically higher antiferromagnetic electronic state was calculated as the solution to the Kohn-Sham equations, and in these cases the guess = mix keyword was applied in an additional calculation at the same level of theory in an attempt to calculate a lower energy antiferromagnetic state. The guess = mix calculations all corresponded to lower energy electronic states when compared to the initial results. The spin densities for all molecules were calculated using the natural population analysis developed by Weinhold and coworkers.[53] All calculations were done using tight convergence criteria,[54] with a molecular charge of +1 for the nickel and +2 for the chromium complexes. The point groups of all molecules were determined to be C_1 in the Gaussian software.

5.3 Results and Discussion

5.3.1 Synthesis and Characterization of Nickel(II) 2,7-di-R-Phenanthrenesemiquinone Complexes.

Synthesis. The general synthetic procedure for the Ni-2,7-di-R-PSQ complexes was adapted from a procedure by Bencini et al.[31] and is depicted in Chart 5-3. The deprotonated ligands are very air-sensitive in solution, and care must be taken to handle solutions of these compounds only under inert atmospheres. The methanol solvent used in the reaction has to be thoroughly degassed to facilitate clean reactions. The Ni-PSQ complexes were made in reasonable yield by oxidation of the Ni^{II}-phenanthrenecatechol species with ferrocenium hexafluorophosphate, followed by precipitation with excess $NaBPh_4$ salt out of a methanol solution. The phenanthrenecatechol (PCAT) complexes were made initially due to the large amount of negative charge density at the oxygen atoms in these dianions, making these ligands stronger Lewis bases than the semiquinone analogues. The isolated solids were stable in air for magnetic measurement purposes, but are highly air sensitive in solution. Nevertheless, the solid compounds were kept under vacuum or inert atmosphere to ensure no decomposition during storage.

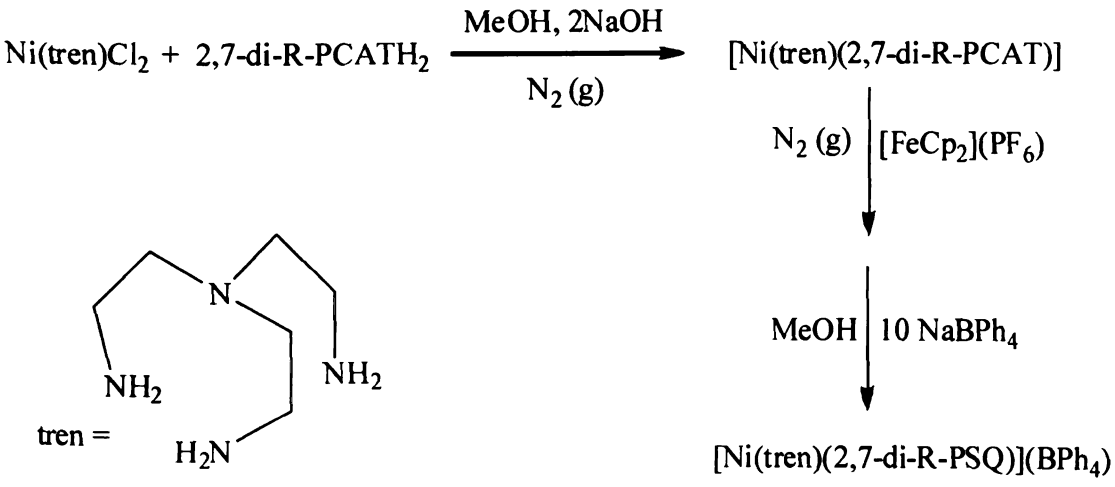

Chart 5-3. General synthetic procedure for the [Ni(tren)(2,7-di-R-PSQ)](BPh4) complexes.

Ground State Characterization: X-ray Crystallography. ORTEP drawings of the crystal structures of complexes **1** (Ni-PSQ), **2** (Ni-2,7-di-NO_2-PSQ), and **4** (Ni-2,7-di-NH_2-PSQ) are shown in Figure 5-1.

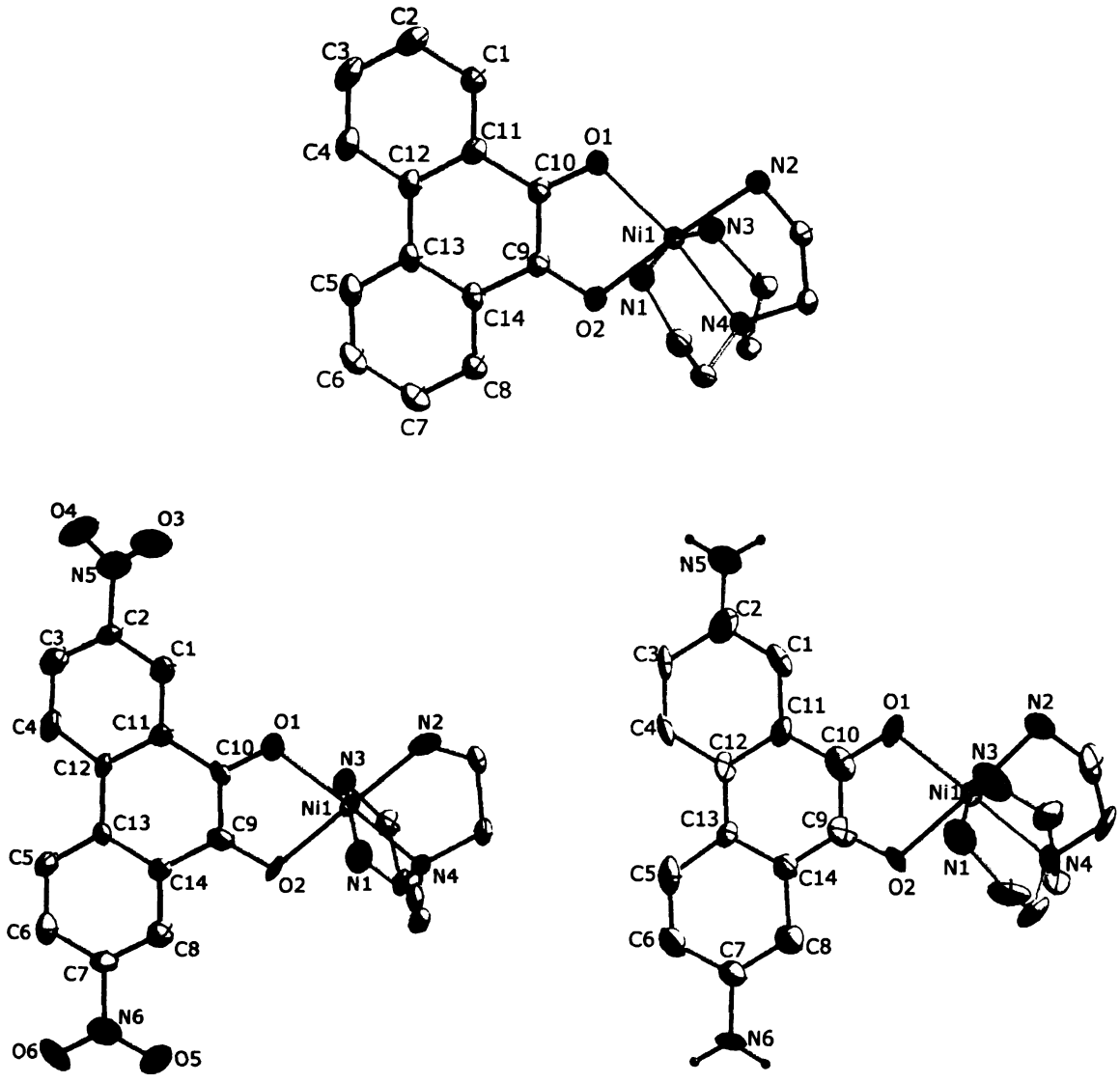

Figure 5-1. Drawings of the cations of $[Ni(tren)(PSQ)]^+$ (**1**) (top), $[Ni(tren)(2,7\text{-di-}NO_2\text{-PSQ})]^+$ (**2**) (bottom left), and $[Ni(tren)(2,7\text{-di-}NH_2\text{-PSQ})]^+$ (**4**) (bottom right) obtained from X-ray structure determinations. Atoms are represented as 50 % probability ellipsoids.

The selected bond distances and angles for the compounds are listed in Table 5-1, and crystallographic data are reported in Table 5-2.

Table 5-1. Selected bond distances and angles for **1**, **2**, and **4**.

	1	**2**	**4**
	Bond Distances (Å)		
Ni(1)–O(1)	2.0561(10)	2.055(4)	2.078(7)
Ni(1)–O(2)	2.0685(10)	2.061(5)	2.138(6)
Ni(1)–N(1)	2.1413(12)	2.113(5)	2.159(10)
Ni(1)–N(2)	2.0857(11)	2.061(5)	2.086(9)
Ni(1)–N(3)	2.1381(12)	2.135(5)	2.063(9)
Ni(1)–N(4)	2.0786(11)	2.073(4)	2.093(9)
C(10)–O(1)	1.2829(15)	1.283(6)	1.336(7)
C(9)–O(2)	1.2797(16	1.268(7)	1.268(8)
C(9)–C(10)	1.4398(18)	1.441(8)	1.39[a]
C(9)–C(14)	1.4502(18)	1.468(8)	1.39[a]
C(14)–C(13)	1.4111(19)	1.415(7)	1.39[a]
C(13)–C(12)	1.4731(19)	1.455(8)	1.39[a]
C(12)–C(11)	1.4144(18)	1.421(8)	1.39[a]
C(11)–C(10)	1.4560(18)	1.460(8)	1.39[a]
	Bond Angles (deg)		
O(1)–Ni(1)–N(1)	94.27(4)	103.33(18)	102.5(4)
O(1)–Ni(1)–N(2)	103.41(4)	100.71(18)	98.3(3)
O(1)–Ni(1)–N(3)	98.49(4)	89.10(17)	92.3(4)
O(1)–Ni(1)–N(4)	172.10(4)	170.27(18)	174.5(4)
O(1)–Ni(1)–O(2)	80.54(4)	80.05(16)	78.5(3)
O(2)–Ni(1)–N(1)	86.44(5)	84.38(17)	82.9(4)
O(2)–Ni(1)–N(2)	175.83(4)	179.19(18)	175.5(3)
O(2)–Ni(1)–N(3)	85.71(4)	85.84(17)	89.3(4)
O(2)–Ni(1)–N(4)	91.91(4)	95.20(16)	99.4(3)
N(1)–Ni(1)–N(2)	94.50(5)	95.2(2)	94.7(4)
N(1)–Ni(1)–N(3)	163.71(5)	162.58(19)	161.5(4)
N(1)–Ni(1)–N(4)	82.86(4)	84.52(18)	82.2(4)
N(2)–Ni(1)–N(3)	92.36(5)	94.44(19)	94.1(4)
N(2)–Ni(1)–N(4)	84.18(4)	84.09(18)	84.0(4)
N(3)–Ni(1)–N(4)	83.16(4)	82.05(17)	82.6(4)
C(9)–O(2)–Ni(1)	110.77(8)	109.8(4)	110.7(4)
C(10)–O(1)–Ni(1)	110.98(8)	110.7(4)	110.4(5)
O(1)–C(10)–C(9)	118.64(11)	118.4(5)	119.1(5)
O(2)–C(9)–C(10)	118.55(11)	119.2(6)	118.1(5)

[a] Larger errors due to crystal quality.

Table 5-2. Crystallographic data for [Ni(tren)(PSQ)](BPh_4) (**1**), [Ni(tren)(2,7-di-NO_2-PSQ)](BPh_4) (**2**), and [Ni(tren)(2,7-di-NH_2-PSQ)](BPh_4) (**4**).

	1	**2**	**4**
formula	$C_{44}H_{46}BN_4NiO_2$	$C_{44}H_{44}BN_6NiO_6$	$C_{44}H_{48}BN_6NiO_2$
M_w	732.37	822.37	762.4
cryst syst	Monoclinic	Triclinic	Monoclinic
space group	*P*2(1)/*c*	*P*-1	*P*2(1)/*c*
a/Å	19.766 (5)	10.7720 (13)	41.270 (6)
b/ Å	9.143 (2)	10.9028 (13)	10.1298 (14)
c/ Å	20.466 (5)	19.510 (3)	18.190 (3)
β/ °	100.779 (4)	87.794 (3)	102.700 (3)
V/ $Å^3$	3633.4 (15)	1925.7 (4)	7418.5 (18)
Z	4	2	8
T/K	173(2)	173(2)	173(2)
D_c/ g cm^{-3}	1.339	1.418	1.365
θ_{max}	28.3	22.5	22.5
reflns measured	41984	15583	44927
independent reflns	8750	5030	8830
observed reflns [$I > 2\sigma(I)$]	7175	2933	2269
μ(Mo *K*α)/ mm^{-1}	0.58	0.56	0.57
R_{int}	0.04	0.098	0.098
R1[a]	0.029	0.059	0.073
*w*R2[b]	0.083	0.146	0.206
GOF	1.06	0.97	1.00

[a] $R1 = \Sigma||F_O| - |F_C||/ \Sigma|F_O|$. [b] $wR2 = [\Sigma w(F_O^2 - F_C^2)/\Sigma w(F_O^2)^2]^{1/2}$, $w = 1/[\sigma^2(F_O^2) + (aP)^2 + bP]$, where $P = (F_O^2 + 2F_C^2)/3$.

The X-ray structures show distorted *cis*-octahedral symmetry around the Ni^{II} ion, and the Ni–O bond distances for the complexes fall within the range observed for analogous Ni^{II}-SQ complexes.[17,31] The axial Ni–N distances are significantly longer than the equatorial Ni–N bonds in each complex analogous to what was found for [Ni(CTH)(PSQ)](PF_6), indicating an elongated octahedron type geometry.[31] One way to confirm the oxidation state of the semiquinone ligands is to examine the C–O and the intradiol (C(9)-C(10)) bonds. Based on the X-ray data of several semiquinone complexes, the distances of C–O ≅ 1.29 Å and C(10)-C(9) ≅ 1.44 Å indicate the semiquinone oxidation state.[55] The

average C–O bonds (Table 5-2) for **1**, **2**, and **4** of 1.28, 1.28, and 1.30 Å and the intradiol distances of 1.44, 1.44, and 1.39 Å, respectively, for the complexes agree with the literature values, except a larger deviation is seen for the intradiol distance in **4**. This is most likely due to the quality of the single crystal. Despite this the X-ray data does provide experimental evidence for the identification of the Ni-2,7-di-NH_2-PSQ (**4**) complex.

Electronic Absorption Spectra. The electronic absorption spectra of acetonitrile solutions of the Ni^{II}-PSQ compounds are shown in Figure 5-2.

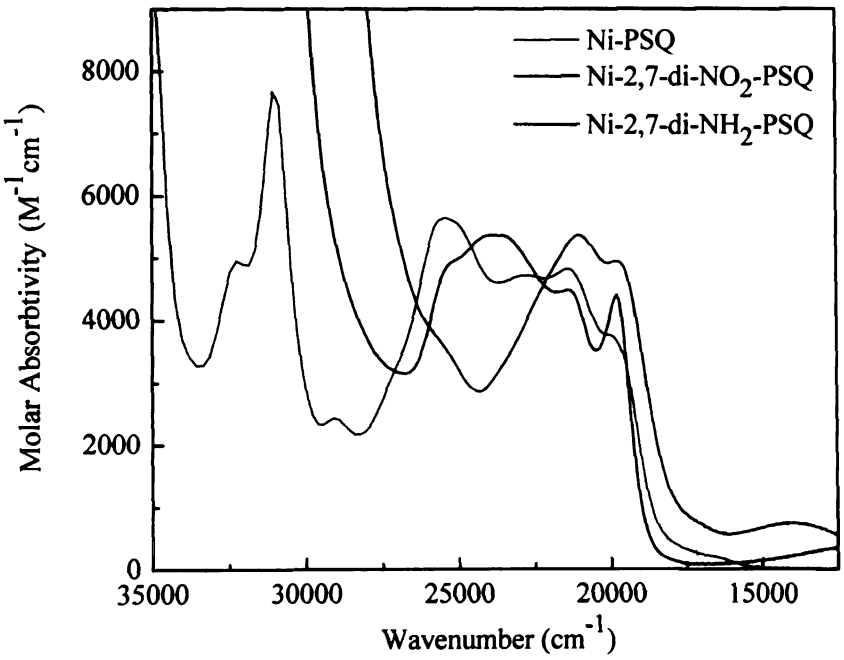

Figure 5-2. Electronic absorption spectra of [Ni(tren)(PSQ)](BPh_4) (**1**) (red), [Ni(tren)(2,7-di-NO_2-PSQ)](BPh_4) (**2**) (green), and [Ni(tren)(2,7-di-NH_2-PSQ)](BPh_4) (**4**) (blue), in ACN at 25 °C.

The electronic absorption spectrum of [Ni(CTH)(PSQ)](PF_6) has been recorded previously by Bencini et al.,[31] and the observed transitions qualitatively match what is observed in the [Ni(tren)(PSQ)](BPh_4) spectrum in Figure 5-2. Slight differences in the energy of the transitions could be attributed to different solvent and capping ligand used

in the experiments. A comparison of the data is shown in Table 5-3. Bencini et al. determined that the transitions observed at 20400, 21600, and 29200 cm^{-1} are MLCT in nature and the transitions at 25800 and 31400 cm^{-1} are intraligand in nature based on comparisons with a Zn^{II} analogue. Several attempts to synthesize the $[Zn(tren)(PSQ)]^{+}$ complex were unsuccessful, but Gallium(III)-semiquinone molecules have been reported.[56] $[Ga(tren)(PSQ)](BPh_4)$ (**12**) or Ga-PSQ was then synthesized to help assign the electronic absorption spectrum. The X-ray crystal structure of the Ga-PCAT precursor, $[Ga(tren)(PCAT)](BPh_4)$ (**11**), is shown in Figure 5-3, but unfortunately single crystals of the semiquinone analogue could not be obtained. The crystallographic data is listed in Table 5-4, and the selected bond distances and angles are also listed in Table 5-5.

Table 5-3. Comparison of electronic absorption transitions in $[Ni(tren)(PSQ)](BPh_4)$ (**1**), $[Ni(CTH)(PSQ)](PF_6)$, $[Ni(tren)(2,7\text{-di-}NO_2\text{-PSQ})](BPh_4)$ (**2**), $[Ni(tren)(2,7\text{-di-}NH_2\text{-PSQ})](BPh_4)$ (**4**), and in the last column the diamagnetic $[Zn(CTH)(PSQ)](BPh_4)$, and $[Ga(tren)(PSQ)](BPh_4)$ (**12**) analogues, where MLCT = metal-to-ligand-charge transfer and IL = intraligand.

Electronic Absorptions (cm^{-1}):		
$[Ni(CTH)(PSQ)](PF_6)$[a,b]	$[Ni(tren)(2,7\text{-di-}NO_2\text{-PSQ})](BPh_4)$[c]	$[Zn(CTH)(PSQ)](ClO_4)$[a,b]
20400 (MLCT)	19800 (MLCT)	19800 (IL)
21600 (MLCT)	21000 (MLCT)	24700 (IL)
25800 (IL)		31000 (IL)
29200 (MLCT)		
31400 (IL)		
$[Ni(tren)(PSQ)](BPh_4)$[c]	$[Ni(tren)(2,7\text{-di-}NH_2\text{-PSQ})](BPh_4)$[c]	$[Ga(tren)(PSQ)](BPh_4)_2$[c]
20000 (MLCT)	19800 (MLCT)	21000 (IL)
21400 (MLCT)	21400 (MLCT)	22400 (IL)
25400 (IL)	23800 (IL)	24100 (IL)
29000 (MLCT)	23800 (sh)	29500 (IL)
31100 (IL)		31800 (IL)
		33200 (IL)

[a] Ref 13. [b] In $CH_3CH_2Cl_2$. [c] In CH_3CN.

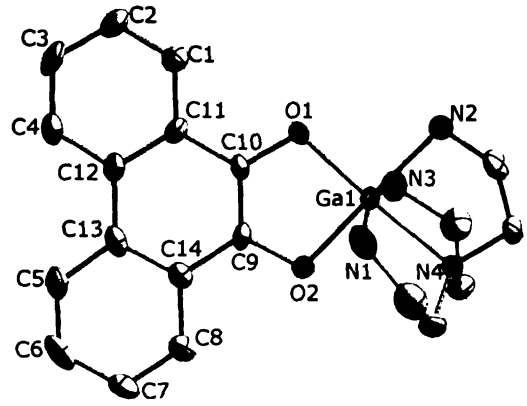

Figure 5-3. X-ray crystal structure of [Ga(tren)(PCAT)](BPh$_4$) (**11**).

The Ga-PCAT Ga–O and Ga–N bond lengths are in the range of the reported values of a similar Ga-catechol complex.[56] The C–O and intradiol (C(10)–C(9)) bond lengths are one diagnostic measure of the oxidation state of the catechol ligand, and based on the X-ray studies of multiple transition metal catechol complexes the distances should be, C–O ≈ 1.35 Å and C(10)–C(9) ≈ 1.39 Å. The Ga C–O = 1.36 Å and C(10)–C(9) = 1.37 Å bond distances agree well with this formalism.

Table 5-4. Crystallographic data for [Ga(tren)(PCAT)](BPh$_4$) (**11**).

[Ga(tren)(PCAT)](BPh$_4$)			
formula	$C_{44}H_{46}BGaN_4O_2$	T/K	173(2)
M_w	743.38	D_c/ g cm^{-3}	1.363
cryst syst	Orthorhombic	θ_{max}	25
space group	Pbca	reflns measured	67369
a/Å	10.194 (2)	independent reflns	6352
b/ Å	17.807 (4)	observed reflns [$I > 2\sigma(I)$]	4098
c/ Å	39.916 (9)	μ(Mo $K\alpha$)/ mm^{-1}	0.8
β/ °	90	R_{int}	0.138
V/ Å^3	7246	R1[a]	0.062
Z	8	wR2[b]	0.164
		GOF	1.07

[a] $R1 = \Sigma||F_O| - |F_C||/ \Sigma|F_O|$. [b] $wR2 = [\Sigma w(F_O^2 - F_C^2)/\Sigma w(F_O^2)^2]^{1/2}$, $w = 1/[\sigma^2(F_O^2) + (aP)^2 + bP]$, where $P = (F_O^2 + 2F_C^2)/3$.

Table 5-5. Selected bond distances and angles for [Ga(tren)(PCAT)](BPh$_4$) (**11**).

Bond Distances (Å)		Bond Angles (deg)	
Ga(1)–O(1)	1.895(3)	O(1)–Ga(1)–N(1)	97.11(14)
Ga(1)–O(2)	1.933(3)	O(1)–Ga(1)–N(2)	92.62(13)
Ga(1)–N(1)	2.193(4)	O(1)–Ga(1)–N(3)	100.78(14)
Ga(1)–N(2)	2.076(4)	O(1)–Ga(1)–N(4)	174.46(13)
Ga(1)–N(3)	2.100(4)	O(1)–Ga(1)–O(2)	88.43(12)
Ga(1)–N(4)	2.108(3)	O(2)–Ga(1)–N(1)	84.47(14)
C(10)–O(1)	1.356(5)	O(2)–Ga(1)–N(2)	175.74(14)
C(9)–O(2)	1.358(5)	O(2)–Ga(1)–N(3)	90.74(14)
C(9)–C(10)	1.369(6)	O(2)–Ga(1)–N(4)	95.93(13)
C(9)–C(14)	1.434(6)	N(1)–Ga(1)–N(2)	91.30(15)
C(14)–C(13)	1.423(6)	N(1)–Ga(1)–N(3)	161.35(15)
C(13)–C(12)	1.442(6)	N(1)–Ga(1)–N(4)	79.96(15)
C(12)–C(11)	1.422(6	N(2)–Ga(1)–N(3)	93.11(15)
C(11)–C(10)	1.438(6)	N(2)–Ga(1)–N(4)	82.80(14)
		N(3)–Ga(1)–N(4)	82.63(14)
		C(9)–O(2)–Ga(1)	106.8(3)
		C(10)–O(1)–Ga(1)	107.4(3)
		O(1)–C(10)–C(9)	119.2(4)

The Ga-PSQ absorptions may be shifted when compared to the Zn^{II}-PSQ due to the different solvent dielectric media of $CH_3CH_2Cl_2$ and CH_3CN. An additional transition at 29000 cm^{-1} can also be assigned as intraligand due to a similar peak seen in the Ga-PSQ spectrum at 29500 cm^{-1} (Table 5-3); Bencini et al. did not report this peak. The transitions at 20000 and 21400 cm^{-1} are then assigned as MLCT bands. Complex **2** has two main features at 19800 and 21000 cm^{-1} and these transitions are assigned as MLCT in nature based upon comparisons with the Ni-PSQ complex. Compound **4** has three main features at 19800, 21400, and 23800 cm^{-1}, with a shoulder at 25200 cm^{-1}. The two transitions at 19800 and 21400 cm^{-1} are assigned as MLCT, and the band at 23800 cm^{-1} is assigned as intraligand in nature based upon comparisons with the Ni-PSQ complex.

Magnetic Susceptibility. The effect of electron exchange on the ground-state configuration of these molecules can be probed by variable temperature magnetic susceptibility measurements. The exchange coupling in these molecules can be described by a simple Heisenberg exchange Hamiltonian, shown in Equation 1,

$$\mathbf{H} = J_{12}\mathbf{S}_1 \cdot \mathbf{S}_2 \qquad (1)$$

where $\mathbf{S}_1$ and $\mathbf{S}_2$ are spin operators on the two spin centers, the Ni^{II} ion and the PSQ radical, and J is the electron exchange integral that gauges the magnitude of the electronic coupling between the two spin centers. Other formalisms of Equation 1 with $-J$, $-2J$, and $2J$ are also encountered in the literature. In the representation of Equation 1, when J is negative a ferromagnetic interaction will occur or if J is positive an antiferromagnetic coupling will operate.

Plots of the effective magnetic moment versus temperature in the range of 5–350 K for solid samples of **1**, **2**, and **4** are shown in Figure 5-4. Complexes **1** and **4** will be discussed first, and the Ni-2,7-di-NO_2-PSQ data will be discussed below. The value of $\mu_{eff} = 3.92 \pm 0.1\ \mu_B$ (μ_B = BM = Bohr Magneton) for **1** and **4** are in excellent agreement with the spin-only value of 3.87 μ_B expected for a $S = {}^3/_2$ ground state and is consistent with ferromagnetic coupling between the Ni^{II} and PSQ unpaired spins. The temperature profile of both complexes is essentially flat from 75-350 K, with a slight decrease in the low temperature range. The experimental data is in agreement with the $\mu_{eff} = 4.11\ \mu_B$ reported for the [Ni(CTH)(PSQ)](PF_6) analogue, and the slight drop at low temperature was tentatively assigned to zero field splitting.[17,31] The lack of temperature dependence in the susceptibility data for **1** and **4** indicate that only an isolated ground quartet state is present, and no population of the doublet state is seen up to 350 K (Figure 5-5) indicating

the $^3/_2$ J >> k_BT. Due to the lack of population in the doublet state, the data in Figure 5-4 could not be fit to extract a *J* value, and this agrees with what Bencini et al.[31] had determined.

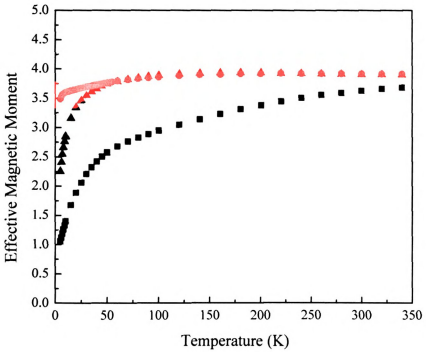

Figure 5-4. Plots of the effective magnetic moment versus temperature for [Ni(tren)(PSQ)](BPh_4) (**1**) (red circles), [Ni(tren)(2,7-di-NO_2-PSQ)](BPh_4) (**2**) (green squares), and [Ni(tren)(2,7-di-NH_2-PSQ)](BPh_4) (**4**) (blue triangles).

Higher temperature SQUID measurements were undertaken to see if increasing the thermal energy of the systems would lead to an observed temperature dependence in the effective magnetic moment. Before these measurements could be taken, thermal gravimetric analysis (TGA) of the samples was needed to determine the decomposition temperature of the complexes. TGA is a simple analytical technique that measures weight loss of a sample as a function of temperature. The resulting TGA plots for all the Ni-PSQ complexes are depicted in Figure 5-6. Complex **1** starts to loose mass at 490 K,

and compounds **2** and **4** loose mass at 510 K. The Ni-PSQ complex was chosen to be the test molecule to examine if increasing the temperature would lead to an observed temperature dependence in the susceptibility.

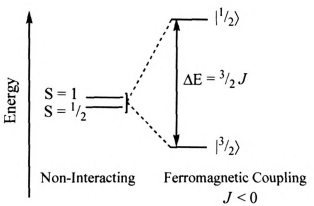

Figure 5-5. The exchange coupling interaction between the Ni^{II} S = 1and PSQ S = $^1/_2$ spins.

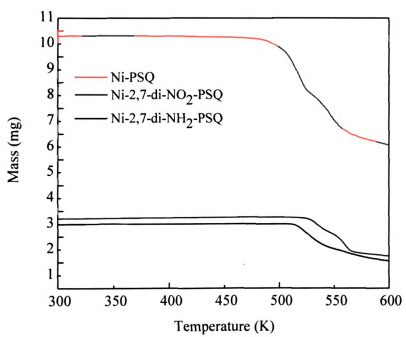

Figure 5-6. TGA plots of [Ni(tren)(PSQ)](BPh_4) (**1**) (red), [Ni(tren)(2,7-di-NO_2-PSQ)](BPh_4) (**2**) (green), and [Ni(tren)(2,7-di-NH_2-PSQ)](BPh_4) (**4**) (blue).

To ensure that the mass of the sample remains unchanged during the high temperature SQUID experiment, the experiment was run from 300-450 K. A high temperature quartz cell had to be fabricated for use in the SQUID oven. The quartz cell had the following dimensions: 3 mm OD, 2 mm ID with 45 mm of open tube to the quartz plug (approx. 5 mm), then an additional 130 mm of open ended tube above the plug. The tube had holes drilled just below the top to allow for attachment to the SQUID sample holder. The plot of the high temperature data for the Ni-PSQ complex is shown in Figure 5-7. The experimental conditions of loading the sample in the high temperature tube left part of the powder on the sides on the tube, and not all the sample was in the sampling region.

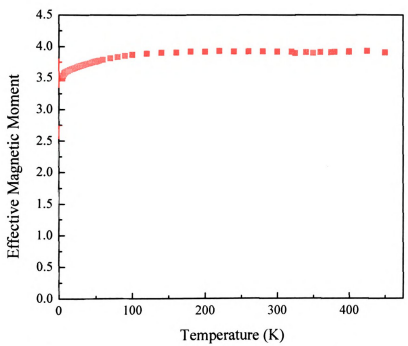

Figure 5-7. Plot of effective magnetic moment versus temperature for a high temperature (300-450 K) SQUID experiment of [Ni(tren)(PSQ)](BPh$_4$) (**1**). The low temperature data (5-350 K) was done under normal conditions.

Since all the powder was not in the sampling area, decreased magnetization was observed compared to the data run under normal conditions. The decreased magnetization was

accounted for by normalizing the high temperature data to the data collected under normal conditions. The normalization was achieved by decreasing the measured mass of 0.0108 g to 0.00978 g used in the calculation of the effective magnetic moment to account for the loss of the sample on the sides of the tube. The high temperature experiment shows that only the quartet state is populated up to 450 K, with no population of the doublet state (Figure 5-5). The thermal energy available at 450 K is approx. 320 cm^{-1}, and since no population of the doublet state could be detected at this temperature, the energy gap must be larger than 320 cm^{-1}. The high temperature experiments agree with Bencini et al. and the *J* value is too strong to be determined, and Bencini et al. was able set a lower limit of 400 cm^{-1} to the true value of *J*.[17,31] DFT calculations may reveal additional information to explain the large exchange coupling constants in these molecules (vide infra).

Interestingly, the susceptibility data for complex **2** has a maximum value of μ_{eff} = 3.67 μ_B at 350 K, and the overall temperature profile displays decreased effective magnetic moment values compared to complexes **1** and **4**. This anomalous data has not been observed in any other Ni^{II}-semiquinone complex reported in the literature, and could possibly be explained by strong intermolecular interactions in the solid compound. In order to determine if intermolecular interactions are present, the crystal packing diagram showing the ligand stacking is depicted in Figure 5-8. It is evident that there is strong π-stacking between the 2,7-di-NO_2-PSQ rings, with the shortest center-to-center distance equal to 3.57 Å. This π-stacking between the 2,7-di-NO_2-PSQ rings can lead to an antiferromagnetic interaction between the S = $^1/_2$ radicals, which would yield decreased effective magnetic moments across the entire temperature range. The packing diagram of

complex **1** is shown in Figure 5-9 for comparison purposes, where the shortest center-to-center distance is 6.28 Å.

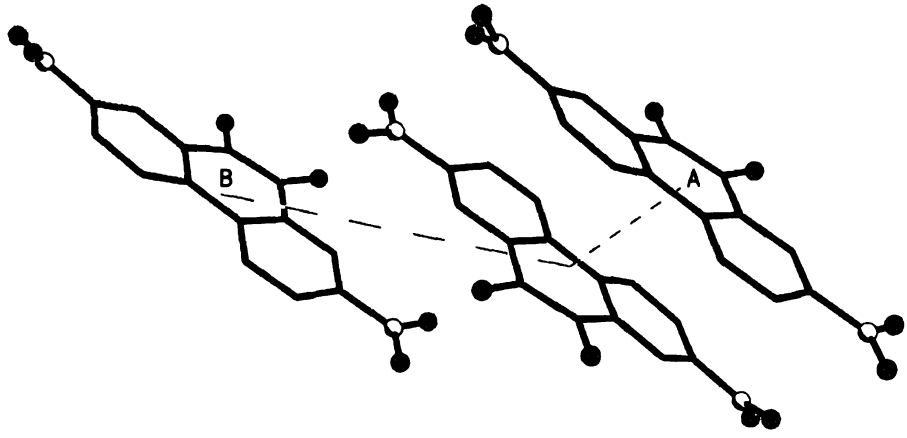

labels	Symmetry	Plane-to-plane Angle (degree)	Center-to-center distances (Å)	Shortest atom-to-atom distances (Å)
A	-x, 4-y, 1-z	0	3.57	3.30 (C7...C13A)
B	-1-x, 4-y, 1-z	0	8.20	3.67 (C3...C4B)

Figure 5-8. The packing diagram for [Ni(tren)(2,7-di-NO_2-PSQ)](BPh_4) (**2**).

Although the center-to-center distance is longer in **1** compared to **2** weaker intermolecular interactions in **1** can not be ruled out in the low temperature data. It is highly likely then that an intermolecular π-stacking antiferromagnetic interaction between the 2,7-di-NO_2-PSQ radicals is responsible for the observed lower effective magnetic moment of **2**. In order to prove this experimentally, Evans NMR and liquid phase SQUID experiments will be undertaken. A liquid phase experiment is necessary to experimentally show that there are no intermolecular interactions, since in solution a completely random and dilute orientation of the complex will occur that should significantly reduce π-π interactions.

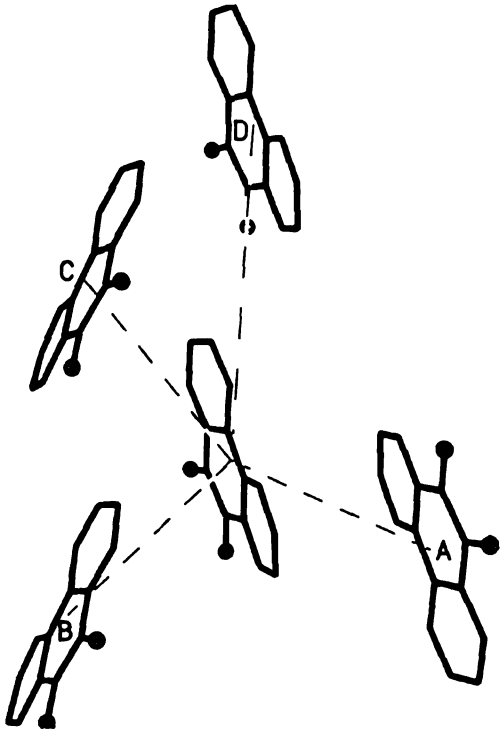

labels	Symmetry	Plane-to-plane Angle (degree)	Center-to-center distances (Å)	Shortest atom-to-atom distances (Å)
A	1-x, 1-y, -z	0	6.69	3.39 (C5...C6A)
B	1-x, -0.5+y, 0.5-z	32.4	6.28	3.57 (C10...C14B)
C	1-x, 0.5+y, 0.5-z	32.4	6.28	3.48 (C11...C7C)
D	X, 1+y, z	0	9.14	3.57 (C12...C20D)

Figure 5-9. Packing diagram for the [Ni(tren)(PSQ)](BPh_4) (**1**) complex.

Solution susceptibility measurements have been done since 1959 by the Evans NMR method.[57] The Evans method uses the measured difference in the chemical shift of a signal from a reference material in the absence and presence of a paramagnetic solute. The simplest way to accomplish this is by placing a spiked solution of the paramagnetic material with a standard in a sealed melting point tube inside of an NMR tube.[47] The susceptibility can then be measured by the following equation:[58]

$$\chi = \frac{\delta\nu}{\nu_0 S_f [C]} \qquad (2)$$

where, χ is the mass susceptibility (ml/g) of the dissolved substance, $\delta\upsilon$ is the shift in frequency (Hz) from the value found for the pure solvent, [C] is the concentration of the solute (g/ml), S_f is the shape factor of the magnet ($4\pi/3$ for a superconducting magnet), and υ_0 is the operating frequency of the NMR spectrometer. The results of the variable temperature Evans NMR experiment for **2** are plotted in Figure 5-10.

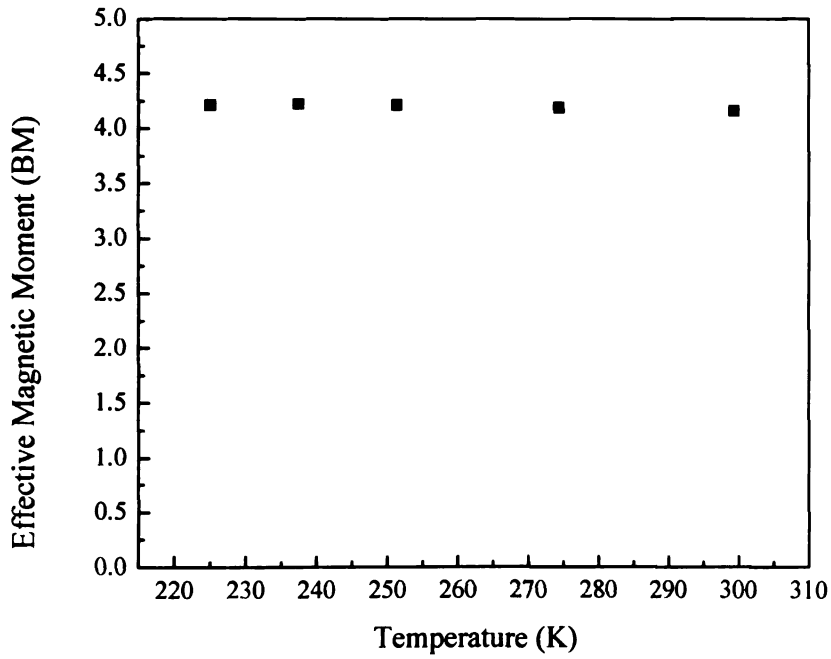

Figure 5-10. Variable temperature Evans NMR of [Ni(tren)(2,7-di-NO_2-PSQ)](BPh_4) (**2**) in d_7 DMF. The experimental was conducted using a 500 MHz NMR spectrometer with 2 % *t*-butanol used as the reference solvent.

The $\mu_{eff} = 4.2 \pm 0.1\ \mu_B$ observed across the 225-300 K temperature range is in agreement with the previous measurements form Bencini et al. for Ni-SQ's and the solid powder SQUID measurements for complexes **1** and **4**. Although the experiment was limited by the freezing point of the NMR solvent, the data do indicate that intermolecular interactions are responsible for the lower effective magnetic moment observed for the 225-300 K temperature range. It can be hypothesized that the lower temperature regime

also has a decreased effective magnetic moment due to intermolecular interactions. A full temperature range from 5-350 K in solution is needed to experimentally prove this, so liquid phase SQUID experiments were attempted.

Liquid phase SQUID experiments have been done previously by Hendrickson and coworkers in valence tautomeric cobalt-quinone complexes; the quartz sample holder used in our experiments was based on their designs.[48,49] Hendrickson and coworkers used toluene-d_8 to dissolve their sample to a concentration of approximately 1.0×10^{-3} M, and operated at a 1.0 T magnetic field over a temperature range of 2-400 K. Several attempts at using the paramagnetic copper standard tetramethylethylenediammonium tetrachlorocuprate(II),[59] $[(CH_3)_2NHCH_2CH_2NH(CH_3)_2]CuCl_4$, for susceptibility measurements at 1.0×10^{-3} M and either 1.0 T or 5.5 T gave very poor results in CD_3CN, CH_3CN, H_2O, and D_2O. Increasing the concentration of the sample gave somewhat better results. To determine the proper concentration of samples appropriate for our laboratory fabricated quartz cell, a concentration study was then done with $Cu(NO_3)_2 \cdot 3H_2O$ due its high solubility in water. The experiments were also run at 5.5 T to get an increased signal response, since the magnetization (M) is directly proportional to the magnetic field (B) multiplied by the magnetic susceptibility (χ), i.e. $M = \chi B$. The results of the concentration study with $Cu(NO_3)_2 \cdot 3H_2O$ are shown in Figure 5-11. The literature reported effective magnetic moment for $Cu(NO_3)_2 \cdot 3H_2O$ is $\mu_{eff} = 1.94\ \mu_B$ at 300 K.[60] The data in Figure 5-11 clearly show for the 1.0 M, 2.0 M, and 4.0 M concentrations the effective magnetic moment deviates to a higher value. For the 5.6 M water solution, $\mu_{eff} = 1.97\ \mu_B$ at 300 K and matches the known experimental data quite nicely. The less concentrated solutions show the greatest deviations from the known

experimental values, and this could be due to dominating background signal from the quartz cell. Thus for this particular experimental setup to work, the highest concentration possible must be used to observe good data. Complex **1** will be the first to be examined in liquid phase.

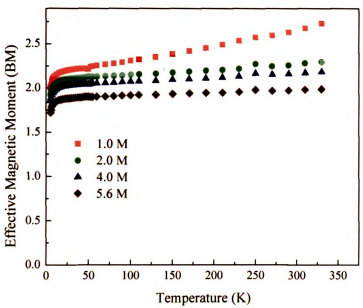

Figure 5-11. Liquid phase SQUID susceptibility of $Cu(NO_3)_2 \cdot 3H_2O$ in water at 5.5 T, at 1.0 M (red square), 2.0 M (green circle), 4.0 M (blue triangle), and 5.6 M (brown diamond) concentrations.

The plot of the effective magnetic moment for **1** in DMF is depicted in Figure 5-12. The experimental conditions for loading the liquid SQUID sample left some solution on the sides of the tube, and again the data had sub-normal moments as a result. To correct this problem we applied the same normalization condition that was used for the high temperature data by subtracting mass from the sample (0.0062 g), and the corrected data are shown in Figure 5-12. The data agrees with the high temperature side quite well and asymptotes to 3.9 μ_B, and an additional drop is observed in the low temperature regime. The drop starting at 40 K can be assigned to zero field splitting in the Ni-PSQ

complex, since intermolecular interactions should not be operative in solution. However, to inconclusively determine the magnitude of the zero field splitting present in the low temperature data high field EPR experiments will be required (vide infra). The zero field splitting energy diagram can be seen in Figure 5-13.

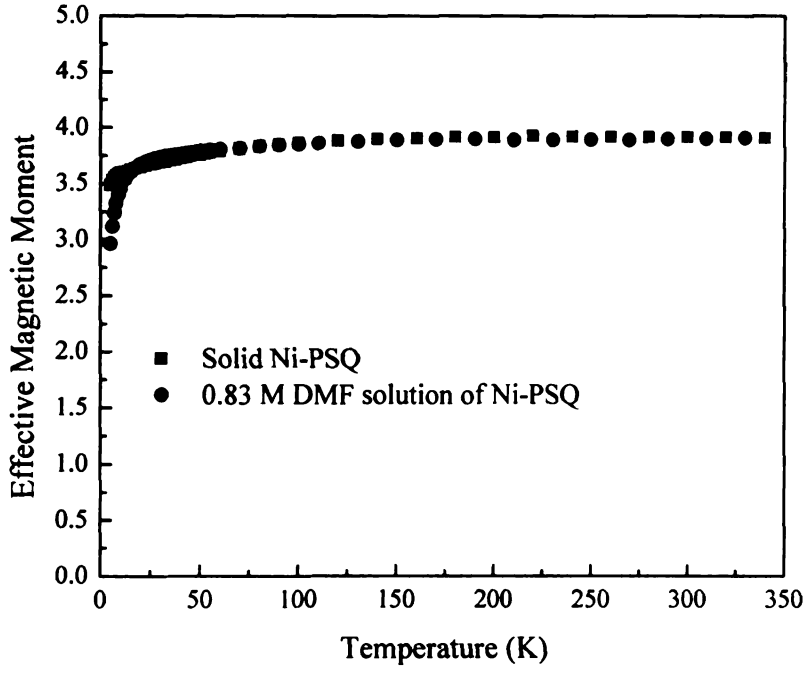

Figure 5-12. The 0.83 M DMF solution of **1** (blue circles), and the solid state data (red square) is also shown for comparison.

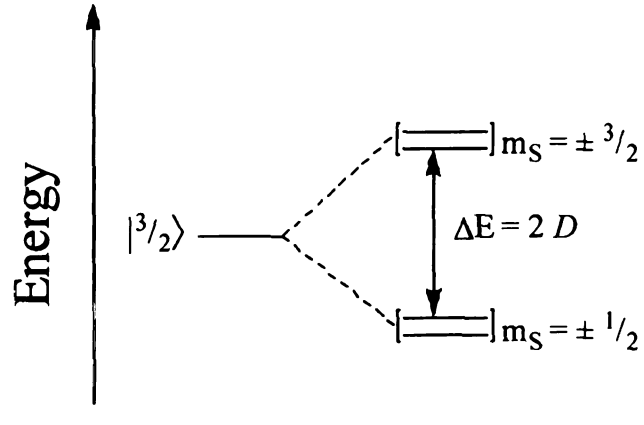

Figure 5-13. The energy splitting caused by zero field splitting for an S = $^3/_2$ ground state.

Zero field splitting is one possible mechanism that lifts the ground state degeneracy and results in the splitting of the $S = {}^3/_2$ into the $m_S = \pm {}^3/_2$ and $\pm {}^1/_2$ states as depicted in Figure 5-13. The contribution from zero field splitting to lift the degeneracy of the $S = {}^3/_2$ ground state of **1** is a symmetry effect. This state is 4-fold degenerate (2S +1) and the symmetry of the complex can be approximated by the C_{2v} point group which can only support 1-fold degeneracy, thus the ground state must split according to symmetry rules. The data indicate that there is population of the $m_S = \pm {}^1/_2$ states at low temperature, since $\mu_{eff} = 2.96$ at 5 K and this value reflects contributions from the partially filled $S = {}^1/_2$ ($\mu_{eff} = 1.73\ \mu_B$) and $S = {}^3/_2$ ($\mu_{eff} = 3.87\ \mu_B$) states. Then as the thermal energy increases to 40 K, the population is localized in the $S = {}^3/_2$ state and the data asymptote to $\mu_{eff} = 3.9\ \mu_B$. The reason for the larger dip in the low temperature data for the Ni-PSQ liquid phase data could be due to weak ferromagnetic intermolecular interactions in the solid state, which is not observed in solution. The interactions would be weak, since the packing diagram in Figure 5-9 indicates long center-to-center distances between the PSQ rings. Thus, the liquid phase data for complex **1** has experimentally indicated that the drop below 40 K is due to ZFS, and weak ferromagnetic interactions are likely in the solid state.

Several attempts at collecting liquid phase data on [N(tren)(2,7-di-NO_2-PSQ)](BPh_4) (Complex 2) were unsuccessful due to solubility problems in all laboratory available solvents examined. The [Ni(tren)(2,7-di-NO_2-PSQ)](BAr^f) (**3**) complex, where BAr^f is the tetrakis{3,5-bis-(trifluoromethyl)phenyl}borate anion, was synthesized to help increase the solubility, since salts with the BAr^f counterion are well known to increase solubility in organic solvents.[41] Increased solubility was observed in lower

dielectric constant solvents such as dichloromethane, but no large improvement in the solubility of **3** in DMF was observed. Solution SQUID data for **3** was then collected in dichloromethane and the results are depicted in Figure 5-14. The solution phase data depict an overall elevated effective magnetic moment compared to the solid sample, which is consistent with intermolecular interactions in the solid state suppressing the effective magnetic moment. The dip in the low temperature side of the data at 25 K can be assigned to zero field splitting, and at higher temperatures the data displays a positive slope from 50 – 280 K. The positive slope in the solution data implies that the concentration of the sample is not high enough, since the $Cu(NO_3)_2{\cdot}3H_2O$ standard also displays a positive slope in less concentrated samples. Overall, the solution phase SQUID and the Evans NMR data support that intermolecular interactions are responsible for the unique solid state magnetic data for the Ni-2,7-di-NO_2-PSQ complex.

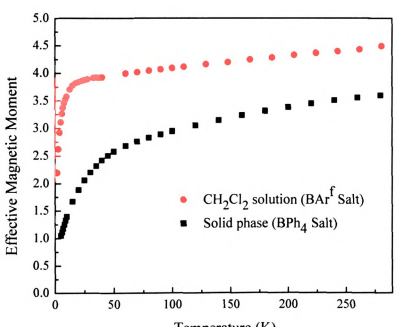

Figure 5-14. SQUID susceptibility of a 0.41 M dichloromethane solution of [Ni(tren)(2,7-di-NO_2-PSQ)](BAr^f) (**3**) (red circles) compared with the solid BPh_4 (**2**) salt (green squares).

The above data does indicate that the exchange coupling between the PSQ radicals and the Ni(II) center is strong and ferromagnetic, but unfortunately the *J* values could not be experimentally determined. As discussed in Chapter 3, the spin density at the oxygen atoms was found to differentially polarize at the oxygen atoms for the NO_2 and NH_2 substituents, and it was hypothesized that the *J* value should be modulated by the changes in spin at oxygen. The experimental results disagree with the free ligand spin density hypothesis, and this it is not too surprising since in Chapter 4 it was found that the spin density distribution shifts upon binding to a metal center. In an attempt to explain the deviations, broken symmetry DFT calculations will be used to calculate the *J* values and the electronic structures of the Ni-PSQ, Ni-2,7-di-NH_2-PSQ, and the Ni-2,7-di-NO_2-PSQ complexes.

Density Functional Theory. The singly occupied orbitals (SOMOs), corresponding to the unpaired electrons in the Ni-PSQ cation, have been computed with the UB3LYP functional and are shown pictorially in Figure 5-15 for the quartet state. Only the Ni-PSQ complex's orbitals are shown, since the orbitals of Ni-2,7-di-NH_2-PSQ and Ni-2,7-di-NO_2-PSQ are qualitatively similar. The orbital descriptions are in agreement with what has been found by Bencini et al. for $[Ni(CTH)(PSQ)]^+$. The PSQ radical SOMO is α-110 and it is delocalized over the PSQ ring with a large contribution from the C–O π^* molecular orbital, and this orbital is weakly interacting with the 3d Ni^{II}-d_{xz} orbital. The α-108 (d_z^2-like) and α-109 ($d_{x^2-y^2}$ like) orbitals are the two σ^*-type orbitals of Ni^{II} that interact with the oxygen atoms of the PSQ. The observed ferromagnetism in the temperature dependent SQUID measurements for **1**, **2**, and **4** can be qualitatively explained by examining the magnetic orbitals in Figure 5-14. The Ni-

PSQ complexes have C_{2v} symmetry and the α-108 and α-109 orbitals transform as the a_1 irreducible representation and the α-110 orbital spans b_1, and an overall ferromagnetic interaction will then operate due to the orthogonality of the magnetic orbitals.

α–110

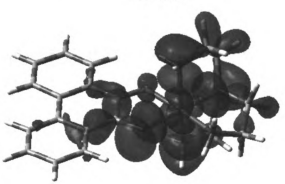

α–108

α–106

Figure 5-15. Magnetic orbitals for the $[Ni(tren)(PSQ)]^+$ complex.

One of the most theoretically sound DFT approaches to calculate the exchange coupling constant is the approximate spin projection method of Yamaguchi.[61-63] The

equation used is shown in Equation 3 below, and the derivation has been reported by Rodriguez and McCusker.[64]

$$J_{12} = 2\frac{E(HS) - E(BS)}{\langle S^2 \rangle_{HS} - \langle S^2 \rangle_{BS}} \quad (3)$$

where E(HS) is the energy of the high spin (HS) state, E(BS) is the energy of the low spin or broken symmetry (BS) state, $\langle S^2 \rangle_{HS}$ and $\langle S^2 \rangle_{BS}$ are the spin expectation values of the HS state and BS state, respectively. The broken symmetry state is a single determinant wavefunction of the type,[28,65,66]

$$|BS\rangle = |\tau_a \bar{\tau}_b| \quad (4)$$

where τ_a and $\bar{\tau}_b$ are the BS spin-orbitals that are essentially localized on sites a and b. In the case of the Ni-PSQ complexes, we then expect a net β-spin density on the oxygen atoms of the PSQ radical and a net α-spin density on the Ni^{II} center of the antiferromagnetic or BS doublet state. As for the HS state we expect net α-spin density at both the Ni^{II} and PSQ radical centers. The spin density distributions in the Ni-2,7-di-R-PSQ complexes are listed in Table 5-6, and the α and β spin densities match what is predicted for both the HS wavefunction and the BS state. The spin density at the Ni^{II} center is essentially identical in all three substituted Ni-2,7-di-R-PSQ's, and the largest localization of spin density on the PSQ rings is found at the oxygen atoms. The results of the calculations of the exchange coupling constants at the B3LYP/6-311g** level are shown in Table 5-7. The average Ni–O DFT bond lengths are within 0.02 Å of the X-ray values, indicating that DFT accurately models the distance between the magnetic centers. The calculation of the *J* values in Equation 3 were done with $\langle S^2 \rangle_{HS} = 3.75$, since the unrestricted Kohn-Sham wave functions for the quartet state are nearly pure (i.e. $\langle S^2 \rangle_{HS} =$

S(S + 1)). The $\langle S^2 \rangle_2$ indicates considerable spin contamination of the broken symmetry state, and $\langle S^2 \rangle_2 = 1.76$ implies nearly a linear combination of a quartet and doublet state.

Table 5-6. The NPA UB3LYP/6-311g** spin density distribution in the Ni-2,7-di-R-PSQ complexes, where the spin density was summed for all atoms in the fragment.

Spin Density Quartet:				
	Ni	**Oxygen (avg)**	**PSQ**	**tren**
$[Ni(tren)(PSQ)]^+$	1.68176	0.25357	0.59828	0.2128
$[Ni(tren)(2,7\text{-di-}NO_2\text{-}PSQ)]^+$	1.68537	0.26344	0.56411	0.22362
$[Ni(tren)(2,7\text{-di-}NH_2\text{-}PSQ)]^+$	1.68005	0.25259	0.60654	0.20827
Spin Density Doublet:				
$[Ni(tren)(PSQ)]^+$	1.67995	-0.13841	-0.60655	0.20338
$[Ni(tren)(2,7\text{-di-}NO_2\text{-}PSQ)]^+$	1.6819	-0.16135	-0.57265	0.21344
$[Ni(tren)(2,7\text{-di-}NH_2\text{-}PSQ)]^+$	1.6788	-0.1316	-0.61447	0.19892

Table 5-7. DFT calculations of *J* at the UB3LYP/6-311g** level for the Ni-2,7-di-R-PSQ complexes (using Equation 3), and the corresponding spin densities at the Ni and O atoms in the quartet state.

Complex	**ρ (Ni)**	**ρ (O)**[a]	$\langle S^2 \rangle_2$	$\langle S^2 \rangle_4$	**Ni-O (Å)**[b]	***J* (cm^{-1})**
$[Ni(tren)(PSQ)]^+$	1.682	0.254	1.76	3.76	2.068	**-258**
$[Ni(tren)(2,7\text{-di-}NH_2\text{-}PSQ)]^+$	1.680	0.253	1.76	3.76	2.059	**-258**
$[Ni(tren)(2,7\text{-di-}NO_2\text{-}PSQ)]^+$	1.685	0.263	1.76	3.76	2.088	**-268**

[a] Average spin density at oxygen. [b] Average Ni–O bond length (within 0.02 Å of the X-ray values).

The assumption of admixture observed in the BS state calculations agrees with previous reports in Ni^{II} and Cr^{III}-semiquinone complexes.[31,32] Accordingly, we can write

$$\Phi_2 \approx C_2\Phi_2 + C_4\Phi_4 \qquad (5)$$

And then we apply the normalization condition that follows from Equation 5.

$$C_2^2 + C_4^2 = 1 \tag{6}$$

The spin expectation values for the contaminated state $\langle S^2 \rangle_{mix}$, the doublet state in this case, can be calculated by Equation 7.

$$\left\langle \mathbf{S}^2 \right\rangle_{mix} \approx C_2^2 S_2(S_2+1) + C_4^2 S_4(S_4+1) \tag{7}$$

Using Equations 6 and 7 the coefficients can be determined

$$C_2^2 = \frac{\left\langle \mathbf{S}^2 \right\rangle_2 - S_4(S_4+1)}{S_2(S_2+1) - S_4(S_4+1)} \tag{8}$$

$$C_4^2 = \frac{S_2(S_2+1) - \left\langle \mathbf{S}^2 \right\rangle_2}{S_2(S_2+1) - S_4(S_4+1)} \tag{9}$$

For a perfect admixture of quartet and doublet spin states the spin expectation value is $\langle S^2 \rangle_{mix} = 1.75$, which indicates the calculated antiferromagnetic state ($\langle S^2 \rangle_2 = 1.76$) for the Ni-PSQ's is a mixture of quartet and doublet states.

The calculated J value for the Ni-PSQ complex is in good agreement with the calculated value of -285 cm^{-1} for the [Ni(CTH)(PSQ)](PF$_6$) complex.[31] The calculated J values for Ni-PSQ and Ni-2,7-di-NH$_2$-PSQ are identical, and there is a slight increase of 10 cm^{-1} in the coupling constant of the Ni-2,7-di-NO$_2$-PSQ complex. The strength of the ferromagnetic interaction between two centers is given by the magnitude of the exchange integral between the magnetic orbitals, or it can be described as the self repulsion of the overlap density $\rho(i)$, where J is proportional to the two electron exchange integral K.[16,67]

$$\rho(i) = \Phi_{Ni}(i)\Phi_{PSQ}(i) \tag{10}$$

$$J_{ij} = K = 2\iint_{space} \frac{\rho(i)\rho(j)}{r_{ij}} d\tau(i) d\tau(j) \qquad (11)$$

Since the spin density is the square of the square of the SOMO wavefunction, and the product of the spin densities is proportional to the overlap integral of the natural orbitals, and therefore to J,[12,68]

$$J_{M-SQ} \approx \rho_M \rho_{SQ} \qquad (12)$$

where ρ_M and ρ_{SQ} are the spin densities on the metal and semiquinone radical, respectively. As long as the spin densities are a contributing factor to the J value the approximation in Equation 12 should hold. The calculated spin densities at the Ni^{II} centers are nearly equivalent, and we have hypothesized that the other variable responsible for the changes in the magnitude of J is the spin density at oxygen. There is an observed correlation (a small change) with the spin density at oxygen and the coupling constant, and if the spin density is increased the J value increases. The other observable in Table 5-7 is that if the spin density at oxygen stays the same, then the magnitude of J remains unchanged. The observed changes agree with Equation 12, even though the observed differences are small. The calculations of the free ligands indicated more spin delocalization than was seen in the metal complexes. Upon examination of the α-SOMOs in Figure 5-15 and the spin density distributions in Figure 5-16, there is no excess α-spin density at the 2,7-carbon atoms. The lack of spin density at the 2,7-carbon atoms is the likely reason responsible for the small observed changes in J, since no spin density can be delocalized to the substituent atoms. Another observation in Figure 5-16 is that there is net α-spin density at the 3,6-carbon atoms. Possibly placing the substituents there would increase spin delocalization and reduce the J value.

Figure 5-16. The UB3LYP/6-311g** spin density plots for the $[Ni(tren)(2,7\text{-di-}NO_2\text{-PSQ})]^+$, $[Ni(tren)(2,7\text{-di-}NH_2\text{-PSQ})]^+$, and $Ni(tren)(PSQ)]^+$ complexes.

The 3,6-di-NO_2-PQ ligand (from which the 3,6-di-R-PCAT ligands are made) can be synthesized, but its preparation is much more intensive compared to the 2,7-di-NO_2-PQ ligand. Before the preparation of the complexes, we decided to run DFT calculations at the same level of theory on $[Ni(tren)(3,6\text{-di-}NO_2\text{-PSQ})]^+$ (Ni-3,6-di-NO_2-PSQ) and $[Ni(tren)(3,6\text{-di-}NH_2\text{-PSQ})]^+$ (Ni-3,6-di-NH_2-PSQ) to see if there were any noticeable changes in the spin density and/or *J*. The results of the UB3LYP/6-311g** calculations using Equation 3 are shown in Table 5-8, and the most striking result (golden row) is that the *J* value for the Ni-3,6-di-NH_2-PSQ complex is approximately 50 cm^{-1} less than the Ni-PSQ complex. Upon examination of the spin densities at the Ni^{II} center, they were found to be almost identical as was seen in the Ni-2,7-di-R-PSQ complexes. The average spin density at oxygen for Ni-3,6-di-NH_2-PSQ does show a larger decrease compared to the 2,7-isomer (Table 5-3), and as a result the magnitude of the *J* value is also reduced. Interestingly, the Ni-3,6-di-NO_2-PSQ isomer has nearly the exact calculated *J* value as the 2,7-cation and the spin densities at oxygen are almost identical.

Table 5-8. DFT calculations at the UB3LYP/6-311g** level for exchange coupling constants of the Ni-3,6-R-PSQ complexes and the spin densities (ρ) at Ni and O in the quartet state.

Complex	ρ (Ni)	ρ (O)[a]	$\langle S^2 \rangle_2$	$\langle S^2 \rangle_4$	Ni-O (Å)[b]	J (cm^{-1})[c]
$[Ni(tren)(PSQ)]^+$	1.682	0.254	1.76	3.76	2.068	**-258**
$[Ni(tren)(3,6\text{-di-}NH_2\text{-PSQ})]^+$	1.680	0.220	1.76	3.76	2.057	**-210**
$[Ni(tren)(3,6\text{-di-}NO_2\text{-PSQ})]^+$	1.685	0.261	1.76	3.76	2.085	**-267**

[a] Average spin density at oxygen. [b] The average Ni–O bond length is within 0.005 Å of the X-ray data, indicating an accurate model of the distances between the magnetic centers. [c] Calculated using Equation 3.

The DFT calculated J values and spin densities support the proportionality in Equation 12, and in these systems the spin density at oxygen seems to be modulating the J value. An additional factor that could have an effect on the J value is the bond distance between the two centers. Intuitively one would guess that the shorter the distance between the spins, the stronger the exchange coupling. Table 5-3 also lists the average bond distances for the complexes, and it can be seen that even though the bond length is shortened Ni-3,6-di-NH_2-PSQ compared to the Ni-PSQ the J value is decreased. The opposite trend is seen for the Ni-3,6-di-NO_2-PSQ complex, and J increases despite the Ni–O bond distance elongating. The combined structural evidence also supports the observation that the spin density at oxygen is a major variable modulating the J value. The spin density distribution in the Ni-3,6-di-NO_2-PSQ complexes is depicted in Figure 5-17, and it can be seen that the spin density is delocalized onto the substituents groups. As a consequence of this the spin density is more delocalized away from the oxygen atoms in the complexes. Interestingly, even though spin is delocalized onto the oxygen atoms of the NO_2 group in the Ni-3,6-di-NO_2-PSQ complex, there is a small net increase in spin

population at the PSQ oxygen atoms. Strong electron withdrawing substituents have been shown to be destabilizing in radical systems due to their σ-withdrawing character,[69,70] and this is one possibility for the predicted increase in spin density at oxygen.

Figure 5-17. The UB3LYP/6-311g** spin density plots for the $[Ni(tren)(3,6\text{-di-}NO_2\text{-PSQ})]^+$, $[Ni(tren)(3,6\text{-di-}NH_2\text{-PSQ})]^+$, and $Ni(tren)(PSQ)]^+$ complexes.

A larger set of substituents will need to be examined to determine if the withdrawing ability plays a role in destabilizing the radical (vide infra). Previous literature examinations have shown that the *J* value has been correlated with the spin density at a transition metal center in metal cluster compounds.[71-73] To our knowledge, this is the first instance of correlating the calculated spin density in a series of transition metal organic radicals with the *J* value. In order to prove the DFT results, the $[Ni(tren)(3,6\text{-di-}NO_2\text{-PSQ})](BPh_4)$ and $[Ni(tren)(3,6\text{-di-}NH_2\text{-PSQ})](BPh_4)$ complexes will be prepared and analyzed by SQUID magnetometry.

5.3.2 Synthesis and Characterization of $[Ni(tren)(3,6\text{-di-R-PSQ})](BPh_4)$ Complexes

Synthesis of $[Ni(tren)(3,6\text{-di-R-PSQ})](BPh_4)$ complexes. The synthesis of the 3,6-di-NO_2-PSQ ligand involved the photochemical reaction of 9,10-phenanthrenequinone with SO_2 (g) to make the PCAT-cyclic sulfate complex, followed

by its nitration, and subsequent pyrolysis to remove SO_2 (g).[74] The yield of the overall reaction from PCAT-SO_2 to the 3,6-di-NO_2-PQ was ≈ 33 %, which is lower than the 45 % yield for the 2,7-di-NO_2-PSQ isomer. The total reaction time and workup was also 3-4 days longer (mostly due to the PCAT-SO_2 synthesis time) to prepare the 3,6-di-NO_2-PQ compared to the 1 day prep of the 2,7-di-NO_2-PQ. Once the 3,6-di-NO_2-PQ ligand was in hand, the same synthetic procedures for the 2,7-di-R-PCAT and Ni-2,7-di-R-PSQ complexes were utilized to make the corresponding 3,6-di-R-PCAT ligands and the metal complexes in reasonable yields. Solutions of the complexes were found to be very air sensitive, especially the Ni-3,6-di-NH_2-PSQ complex, and the Ni^{II} complexes were stored under inert atmosphere to circumvent any decomposition.

Ground State Characterization: X-ray Crystallography. The Ni-3,6-di-R-PSQ complexes are isostructural with the Ni-2,7-di-R-PSQ analogues, and ORTEP drawings of the $[Ni(tren)(3,6\text{-di-}NO_2\text{-PSQ})]^+$ (**5**) and $[Ni(tren)(3,6\text{-di-}NH_2\text{-PSQ})]^+$ (**6**) compounds are depicted in Figure 5-18. Selected bond distances and angles are listed in Table 5-9 and the crystallographic data is listed in Table 5-10

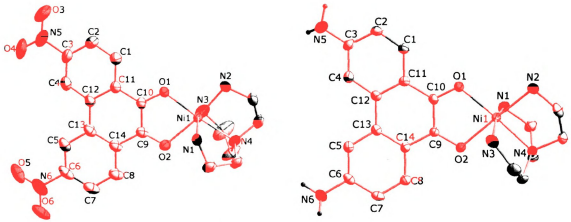

Figure 5-18. Drawings of the cations of $[Ni(tren)(3,6\text{-di-}NO_2\text{-PSQ})]^+$ (**5**) (left) and $[Ni(tren)(3,6\text{-di-}NH_2\text{-PSQ})]^+$ (**6**) (right) cations obtained from single crystal X-ray structure determinations. Atoms are represented as 50 % probability thermal ellipsoids.

Table 5-9. Selected bond distances and angles for [Ni(tren)(3,6-di-NO_2-PSQ)](BPh_4) (**5**) and [Ni(tren)(3,6-di-NH_2-PSQ)](BPh_4) (**6**).

	5	**6**
	Bond Distances (Å)	
Ni(1)–O(1)	2.0352(15)	2.0372(16)
Ni(1)–O(2)	2.1357(16)	2.0877(16)
Ni(1)–N(1)	2.1093(18)	2.105(2)
Ni(1)-N(2)	2.0634(19)	2.097(2)
Ni(1)–N(3)	2.122(2)	2.145(2)
Ni(1)–N(4)	2.0993(18)	2.074(2)
C(10)–O(1)	1.270(3)	1.287(3)
C(9)–O(2)	1.263(3)	1.285(3)
C(9)–C(10)	1.451(3)	1.441(3)
C(9)–C(14)	1.455(3)	1.451(3)
C(14)–C(13)	1.413(3)	1.415(3)
C(13)–C(12)	1.461(4)	1.465(3)
C(12)–C(11)	1.417(3)	1.420(3)
C(11)–C(10)	1.449(3)	1.446(3)
	Bond Angles (deg)	
O(1)–Ni(1)–N(1)	101.86(7)	94.61(8)
O(1)–Ni(1)–N(2)	92.97(7)	100.69(7)
O(1)–Ni(1)–N(3)	94.77(7)	98.31(8)
O(1)–Ni(1)–N(4)	175.04(7)	175.45(8)
O(1)–Ni(1)–O(2)	79.24(6)	81.10(6)
O(2)–Ni(1)–N(1)	84.19(7)	87.14(8)
O(2)–Ni(1)–N(2)	172.16(7)	178.13(8)
O(2)–Ni(1)–N(3)	83.57(8)	84.74(8)
O(2)–Ni(1)–N(4)	103.94(7)	94.62(7)
N(1)–Ni(1)–N(2)	96.73(8)	93.23(9)
N(1)–Ni(1)–N(3)	157.09(8)	163.48(8)
N(1)–Ni(1)–N(4)	82.35(7)	83.57(8)
N(2)–Ni(1)–N(3)	98.03(9)	94.44(9)
N(2)–Ni(1)–N(4)	83.90(8)	83.60(8)
N(3)–Ni(1)–N(4)	81.91(8)	82.77(8)
C(9)–O(2)–Ni(1)	110.16(14)	109.67(14)
C(10)–O(1)–Ni(1)	113.31(14)	111.29(14)
O(1)–C(10)–C(9)	118.4(2)	118.6(2)

The C–O_{avg} = 1.29 Å and C(10)–C(9)) = 1.45 Å for **6** and C–O_{avg} = 1.27 Å and C(10)–C(9)) = 1.44 Å for **5** agree well with the ranges reported in the literature for

semiquinone ligands. Another structural feature of the semiquinone form of the ligand is the bond lengths in the carbon ring. Specifically, the semiquinone should exhibit alternating short and long C–C bond distances because of the more localized nature of the double bonds in the rings, and this is clearly seen for the Ni-3,6-R-PSQ complexes depicted in Table 5-10.[75-77] The axial Ni–N distances are significantly longer than the equatorial Ni–N bonds in each complex analogous to what was found for [Ni(CTH)(PSQ)](PF$_6$), indicating an elongated octahedron-type geometry.[31] Additionally, the Ni–O and Ni–N bond lengths are in agreement with the Ni-2,7-di-R-PSQ complexes and similar Ni-SQ compounds in the literature.[17,31]

Table 5-10. Crystallographic data for **5** and **6**.

	5	**6**
formula	$C_{45}H_{47}BN_6NiO_{6.50}$	$C_{45}H_{52}BN_6NiO_3$
M_w	845.41	794.45
cryst syst	Triclinic	Orthorhombic
space group	*P*-1	*Pna*2(1)
a/Å	10.26900 (10)	18.434 (2)
b/ Å	19.8542 (3)	10.3031 (13)
c/ Å	20.1780 (3)	20.582 (3)
β/ °	91.0240 (10)	90
V/ Å^3	4111.65 (10)	3909.0 (8)
Z	4	4
T/K	173(2)	173(2)
D_c/ g cm^{-3}	1.366	1.35
θ_{max}	25	27.5
reflns measured	52040	44033
independent reflns	14433	8941
observed reflns [$I > 2\sigma(I)$]	12442	8263
μ(Mo *K*α)/ mm^{-1}	0.53	0.55
R_{int}	0.021	0.048
R1	0.038[a]	0.041
*w*R2	0.113[b]	0.084
GOF	1.09	1.08

[a] $R1 = \Sigma||F_O| - |F_C||/ \Sigma|F_O|$. [b] $wR2 = [\Sigma w(F_O^2 - F_C^2)/\Sigma w(F_O^2)^2]^{1/2}$, $w = 1/[\sigma^2(F_O^2) + (aP)^2 + bP]$, where $P = (F_O^2 + 2F_C^2)/3$.

Electronic Absorption Spectroscopy. The electronic absorption spectra of an acetonitrile solution of compounds **1**, **5**, and **6** are shown in Figure 5-19, and the main transitions are listed in Table 5-11. The absorption spectra of the Ni-3,6-di-R-PSQ isomers are quite different compared to the Ni-2,7-di-R-PSQ complexes. Complex **6** has two main features at 20700 and 28700 cm^{-1} with shoulders at 15000, 23200, and 24600 cm^{-1}. Based on comparisons with the assignments of complex **1** (Table 5-3), the transition at 20700 cm^{-1} is MLCT and the band at 28700 cm^{-1} is intraligand in nature. Complex **5** has 4 main features at 16200, 21500, 24600, and 31000 cm^{-1}, with a shoulder at 26000 cm^{-1}. Again using the transitions of **1** as a guide, the band at 31000 cm^{-1} is assigned as MLCT and all other transitions are intraligand in nature. It should be noted that these are tentative assignments, and gallium analogues will be needed to properly assign the intraligand bands.

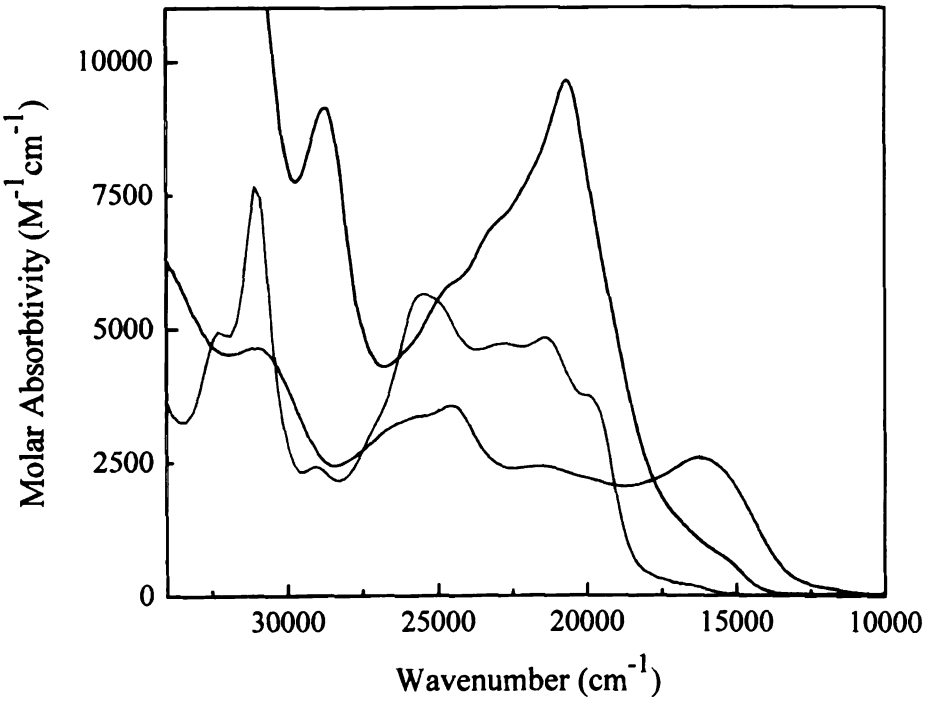

Figure 5-19. Electronic absorption spectra of [Ni(tren)(PSQ)](BPh_4) (**1**) (red), [Ni(tren)(3,6-di-NO_2-PSQ)](BPh_4) (**5**) (green), and [Ni(tren)(3,6-di-NH_2-PSQ)](BPh_4) (**6**) (blue) in acetonitrile.

Table 5-11. Transitions in [Ni(tren)(3,6-di-NO_2-PSQ)](BPh_4) (**5**) and [Ni(tren)(3,6-NH_2-PSQ)](BPh_4) (**6**), where MLCT = metal-to-ligand-charge transfer and IL = intraligand.

[Ni(tren)(3,6-di-NO_2-PSQ)](BPh_4)	[Ni(tren)(3,6-di-NH_2-PSQ)](BPh_4)
16200 (MLCT)	20700 (MLCT)
21500 (IL)	28700 (IL)
24600 (IL)	
31000 (IL)	

Electrochemistry. Metal complexes containing quinoidal ligands typically exhibit rich electrochemistry due to the multiple oxidation states that can be accessed by the ligand. The plots of the voltammograms for **1**, **5**, and **6** are shown in Figure 5-20.

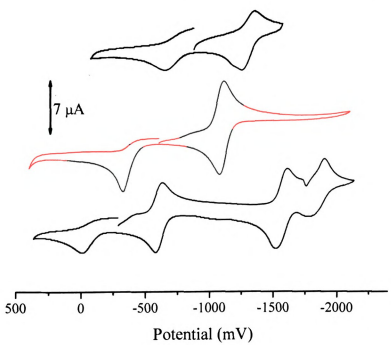

Figure 5-20. Cyclic voltammograms of the [Ni(tren)(3,6-di-NH_2-PSQ)](BPh_4) (**6**) (top), Ni(tren)(PSQ)](BPh_4) (**1**) (middle), and [Ni(tren)(3,6-di-NO_2-PSQ)](BPh_4) (**5**) (bottom). All data were acquired in degassed acetonitrile containing 0.1 M NBu_4PF_6 at a scan rate of 100 mV s^{-1}. All potentials are referenced to the ferrocenium/ferrocene couple as an internal standard.

Bencini et al. have reported the electrochemistry of [Ni(CTH)(PSQ)](PF_6),[31] and observed a reversible process at -1.10 V *vs.* Fc^+/Fc which was attributed to the

semiquinone/catechol couple, and an additional irreversible process observed at -0.18 V *vs.* Fc^+/Fc, which was attributed to the semiquinone/quinone couple. The assignment of these processes to the ligand are straightforward, due to oxidation and reduction processes involving Ni^{II} being at significantly more positive and negative potentials, respectively.[17,78,79] For **1** the redox couples at –1.09 V (semiquinone/catechol) and at –0.36 V (semiquinone/quinone) are in excellent agreement with the previous work. Complex **6** exhibits a irreversible redox couple at -0.772 V (semiquinone/quinone) and a reversible couple at -1.37 V (semiquinone/catechol) *vs.* Fc^+/Fc. Analogously, complex **5** has an irreversible redox couple at 0.03 V (semiquinone/quinone) and a reversible couple at -0.620 V (semiquinone/catechol). The two additional couples for **5** at –1.71 V and –1.51 V are most likely due to the reduction of the NO_2 to NH_2 group. The $E_{1/2}$ values for the semiquinone/catechol redox couple for the series of compounds corresponds to the electron accepting character of the ligands, and follows the order Ni-3,6-di-NO_2 > Ni-PSQ > Ni-3,6-di-NH_2-PSQ. The redox potentials were also found to correlate with the Hammett σ_p parameter yielding a correlation coefficient of 0.999, suggesting that the Ni-PSQ complexes are stabilized by transfer of negative charge from the substituents to the radical centers.[80-82] This idea is also supported by the DFT data, since the strong π-donor NH_2 delocalizes the spin to the greatest extent in the Ni-3,6-di-R-PSQ complexes.

EPR Spectroscopy. The EPR spectra of **1**, **5**, and **6** can be considered in the strong exchange limit, where exchange coupling is much greater than the other spin parameters, such as the Zeeman interaction or zero field splitting effects, based upon the experimental and theoretically determined *J* values. In the strong exchange limit, the

effects of other operators acts as a perturbation of the isotropic exchange Hamiltonian (Eq 1), and the following linear relationships hold for the various spin exchange levels.

$$\mathbf{g_S} = c_1\mathbf{g_A} + c_2\mathbf{g_B} \tag{13}$$

$$\mathbf{D_S} = d_1\mathbf{D_A} + d_2\mathbf{D_B} + d_{12}\mathbf{D_{AB}} \tag{14}$$

where $\mathbf{g_S}$ and $\mathbf{D_S}$ are the g and zero-field splitting tensors, respectively, and $\mathbf{g_A}$ and $\mathbf{g_B}$ are the g tensors of the individual spins centers. $\mathbf{D_A}$ and $\mathbf{D_B}$ are the zero field splitting tensors of the individual spin centers, while $\mathbf{D_{AB}}$ is the asymmetric exchange tensor, and arises via the exchange interaction. Bencini and Gatteschi[83] provide the scalar values c_1, c_2, d_1, d_2, and d_{12} for various spin pairs, and for a S = $^1/_2$ and S = 1 spin pair the resulting equations for the $S_T = {}^3/_2$ manifold are:

$$\mathbf{g_S} = \frac{1}{3}\mathbf{g_A} + \frac{2}{3}\mathbf{g_B} \tag{15}$$

$$\mathbf{D_S} = 0\mathbf{D_A} + \frac{1}{3}\mathbf{D_B} + \frac{1}{3}\mathbf{D_{AB}} \tag{16}$$

where the coefficient of D_A is zero, because there can be no zero field splitting in an S = $^1/_2$ system. Using the above equations and the standard g-values for a phenoxy radical (g = 2.00) and for Ni(II) (g = 2.2), the equation predicts a g-value for the exchange coupled system of g = 2.13. The frozen solution EPR spectra of complexes **1**, **5**, and **6** are shown in Figure 5-21. The EPR spectra were simulated with XSOPHE[84] (not shown) to yield the following isotropic g-values: **1**: g = 2.11, **5**: g = 2.12, and **6**: g = 2.12. Due to the breadth of the EPR transitions the accuracy in the g values is not high, but due agree with the calculations. These g values are lower than what has been observed for other Ni-SQ complexes (g = 2.2),[17] but are in relative agreement with a similar Ni(II)-phenoxy radical

complex from Weighardt and coworkers,[85] where they determined the isotropic g = 2.11. Recall, for an EPR transition to occur,

$$\Delta E = h\upsilon = g_{eff}\beta B \tag{17}$$

$$g_{eff} = \frac{h\upsilon}{\beta B} \tag{18}$$

where h is Planck's constant, υ is the frequency, β is the Bohn magneton, B is the magnetic field, and g_{eff} is the effective g value.

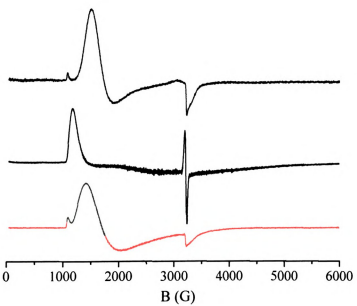

Figure 5-21. The X-band EPR spectra of the [Ni(tren)(3,6-di-NO_2-PSQ)](BPh_4) (**5**) (top), [Ni(tren)(3,6-di-NH_2-PSQ)](BPh_4) (**6**) (middle), and Ni(tren)(PSQ)](BPh_4) (**1**) (bottom) complexes. The spectra were acquired at 4 K in a 9:2 propionitrile to butyronitrile glass at 9.465 GHz with a 10 G modulation amplitude.

The transition observed at $g_{eff} = 2$ (3340 G) is due to transitions between the $m_S = \pm {}^1/_2$ manifold, and the absorptions at $g_{eff} \cong 4$ ($\cong$ 1700 G) are due to transitions between the $m_S = \pm {}^3/_2$ manifold (Figure 5-12) and are typical of a Kramers doublet.[17] The transitions in the $m_S = \pm {}^3/_2$ manifold are formally forbidden due to the EPR selection rule ($\Delta m_S = \pm 1$), but due to mixing of the $m_S = {}^1/_2$ and $m_S = {}^3/_2$ states the transitions can become

allowed. In the spectra, no transitions were observed that could be formally assigned as transitions between the $m_S = \pm {}^3/_2$ and $m_S = \pm {}^1/_2$ states (Figure 5-12). The zero field splitting constant (D) could not be accurately determined, since $2D$ (Figure 5-12) is larger than the microwave quantum available for the spectrometer used in the experiment (0.3 cm^{-1}). Temperature dependent (4-75 K) EPR data were also collected to see if increasing the thermal energy would lead to transitions observed between the $m_S = \pm {}^3/_2$ and $m_S = \pm {}^1/_2$ states, but these transitions were not observed. High frequency EPR was needed to accurately determine the zero field splitting constants in these samples.

Along these lines, complex **1** was sent to Dr. Naresh Dalal at the National High Magnetic Field Laboratory in Tallahassee to determine the D value. The results of the temperature dependent high frequency (up to 406 GHz) measurements on a powder sample of **1** are shown in Figure 5-22.

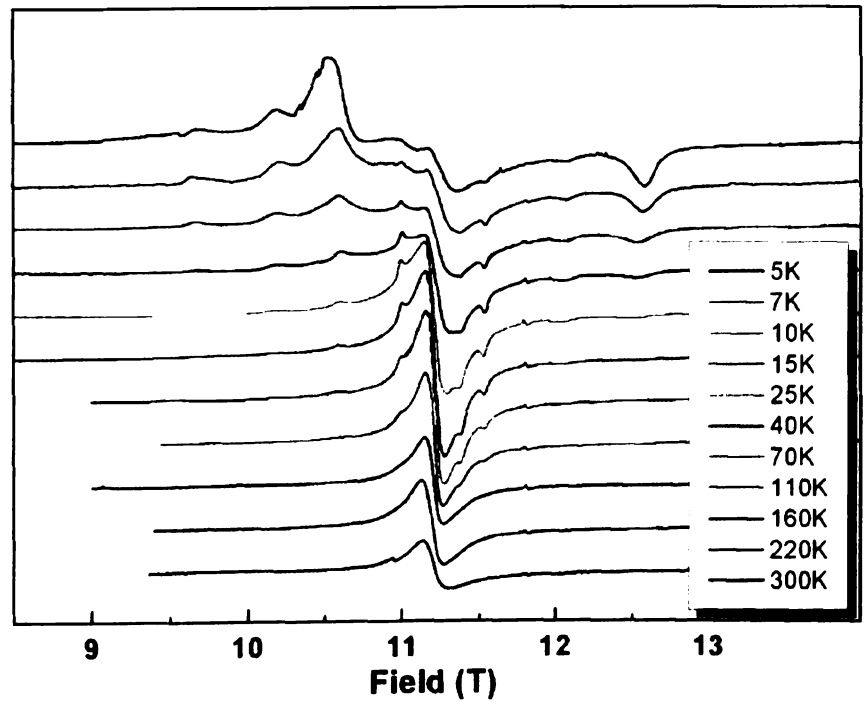

Figure 5-22. Temperature dependence of a powder sample of [Ni(tren)(PSQ)](BPh$_4$) (**1**) at 331.2 GHz.

As the temperature increases in the spectrum, the side peaks become weaker showing that the spectra originate from the S = $^3/_2$ ground state. The spectrum at 10 K and 331.2 GHz was simulated to yield $g_X = 2.127$, $g_Y = 2.127$, $g_Z = 2.13$, $D = 0.651$ cm^{-1}, and E = 0.064 cm^{-1}. The isotropic g value is in good agreement with the value derived from X-band measurements and calculated by Equation 15, and the *D* value is in the range of the lower limit estimate of what has been determined by Weighardt and coworkers for the Ni-phenoxy radical system.[85]

Interestingly, a radical spin delocalization constant is based upon the zero field splitting constant of 1,3-diaryl-substituted triplet diradicals, where the magnitude of the *D* parameter depends upon the magnetic dipole interaction of the two uncoupled spins,[86,87]

$$D = C\frac{\rho_A \rho_B}{d_{AB}^3} \qquad (19)$$

where ρ_A and ρ_B are the π-spin densities on the two radical centers and d_{AB} is the distance between the uncoupled radical centers and is constant. The *D* value was found to provide a reliable measure of radical stabilization due to a strong correlation with the *D* parameter found from experiments and the calculated spin densities at the same radical center using semiempirical methods.[88] It is hypothesized that the spin delocalization predicted by DFT in the Ni-PSQ systems may correlate with the magnitude of the zero field splitting parameter, in essence an experimentally determined transition metal-radical stabilization scale. It must be noted that the physical origin of the zero field splitting in the Ni-PSQ complexes arises from symmetry arguments. The C_{2V} symmetry of the complexes dictates that there can only be 1-fold degeneracy, and as a result the 4-fold degenerate (2S +1) S = $^3/_2$ ground state must split into Kramers doublets in zero magnetic field. Since the zero field interaction in the biradical has a different physical origin from the Ni-PSQ

complexes it is unclear if a correlation will be found. Future work along these lines with the other members of the Ni-3,6-di-R-PSQ series will be conducted to ascertain if this hypothesis can be justified.

Magnetic Susceptibility. The magnetic susceptibility plots for complexes **1**, **5**, and **6** are shown in Figure 5-23.

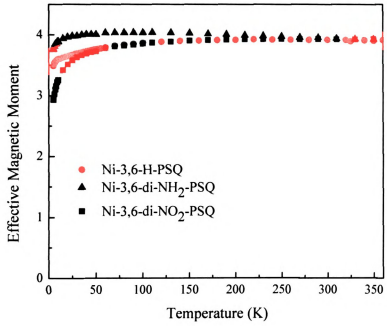

Figure 5-23. The effective magnetic moment vs. temperature for the Ni(tren)(PSQ)](BPh$_4$) (**1**) (red circle), [Ni(tren)(3,6-di-NO$_2$-PSQ)](BPh$_4$) (**5**) (green square), and [Ni(tren)(3,6-di-NH$_2$-PSQ)](BPh$_4$) (**6**) (blue triangle) complexes.

The data show a slight rise in the effective magnetic moment at low temperature to 50 K, and then the moment flattens out to μ_{eff} = 3.9 BM. The data are in agreement with what was observed for the Ni-2,7-di-R-PSQ isomers, and an S = $^3/_2$ ground state is again experimentally confirmed. The rise at low temperature can be assigned to zero field splitting, based on the liquid phase Ni-PSQ data (vide supra). The DFT calculations predicted that the Ni-3,6-di-NH$_2$-PSQ complex would have a reduced *J* value in

comparison to the Ni-PSQ complex, due to decreased spin density at the oxygen atoms. Upon closer examination of Figure 5-23, the data for **6** do show temperature dependence over the observed range as seen in Figure 5-24.

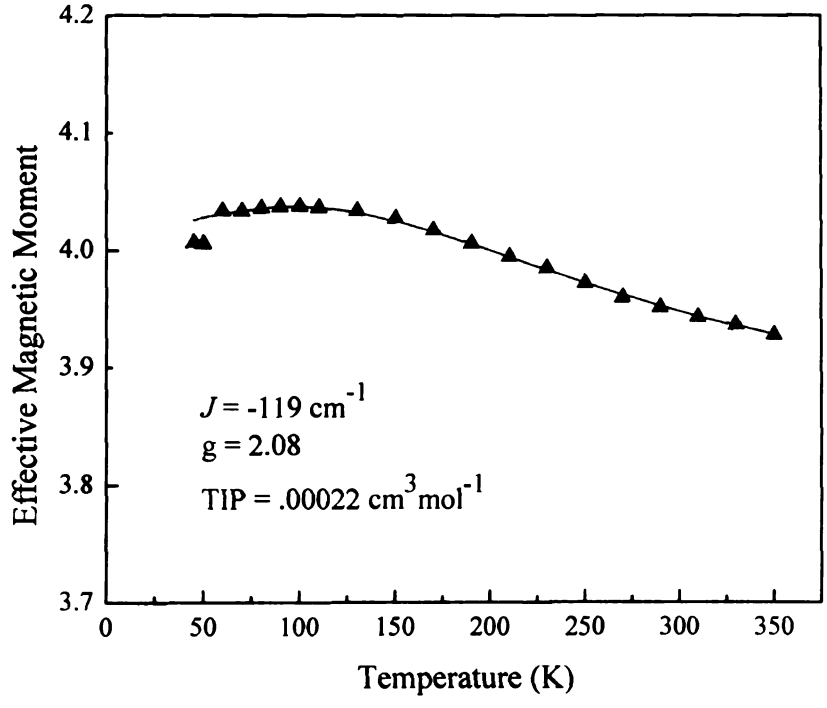

Figure 5-24. The effective magnetic moment of [Ni(tren)(3,6-di-NH_2-PSQ)](BPh_4) (**6**) (blue triangle), and the solid line represents a fit to the data using parameters described in the text.

The value for μ_{eff} at 50 K is 4.04 μ_B for **6**, which well represents the S = $^3/_2$ ground state; however, upon increasing the temperature to 350 K μ_{eff} = 3.92 μ_B. The observed temperature dependence was quantitatively fit with MAGFIT[89] by using a form of the Van Vleck equation,[68] shown in Equation 20

$$\chi = \frac{N_A g^2 \mu_B^2}{3kT} \frac{\sum_S S(S+1)(2S+1)e^{-E(S)/kT}}{\sum_S (2S+1)e^{-E(S)/kT}} \qquad (20)$$

where N_A is Avogadro's number, g is the gyromagnetic factor of the electron, μ_B is the Bohr Magneton, T is the temperature, S is the total spin quantum number of a given spin state, and E(S) are the eigenvalues from the Heisenberg Hamiltonian (Equation 1) that depend on J.[63] Equation 20 is then compared with the measured values of χ and the exchange coupling constants can be determined by a least-squares fitting. The J and g values were the only two variables allowed to vary and the temperature independent paramagnetism (TIP) was fixed at 0.00022 cm^3mol^{-1} analogous to a Ni^{II}-verdazyl radical complex.[90] The fit to the experimental data gave J = -119 cm^{-1} and g = 2.08. It must be noted that the MAGFIT program utilizes $\mathbf{H} = 2J_{12}\mathbf{S}_1\cdot\mathbf{S}_2$ for the data analysis, where the energy difference between the spin states is then $3J$ with this Hamiltonian. Using our experimental and calculated J values, the energy gap between the spin states is ΔE_{exp} = 357 cm^{-1} and ΔE_{DFT} = 330 cm^{-1}. The experimental and theoretical quartet-doublet energy gaps agree satisfactorily, but remember that our goal is to find a trend in J not exact J values. The g value also agrees well with the above EPR measurements. Unfortunately, complexes **1** and **5** did not show any temperature dependence, and experimental J values could not be determined. High temperature SQUID data was attempted for complex **5** (TGA decomposition temperature is 480 K), but no temperature dependence was observed. Three important conclusions arise out of the above examination. First, the J value was modulated by the NH_2 substituent to lead to an observable decrease in the effective magnetic moment vs. temperature. Secondly, the modulation in J is most likely due to the spin delocalizing effect of the 3,6-di-NH_2 substituents as predicted by the DFT calculations. Thirdly, the J values for **1** and **5** are too large to be determined experimentally, confirming an isolated S = $^3/_2$ ground state. DFT did predict that the spin

density is more localized at the oxygens in these complexes, and this suggests that we should have a large J value. Experimentally, J does decrease as predicted for **6** and remains strong for both **1** and **5**, and as a result we only have two pieces of experimental data to confirm the relationship in Equation 12. A general trend of experimentally determined J values between at least three complexes is needed to soundly prove the hypothesis. To investigate the presence of a firm correlation between the spin density at oxygen and the J value according to Equation 12, a larger set of substituents will be examined with broken symmetry DFT calculations to see if the trend is indeed general.

5.3.3 Density Functional Theory Study of Substituted [Ni(tren)(3,6-di-R-PSQ)]$^+$.

The above DFT results for the three Ni-3,6-di-R-PSQ complexes indicated a trend for modulating the J value, and to examine if this trend is indeed general a set of 17 substituents including π-donors (NH_2, NMe_2, and OMe), π-acceptors (NO_2, CN, SO_2CN, and vinyl), σ-donors (CH_3, $C(CH_3)_3$, and $Si(CH_3)_3$), σ-acceptors (CF_3, IF_4, and $C(CF_3)_3$), and π-donors, σ-acceptors (F, Cl, and Br) were examined, where H was used as the reference point. Equation 3 was used to calculate all J values, and the results indicated a strong correlation of J with the average spin density at the oxygen atom, with $r = 0.998$, shown in Figure 5-25. Figure 5-25 indicates that as the magnitude of J is increased (becomes more negative), the spin density at the oxygen atoms also increases. The opposite trend is also true, when the spin decreases at the oxygen atoms, the J value also decreases. The substituents responsible for increasing J are strongly electron withdrawing, and those responsible for decreasing J are more electron donating. The high correlation coefficient and number of substituents used indicate that the trend is

general for the ferromagnetic exchange interaction between Ni^{II} and an organic radical. The Ni^{II} α-unpaired spin density remains largely unchanged throughout the entire series, and according to Equation 12 a correlation should also be seen between the product of spin densities at the nickel and oxygen centers. The correlation between the product of the spin densities is depicted in Figure 5-26.

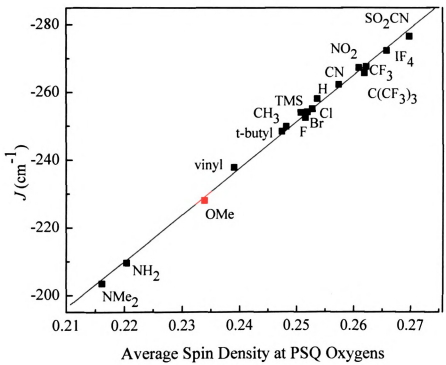

Figure 5-25. Correlation between the UB3LYP/6-311g** calculated average α-spin density (NPA) at the PSQ oxygen atoms and the *J* value calculated with Equation 3.

The correlation coefficient in Figure 5-26 is strong with r = 0.998, and it is identical to the correlation coefficient seen in Figure 5-25 for the *J* vs. average spin density at oxygen. This attests to the unchanging spin density population at the nickel center, and indicates that the spin at oxygen is the main factor modulating the *J* value in these systems. The correlation in Figure 5-26 also supports the proportionality between the

two electron exchange integral and the product of the spin densities suggested in Equation 12, and gives theoretical evidence for the applicability of the equation.

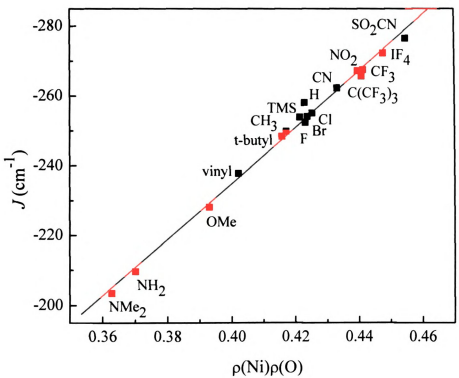

Figure 5-26. The correlation between J calculated with Equation 3 and the product of the NPA Ni^{II} and average oxygen α-spin densities, calculated at the UB3LYP/6-311g** level.

The electron withdrawing nature of the PSQ ligands seemed to be playing a role in the spin delocalization as seen in Figures 5-25 and 5-26, and another correlation that was identified is between the J value and the Hammett σ_p^+ substituent constant,[91] and this is shown in Figure 5-27. Not all substituents could be used, since the σ_p^+ parameters for SO_2CN, IF_4, and $C(CF_3)_3$ have not been experimentally determined. The correlation in Figure 5-26 is strong with r = 0.97, and indicates that the strongly electron withdrawing substituents (large positive σ_p^+) increase the J value, while the strong electron donating groups (large negative σ_p^+) decrease the J value.

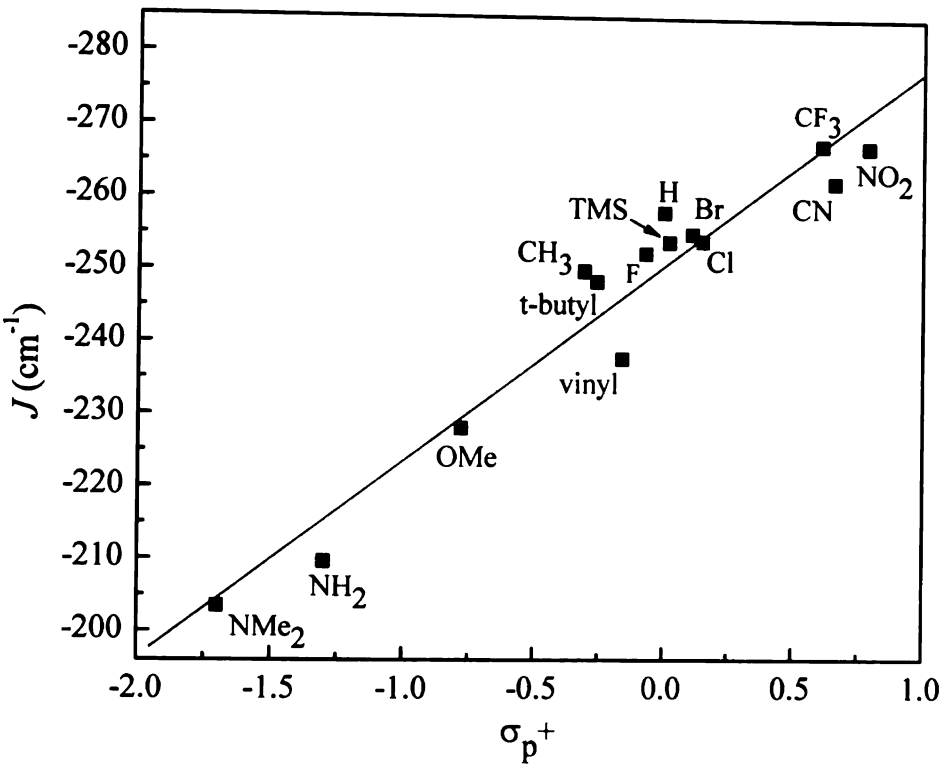

Figure 5-27. The correlation between the UB3LYP/6-311g** *J* value calculated with Equation 3 and the Hammett σ_p+ substituent constant. The substituent constants were taken from Hansch and coworkers.[92]

The above series of correlations imply yet another correlation: that as the spin density at oxygen decreases, the charge density increases at the oxygen atoms. The opposite trend is also observed, and if the spin is increased at the oxygen atom, then the charge density decreases. This correlation (r = 0.97) is different from the phenoxy and free semiquinone radicals studied thus far, because in each substituent spin and charge density at the oxygen centers move with opposite polarization. In order to try to develop a model for the movement of spin density in these systems, and then try to relate it to the spin and charge density correlations, the molecular orbitals were examined for any similar trends that were developed for the phenoxy and semiquinones radical systems.

Similar to the phenoxy radical case, a correlation was discovered between the α-HOMO-α-LUMO gap and the spin density, depicted in Figure 5-28.

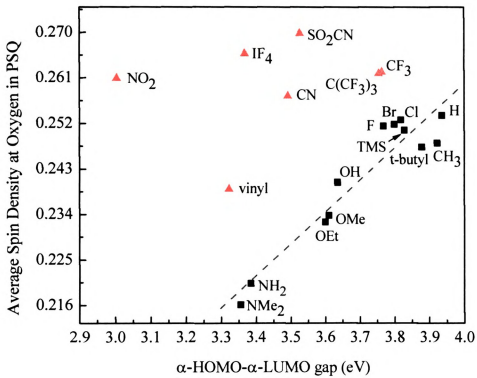

Figure 5-28. The correlation between the average α-spin density at oxygen with the α-HOMO-α-LUMO gap, calculated at the UB3LYP/6-311g** level.

A general conclusion can be drawn from Figure 5-28, and as the α-HOMO-α-LUMO gap decreases, the spin density at the oxygen atoms also decreases. This is in agreement with the previous data for substituted phenoxy radicals and semiquinones: the α-HOMO-α-LUMO gap is a marker which describes the spin delocalization in these systems. Another striking piece of data in Figure 5-28 is the lack of a correlation for the strong electron withdrawing groups. These substituents all have an artificially small α-HOMO-α-LUMO gap based upon their calculated spin delocalizing ability. Strong electron withdrawing groups were also found to be outliers in the phenoxy radical case, and the smaller α-HOMO-α-LUMO gaps were accounted for by a simple four-orbital, three-electron molecular orbital interaction.[34] Analogous MO interactions were sought after to

explain the outliers and correlation in Figure 5-28. First the general correlation with the α-HOMO-α-LUMO will be examined, then the outliers will be explained using molecular orbital models.

A weak interaction can occur between the filled d_{xz} orbital of Ni^{II} and the PSQ SOMO orbital, since they both span the b_1 irreducible representation of the C_{2v} point group (Figure 5-29).

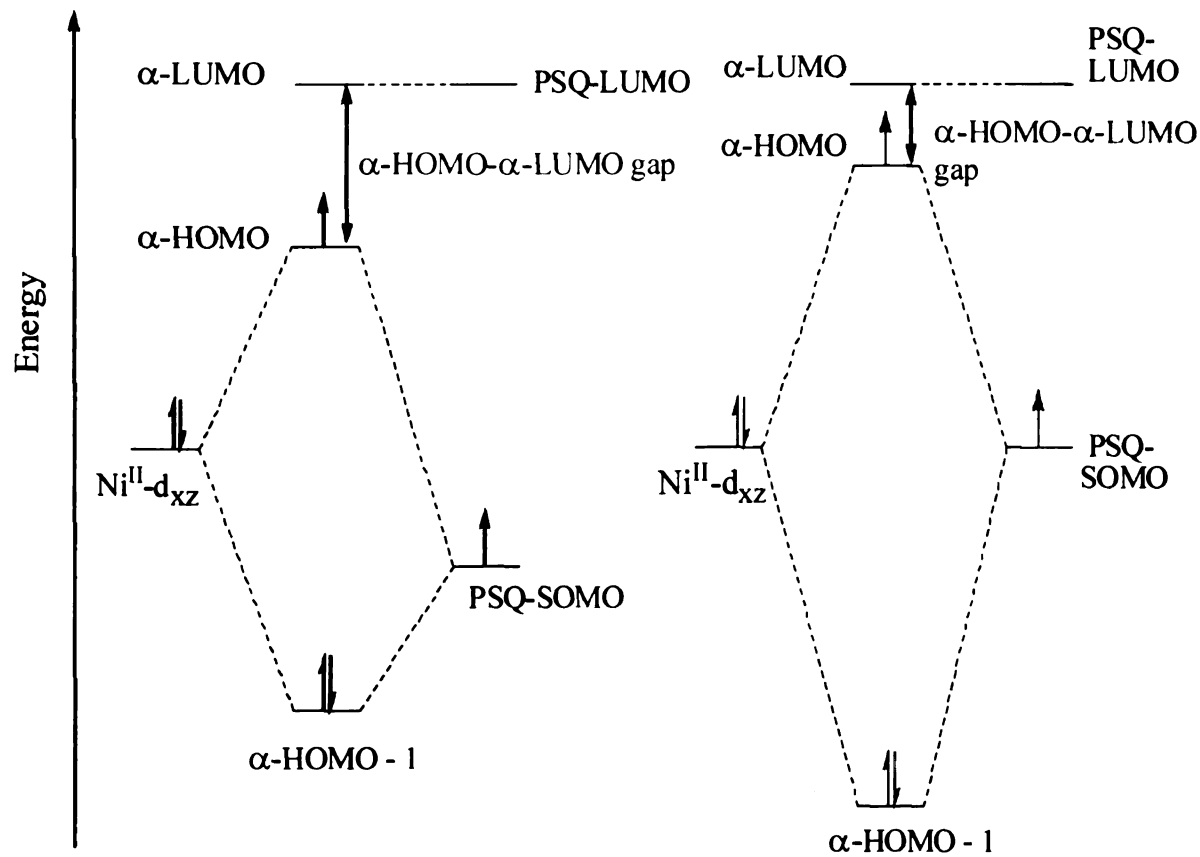

Figure 5-29. Weak bonding interaction between the filled Ni^{II}-d_{XZ} and two energetically different PSQ-SOMO orbitals, where the α-HOMO-α-LUMO gap is labeled in blue.

The highest occupied α-SOMO of the Ni^{II}-PSQ complex (α-110 in Figure 5-15) depicts the delocalization of the SOMO over the PSQ ligand, and the weak interaction with the Ni^{II} d_{XZ} orbital. Recall that the general molecular orbital model used to describe the spin delocalization in the phenoxy radical was a three-electron, two-orbital interaction, where

a filled lone pair orbital of a donor group interacted with the phenoxy radical SOMO. In the case of the Ni-3,6-di-R-PSQ complexes, a three-electron, two-orbital interaction can also be invoked. This MO model assumes that the energy of the PSQ-LUMO and Ni^{II}-d_{XZ} orbitals remain unchanged, while the energy of the PSQ-SOMO will depend on the nature of the substituents. If the substituents are strongly electron withdrawing, the energy of the PSQ-SOMO will decrease (Figure 5-29 left) and less mixing between the PSQ-SOMO and the Ni^{II}-d_{XZ} orbitals will occur, lowering the energy of the α-HOMO, thereby decreasing the α-HOMO-α-LUMO gap. Increased spin localization at the oxygen atoms will also occur as a consequence of the decreased orbital mixing, since less spin can be delocalized away from the oxygen atoms of the PSQ radical. If a substituent is strongly electron donating, then the energy of the PSQ-SOMO will increase (Figure 5-29 right) and increased orbital mixing with the Ni^{II}-d_{XZ} orbitals will occur, and this has two consequences: (1) the spin density will be more delocalized, and less spin population will be observed at the oxygen atoms, and (2) the energy of the α-HOMO will increase resulting in the α-HOMO-α-LUMO gap decreasing. These observations are all predicated upon the energy of the α-LUMO remaining unchanged. The MO model above supports the observed decreased spin density at the oxygen atoms for the donors and weak acceptor substituents, but does not account for the deviations of the strong electron withdrawing groups.

Using the molecular orbital model for the outliers of the phenoxy radical case as a guide, an analogous four-orbital, three-electron interaction can be invoked for the Ni-PSQ complexes and is depicted in Figure 5-30. The proposed MO diagram to describe the decreased α-HOMO-α-LUMO gap involves the interaction between a π^*-PSQ orbital

that is low enough in energy due to the electron withdrawing nature of the 3,6-acceptor-PSQ radicals and can interact with the LUMO orbital of the Ni^{II} cation. The three-electron, two-orbital model above assumed no interaction with the unoccupied π^*-PSQ orbital. If this orbital is interacting the α-HOMO-α-LUMO gap will exhibit artificially decreased values compared to cases where this interaction is not operative (Figure 5-29). Examination of the percent contributions to each orbital may possibly give additional theoretical evidence for suggesting the molecular orbital diagrams above. The data for the analysis of the molecular orbitals for the all complexes along with the protio reference is given in Table 5-12.

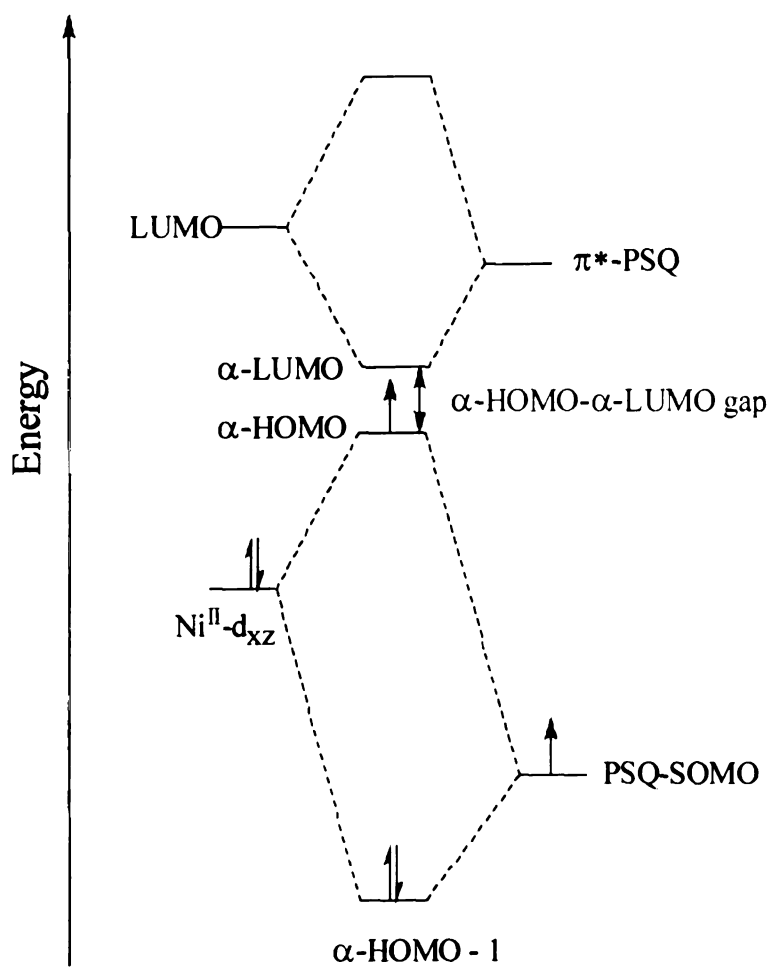

Figure 5-30. The four-orbital, three-electron interaction of the outliers in the Ni-3,6-di-R-PSQ complexes.

Table 5-12. The % nickel (% Ni) and average % oxygen (% O) in the highest occupied α-HOMO (α-110), along with the average α-spin density at the oxygen atoms (ρ(O) in α-electron units).

Complex	% Ni[a]	% O[a]	ρ(O)
$[Ni(tren)(3,6\text{-di-}NMe_2\text{-PSQ})]^+$	0.267	9.44	0.2161
$[Ni(tren)(3,6\text{-di-}NH_2\text{-PSQ})]^+$	0.308	10.69	0.2200
$[Ni(tren)(3,6\text{-di-OEt-PSQ})]^+$	0.364	12.12	0.2330
$[Ni(tren)(3,6\text{-di-OMe-PSQ})]^+$	0.370	12.28	0.2338
$[Ni(tren)(3,6\text{-di-vinyl-PSQ})]^+$	0.411	12.96	0.2390
$[Ni(tren)(3,6\text{-di-OH-PSQ})]^+$	0.415	13.25	0.2404
$Ni(tren)(3,6\text{-di-}t\text{-butyl-PSQ})]^+$	0.466	14.31	0.2473
$[Ni(tren)(3,6\text{-di-Me-PSQ})]^+$	0.479	14.63	0.2481
$[Ni(tren)(3,6\text{-di-TMS-PSQ})]^+$	0.491	14.78	0.2507
$[Ni(tren)(3,6\text{-di-F-PSQ})]^+$	0.497	15.02	0.2514
$[Ni(tren)(3,6\text{-di-Br-PSQ})]^+$	0.463	13.96	0.2518
$[Ni(tren)(3,6\text{-di-Cl-PSQ})]^+$	0.481	14.39	0.2527
$[Ni(tren)(PSQ)]^+$	**0.518**	**15.68**	**0.2540**
$[Ni(tren)(3,6\text{-di-CN-PSQ})]^+$	0.545	15.54	0.2574
$[Ni(tren)(3,6\text{-di-}C(CF_3)_3\text{-PSQ})]^+$	0.564	16.03	0.2619
$[Ni(tren)(3,6\text{-di-}CF_3\text{-PSQ})]^+$	0.566	16.05	0.2622
$[Ni(tren)(3,6\text{-di-}NO_2\text{-PSQ})]^+$	0.589	16.24	0.2610
$[Ni(tren)(3,6\text{-di-}IF_4\text{-PSQ})]^+$	0.608	16.70	0.2658
$[Ni(tren)(3,6\text{-di-}SO_2CN\text{-PSQ})]^+$	0.637	16.96	0.2698

[a] $[\Sigma n^2_{a.o.} / \Sigma n^2_{m.o.}] * 100$ = % contribution. $\Sigma n^2_{a.o.}$ is the sum of the squares of the atomic orbital coefficients of the atom or group of interest, and $\Sigma n^2_{m.o.}$ is the sum of the squares of all atomic orbital coefficients in a specific molecular orbital.

Table 5-12 shows strong support for the modulation of the energy of the α-HOMO as shown in Figures 5-29 and 5-30. As the energy of the α-HOMO orbital is raised by a strong electron donating group like NH_2 there is more mixing between the orbitals, and as a result the % Ni and % O should decrease compared to the protio case. This is exactly what is observed in the data in Table 5-12. Additionally, the energy of the α-HOMO will be decreased by a strong electron withdrawing group like NO_2, and as a result there is less mixing between the orbitals and the % Ni and % O will increase compared to hydrogen. This increase in % Ni and % O is also observed in Table 5-12. The data also

support the correlation observed for the opposite polarization of spin and charge density at the oxygen atoms of the PSQ radical. As the electron withdrawing character of the PSQ ligand is increased (charge density at oxygen decreases), the spin density is more localized due to less mixing. The opposite trend was also found to be true of an electron donor increasing the charge density at the oxygen atoms, but the spin is decreased due to more orbital mixing. The % Ni and % O values then give reasonable evidence for the variation in the relative energy of the α-HOMO orbital.

The four-orbital, three-electron MO diagram is also supported by the % Ni and % O data. However, the energy of the α-LUMO is also proposed to be effected by an interaction with higher lying orbitals. As before in the phenoxy case, a large % substituent in the α-LUMO was indicative of the four-orbital, three-electron interaction, but in the Ni-PSQ complexes the α-LUMO is mostly dominated by the PSQ contribution. As a result of this the changes in % substituent are difficult to interpret. Certainly the possibility of multiple orbitals interacting with the LUMO of Ni^{II} to decrease the HOMO-LUMO gap may also be important in these molecules. Indirect evidence of this possibility is given in Figure 5-23, where a large random range of deviations is seen. Since the deviations are like "shot gun scatter" no clear trend can be determined, and the mechanism for spin polarization can't be firmly established.

The DFT data for the Ni-3,6-di-R-PSQ complexes yields strong support for the proportionality in Equation 12, where the spin density at the oxygen magnetic center was found to be directly proportional to the exchange coupling constant *J*. The spin density was found to vary with opposite polarization as the charge density at the oxygen atoms, in contrast to the PSQ and phenoxy systems. The α-HOMO-α-LUMO gap was again

found to be a marker for the spin delocalization of the substituents, as increasing the gap increases the α-spin population and decreasing the gap decreases the spin density at the oxygen centers. The mechanism responsible for the spin delocalization is the three-electron, two-orbital interaction, and this MO description is comparable to that proposed for the radical ligands. The strongly electron withdrawing substituents were again outliers in the α-HOMO-α-LUMO gap correlation, and interactions with higher lying orbitals are the likely cause. In order to see if the α-HOMO-α-LUMO gap correlation is general for all exchange coupling interactions, antiferromagnetic coupling in Cr-PSQ complexes will be examined to see if any of the same trends are observed.

It should also be noted that another functional, BLYP, was also used to ensure that all of the above correlations and results were not functional dependent, and although the numbers for the variables were different the exact same correlations are observed. The effect of bond distance on the *J* value was also examined, and the same set of calculations at the UB3LYP/6-311g** level were done using identical Ni–O bond distances (2.07 Å) in all cases. The results of fixing the bond distance again produced different numbers, but in all cases the correlations held. This data lends additional support for the spin density at the oxygen atom being the major variable responsible for the modulation of the *J* value in these systems.

5.3.4 Antiferromagnetic Coupling in $[Cr(tren)(3,6\text{-di-R-PSQ})]^{2+}$ Complexes.

Cr^{III} was chosen to study antiferromagnetic exchange coupling in the $[Cr(tren)(3,6\text{-di-R-PSQ})]^{2+}$ (Cr-PSQ) complexes. Cr^{III} is a d^3 transition metal with its unpaired electrons in the d_{XZ}, d_{XY}, and d_{YZ} orbitals. These orbitals in Cr^{III} have the same

π-symmetry as the PSQ π*-SOMO which results in orbital overlap and an antiferromagnetic interaction. The energy level diagram for this interaction is shown in Figure 5-31, where the energy separation between the S = 1 and S = 2 states is 2*J*.

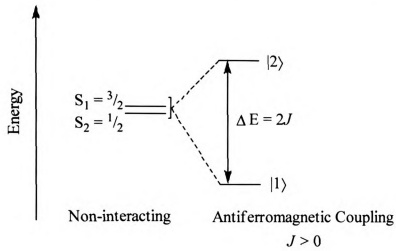

Figure 5-31. The antiferromagnetic coupling interaction in Cr-3,6-di-R-PSQ complexes. States are labeled as $|S_T\rangle$, where S_T is the total spin.

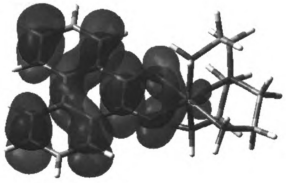

Figure 5-32. The UB3LYP/6-311g** calculated β-HOMO orbital of $[Cr(tren)(3,6\text{-di-R-PSQ})]^{2+}$ of the triplet ground state.

In the case of the Cr-PSQ complexes, the β-HOMO is now important because it is the β-spin on the PSQ ligands that communicates electronically with the Cr^{III} α-spin density to yield the weak bonding-type interaction. The weak bonding-type antiferromagnetic

interaction between the Cr^{III}-d_{XZ} and the PSQ π^*-SOMO is depicted in the β-HOMO wavefunction in Figure 5-32 above. The strength of the antiferromagnetic coupling will depend upon the overlap integral between the magnetic orbitals, i.e.[16]

$$S_{12} = \langle \Psi(1) | \Psi(2) \rangle \tag{21}$$

where S_{12} is the overlap integral and J is proportional to the absolute value of S_{12}^2.[16,93] Due to the success of the proportionality between the product of the spins at the two paramagnetic centers and the ferromagnetic J in Ni-PSQ, it is hypothesized that an analogous relationship to Equation 12 can be suggested for the antiferromagnetic coupling constant in the Cr-PSQ complexes, i.e.

$$J_{Cr-PSQ} \approx \rho_{Cr}\rho_{PSQ} \tag{22}$$

where ρ_{Cr} is the α-spin density on Cr^{III} and ρ_{PSQ} is the average β-spin density at the oxygen centers of the PSQ radical. In order to test this hypothesis, DFT calculations were undertaken on substituted Cr-3,6-di-R-PSQ complexes using the same 17 substituents as the Ni-3,6-di-R-PSQ complexes.

The J vs. spin density and J vs. $\rho_{Cr}\rho_{PSQ}$ results for the 17 Cr-3,6-di-R-PSQ complexes are depicted below in Figures 5-33 and 5-34, respectively. Recall that the J value should be positive in the Cr-PSQ complexes (according to Equation 1), and since an antiferromagnetic interaction is operating the spin density at the oxygen atoms should be negative. The correlations are quite strong with r = 0.99 in both cases. The proposed proportionality in Equation 21 seems to be valid for antiferromagnetic coupling, and applies for both ferromagnetism and antiferromagnetism for metal semiquinone complexes. The spin density at the oxygen centers is again the major variable responsible for the changes in the J value, since the spin at Cr^{III} remains constant.

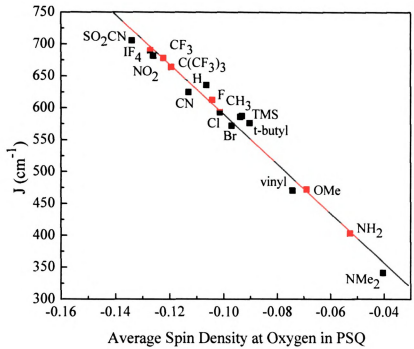

Figure 5-33. *J* (calculated with Equation 3) vs. the average β-spin at the oxygen atoms for $[Cr(tren)(3,6\text{-di-R-PSQ})]^{2+}$ complexes calculated at the UB3LYP/6-311g** level.

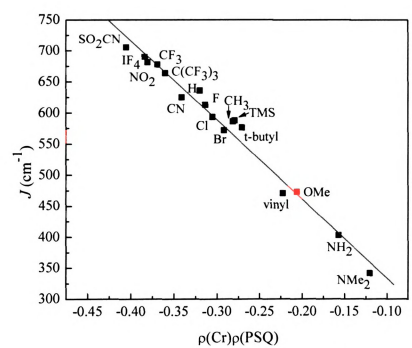

Figure 5-34. *J* (calculated with Equation 3) vs. the product of the average β-spin at the oxygen atoms and Cr^{III} centers for $[Cr(tren)(3,6\text{-di-R-PSQ})]^{2+}$ complexes calculated at the UB3LYP/6-311g** level.

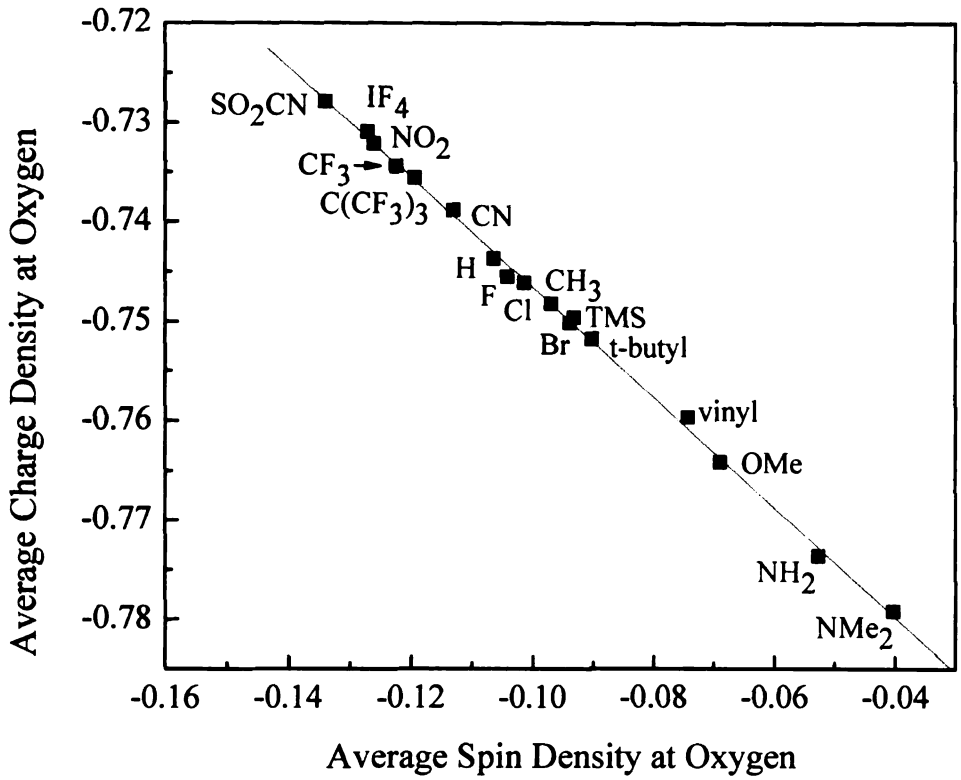

Figure 5-35. The correlation between the average β-spin and charge density at the oxygen center in $[Cr(tren)(3,6\text{-di-R-PSQ})]^{2+}$ compounds.

The spin population is controlled by the choice of substituents, and the electron withdrawing groups increase *J* by increasing spin localization, while the donating groups decrease *J* by increasing spin delocalization. The charge density was again found to correlate very strongly with the spin density at the oxygen centers, and this is depicted in Figure 5-35. The correlation coefficient of r = 0.999 is very strong, and as the charge density increases/decreases at the oxygen atoms, the spin density decreases/increases. The exact same correlations are seen in both the Ni-PSQ and Cr-PSQ complexes. In order to identify the mechanism for the spin delocalization in these systems we once again identified a correlation with the HOMO-LUMO gap. In this case the spin density correlates strongly with the β-HOMO-β-LUMO gap as shown in Figure 5-36. The most salient feature of Figure 5-36 is that the average spin density at the oxygen centers for

every substituent correlates with the β-HOMO-β-LUMO gap. Recall, that in the Ni-PSQ complexes all strongly electron withdrawing substituents deviated from the correlation.

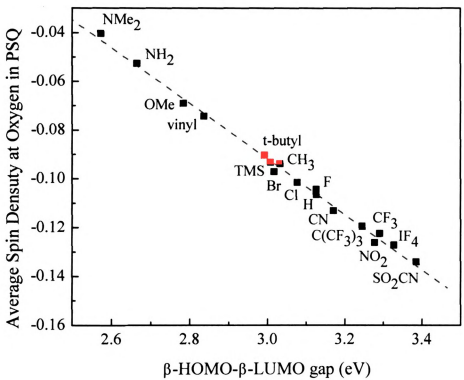

Figure 5-36. The correlation between the average β-spin density at the oxygen atoms with the β-HOMO-β-LUMO gap for the $[Cr(tren)(3,6\text{-di-R-PSQ})]^{2+}$ complexes.

The difference in the two systems can be explained with a simple molecular orbital diagram similar to Figure 5-29 where the Cr^{III}-$3d_{XZ}$ has the proper symmetry to interact with the π-PSQ-SOMO orbital. The MO comparison between the unsubstituted complex and the electron withdrawing NO_2-PSQ ligand is depicted in Figure 5-37, and the comparison with the donor NH_2-PSQ is shown in Figure 5-38. The molecular orbital model proposed is a two-orbital, two-electron interaction, where there is a net bonding-type stabilization of two electrons. In this case there is no involvement with energetically

higher lying orbitals, as only the Cr^{III}-$3d_{XZ}$ and PSQ-SOMO orbitals determine the β-HOMO-β-LUMO gap. The lack of any interactions with energetically higher orbitals is likely the reason why there are no outliers in the substituted Cr-PSQ β-HOMO-β-LUMO gap correlation.

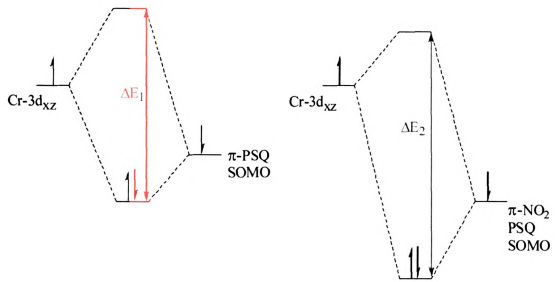

Figure 5-37. The changes in the β-HOMO-β-LUMO gap for the 3,6-di-H-PSQ vs. 3,6-di-NO_2-PSQ substituted Cr-PSQ's.

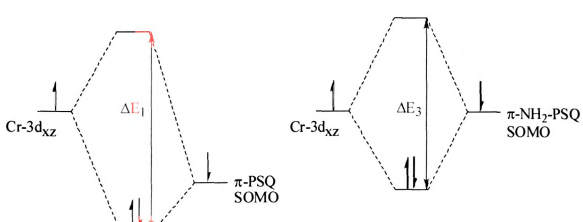

Figure 5-38. The changes in the β-HOMO-β-LUMO gap for the 3,6-di-H-PSQ vs. 3,6-di-NH_2-PSQ substituted Cr-PSQ's.

In the case of the Ni^{II}-PSQ and phenoxy radicals, it was proposed that there were interactions with higher lying orbitals that produced outliers in the correlations with the α-HOMO-α-LUMO gap. By comparison, the lack of outliers in the Cr-PSQ case gives evidence to support the previous arguments that higher lying orbitals must have been involved in the deviations in the Ni-PSQ and phenoxy complexes, since all substituents correlate very strongly in the Cr-PSQ case.

The correlations with the β-HOMO-β-LUMO are analogous with the Ni-PSQ case: electron withdrawing groups increase the β-HOMO-β-LUMO gap, while electron donors decrease the β-HOMO-β-LUMO gap. In comparison to Cr-PSQ, a strong acceptor electron like NO_2 in Cr-3,6-di-NO_2-PSQ (Figure 5-37) will lower the energy of the PSQ-SOMO, thereby increasing the β-HOMO-β-LUMO gap due to decreased orbital mixing. An electron donor like NH_2 will have the opposite effect (Figure 5-38) and a better energetic match between the PSQ-SOMO and the Cr^{III}-$3d_{XZ}$ orbitals will occur, with the β-HOMO-β-LUMO gap decreasing. Normally one would expect that a stronger orbital interaction would decrease the gap, but due to the energetic ordering of the SOMO orbitals this effect is not observed in these systems. Specifically, the β-HOMO (-11.03 eV) of Cr-PSQ is much lower in energy than the β-HOMO of Cr-3,6-di-NH_2-PSQ (-9.73 eV). This enlarges the gap due to the weaker orbital interactions more than the increased mixing seen in Cr-3,6-di-NH_2-PSQ.

As before in the Ni-PSQ complexes, the molecular orbital contributions of the Cr^{III}-center and the average oxygen contributions were determined for all complexes, and are depicted in Table 5-13. The average % O again correlates quite strongly with the spin density delocalization (r = 0.96), and the donors have smaller % O contributions to the β-

HOMO which reflect the increasing mixing between the PSQ-SOMO and the Cr-$3d_{XZ}$ orbitals.

Table 5-13. The % chromium (% Cr) and average % oxygen (% O) in the highest occupied β-HOMO, of substituted $[Cr(tren)(3,6\text{-di-R-PSQ})]^{2+}$ complexes and the average β-spin density at the oxygen atoms (ρ(O) in β-electron units).

Complex	**% Cr**[a]	**% O**[a]	**ρ (O)**
$[Cr(tren)(3,6\text{-di-NMe}_2\text{-PSQ})]^{2+}$	2.34	4.12	-0.0404
$[Cr(tren)(3,6\text{-di-NH}_2\text{-PSQ})]^{2+}$	2.52	4.87	-0.0530
$[Cr(tren)(3,6\text{-di-OMe-PSQ})]^{2+}$	2.54	5.60	-0.0690
$[Cr(tren)(3,6\text{-di-vinyl-PSQ})]^{2+}$	2.31	5.72	-0.0743
$[Cr(tren)(3,6\text{-di-Br-PSQ})]^{2+}$	2.07	5.94	-0.0971
$[Cr(tren)(3,6\text{-di-}t\text{-butyl-PSQ})]^{2+}$	2.75	7.19	-0.0903
$[Cr(tren)(3,6\text{-di-TMS-PSQ})]^{2+}$	2.73	7.28	-0.0932
$[Cr(tren)(3,6\text{-di-Cl-PSQ})]^{2+}$	2.26	7.35	-0.1015
$[Cr(tren)(3,6\text{-di-CH}_3\text{-PSQ})]^{2+}$	2.77	7.59	-0.0983
$[Cr(tren)(3,6\text{-di-F-PSQ})]^{2+}$	2.62	8.04	-0.1043
$[Cr(tren)(3,6\text{-PSQ})]^{2+}$	**2.85**	**8.79**	**-0.1060**
$[Cr(tren)(3,6\text{-di-CN-PSQ})]^{2+}$	2.35	8.13	-0.1131
$[Cr(tren)(3,6\text{-di-C}(CF_3)_3\text{-PSQ})]^{2+}$	2.60	9.06	-0.1195
$[Cr(tren)(3,6\text{-di-CF}_3\text{-PSQ})]^{2+}$	2.64	9.53	-0.1225
$[Cr(tren)(3,6\text{-di-NO}_2\text{-PSQ})]^{2+}$	2.51	9.61	-0.1260
$[Cr(tren)(3,6\text{-di-IF}_4\text{-PSQ})]^{2+}$	2.56	9.74	-0.1272
$[Cr(tren)(3,6\text{-di-SO}_2\text{CN-PSQ})]^{2+}$	2.40	9.86	-0.1341

[a] $[\Sigma n^2_{a.o.} / \Sigma n^2_{m.o.}] * 100$ = % contribution. $\Sigma n^2_{a.o.}$ is the sum of the squares of the atomic orbital coefficients of the atom or group of interest, and $\Sigma n^2_{m.o.}$ is the sum of the squares of all atomic orbital coefficients in a specific molecular orbital.

The electron acceptors increase the % O character in the β-HOMO, since these substituents increase the spin density at the oxygen atoms. Thus the % O data supports the MO diagrams that have been proposed in Figures 5-37 and 5-38. The % Cr data is more difficult to interpret and the changes are quite small, but a subtle correlation can be suggested. If we consider the NO_2, H, and NH_2 substituted complexes for our comparisons, and by examining Figures 5-37 and 5-38 we can expect the % Cr for the

NO_2 and NH_2 complexes to decrease in comparison with the H substituent. For the NO_2 complex the decreased % Cr is due to a decreased energetic match between the β-HOMO and Cr-$3d_{XZ}$ orbitals, because of the strongly electron withdrawing ability of NO_2. The NH_2 complex will have increased mixing between the β-HOMO and Cr-$3d_{XZ}$ and as a result the % Cr will decrease.

The Cr-PSQ data and correlations were also tested for functional dependence. The UBLYP results indicated identical correlations but different numbers. The Cr–O bond length was also fixed (1.94 Å) to examine any effects of the bond distance on the exchange coupling constant, and although the numbers were different the exact same trends were seen. Overall, the DFT data for the $[Cr(tren)(3,6\text{-R-PSQ})]^{2+}$ complexes have corroborated our hypothesis, and Equation 22 seems to be valid in these systems. The *J* value can be modulated with substituents for both the ferromagnetic and antiferromagnetic exchange coupling regimes, and the spin density at the oxygen atoms of the PSQ ligand is the main variable responsible for the changes in *J*. In an attempt to see if any experimental *J* values could be determined, the synthesis of Cr-3,6-di-NO_2-PSQ, Cr-3,6-di-NH_2-PSQ, and Cr-PSQ complexes will be pursued and if we are successful SQUID measurements will been taken.

5.3.5 Synthesis and Characterization of Cr-3,6-di-R-PSQ complexes

Synthesis. The synthesis of the Cr-PSQ complexes was done in a similar fashion as the Ni-PSQ complexes, and based on other literature reports for the synthesis of $[Cr(tren)(3,6\text{-di-}t\text{-butylsemiquinone})]^{2+}$ and $[Cr(tren)(3,6\text{-di-}t\text{-butylcatechol})]^{2+}$ refluxing conditions are needed in the reactions.[94] In a typical reaction, the 3,6-di-R-$PCATH_2$

ligands were deprotonated in the dry box with NaOH and then cannula transferred to a flask equipped with a reflux condenser containing degassed $[Cr(tren)Cl_2]Cl$ under nitrogen. The solution was then refluxed for 24 hours under N_2, and subsequently filtered under N_2 into a flask containing excess salt ($NaBPh_4$, $NaBF_4$, etc.) to precipitate out the desired Cr-PCAT product. The Cr-PCAT compounds were then oxidized under N_2 with acetylferrocenium tetrafluoroborate to the corresponding semiquinone complexes. The compounds should be stored under vacuum or nitrogen until needed. Unfortunately, the $[Cr(tren)(3,6\text{-di-}NH_2\text{-PCAT})](BPh_4)$ complex could not be made successfully. Part of the problem with the synthesis was the formation of $Cr(3,6\text{-di-}NH_2\text{-PSQ})_3$, which was confirmed by elemental analysis. The other two phenanthrenesemiquinone complexes were successfully prepared, and their properties will be discussed below.

Ground State Characterization: X-ray Crystallography. X-ray structures were obtained for the $[Cr(tren)(PCAT)]^+$ (**7**) and $[Cr(tren)(PSQ)]^{2+}$ (**8**) cations and ORTEP drawing are depicted in Figure 5-39.

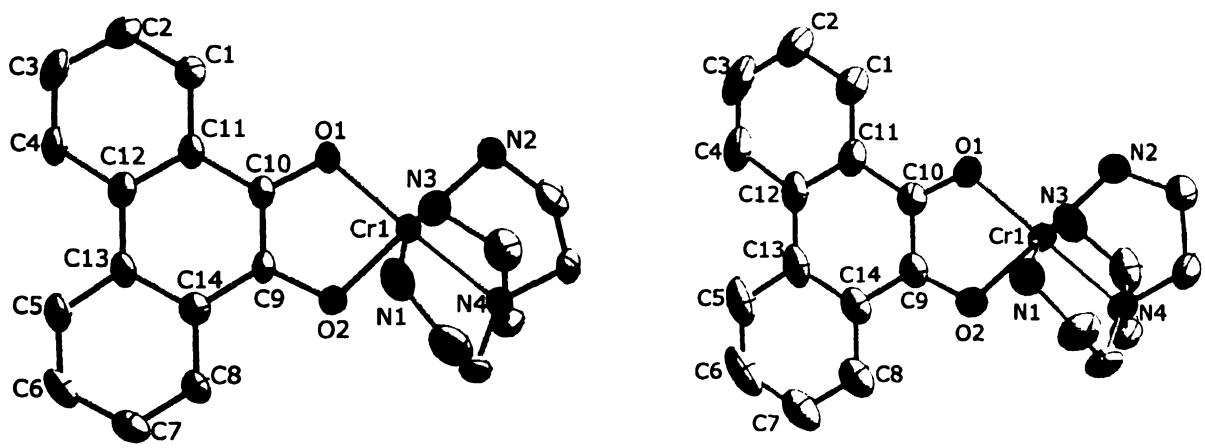

Figure 5-39. Drawings of the cations of $[Cr(tren)(PCAT)]^+$ (**7**) (left) and $[Cr(tren)(PSQ)]^{2+}$ (**8**) (right) obtained from single crystal X-ray structure determinations. Atoms are represented as 50 % probability thermal ellipsoids.

The crystallographic data are listed in Table 5-14 and selected bond distances and angles are listed in Table 5-15. The C–O and intradiol (C(10)–C(9)) bond lengths are again diagnostic of the semiquinone oxidation state, where the Cr-PSQ C–O_{avg} = 1.31 Å and C(10)–C(9)) = 1.40 Å bond distances agree well with literature values.[55] The Cr-PCAT C–O_{avg} = 1.36 Å and C(10)–C(9)) = 1.36 Å bond distances are also diagnostic of the catechol oxidation state of the ligand.[55] The semiquinone exhibits alternating short and long C–C distances because of the more localized nature of the double bonds in the rings and the catechol exhibits more delocalized C–C bond distances due to its aromaticity.[75-77]

Table 5-14. Crystallographic data for [Cr(tren)(PCAT)](BPh$_4$) (**7**) and [Cr(tren)(PSQ)](BPh$_4$)$_2$ (**8**).

	7	**8**
formula	$C_{44}H_{46}BCrN_4O_2$	$C_{69}H_{70}B_2CrN_4O_3$
M_w	725.66	1076.91
cryst syst	Orthorhombic	Orthorhombic
space group	*Pbca*	*Pna2(1)*
a/Å	10.2323 (12)	31.165 (3)
b/ Å	17.838 (2)	10.6549 (12)
c/ Å	39.772 (5)	17.2766 (19)
β/ °	90	90
V/ Å^3	7259.4 (15)	5736.8 (11)
Z	8	4
T/K	173(2)	173(2)
D_c/ g cm^{-3}	1.328	1.247
θ_{max}	25	25
reflns measured	68045	54464
independent reflns	6384	10085
observed reflns [$I > 2\sigma(I)$]	4159	8397
μ(Mo *K*α)/ mm^{-1}	0.36	0.25
R_{int}	0.095	0.065
R1	0.049[a]	0.047
*w*R2	0.13[b]	0.1
GOF	0.99	1.02

[a] $R1 = \Sigma||F_O| - |F_C||/ \Sigma|F_O|$. [b] $wR2 = [\Sigma w(F_O^2 - F_C^2)/\Sigma w(F_O^2)^2]^{1/2}$, $w = 1/[\sigma^2(F_O^2) + (aP)^2 + bP]$, where $P = (F_O^2 + 2F_C^2)/3$.

Table 5-15. Selected bond distances and angles for [Cr(tren)(PCAT)](BPh$_4$) (**7**) and [Cr(tren)(PSQ)](BPh$_4$)$_2$ (**8**).

	7	**8**
	Bond Distances (Å)	
Cr(1)–O(1)	1.914(2)	1.9223(18)
Cr(1)–O(2)	1.936(2)	1.961(2)
Cr(1)–N(1)	2.122(3)	2.075(2)
Cr(1)-N(2)	2.085(3)	2.065(3)
Cr(1)–N(3)	2.071(3)	2.074(2)
Cr(1)–N(4)	2.079(3)	2.057(2)
C(10)–O(1)	1.349(4)	1.303(3)
C(9)–O(2)	1.366(3)	1.311(3)
C(9)–C(10)	1.359(4)	1.400(4)
C(9)–C(14)	1.436(4)	1.429(4)
C(14)–C(13)	1.429(4)	1.424(4)
C(13)–C(12)	1.449(4)	1.450(5)
C(12)–C(11)	1.425(4)	1.411(4)
C(11)–C(10)	1.435(4)	1.438(4)
	Bond Angles (deg)	
O(1)–Cr(1)–N(1)	97.74(10)	100.16(9)
O(1)–Cr(1)–N(2)	95.40(9)	96.90(9)
O(1)–Cr(1)–N(3)	97.97(10)	93.85(9)
O(1)–Cr(1)–N(4)	177.44(10)	176.14(9)
O(1)–Cr(1)–O(2)	86.05(9)	82.24(8)
O(2)–Cr(1)–N(1)	85.03(10)	87.51(10)
O(2)–Cr(1)–N(2)	177.85(10)	178.10(10)
O(2)–Cr(1)–N(3)	89.26(10)	88.29(10)
O(2)–Cr(1)–N(4)	96.38(9)	97.19(9)
N(1)–Cr(1)–N(2)	93.19(11)	90.98(11)
N(1)–Cr(1)–N(3)	162.86(11)	164.69(11)
N(1)–Cr(1)–N(4)	81.70(11)	83.61(10)
N(2)–Cr(1)–N(3)	92.11(11)	93.46(11)
N(2)–Cr(1)–N(4)	82.15(10)	83.78(9)
N(3)–Cr(1)–N(4)	82.90(10)	82.31(10)
C(9)–O(2)–Cr(1)	108.72(17)	111.84(18)
C(10)–O(1)–Cr(1)	109.43(18)	113.27(17)
O(1)–C(10)–C(9)	118.5(3)	116.3(3)

Electronic Absorption Spectroscopy. The normalized absorption spectra of the Cr-PSQ (**8**), Cr-3,6-di-NO$_2$-PSQ (**10**), and Ga-PSQ (**12**) taken in acetonitrile are shown in

Figure 5-40 below. The chromium spectra are quite rich, and the absorption features are listed in Table 5-15 and compared to **12** to aid in the assignments. The transitions at 22300, 23300, 28300, and 30100 cm^{-1} for **8** are due to intraligand transitions upon comparison to the Ga-PSQ analogue. Analogously, the absorptions at 23300, 24900, and 26950 cm^{-1} for **10** are also intraligand transitions. The transitions at 21000 and (18300 and 21150) cm^{-1} are assigned to charge transfer transitions for **8** and **10**, respectively, since these features are not observed in the Ga-PSQ complex for which charge transfer transitions are highly unlikely. The sharp lower energy bands in both chromium complexes (15000-16500 cm^{-1}) are characteristic of intraconfigurational transitions, and their location in the spectrum is consistent with transitions having $^4A_{2g} \rightarrow {}^2E_g$ and/or $^2T_{1g}$ parentage.

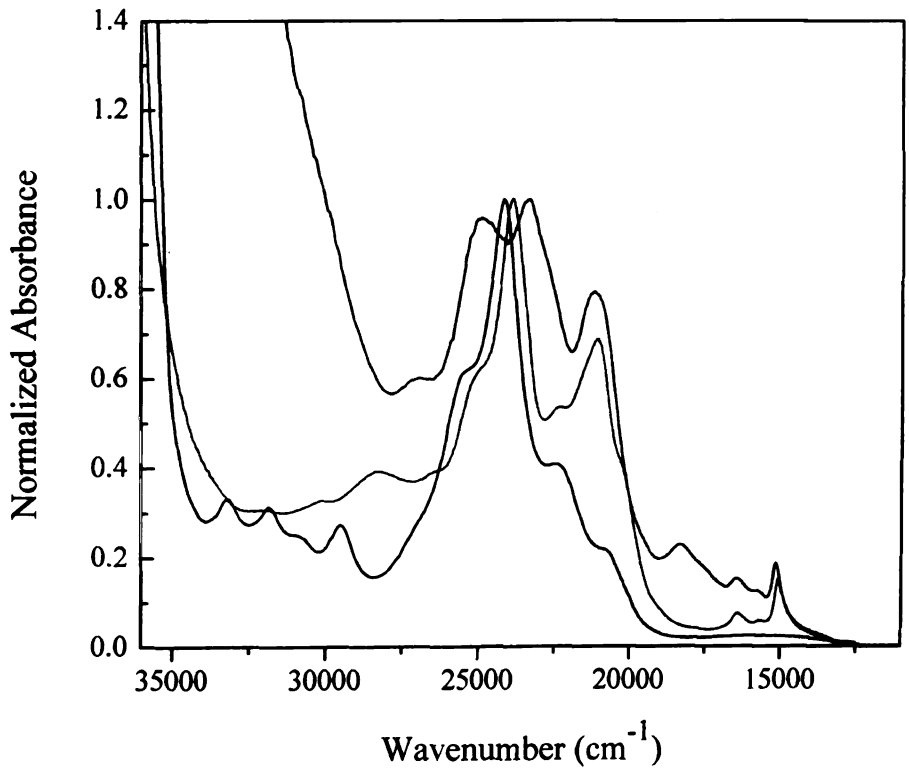

Figure 5-40. The normalized absorption spectra of $[Cr(tren)(PSQ)](BPh_4)_2$ (**8**) (red), $[Cr(tren)(3,6\text{-di-}NO_2\text{-PSQ})](BF_4)_2$ (**10**) (green), and $[Ga(tren)(PSQ)](BPh_4)_2$ (blue) (**12**).

Table 5-15. Comparison of the absorption features in $[Cr(tren)(PSQ)](BPh_4)_2$ (**8**), $[Cr(tren)(3,6\text{-di-}NO_2\text{-}PSQ)](BF_4)_2$ (**10**), and $[Ga(tren)(PSQ)](BPh_4)_2$ (blue) (**12**), where LMCT = ligand-to-metal charge transfer transition.

$[Ga(tren)(PSQ)](BPh_4)_2$	$[Cr(tren)(PSQ)](BPh_4)_2$	$[Cr(tren)(3,6\text{-di-}NO_2\text{-}PSQ)](BPh_4)_2$
	15000 (d-d)	15150 (d-d)
	15600 (d-d)	15700 (d-d)
	16400 (d-d)	16450 (d-d)
	21000 (LMCT)	18300 (LMCT)
22400 (IL)	22300 (IL)	21150 (LMCT)
24100 (IL)	23900 (IL)	23300 (IL)
29500 (IL)	28300 (IL)	24900 (IL)
31800 (IL)	30100 (IL)	26950 (IL)

Their origin is due to exchange-enhanced ligand-field absorptions of the Cr^{III} ion.[19,56,94] Heisenberg exchange coupling in the excited state manifold of these complexes gives rise to the formation of new electronic states with different spin, and as a result formally spin forbidden transitions become spin allowed transitions when exchange coupling is operative. McCusker and coworkers[56,94] have laid out a detailed analysis of the effect of Heisenberg exchange coupling on the electronic structure of these molecules, and this will not be further elaborated upon here.

Magnetic Susceptibility. Plots of the temperature dependent magnetic susceptibility for **8** and **10** are depicted in figure 5-41 below. The data in Figure 5-41 indicate that $\mu_{eff} = 2.81\ \mu_B$ for **8** and $\mu_{eff} = 2.98\ \mu_B$ for **10** at 300 K, which agrees with the spin only value for an S = 1 spin state of $\mu_{eff} = 2.87\ \mu_B$, thus confirming the ground state of the molecule is S = 1. There is a slight rise in the data over the temperature range and according to the similar $[Cr(tren)(3,5\text{-di-}t\text{-butylsemiquinone})](PF_6)_2$ complex in the literature,[94] this can be assigned to temperature independent paramagnetism in the sample, which is manifested as a $T^{1/2}$ dependence in the data. Just as in the Ni-PSQ

complexes, the exchange coupling is strong and J can not be determined. This is not too surprising, since the DFT calculations actually predict that the coupling constants should be at least 2 times greater in magnitude then that of the Ni-PSQ systems. The predicted increase is not surprising either, since the magnetic orbitals actually overlap in the case of the Cr-PSQ complexes and should yield a greater interaction than the repulsion-type interaction observed for ferromagnetism. It is evident then that to observe temperature dependent magnetic data in a series of these types of complexes a new radical ligand system must be designed that greatly reduces the spin density at the oxygen centers.

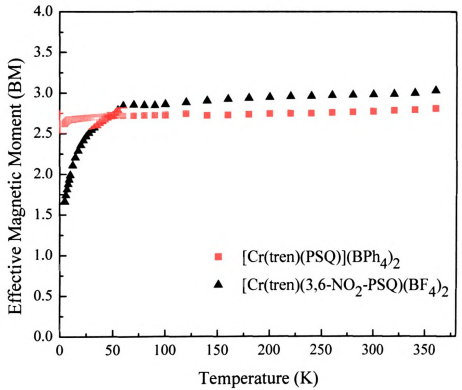

Figure 5-41. The temperature dependent SQUID susceptibility of [Cr(tren)(PSQ)]$(BPh_4)_2$ (**8**) (red square) and [Cr(tren)(3,6-di-NO_2-PSQ)]$(BF_4)_2$ (**10**) (green triangle).

5.3.6 Concluding Comments

Several salient relationships have been developed in this chapter, and most importantly the proper choice of substituents can modulate the *J* value for both ferromagnetic and antiferromagnetic complexes. Electron donors and acceptors were found to decrease and increase the *J* value, respectively. Linear correlations were found between *J* and the average spin density at the oxygen centers in both the Cr^{III}- and Ni^{II}-PSQ complexes, and the spin population at oxygen dictates the magnitude of the Heisenberg exchange coupling constant. The proportionality, $J \sim \rho_M \rho_{SQ}$, has been found to be valid for both ferromagnetic and antiferromagnetic exchange coupling. The spin density also varies with opposite polarization to the charge density for all substituents examined, and the Hammett constants σ_p and σ_p^+ correlate linearly with the exchange coupling constant. The α-HOMO-α-LUMO gap in the Ni^{II}-PSQ's and the β-HOMO-β-LUMO gap in the Cr^{III}-PSQ complexes has been identified as a marker for the spin delocalization in the molecules. Where decreases in the HOMO-LUMO gap mirror increases in spin delocalization, increases in the HOMO-LUMO gap will reflect increased spin localization at the oxygen atoms. The amount of mixing between the M-$3d_{XZ}$ orbitals and the PSQ-SOMO is the main factor that controls the HOMO-LUMO gap. Two main factors have been identified to describe the mixing. First, electron acceptors will lower the energy of the PSQ-SOMO, thereby causing a decreased energetic match between the M-$3d_{XZ}$ and the PSQ-SOMO orbitals, resulting in less spin delocalization. Secondly, electron donors will raise the energy of the PSQ-SOMO, which will result in greater spin delocalization due to the better energetic match between the M-$3d_{XZ}$ and the PSQ-SOMO orbitals. There were outliers observed in the Ni^{II}-PSQ spin density vs. α-HOMO-α-LUMO gap correlation, and interactions with energetically higher

lying orbitals were suggested as being the cause of the deviations. This is similar to what has been observed in the phenoxy radical complexes. The Cr^{III}-PSQ spin density correlation with the β-HOMO-β-LUMO gap does not exhibit any deviations, because only two orbitals are interacting to produce the β-HOMO-β-LUMO gap. This piece of evidence gives strong support for the removal of the outliers in the Ni^{II}-PSQ and phenoxy radical α-HOMO-α-LUMO gap correlations, since the substituents correlate with the HOMO-LUMO gap if no more than two orbitals are involved in the orbital interaction.

Unfortunately, experimental evidence for an entire series of complexes could not be found in this examination, which is a direct result of the strong ferromagnetic and antiferromagnetic exchange coupling constants precluding us from seeing temperature dependence in the magnetic susceptibility data. Temperature dependence was observed in the $[Ni(tren)(3,6\text{-di-}NH_2\text{-PSQ})]^+$ (**6**) complex, and J was determined to be -119 cm^{-1}. DFT had predicted that the spin density at oxygen and thus the J value should be smaller in the case of the **6** versus the $[Ni(tren)(PSQ)]^+$ (**1**) or $[Ni(tren)(3,6\text{-di-}NO_2\text{-PSQ})]^+$ (**5**) complexes. The DFT data is supported in our SQUID data because we were able to fit the susceptibility data to extract a J value in **6**, but **1** and **5** have too strong a coupling constant (not allowing experimental determination of J). These are the only two experimental points that could be determined from the Ni^{II}-PSQ examinations, and to properly describe the correlation between J and the spin density at oxygen at least three complexes with experimentally determined J values are required. The experimental SQUID data for the Cr^{III}-PSQ complexes also indicated that J is too strong to be experimentally determined. Therefore due to the lack of experimental data to confirm the relationship between the magnitude of J and the spin density, a new easily substituted

radical ligand system must be designed to decrease the spin density at the oxygen atoms even greater than in the PSQ radicals. Possible pathways to continue this work will be explored in the future work section of Chapter 6.

5.5 References

1 Luneau, D. *Curr. Opin. Solid State Mater. Sci.* **2001**, *5*, 123.

2 Öhrstrom, L. *C. R. Chimie* **2005**, *8*, 1374.

3 Shultz, D. A. *Polyhedron* **2001**, *20*, 1627.

4 Caneschi, A.; Gatteschi, D.; Sessoli, R.; Rey, P. *Acc. Chem. Res.* **1989**, *22*, 392.

5 Vostrikova, K. E. *Coord. Chem. Rev.* **2008**, *252*, 1409.

6 Kahn, O.; Martinez, C. J. *Science* **1998**, *279*, 44.

7 Mishustin, A. I. *Russ. J. Inorg. Chem.* **2008**, *53*, 1376.

8 Osanai, K.; Okazawa, A.; Nogami, T.; Ishida, T. *J. Am. Chem. Soc.* **2006**, *128*, 14008.

9 McConnell, H., M, *J. Chem. Phys.* **1963**, *39*, 1910.

10 Hicks, R. G.; Lemaire, M. T.; Thompson, L. K.; Barclay, T. M. *J. Am. Chem. Soc.* **2000**, *122*, 8077.

11 Sugiura, K.-I.; Arif, A. M.; Rittenberg, D. K.; Schweizer, J.; Öhrstrom, L.; Epstein, A. J.; Miller, J. S. *Chem. Eur. J.* **1997**, *3*, 138.

12 Shultz, D. A.; Sloop, J. C.; Washington, G. *J. Org. Chem.* **2006**, *71*, 9104.

13 Shultz, D. A.; Sloop, J. C.; Coote, T.-A.; Beikmohammadi, M.; Kampf, J.; Boyle, P. D. *Inorg. Chem.* **2007**, *46*, 273.

14 Gordon, D. J.; Fenske, R. F. *Inorg. Chem.* **1982**, *21*, 2907.

15 Ginsberg, A. P. *Inorg. Chim. Acta. Rev.* **1971**, *5*, 45.

16 Kahn, O.; Charlot, M. F. *Nouv. J. Chim.* **1980**, *4*, 567.

17 Benelli, C.; Dei, A.; Gatteschi, D.; Pardi, L. *Inorg. Chem.* **1988**, *27*, 2831.

18 Benelli, C.; Dei, A.; Gatteschi, D.; Pardi, L. *Inorg. Chem.* **1989**, *28*, 1476.

19 Benelli, C.; Dei, A.; Gatteschi, D.; Güdel, H. U.; Pardi, L. *Inorg. Chem.* **1989**, *28*, 3091.

20 Ciofini, I.; Daul, C. A. *Coord. Chem. Rev.* **2003**, *238-239*, 187.

21 Noodleman, L. *J. Chem. Phys.* **1981**, *74*, 5737.

22 Noodleman, L.; Case, D. A. *Adv. Inorg. Chem.* **1992**, *38*, 423.

23 Noodleman, L.; Norman Jr., J. G. *J. Chem. Phys.* **1979**, *70*, 4903.

24 Chłopek, K.; Muresan, N.; Neese, F.; Wieghardt, K. *Chem. Eur. J.* **2007**, *13*, 8390.

25 Chłopek, K.; Bothe, E.; Neese, F.; Weyhermüller, T.; Wieghardt, K. *Inorg. Chem.* **2006**, *45*, 6298.

26 Ghosh, P.; Bill, E.; Weyermüeller, T.; Neese, F.; Wieghardt, K. *J. Am. Chem. Soc.* **2003**, *125*, 1293.

27 Blanchard, S.; Neese, F.; Bothe, E.; Bill, E.; Weyermüeller, T.; Wieghardt, K. *Inorg. Chem.* **2005**, *44*, 3636.

28 Herebian, D.; Wieghardt, K. E.; Neese, F. *J. Am. Chem. Soc.* **2003**, *125*, 10997.

29 Bencini, A.; Daul, C. A.; Dei, A.; Mariotti, F.; Lee, H.; Shultz, D. A.; Sorace, L. *Inorg. Chem.* **2001**, *40*, 1582.

30 Ovcharenko, V. I.; Gorelik, E. V.; Fokin, S. V.; Romanenko, G. V.; Ikorskii, V. N.; Krashilina, A. V.; Cherkasov, V. K.; Abakumov, G. A. *J. Am. Chem. Soc.* **2007**, *129*, 10512.

31 Bencini, A.; Carbonera, C.; Dei, A.; Vaz, M. G. F. *Dalton Trans.* **2003**, 1701.

32 Rodriguez, J. H.; Wheeler, D. E.; McCusker, J. K. *J. Am. Chem. Soc.* **1998**, *120*, 12051.

33 Kapre, R. R.; Bothe, E.; Weyermüeller, T.; George, S. D.; Muresan, N.; Wieghardt, K. *Inorg. Chem.* **2007**, *46*, 7827.

34 Fehir Jr., R. J. PhD, Michigan State University, 2009.

35 Zipp, S. G.; Madan, S. K. *Inorg. Chem.* **1976**, *15*, 587.

36 Allcock, H. R.; Primrose, A. P.; Silverberg, E. N.; Visscher, K. B.; Rheingold, A. L.; Guzei, I. A.; Parvez, M. *Chem. Mater.* **2000**, *12*, 2530.

37 Anschütz, R.; Meyer, P. *Chem. Ber.* **1885**, *18*, 1942.

38 Aggarwal, R. P.; Connelly, N. G.; Crespo, M. C.; Dunne, B. J.; Hopkins, P. M.; Orpen, A. G. *J. Chem. Soc. Dalton Trans.* **1992**, 655.

39 Cotton, F. A.; Jordan IV, G. T.; Murillo, C. A.; Su, J. *Polyhedron* **1997**, *16*, 1831.

40 Vierling, P.; Guillon, C. *J. Organomet. Chem.* **1994**, *464*, C42.

41 Hughes, R. P.; Lindner, D. C.; Rheingold, A. L.; Yap, G. P. A. *Inorg. Chem.* **1997**, *36*, 1726.

42 Hayashi, Y.; Rohde, J. J.; Corey, E. J. *J. Am. Chem. Soc.* **1996**, *118*, 5502.

43 Perkins, C. M. PhD Thesis, University of Washington, 1980.

44 *SAINT*, ver 6.02a; Bruker AXS, Inc.: Madison, WI, 2000.

45 Sheldrick, G. M.*SADABS*, ver 2.03; Bruker AXS, Inc.: Madison, WI, 2000.

46 Sheldrick, G. M.*SHELXTL*, ver 6.12; Bruker AXS, Inc.: Madison, WI, 2001.

47 Löliger, J.; Scheffold, R. *J. Chem. Educ.* **1972**, *49*, 646.

48 Adams, D. M.; Hendrickson, D. N. *J. Am. Chem. Soc.* **1996**, *118*, 11515.

49 Adams, D. M.; Noodleman, L.; Hendrickson, D. N. *Inorg. Chem.* **1997**, *36*, 3966.

50 *GaussView*, 2.1 ed.; Gaussian, Inc.: Pittsburgh, PA, 2001.

51 Frisch, M. J.; Trucks, G. W.; Schlegel, H. B.; Scuseria, G. E.; Robb, M. A.; Cheeseman, J. R.; Zakrzewski, V. G.; Montgomery, J. A., Jr.; Stratmann, R. E.; Burant, J. C.; Dapprich, S.; Millam, J. M.; Daniels, A. D.; Kudin, K. N.; Strain, M. C.; Farkas, O.; Tomasi, J.; Barone, V.; Cossi, M.; Cammi, R.; Mennucci, B.; Pomelli, C.; Adamo, C.; Clifford, S.; Ochterski, J.; Petersson, G. A.; Ayala, P. Y.; Cui, Q.; Morokuma, K.; Malick, D. K.; Rabuck, A. D.; Raghavachari, K.; Foresman, J. B.; Cioslowski, J.; Ortiz, J. V.; Stefanov, B. B.; Liu, G.; Liashenko, A.; Piskorz, P.; Komaromi, I.; Gomperts, R.; Martin, R. L.; Fox, D. J.; Keith, T.; Al-Laham, M. A.; Peng, C. Y.; Nanayakkara, A.; Gonzalez, C.; Challacombe, M.; Gill, P. M. W.; Johnson, B.; Chen, W.; Wong, M. W.; Andres, J. L.; Gonzalez, C.; Head-Gordon, M.; Replogle, E. S.; Pople, J. A. *Gaussian 98, revision A.4*, Gaussian, Inc.: Pittsburgh, PA, 1998.

52 M. J. Frisch, G. W. T., H. B. Schlegel, G. E. Scuseria; M. A. Robb, J. R. C., J. A. Montgomery, Jr., T. Vreven; K. N. Kudin, J. C. B., J. M. Millam, S. S. Iyengar, J. Tomasi; V. Barone, B. M., M. Cossi, G. Scalmani, N. Rega; G. A. Petersson, H. N., M. Hada, M. Ehara, K. Toyota; R. Fukuda, J. H., M. Ishida, T. Nakajima, Y. Honda, O. Kitao; H. Nakai, M. K., X. Li, J. E. Knox, H. P. Hratchian, J. B. Cross; V. Bakken, C. A., J. Jaramillo, R. Gomperts, R. E. Stratmann; O. Yazyev, A. J. A., R. Cammi, C. Pomelli, J. W. Ochterski; P. Y. Ayala, K. M., G. A. Voth, P. Salvador, J. J. Dannenberg; V. G. Zakrzewski, S. D., A. D. Daniels, M. C. Strain;

O. Farkas, D. K. M., A. D. Rabuck, K. Raghavachari; J. B. Foresman, J. V. O., Q. Cui, A. G. Baboul, S. Clifford; J. Cioslowski, B. B. S., G. Liu, A. Liashenko, P. Piskorz; I. Komaromi, R. L. M., D. J. Fox, T. Keith, M. A. Al-Laham; C. Y. Peng, A. N., M. Challacombe, P. M. W. Gill; B. Johnson, W. C., M. W. Wong, C. Gonzalez, and J. A. Pople, *Gaussian 03*, Revision D.01; Gaussian, Inc.: Wallingford CT, 2004.

53 Glendening, E. D.; Reed, A. E.; Carpenter, J. E.; Weinhold, F. *NBO 3.1*, Theoretical Chemistry Institute, University of Wisconsin: Madison, WI, 1996.

54 Frisch, M. J.; Frisch, A. *Gaussian 98 User's Reference*; Gaussian, Inc.: Pittsburgh, 1998.

55 Zanello, P.; Corsini, M. *Coord. Chem. Rev.* **2006**, *250*, 2000, and references therein.

56 Guo, D.; McCusker, J. K. *Inorg. Chem.* **2007**, *46*, 3257.

57 Evans, D. F. *J. Chem. Soc.* **1959**, 2003.

58 Grant, D. H. *J. Chem. Educ.* **1995**, *72*, 39.

59 Brown, D. B.; Crawford, V. H.; Hall, J. W.; Hatfield, W. E. *J. Phys. Chem.* **1977**, *81*, 1303.

60 *CRC Handbook of Chemistry and Physics*; 89 ed.; CRC Press: Boca Raton, FL., 2009.

61 Yamaguchi, K.; Jensen, F.; Dorigo, A.; Houk, K. *Chem Phys. Lett.* **1988**, *149*, 537.

62 Soda, T.; Kitagawa, Y.; Onishi, T.; Takano, Y.; Shigeta, Y.; Nagao, H.; Yoshioka, Y.; Yamaguchi, K. *Chem Phys. Lett.* **2000**, *319*, 223, and references therein.

63 Bencini, A. *Inorg. Chim. Acta.* **2008**, *361*, 3820.

64 Rodriguez, J. H.; McCusker, J. K. *J. Chem. Phys.* **2002**, *116*, 6253.

65 Ruiz, E.; Cano, J.; Alvarez, S.; Alemany, P. *J. Comp. Chem.* **1999**, *20*, 1391.

66 Caballol, R.; Castell, O.; Illas, F.; de P. R. Moreira, I.; Malrieu, J. P. *J. Phys. Chem. A* **1997**, *101*, 7860.

67 Kahn, O.; Prins, R.; Reedijk, J.; Thompson, J. S. *Inorg. Chem.* **1987**, *26*, 3557.

68 Kahn, O. *Molecular Magnetism*; VCH Publishers: New York, 1993.

69 Krenske, E. H.; Coote, M. L. *J. Phys. Chem. A* **2007**, *111*, 8229.

70 Creary, X. *J. Org. Chem.* **1980**, *45*, 280.

71 Zhang, Y. Q.; Luo, C. L. *J. Mater. Chem.* **2006**, *16*, 4657.

72 Zhang, Y. Q.; Luo, C. L. *Eur. J. Inorg. Chem.* **2006**, *11*, 2292.

73 Zhang, Y. Q.; Luo, C. L. *J. Phys. Chem. A* **2006**, *110*, 5096.

74 Schenck, G. O.; Schmidt-Thombée, G. A. *Ann. Chem.* **1953**, *584*, 199.

75 Pierpont, C. G.; Buchanan, R. M. *Coord. Chem. Rev.* **1981**, *38*, 45.

76 Pierpont, C. G.; Attia, A. S. *Collect. Czech. Chem. Commun.* **2001**, *66*, 33.

77 Pierpont, C. G.; Lange, C. W. *Prog. Inorg. Chem.* **1994**, *41*, 331.

78 Olson, D. C.; Vasilevskij, J. *Inorg. Chem.* **1969**, *8*, 1611.

79 Nag, K.; Chakravorty, A. *Coord. Chem. Rev.* **1980**, *33*, 87.

80 Jovanovic, S. V. *J. Phys. Chem.* **1991**, *95*, 10824.

81 Bordwell, F. G.; Cheng, J.-P. *J. Am. Chem. Soc.* **1991**, *113*, 1736.

82 Lind, J.; Shen, X.; Eriksen, T. E.; Merényi, G. *J. Am. Chem. Soc.* **1990**, *112*, 479.

83 Bencini, A.; Gatteschi, D. *EPR of Exchange Coupled Systems*; Springer-Verlag: Berlin, Heidelberg, 1990.

84 *XSOPHE*, Computer Simulation Software Suite 1.1.4; Center for Magnetic Resonance and Department of Mathmatics, The University of Queensland (Brisbane, Queensland, Australia 4072) and Bruker Biospin GMBH (formerly Buruker Analytik; Rheinstetten, Germany): 1993-2004.

85 Mueller, J.; Kikuchi, A.; Bill, E.; Weyermueller, T.; Hildebrandt, P.; Ould-Moussa, L.; Wieghardt, K. *Inorganica Chimica Acta* **2000**, *297*, 265.

86 Adam, W.; Barneveld, C. V. *J. Am. Chem. Soc.* **1999**, *121*, 10820.

87 Adam, W.; Kita, F.; Harrer, H. M.; Nau, W. M.; Zipf, R. *J. Org. Chem.* **1996**, *61*, 7056.

88 Adam, W.; Schulte, C. M. O. *J. Org. Chem.* **2002**, *67*, 4569.

89 Schmitt, E. A., Department Of Chemistry, University of Illinois, 1996.

90 Barclay, T. M.; Hicks, R. G.; Lemaire, M. T.; Thompson, L. K. *Chem. Commun.* **2000**, 2141.

91 Brown, H. C.; Okamoto, Y. *J. Am. Chem. Soc.* **1958**, *80*, 4979.

92 Hansch, C.; Leo, A.; Taft, R. W. *Chem. Rev.* **1991**, *91*, 165.

93 Liu, C.; Hu, H.; Yang, X. *Chem. Phys. Lett.* **2001**, *349*, 89.

94 Wheeler, D. E.; McCusker, J. K. *Inorg. Chem.* **1998**, *37*, 2296.

Chapter 6. Concluding Comments and Future Directions

6.1 Concluding Comments

All of the research in this dissertation has been focused on using substituents to develop a prescription for the movement of spin and charge density in radicals and transition metal radical complexes. Based on the reasonable assumption that one of the major variables responsible for the modulation of J was the spin density population at the oxygen magnetic centers, it was the overall goal of this work to develop a theoretical model for the substituent modulation of the exchange coupling constant based on DFT calculations. Then experimental magnetic susceptibility measurements of transition metal radical complexes would be done to verify this theory. The majority of the work was split up into two fronts, one computational and one experimental; the major successes of each realm of the project will be elaborated upon below.

To begin this examination, it was necessary to understand the fundamental polarization of spin and charge density in simple systems. It is known that spin and charge can be differentially polarized, but little is known about the mechanism which controls spin and charge density in a molecule. The system chosen was the phenoxy radical, since it is the simplest oxygen center radical that could be used to simulate the semiquinone radicals that we eventually wanted to study. Correlations of the charge density with the Hammett substituent constants were discovered, and easily rationalized based upon simple electronegativity arguments. Similar correlations between the spin density and the Hammett spin delocalization substituent constants produced poor results, so therefore other correlations were sought after. A completely empirical correlation

between the α-HOMO-α-LUMO gap and the change in spin density at the oxygen atoms was found. This correlation can be considered to be a marker which describes the spin delocalization in these systems. A three-electron, two-orbital model was evoked to explain the α-HOMO-α-LUMO gap correlation, where the energy of the α-LUMO orbital was assumed to be largely unchanged in each complex. The energy of the α-HOMO orbital was then influenced by the type of *para*-substituent in the phenoxy radical, and electron-donating substituents increased the energy of the α-HOMO and electron acceptors lowered the energy of the α-HOMO. The mixing between a π-donor lone pair orbital with the phenoxy SOMO was found to influence the energy of the α-HOMO. As the donating character of a substituent was increased, a better energetic match between the π-donor lone pair orbital and the phenoxy SOMO would occur. This has two important consequences. First, the energy of the α-HOMO would increase due to an increased mixing interaction between these orbitals, and the HOMO-LUMO gap would decrease due to the higher energy α-HOMO (assuming the energy of the α-LUMO remains constant). Secondly, the increased mixing between the orbitals also increases the spin delocalization from the oxygen radical center to the substituent. The strong π-accepting substituents were found to deviate from the α-HOMO-α-LUMO gap correlation, and interactions with higher lying orbitals were shown to be the reason for the outliers. Overall, the correlation is quite strong and can be used to predict which substituents will increase or decrease spin density at a radical center. To my knowledge, this was the first instance of a correlation between spin density at a radical center with the α-HOMO-α-LUMO gap. The predictable ability to differentially polarize spin and

charge density in the phenoxy radical led us to see if the same correlations would hold for substituted *o*-semiquinones.

The simplest *o*-1,2-semiquinones to examine are the 4,5-di-R-*o*-1,2-semiquinones and the 3,6-di-R-*o*-1,2-semiquinones, and these systems were examined by the same DFT methods as the phenoxy radicals. It was found that spin and charge density can be differentially polarized, but to a lesser extent than the phenoxy radical case. Similar correlations with the Hammett substituents constants were found, and the charge density at the semiquinone oxygen atoms can be reliably estimated from these constants. In the *o*-semiquinone complexes, it was found that electron acceptors decreased the spin density and strong π-electron donors increased the spin density at the oxygen atoms. A paradigm shift for the π-donor substituents was observed, and now they are spin localizing instead of strongly delocalizing as in the case of the phenoxy radicals. Unfavorable resonance interactions between the charge separated resonance structures and the delocalized negative charge can be cited as the possible cause for this change. For the 3,6-di-R-*o*-1,2-semiquinones the spin density at the oxygen atom correlates with the α-HOMO-α-LUMO gap, and this correlation seems to be present for both neutral and anion radicals. The 9,10-*o*-phenanthrenesemiquinones substituted at the 3,6- and 2,7-positions were also examined, since their more delocalized structures may better shift the spin density away from the oxygen atoms. This was indeed confirmed and the α-spin population at the oxygen atoms in the unsubstituted *o*-1,2-semiquinone is 0.2634 electrons and in phenanthrenesemiquinone it is 0.2570 electrons. Analogous to the other semiquinones examined the phenanthrenesemiquinones charge density correlated with the Hammett parameters, and the spin density correlated with the α-HOMO-α-LUMO gap. There were

some deviations in the HOMO-LUMO gap correlations just as in the phenoxy case, but unfortunately the calculated molecular orbital information was inconclusive in aiding in the determination of the mechanism for the outliers. Based upon the phenoxy radical data, we can say to a first approximation that one or more higher lying orbitals are likely involved in causing the observed deviations. The underlying message of the semiquinone work was that the HOMO-LUMO gap was still a marker for the spin delocalization in radicals, but more work is needed to understand the mechanism for spin polarization.

Once we understood the theoretical prescription for the spin density variations, we wanted to see if this could be proved experimentally with EPR measurements. Additionally, we were also interested in the effects on the spin density distribution upon coordination of the radicals to a diamagnetic metal center. To this end, 2,7-di-NO_2 and 3,6-di-NO_2-phenanthrenesemiquinones and Ga^{III}-complexes with these same radical ligands were synthesized and characterized by X-Band EPR and ESEEM spectroscopy as well as DFT calculations. The ^{14}N hyperfine coupling constants (HFC) gave us experimental evidence for the amount of spin density delocalized onto the nitrogen atoms of the NO_2 groups, and thus the spin delocalizing ability of these substituents at these positions was known. The X-band EPR data and the DFT calculations of the ^{1}H and ^{14}N hyperfine coupling constants for the two radical ligands were in excellent agreement, and both predicted small spin density polarizations at the nitrogen atoms. The Ga^{III} complexes exhibited very different spin populations at nitrogen as determined by ^{14}N ESEEM spectroscopy. The small magnitude ^{14}N HFC for the Ga-3,6-di-NO_2-PSQ complex agreed quite well with the DFT data, and also correlated with the free ligand value. The magnitude of the ^{14}N HFC for Ga-2,7-di-NO_2-PSQ was much greater than the

3,6-isomer. The ESEEM data suggested that the spin density at the nitrogen in the Ga-2,7-di-NO_2-PSQ complex was due to direct spin delocalization onto the nitrogen atom, and the Ga-3,6-di-NO_2-PSQ complexes spin population at nitrogen is due to spin polarization interactions. DFT ^{14}N HFC values were a factor of 7 times too small for the Ga-2,7-di-NO_2-PSQ complex. The failure of DFT in this case has been suggested to be due to large self-interaction errors, and the transition metal electric field causes an "overpolarization" of the spin density distribution in the Ga^{III} complexes. This was confirmed by executing a DFT calculation of the free ligands in an electric field applied along the axis of the oxygen atoms, and an identical spin polarization to the gallium cases was observed. Two main points can be made about the above EPR data. First, spin delocalization onto the nitrogen atoms at the 2,7-positons is more significant than the spin polarization onto the 3,6-nitrogen atoms, and substituents at these positions will most likely delocalize spin density to a greater extent. Secondly, DFT may give incorrect predictions for the spin delocalization onto substituents at the 2,7-positions in these systems. A firm mechanism for the spin delocalization/polarization mechanism could not be determined from the experiments and more work is needed to hash it out. Thus the EPR part of the project has opened the door to many possible new experiments that would be required to accurately predict the spin delocalization mechanism in these systems, and this will be elaborated upon in the future work section below.

The final aspect of this thesis work involved applying the knowledge of spin polarization that was learned in the above examinations in an attempt to predict how to increase or decrease the ferromagnetic or antiferromagnetic Heisenberg exchange coupling constants in transition metal radical complexes. The assumption that was made

was that the spin density at the oxygen atoms can be modulated with substituents to control the magnitude of the exchange coupling constants. This idea is not novel and Shultz and coworkers[1] have predicted that $J \sim \rho_M \rho_{SQ}$, but no complete examination of the mechanism to vary J by changing the spin density with substituents in transition metal semiquinones has been accomplished. The Ni^{II}-2,7-di-R-PSQ and Ni^{II}-3,6-di-R-PSQ complexes were examined for substituents effects in the ferromagnetic Heisenberg exchange coupling, and DFT has shown that the spin density correlated strongly with the J value. Additionally, J was found to correlate with the product of the spin density on the Ni^{II} center and the average spin density at the oxygen atoms, which fully supports the proportionality suggested by Shultz. It is also noteworthy that the polarization of the spin and charge density are completely differential in this case. The correlation with the α-HOMO-α-LUMO gap was again observed in the Ni^{II}-PSQ complexes, but several strongly electron-withdrawing substituents deviated from the correlation. Again it was suggested that participation of higher lying orbitals was responsible for the marked deviations, but this could not be proved conclusively using only the Ni^{II} MO data. The Cr^{III}-PSQ complexes were examined to see if the same correlations could be observed for antiferromagnetic coupling, and indeed the J value correlated strongly with average spin density at the oxygen centers and the product of the two spin densities as well. It seems that the Shultz approximation is general for both ferromagnetic and antiferromagnetic coupling, and the main variable that modulates J in these complexes is the spin density at the oxygen atoms. Interestingly, the spin density correlated very strongly with the β-HOMO-β-LUMO gap in this case, since the antiferromagnetic state requires β-spin density on the oxygen atoms, the β-HOMO is the magnetic orbital that properly describes

the exchange coupling. In the Cr^{III}-PSQ case, every single substituent correlated with the β-HOMO-β-LUMO gap and there were no outliers. A two-orbital, two-electron interaction was proposed to describe the spin delocalization in these complexes, where the Cr^{III}-$3d_{XZ}$ and PSQ-SOMO magnetic orbitals underwent a bonding-type interaction. This model only uses two molecular orbitals to generate the β-HOMO-β-LUMO gap, and there can be no interaction with other orbitals that influences this orbital mixing. This point gives additional evidence for the removal of the substituents that deviated in the Ni^{II}-PSQ, *o*-semiquinone, and phenoxy radical complexes, since all substituents correlate strongly in the Cr^{III}-PSQ case, and any other orbital interaction with the LUMO orbital is the likely reason for the outlying substituents. Thus, the Cr^{III}-PSQ and Ni^{II}-PSQ DFT data has indicated that the exchange coupling constant can be varied in a predictable fashion by using the correct substituents.

The ability to predict spin polarization and to modulate the exchange coupling constant can have far reaching applicability to aid chemists in designing molecular magnetic materials,[2-6] and increasing the *J* value in single molecule magnets can increase the temperature when the complex becomes a magnet.[7] Additionally, the control of the exchange coupling constant and spin polarization can also be important in the development of O–O bond catalysts, since it is known that exchange coupling plays a role the oxidation of alcohols to aldehydes coupled with the reduction of oxygen to peroxide in the enzyme galactose oxidase.[9,10] It is hoped that the basic research in this thesis will be a stepping stone for the design of new promising molecular magnetic materials and O–O bond forming catalysts.

6.2 Future directions

This thesis has examined the spin and charge density distribution in neutral and anion radicals, continuing this trend it may be of fundamental interest to see how the spin and charge density distributions are effected in cation radicals. Cation radicals are known to be important in biological electron transfer reactions at the photosynthetic reaction center[11,12] and for use in molecular magnetic conductors and superconductors.[13] It also has been found that the proton dissociation enthalpies of thiophenol[14]and phenol[15] cation radicals depends on the spin density population at the sulfur and oxygen centers, respectively. It would then be advantageous to determine if the spin density delocalization mechanism involves the α-HOMO-α-LUMO gap as was observed in the phenoxy and semiquinone radicals to see if the observed correlations are general for neutral, anion, and cation radicals.

Several EPR experiments should also be conducted in the dinitro-substituted Ga-PSQ complexes and radical ligands to aid in the determination of the spin delocalization/polarization mechanism. EPR or ESEEM of ^{17}O ($I = {}^{5}/_{2}$) labeled PSQ ligands would identify the spin density at the oxygen nucleus. If additional Ga^{III}-complexes/radicals such as the unsubstituted and 3,6- and 2,7-di-NH_2-PSQ were also prepared, then the spin density could then be monitored for a substituent effect. Synthetic procedures for ^{17}O-labeled semiquinones have been published, where exchange with $H_2{}^{17}O$ at 60 °C for 3 days produced the desired compounds.[16] If this simple procedure does not work, an alternate would be an epoxidation reaction of phenanthrene in $H_2{}^{17}O$ followed by reaction with perchloric acid in ^{17}O-labeled water to yield the phenanthrenecatechol ligand (Scheme 6-1).[17,18] Selective deuteration around the PSQ

ring would also be useful, since ^{2}H (I = 1) can be identified in ESEEM experiments and in determining HFC in X-band ENDOR[19] (electron double nuclear resonance spectroscopy) experiments. W-band (~95 GHz) EPR experiments may also prove to be useful, depending on the results of the above X-band experiments.

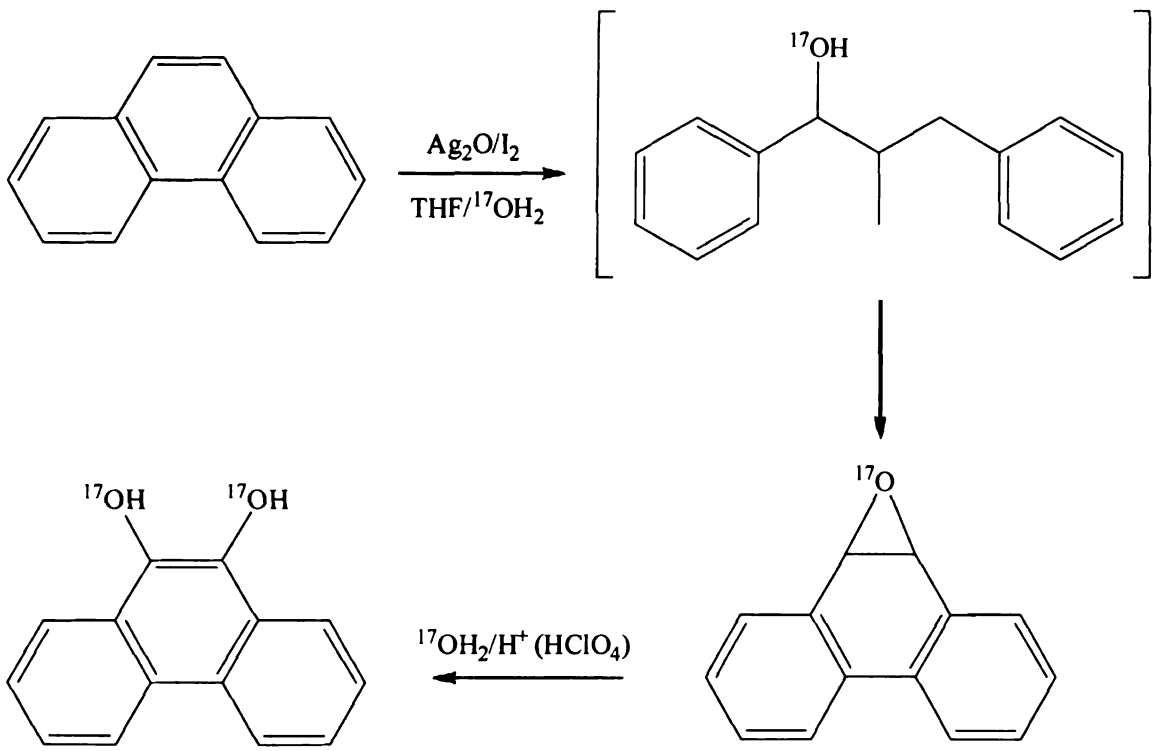

Scheme 6-1. Synthesis of ^{17}O labeled phenanthrenecatechol.

The determination of the signs of all HFC would be highly desired to make a convincing argument for the spin delocalization/polarization mechanism in these systems. A combination of EPR, ENDOR, and TRIPLE[20] (electron nuclear triple resonance) spectroscopy is required to experimentally determine the signs of the HFC. In general, TRIPLE experiments monitor the effect of simultaneous excitation of two nuclear spin transitions on the level of the EPR absorption.[21] From the characteristic intensity changes of the high-frequency and low-frequency signals compared to those of the ENDOR

signals, the relative signs of the HFC's can be determined.[20,21] The signs of the HFC's could then be compared to the DFT calculations and the delocalization/polarization mechanism could be firmly explained.

DFT calculations in the Ga^{III}-radicals have provided inconclusive results between the different radical isomers, suggesting DFT's inability to model the spin density distribution in this particular system. Higher level calculations such as complete active space (CASSCF) or coupled cluster methods CCSD(T) have been shown to qualitatively determine the spin density for polyene radical chains.[22] Additionally, the Pariser-Parr-Pople semiempirical model yielded the correct spin distribution in the chain.[22] Higher level calculations or semiempirical methods such as these may be needed to accurately model the spin delocalization/polarization in these Ga^{III}-PSQ complexes.

The Ni^{II} and Cr^{III}-PSQ complexes did suggest that spin density delocalization by electron donors reduced the magnitude of the exchange coupling constant. Although, more experimental points are needed to unequivocally prove the DFT results. The first experiment to try would be ^{17}O EPR of the series of Ni-PSQ compounds since the ^{17}O HFC would give an experimental spin density at oxygen that could be compared with DFT calculations. To experimentally determine the exchange coupling constants a new ligand system is required that can delocalize spin to a greater degree so that several J values can be determined by SQUID magnetometry. A search of the literature to find more extended π-systems to reduce the magnitude of the spin density at the oxygen atoms was done, and it was found that when heterocycles are conjugated to phenoxy radicals[23] or methylenecyclopropanes[24] they can greatly modulate the spin density. An example of

a possible ligand that utilizes both an extended π-system and a heterocyclic ring is the phenazine ligand,[25] which is a catechol-type ligand that is depicted in Figure 6-1.

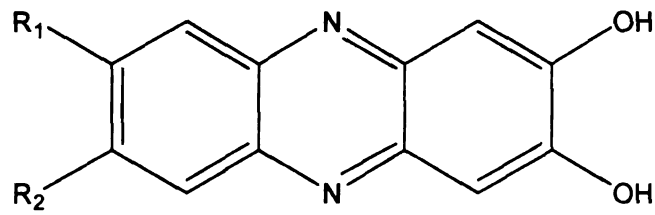

Figure 6-1. Phenazine ligand.

Table 6-1. NPA spin density comparison between the phenanthrenesemiquinone (PSQ), coronenesemiquinone (coronene-SQ), 2,3-anthrasemiquinone (ASQ), and phenazinesemiquinone (phenazine-SQ).

Complex	Avg. spin at O
PSQ	0.25703
coronene-SQ	0.21968
ASQ	0.20605
phenazine-SQ	0.17522

Preliminary DFT studies indicate that the spin density at the oxygen atoms in phenazine-semiquinone is greatly decreased compared to the PSQ ligand as shown in Table 6-1. Additionally, coronenesemiquinone[26] and 2,3-anthrasemiquinone (ASQ) also decrease spin density at the oxygen centers, but to a lesser extent. A broken symmetry DFT calculation was done with $[Ni(tren)(ASQ)]^+$ (Figure 6-2), to ascertain if the above changes in spin density would be reflected in the exchange coupling constant. Using the ASQ ligand (which is an isomer of phenanthrenesemiquinone) the resulting J value was calculated to be -109 cm^{-1} compared to the -258 cm^{-1} value for $[Ni(tren)(PSQ)]^+$ complex, using the same UB3LYP functional and 6-311g** basis set. This decrease in J corresponds to a reduction of 48 % in the magnitude compared to the Ni-PSQ complex. Based upon the DFT data either the ASQ or phenazine nickel complexes would be

excellent candidates for further research. Synthetic procedures for the 2,3-anthracatechol[27,28] and phenazine[25] ligands are known, and similar reactions used to make the Ni-PSQ complex could then be applied to make the Ni-ASQ or Ni-phenazine-SQ compounds.

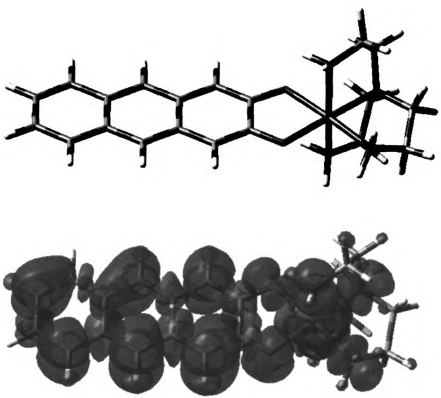

Figure 6-2. Calculated structure (top) and total spin density plot (bottom) for $[Ni(tren)(ASQ)]^{+}$.

If measurable temperature dependence in the magnetic susceptibility of either unsubstituted nickel complex is observed in the SQUID experiments, then the *J* value could possibly be experimentally determined. Subsequent substituted Ni-ASQ or Ni-phenazine-SQ complexes can then be synthesized to examine any substituent effects on the magnitude of the exchange coupling constant. If the DFT predictions hold, then we should be able to experimentally determine the *J* value for a series of complexes and

verify or disprove our hypothesis for the spin density at the paramagnetic centers modulating the exchange coupling constant. Therefore, there are many fruitful avenues in theoretical chemistry, EPR spectroscopy, and synthetic chemistry to pursue in the future work of this project.

6.3 References

1. Shultz, D. A.; Sloop, J. C.; Washington, G. *J. Org. Chem.* **2006,** 71, 9104.

2. Luneau, D. *Curr. Opin. Solid State Mater. Sci.* **2001,** 5, 123.

3. Öhrstrom, L. *C. R. Chimie* **2005,** 8, 1374.

4. Shultz, D. A. *Polyhedron* **2001,** 20, 1627.

5. Caneschi, A.; Gatteschi, D.; Sessoli, R.; Rey, P. *Acc. Chem. Res.* **1989,** 22, 392.

6. Vostrikova, K. E. *Coord. Chem. Rev.* **2008,** 252, 1409.

7. Stumpf, H. O.; Ouahab, L.; Pei, Y.; Grandjean, D.; Kahn, O. *Science* **1993,** 261, 447.

8. Hoganson, C. W.; Babcock, G. T. *Science* **1997,** 277, 1953.

9. Itoh, S.; Taki, M.; Fukuzumi, S. *Coord. Chem. Rev.* **2000,** 198, 3.

10. Whittaker, M. M.; Ekberg, C. A.; Peterson, J.; Sendova, M. S.; Day, E. P.; Whittaker, J. W. *J. Mol. Catal. B.: Enzym.* **2000,** 8, 3.

11. Robotham, B.; O'Malley, P. J. *Biochemistry* **2008,** 47, 13261.

12. Lendzian, F.; Huber, M.; Isaacson, R. A.; Endeward, B.; Plato, M.; Bönigk, B.; K., M.; Lubitz, W.; Feher, G. *Biochimica et Biophysica Acta* **1993,** 1183, 139.

13. Prokhorova, T. G.; Simonov, S. V.; Khasanov, S. S.; Zorina, L. V.; Buravov, L. I.; Shibaeva, R. P.; Yagubskii, E. B.; Morgunov, R. B.; Foltynowicz, D.; Świetlik, R. *Synth. Met.* **2008,** 158, 749, and references therein.

14. Zhang, H. Y.; Ji, H. F. *J. Mol. Struct. THEOCHEM* **2003,** 663, 167.

15. Zhang, H. Y.; Wang, X. L.; Sun, Y. M. *J. Mol. Des.* **2003,** 2, 262.

16. Broze, M.; Luz, Z. *J. Chem. Phys.* **1969,** 51, 738.

17. Borhan, B.; Nazarian, S.; Stocking, E. M.; Hammock, B. D.; Kurth, M. J. *J. Org. Chem.* **1994,** 59, 4316.

18. Kol, M.; Rozen, S. *J. Org. Chem.* **1993,** 58, 1593.

19. Piekara-Sady, L.; Kispert, L. D. *Handbook of Electron Spin Resonance.* AIP Press: New York, 1994; Vol. 1, p 311-357.

20. Möbius, K.; Plato, M.; Lubitz, W. *Phys. Rep.* **1982,** 87, 171.

21. Kay, C. W. M.; Feicht, R.; Schulz, K.; Sadewater, P.; Sancar, A.; Bacher, A.; Möbius, K.; Richter, G.; Weber, S. *Biochemistry* **1999,** 38, 16740.

22. Ma, H.; Cai, F.; Liu, C.; Jiang, Y. *J. Chem. Phys.* **2005,** 122, 104909.

23. Xie, C.; Lahti, P. M.; George, C. *Org. Lett.* **2000,** 2, 3417.

24. Creary, X. *Acc. Chem. Res.* **2006,** 39, 761.

25. Seillan, C.; Brisset, H.; Siri, O. *Org. Lett.* **2008,** 10, 4013.

26. Rieger, R.; Kastler, M.; Enkelmann, V.; Müllen, K. *Chem. Eur. J.* **2008,** 14, 6322.

27. Green, A. *J. Chem. Soc.* **1927**, 554.

28. Pozzo, J. L.; Clavier, G. M.; Colomes, M.; Bouas-Laurent, H. *Tetrahedron* **1997,** 53, 6377.